Identification of novel target genes of the PTH-activated NACA transcriptional coregulator in bone

Hadla M. Hariri

Department of Human Genetics

McGill University, Montreal, Canada

July 2020

A thesis submitted to McGill University in partial fulfillment of the requirements of the degree of

Doctor of Philosophy

Table of Contents

ABSTRACT

The daily injection of parathyroid hormone (PTH) increases bone mass and protects against osteoporotic fractures, however a complete picture of its mechanism of action is still missing. We have shown that PTH induces the phosphorylation of the DNA-binding protein Nascent polypeptide associated complex And Coregulator alpha (NACA), leading to nuclear translocation of NACA and activation of target genes. We performed Chromatin Immunoprecipitation with deep sequencing (ChIP-Seq) against NACA with parallel RNA-sequencing in PTH-treated osteoblast cells. This approach illuminated two novel downstream targets of the PTH-NACA axis in osteoblasts: the nuclear factor interleukin-3-regulated (*Nfil3*) and the ubiquitin specific peptidase 53 (*Usp53*). Our data show that the transcriptional activity of *Nfil3* is activated by the binding of NACA and CREB to its proximal promoter, following PTH induction. Additionally, our differentiation assays of *Nfil3*-knockdown cells reveal a distinct function for *Nfil3* in osteoblasts vs osteocytes, by modulating their differentiation in opposing fashions. Our results serve as the first mechanistic characterization of *Nfil3* transcription and function in osteoblasts. Moreover, our work identified *Usp53* as a novel target of PTH signaling in osteoblasts and uncovered a mechanism involving NACA,JUN, and CREB tuning its transcription. A great deal of our work focused on uncovering the biological function of *Usp53* during development. We show here that USP53 regulates mesenchymal cell lineage selection *in vitro* and *in vivo*. The phenotypic characterization of *Usp53* null mice reveals severe alterations in bone and adipose tissues. The global ablation of *Usp53* leads to low bone mass due to increased osteoclastogenesis and impairs adipogenesis. We also show that USP53 regulates adipogenic commitment and differentiation of mesenchymal cells, osteoblast terminal differentiation, and *Rankl* expression. The underlying mechanism defining USP53 functions involves the interaction with the TAK1/TAB1/TAB2 complex affecting its assembly and signaling. This is the first study uncovering the contribution of *Usp53* to developmental processes and revealing the molecular cascades underlying *USP53*-related pathologies in human. Collectively, the characterization of *Nfil3* and *Usp53* has proven that their biological significance extends beyond PTH signaling regulation to cover crucial developmental processes in multiple tissues.

RÉSUMÉ

L'injection quotidienne d'hormone parathyroïdienne (PTH) augmente la masse osseuse et protège contre les fractures ostéoporotiques. Cependant, le mécanisme d'action n'est pas complètement élucidé. Nous avons démontré que la PTH induit la phosphorylation d'une protéine qui se lie à l'ADN, le complexe associé au polypeptide naissant et corégulateur alpha (NACA). Ceci entraîne la translocation nucléaire de NACA et l'activation de gènes cibles. Nous avons effectué une immunoprécipitation de la chromatine avec un séquençage en profondeur (ChIP-Seq) contre le NACA ainsi qu'en parallèle, un séquençage de l'ARN (RNA-Seq) d'ostéoblastes traités à la PTH. Cette approche a permis d'identifier deux nouvelles cibles en aval de l'axe PTH-NACA dans les ostéoblastes : le facteur nucléaire régulé par l'interleukine-3 (*Nfil3*) et la peptidase 53 spécifique de l'ubiquitine (*Usp53*). Ensuite, nous avons démontré que l'activité transcriptionnelle de *Nfil3* est activée par la liaison de NACA et de CREB à son promoteur proximal, en réponse à la PTH. De plus, nos tests de différenciation dans des cellules déficientes en *Nfil3* suggèrent que cette protéine a une fonction distincte dans les ostéoblastes comparativement aux ostéocytes et module leur différenciation de manière opposée. Nos résultats sont les premiers à caractériser le mécanisme de transcription et la fonction de *Nfil3* dans les ostéoblastes. La deuxième cible identifiée de la signalisation de PTH dans les ostéoblastes est l'*Usp53*. Nous avons découvert que sa transcription est régulée par un mécanisme impliquant NACA, JUN et CREB. Nous nous sommes particulièrement intéressés à élucider le rôle de *Usp53* durant le développement embryologique. Nous montrons ici que l' USP53 régule la sélection de la lignée de cellules souches mésenchymateuses *in vitro* et *in vivo*. Ensuite, la caractérisation phénotypique des souris déficientes en *Usp53* révèle des changements importants au niveau des tissus osseux et adipeux. L'ablation globale de l'*Usp53* altère l'adipogenèse et entraîne une faible masse osseuse suite à une ostéoclastogenèse augmentée. Nous montrons également que USP53 régule la différenciation des cellules souches mésenchymateuses en adipocytes, la différenciation terminale des ostéoblastes et l'expression de *Rankl*. La fonction de USP53 dépend étroitement de son interaction avec le complexe TAK1/TAB1/TAB2, en modulant son assemblage et sa signalisation. Cette thèse est la première étude à découvrir la contribution d'*Usp53* aux processus développementaux. Elle révèle aussi les cascades moléculaires sous-jacentes aux pathologies liées à *USP53* chez l'homme. Collectivement, la caractérisation de *Nfil3* et *Usp53* a prouvé que leur importance biologique

s'étend au-delà de la régulation de la signalisation de la PTH et englobe des processus développementaux cruciaux dans de multiples tissus.

LIST OF ABBREVIATIONS

μm	Micrometer
nm	Nanometer
ABCC	ATP Binding Cassette Subfamily C Member
ABR	Auditory Brainstem Response
ACAN	Aggrecan
Acp5	Acid Phosphatase 5, Tartrate Resistant
AD	Activating domain
AdipoQ	Adiponectin
ALP	Alkaline phosphatase
AP-1	Activator protein 1
ATF4	Activating transcription factor 4
ATP	Adenosine triphosphate
BAT	Brown adipose tissue
BD	Binding domain
BFR	Bone formation rate
BM	Bone marrow
BMAT	Bone marrow adipose tissue
BMI	Body mass index
BMP2	Bone morphogenetic protein 2
BMSC	Bone marrow stem cell
BRC	Bone remodeling compartment
BS	Bone surface
BSA	Bovine serum albumin
BSP	Bone sialoprotein
BTF3	Basic transcription factor 3
BV	Bone volume
BV/TV	Bone volume/tissue volume
cAMP	Cyclic adenosine monophosphate

CCD	Cleidocranial dysplasia
C/EBP	CCAAT enhancer-binding proteins
CFU	Colony forming unit
ChIP	Chromatin Immunoprecipitation
ChIP-reChIP	Sequential chromatin immunoprecipitation
ChIP-Seq	Chromatin Immunoprecipitation with deep sequencing
CHX	Cycloheximide
CIDEA	Cell death-inducing DNA fragmentation factor alpha-like effector A
CK2	Casein kinase 2
CLS	Coffin Lowry syndrome
CM	Centimeter
CMV	Cytomegalovirus
Col1α1	Collagen, type I, α 1
CREB	Cyclic AMP-responsive element-binding protein
CTHRC1	Collagen triple helix repeat containing 1
Ctsk	Cathepsin K
Ct.Th	Cortical Thickness
CTX	Carboxyl-terminal collagen crosslinks
ΔDBD	Deletion in DNA binding domain
DBD	DNA binding domain
dLs/BS	Double-labeled surface/bone surface
DLX5	Distal-Less Homeo box 5
DMP1	Dentin Matrix Acidic Phosphoprotein 1
DNA	Deoxyribonucleic acid
DUB	Deubiquitinating enzyme
E	Embryonic day
EBPRE	E4BP4 response element
ECM	Extracellular matrix
EDTA	Ethylenediaminetetraacetic acid tetrasodium salt dihydrate
EMSA	Electrophoretic mobility shift assay
ERK1/2	Extracellular-signal regulated kinases 1/2

ES	Embryonic stem cells
EUCOMM	European Conditional Mouse Mutagenesis
EuMMCR	European mouse mutant cell repository
FABP4	Fatty acid binding protein 4
FBS	Fetal bovine serum
FDA	U.S Federal and Drug administration
FGF23	Fibroblast growth factor 23
FGFR1	Fibroblast growth factor receptor 1
FKBP1	FK506-binding protein 1A
c-FOS	FBJ osteosarcoma oncogene
FPKM	Fragments per kilobase of exon per million fragments mapped
β-Gal	Beta- Galactosidase
GAPDH	Glyceraldehyde-3-phosphate dehydrogenase
GFP	Green fluorescent protein
GLUT4	Glucose transporter 4
GP	Growth plate
GPRC	G protein-coupled receptor class C group 6 member A
GSK3β	Glycogen synthase kinase 3beta
HDAC	Histones deacetylases
HET	Heterozygous
HFSC	Hair follicle stem cells
HMGU	Helmholtz München German Research Centre for Environmental Health
HPLC	High performance liquid chromatography
HRP	Horseradish peroxidase
IB	Immunoblotting
IBMX	3-Isobutyl-1-methylxanthine
ID (1st)	Indentation Distance, first cycle
IDG-SW3	Immortomouse/Dmp1-GFP-SW3
IDI	Indentation Distance Increase
IFNγ	Interferon gamma

IGF-1	Insulin-like growth factor 1
IgG	Immunoglobulin G
IHH	Indian hedgehog
ILK	Integrin-linked kinase
IP	Immunoprecipitation
JNK	c-Jun N-terminal kinase
c-JUN	Jun proto-oncogene
JUND	Jun D proto-oncogene
KCNJ	G protein-activated inward rectifier potassium channel
kDa	Kilodaltons
KLF	Kruppel-like factors
KO	Knockout
KOMP	Knockout Mouse Project
LDL	Low density lipoprotein
LEF1	Lymphoid Enhancer Binding Factor 1
LRP6	LDL receptor related protein 6
Luc	Luciferase gene
MAPK	mitogen-activated protein kinase
MAR	Mineral Apposition Rate
MAT	Marrow adipose tissue
M-CSF	Macrophage colony-stimulating factor
MEF	Mouse embryonic fibroblasts
MEPE	Matrix extracellular phosphoglycoprotein
MGP	Matrix Gla protein
MicroCT/μct	Micro-computed tomography
MMI	Mean Moment of Inertia
MMP13	Matrix Metalloproteinase 13
MS	Mass Spectrometry
MS/BS	Mineralizing surface/bone surface
MSX2	Msx homeobox 2
Mut	Mutant

MW	Molecular weight
MYC	MYC Proto-Oncogene, BHLH Transcription Factor
Myf5	Myogenic factor 5
MYOZ	Myozenin
NAC	Alpha chain of the nascent-polypeptide-associated complex
NACA	Nascent polypeptide Associated Complex and coregulator alpha
NE	Nuclear extract
Nfatc1	Nuclear factor of activated T cells, cytoplasm, calcineurin dependent 1
NFIL3	Nuclear Factor, Interleukin 3 Regulated
Notch1	Translocation-Associated Notch Protein TAN-1
OB	Osteoblast
OC	Osteoclast
OCN	Osteocalcin
Ocyte	Osteocyte
OMIM	Online Mendelian Inheritance in Man
OPG	Osteoprotegerin
OPN	Osteopontin
OSCAR	Osteoclast-associated immunoglobulin-like receptor
OST-PTP	Osteotesticular protein tyrosine phosphatase
OSX	Osterix
OTUD4	OTU Deubiquitinase 4
P	Postnatal day
P38	Mitogen-Activated Protein Kinase P38 Alpha
PDGF-BB	Platelet-derived growth factor-BB
PGC1α	PPARγ co-activator-1α
PGE	Prostaglandin E2
PHEX	Phosphate regulating endopeptidase homolog X-linked
PINP	Procollagen type I N propeptide
PKA	Protein Kinase A
PLC	Phospholipase C
PMMA	Poly methyl methacrylate

POC	Primary ossification center
PPARγ	Peroxisome proliferator- activated receptor gamma
PRDM16	PRD1-BF-1-RIZ1 homologous domain-containing protein-16
PTH	Parathyroid Hormone
PTH1R	Parathyroid hormone receptor 1
PTM	Post-translational modification
PYD	Post yield displacement
qPCR	Quantitative polymerase chain reaction
RANKL	Receptor activator of nuclear factor-kB ligand
RBC	Red Blood Cells
RE	Response Element
RNA	Ribonucleic acid
RNA-Seq	RNA Sequencing
ROI	Region of interest
RPI	Reference Point Indentation
RUNX	Runt-related transcription factor
RXR	Retinoid X Receptor
SARS	Severe acute respiratory syndrome
SATB2	Special AT-rich sequence binding protein 2
SEMA	Semaphorin 4D
shRNA	Small hairpin ribonucleic acid
SIRP	Signal Regulatory Protein Beta 1
SIRT	Sirtuin 1
SLC2A4	Solute Carrier Family 2 Member 4
sLs/BS	Single-Labeled surface/bone surface
SOC	Secondary ossification center
SOST	Sclerostin
SOX9	SRY-Box Transcription Factor 9
SPARC	Secreted protein acidic and rich in cysteine
SS	Super Shift
SUMO	Small ubiquitin-like modifier

TAB1/2	TGF-Beta Activated Kinase 1 (MAP3K7) Binding Protein 1/2
TAK1	Mitogen-Activated Protein Kinase 7
Tb.N	Trabecular Number
Tbp	TATA-Box Binding Protein
Tb.Th	Trabecular Thickness
TF	Transcription factor
T/F J	Tibia-Fibula Junction
TGF-β	Transforming Growth Factor, beta
TID	Total indentation distance
TJP1/2	Tight junction proteins 1/2
TNFα	Tumor Necrosis Factor α
TRAcP 5b	Tartrate-resistant acid phosphatase 5b
TRAF6	TNF Receptor Associated Factor 6
TRAP	Tartrate resistant acid phosphatase
TREM-2	Triggering Receptor Expressed On Myeloid Cells 2
TSS	Transcription Start Site
Ucp-1	Uncoupling Protein 1
US	Unloading slope
USP	Ubiquitin specific peptidase
Usp53	Ubiquitin Specific Peptidase 53
USPL	Ubiquitin Specific Peptidase Like 1
VDR	Vitamin D Receptor
VEGFA	Vascular endothelial growth factor A
WAT	White adipose tissues
WNT	Wingless integrated
WT	Wild type
X-Gal	5-Bromo-4-Chloro-3-Indolyl β-D-Galactopyranoside

LIST OF FIGURES

LIST OF TABLES

ACKNOWLEDGMENTS

To my family, friends, and fans in Lebanon, and all over the world….

Foremost, I would like to first express my gratitude to my supervisor Dr. René St-Arnaud for his mentorship throughout my PhD. Without your invaluable support and guidance, it would have been impossible to write this doctoral thesis during a lockdown. Your keen scientific interest, dedication, and continuous encouragement have been crucial to my scientific growth.

I would like to extend my sincere gratitude to my supervisory committee members, Dr. Pierre Moffatt and Dr. Robert Sladek, for sharing their knowledge and giving useful feedback over the years. I would also like to thank the *Réseau de recherche en santé buccodentaire et osseuse* (RSBO) and McGill University for granting me two consecutive fellowships over the period of my PhD. Also, I would like to acknowledge Dr. Aimee Ryan and Dr. Anna Naoumova for their departmental assistance and support. A big thank you to Ross Mackay for his departmental assistance, support, and help in resolving all problems.

St-Arnaud's research group is a source of positive energy and a good example of a thriving and welcoming scientific environment. Special thanks to Alice Arabian for her assistance in the laboratory. Her positive and friendly attitude is exceptional. Big thanks to the animal facility technicians Mia Esser, Louise Marineau, and Alexandria Norquay as well as Mark Lepik for his talented graphic designing work. My appreciation also goes to past and present lab members, especially Martin Pellicelli, Corine Martineau, Bahareh Hekmatnejad, and Toghrul Jafarov. To the lab gang that has made this long journey fantastic and joyful, gratitude goes to Abhinav Parashar, Lilit Antonyan, Caitlin Anderson, and Ajay Sahai. I would like to thank Lisa Lamplugh, Hadil Al-Jallad, Paul Richard, and Kerstin Tiedemann for the nice chats and positive vibes. To the Shriners community including the staff, employees, and researchers, it was a pleasure to interact with you over the years.

Waves of gratefulness go to William Addison in Japan, who contributed to my scientific progress and accomplishments, by passing his immense knowledge and sincere friendship over the years. To my master's supervisor Georges Nemer (L3amid), you are my life-time mentor, and a role model. Loads of love goes to Mazen Kurban, Inaam El-Rassy, Mohammad Iskander,

Dina Farran, and Farah Abed-Ali for their precious friendship. To friends who have been always there for me, gratitude goes to Stephaine Saikaly (namli), Charles-De-Gaulle Saloum (charlitto), Michael Forster, and Dominic Nelson.

Finally, the Oscars goes to my small family in Canada, Amanda Gerges (Raba) and Renata Bahous (Borto). This would not have been possible without you guys.

CONTRIBUTIONS TO ORIGINAL KNOWLEDGE

The report presented herein is an accumulation of findings characterizing novel target genes of parathyroid hormone (PTH) signaling in bone.

Briefly, **chapter III** serves as the first report to characterize the transcriptional regulation and function of *Nfil3* in osteoblasts *in vitro.* This characterization of *Nfil3* transcription and function is highly significant and opens the door for an investigation of its function during bone development *in vivo*.

Moreover, the bulk of the work invested to finalize this report is placed in **chapters IV and V**. We focused on examining the biological function of *Usp53 in vitro* (**chapter IV**) and *in vivo* (**chapter V**). We are the first to report the regulation of *Usp53* in response to PTH stimulation in bone. This is the first characterization of *Usp53* function in regulating mesenchymal stem cell lineage selection *in vitro* and *in vivo*. The phenotypic characterization of *Usp53* null mice (generated in our laboratory) reveals prominent developmental defects in skeletal and many other tissues. The identified molecular pathways offer a mechanism by which USP53 functions as a master regulator of developmental processes. Finally, our findings stand as the first and only to highlight the biological function of *Usp53* during development and its relevance to *USP53*-associated diseases in human.

Altogether, our findings will help broaden our basic understanding of bone and fat biology as well as PTH action in bone. This can have potential implications on developing anabolic treatments for skeletal bone diseases.

FORMAT OF THE THESIS

This thesis is written in the traditional format and is comprised of seven chapters. **Chapter I** is the introduction and comprises a review of the literature pertaining to this thesis as well as the rationale and goals of the thesis. Part of **Chapter I (section1.8)** was adapted from my literature review article entitled " *New PTH Signals Mediating Bone Anabolism*" published by Hariri et al. in 2017.

Chapter II details the materials and methods relevant to this thesis.

The work presented in **chapters III, IV, and V** summarizes the research findings and results of the study. These chapters are the bases of three separate manuscripts.

Chapter III focuses on the transcriptional characterization of *Nfil3* in osteoblasts and its distinct functions in osteoblasts and osteocytes. **Chapter III** presents results of a manuscript currently in press in Bone journal. The manuscript was accepted for publication in **Bone** journal. **DOI: 10.1016/j.bone.2020.115624.**

Chapter IV focuses on the *in vitro* characterization of *Usp53* transcription in osteoblasts and its contribution to mesenchymal stem cell differentiation. **Chapter IV** presents results of a manuscript accepted with revisions for publication in the journal of **Molecular and Cellular Biology, MCB00292-2)**.

Chapter V focuses on the *in vivo* characterization of *Usp53* functions during development. **Chapter V** presents results of a manuscript in preparation. We are finishing some experiments that were interrupted due to the crisis caused by SARS-CoV-2 virus.

Connecting texts between **chapters III** to **V** provide a link between the different data chapters.

Chapter VI is a discussion of all the data chapters. **Chapter VII** discusses future directions and conclusions.

CONTRIBUTION OF AUTHORS

Chapter III: Hadla Hariri and **Dr. René St-Arnaud** designed the study**. Hadla Hariri and Martin Pellicelli** generated the data. **Hadla Hariri** and **Dr. René St-Arnaud** participated in data analysis and interpretation. **Dr. René St-Arnaud** obtained the funding. **Hadla Hariri** wrote the initial draft of the manuscript and **Dr. René St-Arnaud** edited the final version of the manuscript:

Hadla Hariri, Martin Pellicelli, René St-Arnaud. *Nfil3, a target of the NACA transcriptional coregulator, affects osteoblast and osteocyte gene expression differentially*. **Bone. DOI: 10.1016/j.bone.2020.115624.**

Chapter IV: Hadla Hariri generated all the data. **Dr. William N. Addison and Hadla Hariri** performed the surgery for the *in vivo* osteogenesis assay. **Hadla Hariri, Dr. William N. Addison, and Dr. René St-Arnaud** participated in data analysis and interpretation as well as study design. **Dr. René St-Arnaud** obtained the funding. **Hadla Hariri** wrote the initial draft of the manuscript and **Dr. René St-Arnaud** edited the final version of the manuscript, which was reviewed by **Dr. William N. Addison:**

Hadla Hariri, William N. Addison, René St-Arnaud. *Ubiquitin specific protease USP53 regulates osteoblast versus adipocyte lineage commitment*. Manuscript accepted with revisions for publication in **Molecular and Cellular Biology. MCB00292-2.**

Chapter V: Hadla Hariri generated all the data. **Dr. William N. Addison and Hadla Hariri** performed LacZ staining of tissues, osmium staining of bones, and mass spectrometry. **Hadla Hariri, Dr. William N. Addison, and Dr. René St-Arnaud** participated in data analysis and interpretation as well as study design. **Dr. René St-Arnaud** obtained the funding. The results will be included in a manuscript written by **Hadla Hariri** and reviewed by **Dr. René St-Arnaud** and **Dr. William N. Addison.**

Hadla Hariri, William N. Addison, René St-Arnaud. *Usp53* regulates mesenchymal stem cell differentiation and bone turnover *in vivo.* **In preparation**

Chapter I: INTRODUCTION

1.1 Bone tissue

Bone is a dynamic connective tissue framing all body parts. Bone serves some static structural functions. The skeleton supports body parts positioning and alignment. It also provides a protective shield to vital internal organs and attachment nodes to contracting muscles. Loaded with minerals, the bone matrix traps the largest reservoir of calcium and phosphate in the form of hydroxyapatite deposits; a main source for ions to maintain mineral homeostasis (1). Bone extracellular matrix (ECM) hosts organic molecules including type I collagen fibers, noncollagenous proteins, water, and lipids (1, 2). Bone cavities are filled with red bone marrow, the primary site of hematopoiesis. The interaction among these different components contribute to the mechanical and metabolic actions of bone.

Skeletal development is one of the hallmarks that differentiate vertebrates from invertebrates. During early embryonic development, the coordinates of each skeletal entity is determined through a process called skeletal patterning. Mesenchymal condensation is a process by which different mesenchymal cells aggregate to contribute to future skeletal elements. Three main mesenchymal cell lineages give rise to the skeleton. Neural crest cells give rise to craniofacial bone and the lateral plate mesoderm forms limb skeleton (3). The somites, segmented mesodermal structures lining the neural tube, give rise to most of the axial skeleton, striated muscle, and dorsal dermis (3, 4). Skeletal patterning is controlled by temporal and spatial-dependent signalling among different cell types and morphogens. One example of this is the anterior-posterior symmetrical patterning of vertebral columns, a process driven by a tight signalling gradient and oscillations (4).

Ossification is another crucial process during skeletal development. It involves two mechanisms: intramembranous and endochondral ossification. Osteochondral progenitor cells undergo intramembranous ossification to form the membranous bone. Examples include the formation of the flat bones of the skull, the mandible, and the clavicles. During endochondral ossification, osteochondral progenitors differentiate into chondrocytes to form a cartilage template for the newly deposited bone. This is the process by which long bones and all other bones are formed (3). We will describe the underlying mechanisms of ossification in the next sections.

1.2 Bone Cells

Three main cell types orchestrate the regeneration of the skeleton through remodeling cycles: 1) osteoblasts; 2) osteocytes; and 3) osteoclasts.

Osteoblasts, the bone-forming cells, are of mesenchymal origin. Mesenchymal stromal/stem cells (MSCs) are multipotent cells capable of self-renewal and differentiation into osteoblasts, chondrocytes, adipocytes, and myocytes. MSCs and osteoprogenitors reside in the bone marrow and general circulation. They are the precursors of osteoblasts. They give rise to osteoprogenitors, which differentiate into preosteoblasts and then mature into fully functional osteoblasts and ultimately osteocytes. The osteogenic differentiation of MSCs is controlled by unique molecular signalling, transcription factors (5, 6), and epigenetic modifications (7-9). Mechanical stimulation has been added to the list of factors enhancing the osteogenic-lineage commitment of MSCs (10) and osteoblast differentiation (11).

Osteoblasts are the building blocks of the skeleton, lining bone surfaces . Episodes of bone formation involves the production of vast quantities of type I collagen protein (COL1A1) and subsequent deposition of several noncollagenous proteins. Noncollagenous proteins include ones with glycan moieties such as: bone sialoprotein (BSP), osteonectin (SPARC), and osteopontin (OPN) and vitamin-K-carboxylated proteins such as: osteocalcin (OCN) and matrix gla protein (MGP). Concomitantly, mature osteoblasts produce alkaline phosphatase (ALP), a classical bone differentiation marker. These events support calcium deposition and proper matrix mineralisation. In the final stages of maturation, some osteoblasts are recruited to bone surfaces and some undergo apoptosis. Another subset of osteoblasts undergoes terminal differentiation and converts into osteocytes. The mechanism behind those decisions is yet to be determined.

Osteocytes are the most abundant (90-95%) cell type in bone tissues. They are derived from bone-forming osteoblasts that got trapped in the bone matrix (12, 13). Osteocytes reside in fluid-filled cavities referred to as “lacunae” and interact with each other and with osteoblasts and osteoclast precursors by dendrite-like extensions. Those appendages travel through the bone in canals referred to as “canaliculi” and radiate past the bone surface to reach the bone marrow. The terminal differentiation of these cells makes them distinct from their osteoblast ancestors at the level of morphology, function, and gene expression pattern (14, 15).

As compared to osteoblasts, osteocytes express a set of unique markers including: E11/gp38, Dentin Matrix Protein 1 (DMP1), matrix extracellular phosphoglycoprotein (MEPE), and phosphate-regulating neutral endopeptidase on the chromosome X (Phex). The expression of the fibroblast growth factor (FGF23) and the WNT-inhibitor sclerostin (SOST) is typical of mature osteocytes. Mature osteocytes also express "osteoclast"specific genes such as Cathepsin K and tartrate- resistant acid phosphatase (TRAP). The identification of these markers helped assign new functions for osteocytes.

Thought to be a passive resident of the bone matrix, emerging studies have highlighted the dynamic role of osteocytes in regulating bone remodeling and mineralisation. Osteocytes drive and regulate collagen-mediated mineralisation of the bone matrix (16) and act as an endocrine entity influencing both local and systemic mineral metabolism (13). The secretion of fibroblast growth factor 23 (FGF-23) is one example where osteocytes regulate phosphate homeostasis, targeting distant organs such as the kidney and the heart (17-19). Moreover, osteocytes act as mechanosensors responding to mechanical loading and unloading by fluid-flow shear stress, via a mechanism involving prostaglandin E2 (PGE2) and the Wnt/β-catenin pathway (20, 21). As modulators of bone formation and resorption, mature osteocytes produce sclerostin; the gene product of *SOST* to inhibit bone formation (22-24) and activate osteoclast-specific genes to remodel the perilacunar matrix during lactation (25, 26).

Osteoclasts are the sole bone-resorbing cells in the skeleton. They are polykaryons derived from mononuclear cells of the monocyte/macrophage cell lineage of hematopoietic origin. Osteoclastogenesis is initiated and controlled by the expression of two major cytokines, the receptor activator of nuclear factor-κB ligand (RANKL) (27) and the macrophage colony-stimulating factor (M-CSF) (28). RANKL is the master regulator of osteoclastogenesis, essential for the formation and activation of osteoclasts (29-31), whereas M-CSF is required for the survival, proliferation, and differentiation of osteoclast precursors (28). Both cytokines regulate signaling pathways critical for osteoclast maturation and its cytoskeletal organization. Shortly after RANKL stimulation, the nuclear factor of activated T cells, cytoplasmic 1 (NFATc1) is induced (32). NFATc1, an important modulator of osteoclast differentiation, is stimulated by calcium influxes, regulating its own promoter in addition to several osteoclast-specific promoters such as cathepsin K and TRAP (33, 34).

In response to M-CSF and RANKL, osteoclast precursors from the bone marrow or circulation migrate to resorption sites, attach to bone matrix, and differentiate into mature multinucleated osteoclasts. Osteoclasts are recruited to prospective resorption sites via integrin α1/β3, creating acidified sealing zones (28). The combined action of proton pumps (H^+- ATPase) and Cl^- channels acidify the resorptive milieu (35) and attract acidified vesicles with cargos of hydrochloric acid (HCl) and acidic proteases such as cathepsin K, MMP9, and MMP13 (36). The secretion of acid and proteases mobilizes the mineralized matrix and degrades its organic matrix.

RANKL is mainly produced by osteoblast- lineage cells including osteoblasts and osteocytes (37, 38). Recent studies have identified marrow adipocytes as a new source for RANKL (39). Osteoclast differentiation and activity have been extensively studied in the context of RANKL signaling. The binding of RANKL to its receptor RANK stimulates the activation of TNF receptor-associated factor (TRAF) 6 and transforming growth factor β-activated kinase 1 (TAK1), that will lead to the subsequent activation of MAPKs including JNK and P38 (40, 41). RANKL can also induce NF-κB as well as cyclic AMP-responsive element-binding protein (CREB) to upregulate the expression of c-Fos, a component of the activator protein 1 (AP-1) complex. This pathway along with others assisted by costimulatory receptors (OSCAR, PIR-A, SIRPβ1 and TREM-2) cooperate to activate calcium signaling and ensure a robust induction of NFATc1 and other osteoclast-specific genes (42-44).

1.3 The biology of bone remodeling

The mineralized skeleton goes through continuous cycles of remodeling. The tightly coupled activities of bone-resorbing osteoclasts and bone-forming osteoblasts ensure proper bone repair. Bone remodeling is carried out by an active bone-remodeling unit, involving four major types of bone cells: osteoblasts, osteocytes, bone-lining cells, and osteoclasts (Figure 1.1).

Osteocytes orchestrate both bone resorption and bone formation events to maintain normal bone mass. Accumulating evidence suggests that osteocytes can sense bone deformations caused by either mechanical loading or microdamage (45). Ligand production by osteocytes stimulates the recruitment and activation of osteoclast precursors (45, 46) from the general circulation by crossing the bone-lining cell monolayer or from capillaries that innervate the remodeling unit. In response to high levels of M-CSF and RANKL, osteoclast precursors attach

to resorptive sites and differentiate into mature resorbing osteoclasts. This resorptive phase proceeds to dominate the remodeling scene, while the recruitment of osteoprogenitors into the remodeling unit is initiated in the backstage. The recruitment and differentiation of osteoprogenitors into mature osteoblasts continue while resorption is taking place. After this phase, osteoid synthesis by mature osteoblasts becomes the predominant event overtaking bone resorption. This phase allows the remodeling unit to resorb more damaged matrix by osteoclasts, while concurrently depositing more osteoid by osteoblasts. Osteoid synthesis continues even after the termination of bone resorption, thus ensuring a balance between bone resorption and bone formation. Finally, the bone remodeling process is concluded by the mineralization of osteoid deposits, with no net change in bone mass (47). Maintaining the integrity of the coupling process between osteoblasts and osteoclasts is crucial, in order to avoid skeletal pathologies such as osteoporosis and osteopetrosis (2).

As compared to remodeling, bone modeling is the process whereby the skeleton is reshaped by the uncoupled actions of both osteoblasts and osteoclasts, thus bone formation and resorption activities occur in an independent manner spatially and temporally. This process defines bone development and growth as well as skeletal responses to loading and strains (48).

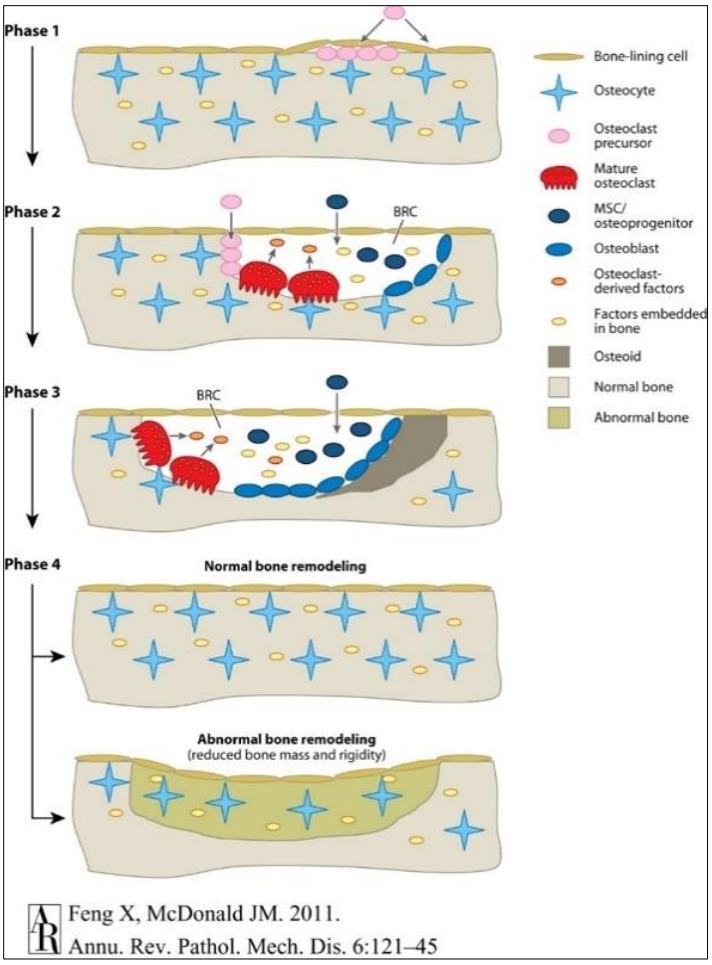

Figure 1. 1 The current model of bone remodeling process.

The remodeling process consists of four major distinct but overlapping phases. Bone remodeling is initiated and activated at specific sites. The second phase of remodeling involves recruitment of osteoclasts, mesenchymal stem cells (MSCs), and osteoprogenitors marking the start of bone resorption in the bone remodeling compartment (BRC). Concurrently, recruited osteoprogenitors will differentiate into osteoblasts and start osteoid synthesis. After overlapping episodes of bone resorption and bone formation, bone remodeling is halted with osteoid mineralization. Normal bone remodeling will lead to no net change in bone mass. However, abnormal remodeling leads to reduced bone mass and strength. (Figure reproduced with permission from the Annual Review of Pathology: Mechanisms of Disease, Volume 6 2011 by Annual Reviews, Feng X, McDonald JM.2011).

1.4 Endochondral ossification

Most of the skeleton is formed by endochondral ossification; a process by which a cartilaginous intermediate is required for bone formation. The traditional mechanism of endochondral ossification has been extensively reviewed (49-53). We can break down this process into five phases: a) mesenchymal condensation; b) chondrogenesis; c) chondrocyte hypertrophy; d) formation of the primary ossification center (POC); e) formation of the secondary ossification center (SOC) (Figure 1.2).

1.4.1 Stages of endochondral ossification

One example of endochondral ossification is the development of limb skeleton. The first phase involves the migration of mesenchymal cell progenitors from the lateral plate mesoderm into the future limb field. During this phase, mesenchymal progenitors proliferate and condense to expand the limb bud and form a cartilage anlage. Episodes of mesenchyme condensation and compaction induce the differentiation of cells within, into mature chondrocytes. Primary ossification starts at embryonic day (E) 14.5-15.5 in rodents. Newly formed chondrocytes (round shape) continue to proliferate, flatten, and align into columns, driving a longitudinal growth of the developing cartilaginous skeleton. The chondrocytes in the proliferating zone produce an extracellular matrix rich in type II collagen (COL2A1) and the proteoglycan aggrecan (ACAN). Chondrocytes close to epiphyseal ends will decrease their proliferation rate whereas flattened chondrocytes (prehypertrophic and hypertrophic) at the center of the growing cartilage rudiments, will further differentiate to initiate hypertrophy. Chondrocyte hypertrophy marks the beginning of the endochondral skeleton calcification and ossification stage. The differentiation of hypertrophic chondrocytes induces a dramatic increase in chondrocyte cell size, and a switch in gene expression from type II collagen to type X collagen (COL10A1). The production of ALP and VEGF drives the calcification and vascularization of the cartilage matrix. These genetic changes will also induce the differentiation of surrounding perichondrial cells into osteoblasts and the vascularization of the calcified cartilage. This will establish the marrow cavity and the POC.

In order to form the POC, terminal hypertrophic chondrocytes secrete the matrix metalloprotease 13 (MMP13) enzyme to degrade calcified matrices (52, 54) and some hypertrophic cells undergo transdifferentiation into osteoblasts (55). The combined and

continuous events of calcified matrix degradation and chondrocyte transdifferentiation, will promote bone formation within the POC. Differentiating osteoblasts derived from perichondrial cells and circulating mesenchymal progenitors will also use the degrading cartilage as a scaffold to form more bone. Collectively, the continuous episodes of chondrocyte proliferation and hypertrophy, calcification and vascularization, cartilage matrix degradation, transdifferentiation, and bone formation will dictate embryonic and postnatal bone growth.

During early post-natal endochondral ossification (P) 7-8, the maturation of epiphyseal chondrocytes gives rise to the SOC. In this context, epiphyseal chondrocytes undergo a similar maturation process like the one described above. The formation of SOC supports the articular cartilage in the articulating joints to bear weights and separate the articular cartilage from growth plate cartilage within the adult endochondral skeleton. The process of endochondral ossification will be terminated, as the cartilage turnover decreases in the adult skeleton. Primary ossification is mainly implicated in longitudinal bone growth, whereas secondary ossification is more involved in the peripheral widening of the bone (51, 56).

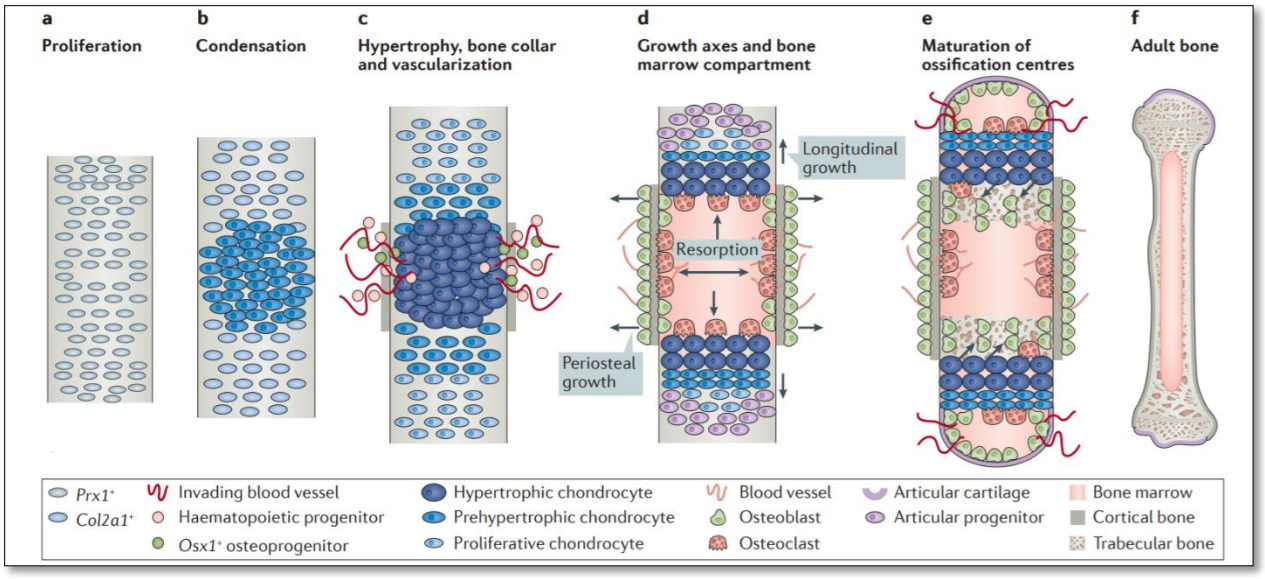

Figure 1. 2 Key steps of endochondral bone formation.

(a and b) $Prx1^+$ progenitors proliferate in the prospective limb bud and undergo mesenchymal condensation near the centre. Mesenchymal condensation drives chondrogenic differentiation of cells expressing Col2α1 and initiate the deposition of a cartilage template. (c and d) Prehypertrophic chondrocytes express high levels of Col10α1 and undergo hypertrophy, thus triggering the formation of a bone collar. Concurrently, blood vessels invade the cartilage template to deliver haematopoietic cells that give rise to resorbing osteoclasts and $Osx1^+$ osteoprogenitors. In the newly formed marrow cavity, resorbing osteoclasts will excavate the cartilage template stimulating longitudinal bone growth and the formation of two opposing growth plates. Periosteal osteoblasts will trigger the periosteal growth and bone widening. (e and f) A second wave of vascularization will give rise to secondary ossification centres, marking the completion of endochondral ossification. (Reproduced by permission from Springer Nature: Nature Reviews Endocrinology, BMP signalling in skeletal development, disease and repair, Salazar VS et al. 2016).

1.4.2 Molecular mediators of endochondral ossification

Multiple transcription factors and developmental pathways are crucial for chondrogenesis and endochondral ossification. Mesenchymal progenitors differentiate into osteochondral progenitors before committing into either chondrocytes or osteoblasts (Figure 1.3).

1.4.2.1 Chondrocyte differentiation

As for chondrocyte differentiation, mature chondrocytes proceed into prehypertrophic and hypertrophic chondrocytes before either undergoing apoptosis or transdifferentiating into osteoblasts. The master regulator of cartilage development is the Sry-box 9 (SOX9) transcription factor. SOX9 is expressed in mesenchymal progenitor cells, osteochondral progenitors, and immature chondrocytes. Along with other SOX factors, SOX9 coordinate mesenchymal condensation driving the transition into chondrocytes (57, 58), while modulating the expression of key chondrogenic factors such as: *Col2a1*, *Col11a1*, *Col9a1*, and *Acan* (59).

Chondrocyte hypertrophy is governed by the balanced expression of several transcription factors including SOX9, runt-related transcription factor 2 (RUNX2), osterix (OSX), runt-related transcription factor 3 (RUNX3), myocyte enhancer factor 2c (MEF2C), myocyte enhancer factor 2d (MEF2D), and histone deacetylase 4 (HDAC4). RUNX2 and OSX are expressed in prehypertrophic and hypertrophic chondrocytes, regulating hypertrophic differentiation, calcification, and degradation of the calcified cartilage. *Col10a1*, *Alpl*, and *Mmp13* are examples of transcriptional targets of RUNX2 and OSX during chondrocyte hypertrophy (60). HDAC4 and MEF2C are two other important regulators of chondrocyte hypertrophy. Studies have highlighted the regulatory functions of the two factors, converging at *Runx2* transcriptional regulation (61). Finally, SOX9 maintains hypertrophic chondrocytes by regulating *Col10a1* transcription and oppose RUNX2 and OSX activities inhibiting osteoblast differentiation of chondrocytes (62).

The interplay of several developmental signaling pathways define mesenchymal condensation patterns, lineage commitment of osteochondral progenitors, and hypertrophy. The induction of *Sox9* by the BMP and related TGFβ pathways is crucial to shape condensation patterns and promote chondrogenesis (57, 63-65). On the other hand, other pathways including the WNT and NOTCH signalling pathways antagonize mesenchymal condensation and inhibit chondrocyte differentiation (66-68). Another example is the regulation of chondrocyte

hypertrophy by the Indian hedgehog (Ihh), PTHrP, and NOTCH signalling molecules. All mentioned signaling regulators impact chondrocyte differentiation and endochondral ossification positively or negatively. Molecular signals driving the transdifferentiation of chondrocytes into osteoblasts, are yet to be determined.

1.4.2.2 Osteoblast differentiation

Osteoblast differentiation starts with the condensation of mesenchymal stromal/stem cells and the specification of osteochondral progenitors. Committed osteochondral progenitors will differentiate into preosteoblasts and then mature osteoblasts, before getting trapped in bone matrix as osteocytes. Cellular sources of osteoblasts include perivascular mesenchymal progenitors (pericytes) (69), perichondrial cells, hypertrophic chondrocytes (70, 71), circulating progenitors, and other mesenchymal cells of the bone marrow.

Several transcription factors and signaling molecules regulate osteoblast differentiation. Differentiating osteoblasts express master transcriptional regulators including *Sox9* (mesenchymal progenitors), *Runx2* (osteochondral progenitors and mature osteoblasts), *Osterix* (*Osx*/*Sp7*) (preosteoblasts and mature osteoblasts), and *Atf4* (mature osteoblasts).

RUNX2 is a member of the Runx family consisting of RUNX1, RUNX2, and RUNX3. Members of this family have the DNA-binding domain runt (72). RUNX2 is the master regulator of osteogenesis. RUNX2 is expressed in osteochondral progenitors, and its expression increases in preosteoblasts to reach its maximum in immature osteoblasts. As the key driver of osteogenesis, RUNX2 regulates all aspects of osteoblast differentiation. It regulates the proliferation of osteoprogenitors, their commitment to osteoblast lineage, and bone matrix deposition. The deletion of *Runx2* (*Runx2*$^{-/-}$) in mice blocks bone formation and inhibits chondrocyte maturation (73-77). The expression of bone matrix protein genes including *Spp1*, *Ibsp*, *Bglap2*and *Col1a1* is halted in *Runx2* null mice. Moreover, *RUNX2* haploinsufficiency causes cleidocranial dysplasia (CCD) in humans (77). Open fontanelles and sutures in addition to hypoplastic clavicles are all typical features of CCD. It is still unclear why the development of the calvaria and clavicles is severely affected, despite that both intramembranous and endochondral bone development are disrupted in CCD. Under the control of the *Prrx1* promoter, the overexpression of *Runx2* enhances osteoblast differentiation and blocks chondrocyte differentiation, causing ectopic bone formation and limb defects (78). The interaction of RUNX2

with coactivators and corepressors controls pro-osteogenic signaling and osteoblastic gene expression through differentiation (79). In addition to bone matrix protein genes, RUNX2 engages with major signaling pathways including Fgf, Wnt and PTH and transcription factors including Sp7 and Dlx5 via reciprocal regulation.

OSTERIX/Sp7 (OSX) has been identified as an osteoblast gene in BMP2-treated C2C12 cultures (60). It is characterized by a proline-rich activation domain at the N-terminus and three C_2H_2-type zinc finger DNA-binding domains at the C-terminus. Osterix is also referred to as *Sp7* due to the striking degree of homology of its DNA-binding domain with *Sp1*, *Sp3* and *Sp4* motifs. During embryonic development, *Osx* is expressed as early as E13.5 in calvaria and perichondrium of long bones. This expression becomes more robust by E15.5, where *Osx* is expressed in all osseus elements. After birth, *Osx* is exclusively detected in periosteal bone surfaces, the endosteum, and cells of the bone matrix (80).

Osx and *Runx2* regulate each other reciprocally. RUNX2 is an upstream direct regulator of *Osx* expression, as it is normally expressed in $Osx^{-/-}$ mice. OSX along with DLX5 and MEF2 control the activation of the *Runx2* enhancer in osteoblasts (81). Both *Runx2* and *Osx* null mice lack osteoblasts and bone formation (60). One striking difference between the two mouse models is the low density of mesenchymal cells in $Runx2^{-/-}$ mice, suggesting that RUNX2 is essential for mesenchymal cell expansion (82). OSX is crucial for osteoblast differentiation and bone formation during embryonic development. OSX plays a dual role inhibiting chondrocyte differentiation and promoting osteoblast differentiation. *Runx2*-positive *Osx*-null cells are committed to follow a chondrocytic fate, unless *Osx* is expressed to switch their lineage-fate decision into osteoblasts. Despite normal expression of *Runx2*, *Osx*-null embryos exhibit arrested osteoblast differentiation, with undetectable expression of *Collagen type I*, *Osteonectin*, and *Osteopontin*. The expression of *Osteocalcin*, a late-osteoblastic differentiation marker, is also absent in *Osx*-null embryos (60).

Studies have characterized the role of OSX in adult bone formation. The global ablation of *Osx* in adult mice results in arrested bone formation, abnormal cartilage development, and defective osteocyte maturation (83). During endochondral ossification, OSX plays a role in the degradation of the cartilaginous matrix. Both the conditional and global depletion of *Osx* target the activation of MMP-13 in the hypertrophic zone of the growth plate and arrest cartilage-

matrix ossification (83, 84). Despite the unobvious skeletal defects at the embryonic stage, the osteoblast-specific inactivation of *Osx* causes an osteopenic phenotype at the adult stage (85). Under the control of *Col1a1* promoter, transgenic mice overexpressing *Osx* exhibit osteopenia, woven-structured cortical bone, and reduced expression of osteoblast genes, mainly *Osteocalcin (86)*. The compilation of genetic mice studies modulating the dosage of *Osx* revealed the importance of OSX as a modulator of bone formation in embryos and adults.

ATF4 (activating transcription factor-4, or cyclic AMP-responsive element binding 2, CREB2) is another key transcription factor, essential for the terminal differentiation of osteoblasts and bone matrix production. ATF4 is a basic domain-leucine zipper (bZIP) transcription factor and a partner of RUNX2, implicated in the transcriptional regulation of osteogenic genes. One example is the regulation of *Osteocalcin* expression by ATF4 and RUNX2 (87). Through its expression in osteoblasts, ATF4 regulates osteoclast differentiation and bone resorption by binding to the *Rankl* promoter (88, 89). At the molecular level, both PTH and sympathetic signaling promote *Rankl* expression through ATF4 (90).

The homozygous deletion of *Atf4* delays osteoblast differentiation and bone formation during embryonic development, leading to low bone mass postnatally. The identification of ATF4 as a substrate of RSK2, defined the function of ATF4 in bone matrix production and its contribution to the skeletal phenotype of Coffin-Lowry syndrome (CLS). ATF4 enhances amino acid uptake facilitating protein synthesis and bone matrix deposition. One example is the regulation of COL1A1 protein. Through posttranslational modifications, RSK2 and ATF4 regulate the synthesis of type I collagen protein, rendering its expression untouched. This has been regarded to be the primary role of ATF4 in osteoblasts, as feeding *Atf4*$^{-/-}$ mice with a high protein diet corrects the skeletal deformities (91). In the context of human disease, the disruption of ATF4 phosphorylation by RSK2 has been linked to CLS, a condition characterized by mental retardation and skeletal abnormalities(6). Beyond the regulatory trio mentioned above, other transcription factors contribute to osteoblast function and differentiation, including DLX5, MSX2, SATB2, and LEF1.

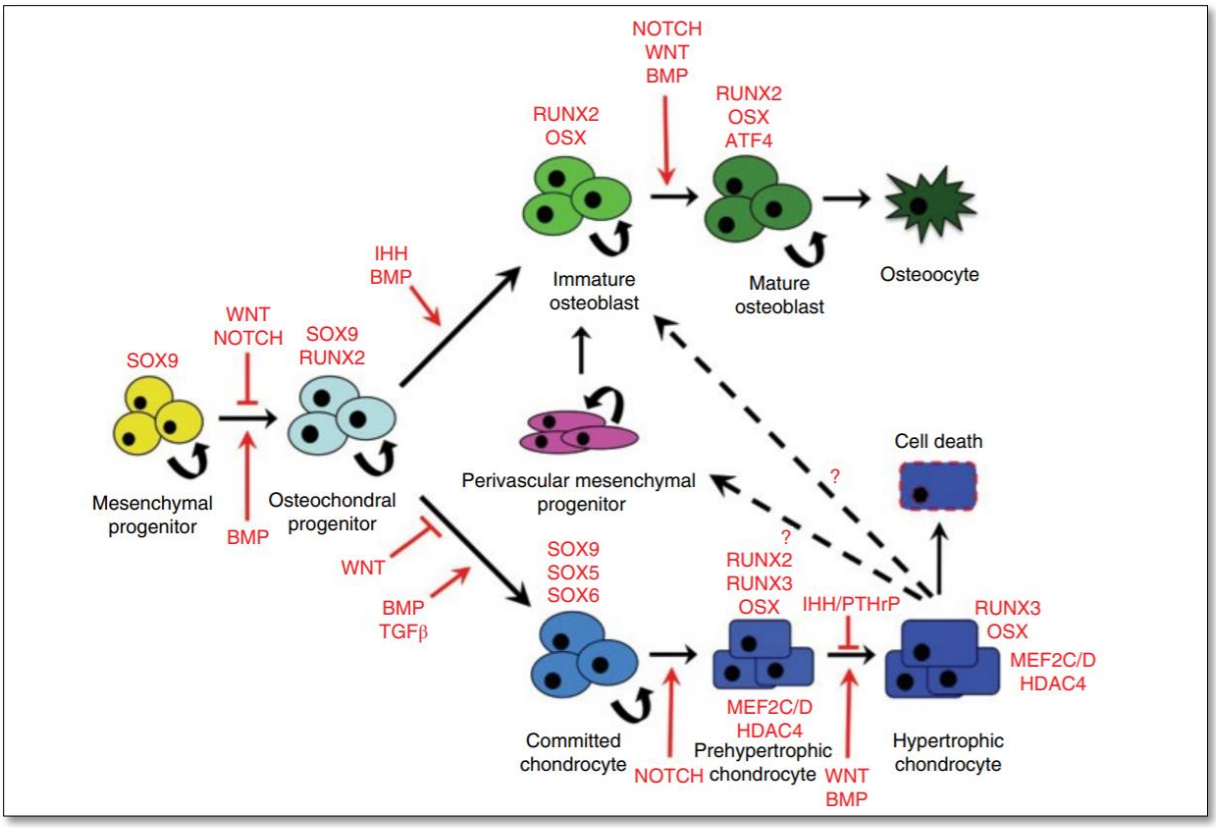

Figure 1. 3 Molecular modulators of endochondral ossification

Mesenchymal progenitor cells differentiate into osteochondral progenitors before committing to either the osteoblast or chondrocyte lineage. Immature osteoblasts differentiate into mature osteoblasts and further into osteocytes. Chondrocyte differentiation proceeds from committed chondrocytes to prehypertrophic and hypertrophic chondrocytes. Hypertrophic chondrocytes can undergo cell death or transdifferentiate into osteoblasts. Key signaling pathways including: NOTCH, BMP, TGFβ, IHH, and WNT pathways orchestrate chondrocyte and osteoblast differentiation during endochondral ossification. Question marks indicate unknown molecular mechanisms. Figure reproduced by permission of John Wiley and Sons, Wiley books, eBook: Primer on the metabolic bone diseases and disorders of mineral metabolism, ninth edition, chapter 2, Endochondral Ossification, pages (12-19), Karner CM, Hilton MJ. 2018.

1.5 Paracrine functions of the bone

We have previously reviewed the phases of bone remodeling responsible for the maintenance of the skeleton. Through this process, paracrine signalling drives and regulates the crosstalk among bone cells, thereby maintaining a balance between bone formation and bone resorption. In this section we will highlight the paracrine functions of secreted proteins circulating among osteoblasts, osteocytes, and osteoclasts (Figure 1.4).

Bone cells communicate with each other by secreting paracrine signaling molecules including cytokines, chemokines, and growth factors. Within the bone niche, osteoblasts and osteocytes synthesize and secrete proteins to regulate osteoclastogenesis. The production of RANKL by osteocytes mediate the crosstalk between osteoclasts and osteocytes (37, 92). Because they are the main producers of RANKL, osteocytes have leverage over osteoblasts and bone marrow stromal cells supporting osteoclastogenesis and initiating the remodeling process (37). In this context, studies have highlighted the role of apoptotic or damaged osteocytes in triggering osteoclast formation and invasion (93-95). Besides, osteocytes secrete sclerostin to inhibit osteoblast differentiation and consequently bone formation. The cross talk between osteoblasts and osteoclasts is also maintained through paracrine coupling factors. Osteoblasts activate osteoclastogenesis via expressing M-CSF, RANKL, and WNT5A and inhibit osteoclast activity through osteoprotegerin (OPG), a decoy receptor of RANKL, SEM3A, and WNT16 (96). The production of OPG by osteoblasts antagonize the effect of RANKL and disrupts the coupling between osteoblasts and osteoclasts (97). The OPG/RANK/RANKL axis is one of the most studied pathways underlying bone resorption disorders (98).

Due to reciprocal paracrine regulation, osteoclasts secrete coupling proteins to regulate osteoblast function and differentiation (99, 100). Osteoclast-derived factors such as SEMA4D, BMP6, EFNB2, CT-1, WNT10B and CTHRC1 regulate osteoblast/ MSCs migration and differentiation (101). Bone formation and bone resorption are also coupled to angiogenesis through paracrine signaling. This is not surprising as angiogenesis is involved in bone fracture healing and bone-related disorders such as osteoporosis and bone cancer (102). The vascular endothelial growth factor A (VEGFA) is a key pro-angiogenic factor produced by pre-osteoblasts and chondrocytes. VEGFA stimulate the proliferation, survival, and migration of MSCs during the reversal phase of bone remodeling (103). Similarly, pre-osteoclasts produce the platelet

derived growth factor-BB (PDGF-BB), another angiogenic factor enhancing MSCs migration and osteoblast differentiation (104, 105).

The well-rounded communication among bone cells has proven to not only maintain bone homeostasis, but also reveal connections between the skeleton and other tissues in the body.

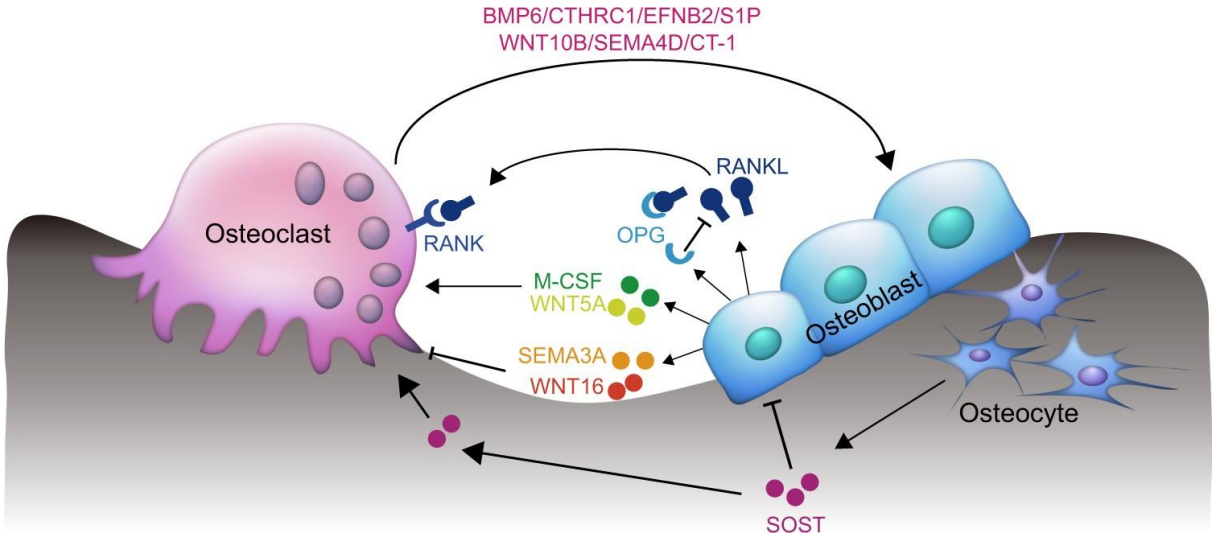

Figure 1. 4 A paracrine cross talk among osteoblasts, osteoclasts, and osteocytes

To maintain bone homeostasis, bone cells communicate with each other in a paracrine manner secreting ligands and molecules. Osteoblasts induce osteoclast formation and activation by expressing M-CSF, RANKL, and WNT5A and block osteoclast activity through OPG, a decoy receptor of RANKL, SEMA3A, and WNT16. Osteocytes produce high levels of SOST to inhibit osteogenesis and stimulate osteoclastogenesis. Osteoclasts regulate the activity of osteoblasts and osteocytes by producing BMP6, CTHRC1, EFNB2, S1P, WNT10B, SEMA4D, and CT-1, thereby controlling bone formation. (Reproduced from Springer Nature, Bone Research, open access article, Paracrine and endocrine actions of bone—the functions of secretory proteins from osteoblasts, osteocytes, and osteoclasts, Han Y et al. 2018).

1.6 Endocrine functions. "The soft functions of the bone"

In addition to its static structural functions, the skeleton has been recognized as an endocrine organ that regulates systemic energy metabolism. The skeleton exerts an endocrine control over different organs by secreting regulatory proteins. This is exemplified by the inter-organ regulation of phosphate levels by the kidneys, parathyroid glands, and bone. The bone-derived fibroblast growth factor 23 (FGF23), mainly synthesized by osteoblasts and osteocytes, inhibits phosphate reabsorption and 1,25-dihydroxyvitamin D_3 [$1,25(OH)_2D_3$] kidneys as well as PTH synthesis and secretion. FGF23 binds a complex of FGFR1 and the co-receptor Klotho to activate FGF signaling, targeting kidneys and parathyroid gland (96). Reciprocally, both PTH and $1,25(OH)_2D_3$ stimulate the synthesis and secretion of FGF23. $1,25(OH)_2D_3$ triggers the secretion of FGF23 by osteocytes through the VDR/RXR dimer, while the renal actions of PTH is mediated through its binding to its receptor PTH1R, thus increasing $1,25(OH)_2D_3$ synthesis (106). This regulatory loop connecting bone and other tissues, maintains phosphate homeostasis and proper matrix mineralization.

Another example of endocrine control is conveyed through osteoblasts by osteocalcin (OCN), the most abundant osteoblast-specific non-collagenous protein (46 aa in mice and 49 aa in humans). It has been commonly used as a serum determinant of bone formation and recent accumulating evidence has uncovered its role as a master endocrine regulator in liver, muscle, pancreas, testis, brain, and adipose tissues (96) (Figure 1.5).

Osteocalcin is initially synthesized as a pro-hormone (pro-OCN) and then cleaved by Furin, an intracellular proprotein convertase in osteoblasts (107). The cleavage by Furin is essential for pro-OCN maturation and subsequently its bone endocrine functions (107). OCN resides in the general circulation in three different forms: fully carboxylated (inactive, GlaOCN), partially carboxylated, and uncarboxylated (active, GluOCN). Prior to secretion, OCN is ɣ-carboxylated on 3 glutamic acid residues in the endoplasmic reticulum (ER) of osteoblasts. Fully carboxylated OCN binds calcium and hydroxyapatite matrices with high affinity, supporting bone ECM. Trapped peptides of carboxylated OCN are mobilized during bone resorption. The acidification (pH ~ 4.5) of the resorptive milieu by osteoclasts promotes the decarboxylation of GlaOCN into uncarboxylated form (GluOCN) and therefore its release into the circulation (108,

109). Increased levels of GluOCN, improved glucose tolerance and insulin sensitivity have been reported in mice with increased osteoclast activity (109).

In addition to bone, OCN targets different tissues and organs to regulate energy metabolism. It has been demonstrated that the uncarboxylated form of OCN is the active circulating form, responsible for endocrine functions in mice and humans (108, 110, 111). The osteoblast-specific inactivation of ɣ-carboxylase (*Ggcx*) resulted in increased levels of GluOCN and enhanced glucose tolerance in mice (112). *Ocn*- null mice exhibited impaired glucose metabolism, reduced insulin sensitivity, and increased fat mass (113). This phenotype indicated that OCN extends multiple regulatory arms to handle glucose and energy metabolism. OCN regulates systemic glucose levels by enhancing β-cell proliferation and insulin secretion, by promoting glucose and fatty acid uptake into myofibers, and by improving energy expenditure through *Adiponectin* in adipose tissues (96). Taken together, these studies identified a list of targets of OCN including pancreas, muscle, and adipose tissues and expanded our understanding of its impact on obesity and insulin resistance disorders.

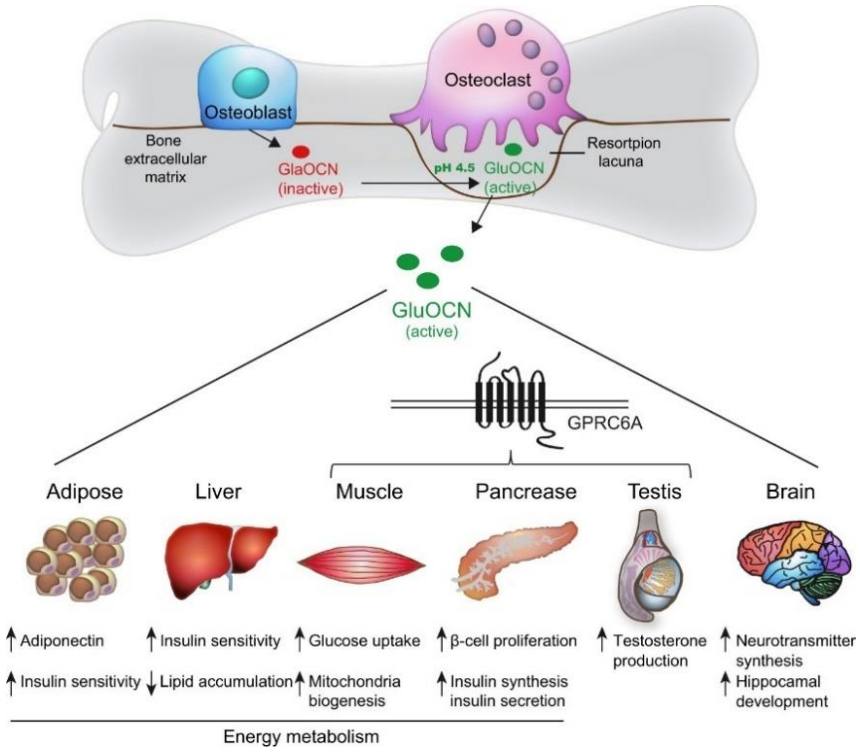

Figure 1. 5 OCN is the master bone-derived hormone.

The inactive carboxylated form of OCN (GlaOCN) is secreted by osteoblasts into the bone extracellular matrix. During bone resorption, the acidification pH (~4.5) of the resorption lacunae induces the decarboxylation of GlaOCN into undercarboxylated active form (GluOCN). The undercarboxylated form (GluOCN) acts as an active hormone regulating multiple tissues and organs. It regulates energy metabolism by enhancing glucose uptake in muscle, insulin production in the pancreas, insulin sensitivity in the liver and adipose tissue, upregulation of adiponectin expression in adipose tissue and promotion of β-cell proliferation in the pancreas. Moreover, OCN promotes male fertility by stimulation of testosterone synthesis in Leydig cells which improves cognitive function of the brain through an increase in neurotransmitter synthesis and facilitation of hippocampus development. It is important to note that OCN functions in testis, pancreas, and muscle through its binding to the receptor GPRC6A while receptor(s) of OCN in adipose tissues and liver are yet to be determined. Figure reproduced from Springer Nature, Bone Research, open access article, Paracrine and endocrine actions of bone—the functions of secretory proteins from osteoblasts, osteocytes, and osteoclasts, Han Y et al. 2018.

1.7 Bone marrow stromal cells

The bone marrow harbors populations of multipotent mesenchymal stromal cells (MSCs), originally identified by Friedenstein and colleagues in the 1970s. MSCs are usually referred to as colony-forming-unit fibroblasts (CFU-F), due to their fibroblastic morphology and clonogenic capacity. Bone marrow-derived MSCs (BMSCs) have the plasticity to differentiate into osteoblasts, adipocytes, and chondrocytes both *in vitro* and *in vivo* (114), and differentiate along the myogenic lineage, at least *in vitro*. A better understanding of the regulatory mechanisms orchestrating the lineage making decisions of BMSCs is crucial, considering their promising therapeutic contribution to disorders of low bone mass and compromised fracture healing (114, 115). We have highlighted the molecular mechanisms driving the recruitment and differentiation of progenitors into the osteoblastic and chondrocytic lineages, whether during bone development, growth, or remodeling. In the next part, we will focus on adipocyte development and the molecular cascades regulating the adipogenic differentiation of mesenchymal progenitors.

1.7.1 Adipose tissues: " A connective tissue with lipid droplets"

Adipose tissues are loose connective tissues that develop in multiple discrete locations in the body. They form large aggregates recognized as fat depots, composed of adipocytes, vascular endothelial cells, fibroblasts, and some immune cells. They are the only form of connective tissues that can store energy in the form of lipids and exhibit a substantial increase in size, even after adulthood. Fat pads can offer some cushioning to delicate organs such as the eyes and body parts exposed to high mechanical pressure including heels and toepads. The evolving incessant interest in adipose biology is credited to its central role in maintaining energy and glucose homeostasis and the drastic increase in global rates of obesity, diabetes, and metabolic diseases. Additionally, the adipose tissue has been considered a knot connecting energy homeostasis and reproduction, as it regulates the hypothalamic-pituitary-gonadal axis in both genders through hormonal signalling.

1.7.2 Adipose tissues: Developmental origins and types

Most of the adipocytes in the body develop from mesoderm-derived mesenchyme, except for the cephalic region where mesenchyme is derived from the neuroectoderm. The developmental clock of fat formation is variable among species and within the same specie

depending on the type of adipocytes. At least in rodents, white adipose tissues (WAT) including subcutaneous and visceral fat are largely detected after birth, whereas brown adipose tissues (BAT) such as interscapular fat can be identified during embryogenesis. There are three different types of adipocytes, distinguished, in part, by the color of the fat tissue: white, brown, and beige/ brit. Each type has a unique gene expression program that dictates different functions and responses to external environmental factors. Lineage-tracing studies using transgenic Cre lines and antibody-based cell sorting have shown that both white and beige adipocytes derive from $Pax7^{-}/Myf5^{-}$ cells via distinct progenitors. In contrast, classic brown adipocytes originate from a $Pax7^{+}/Myf5^{+}$ lineage, the very same precursor of skeletal muscles (116) (Figure 1.6). Tracing the developmental origins of each type of adipocytes has been a hot and debatable topic among different scientific groups and more information is needed to form a cohesive developmental scheme.

White adipocytes are unilocular adipocytes specialized for energy storage. They make up the bulk of fatty tissues in the body, where they can expand (hypertrophy; cell size increase) and accumulate (hyperplasia; cell number increase), mainly supporting prolonged fasting periods. The classical broad classification of WATs distinguishes between subcutaneous and visceral fat. Increased visceral adiposity has been associated with increased risk of metabolic diseases in humans, as opposed to no risk or even better immunity in case of high subcutaneous adiposity (116). WATs store energy in the form of triglycerides and release fatty acids by lipolysis to fuel other organs. WATs regulate lipid metabolism by adipokine production through adiponectin and leptin. These adipokines stimulate fatty acid oxidation in the liver to decrease lipid content. Additionally, the production of leptin by adipose tissues alters bone mass and modulates the endocrinology of the skeleton. Leptin acts on the brain to increase sympathetic nervous system (SNS) signaling to trigger an increase in *Esp* expression (encodes the protein tyrosine phosphatase, OST-PTP) in osteoblasts through β2- adrenergic receptor (Adrβ2), thus inhibiting osteocalcin decarboxylation and activity. Inactivating osteocalcin will in turn inhibit insulin production and secretion by the pancreas (117). This hypothalamic-bone circuit counteracts the bone-pancreas endocrine loop, highlighting the role of adipose tissues in modulating the fascinating interdependence between bone remodeling and energy metabolism.

Brown adipocytes are multilocular highly specialized cells that dissipate stored chemical energy in the form of heat. In rodents, brown adipocyte depots cluster in defined anatomical sites such as the scapulae (interscapular) and perirenal areas. BATs have been considered the main node of nonshivering thermogenesis in mammals, due to the actions of uncoupling protein-1 (UCP-1), a BAT-specific protein. Brown adipocytes are densely loaded with mitochondrion that express high levels of UCP-1 which actively oxidize metabolic substrates to produce heat. In addition to thermogenesis, the induction of BAT in mice stimulates energy expenditure and protects mice from diet-induced obesity (116).

Cold exposure as well as triggered activation of the sympathetic nervous system can promote UCP-1- dependent "browning" of adipocytes within WATs depots in rodents. These inducible cells have been called beige/brite adipocytes, which are predominantly located in inguinal and retroperitoneal fat depots and very poorly seen in perigonadal fat. Both classic brown and beige adipocytes implement an overlapping though distinct genetic program, sharing thermogenic and mitochondrial genes, including *Ucp1*. As compared to brown adipocytes, beige adipocytes have lower basal levels of UCP1, which increase in response to thermogenic stimuli. Consequently, beige adipocytes are suited to play a dual role, thus storing energy in the absence of thermogenic stimuli and releasing heat when triggered. Interestingly, beige adipocytes are induced to compensate for the selective loss of brown adipocytes, restoring body temperature and resistance to diet-induced obesity (116).

1.7.3 Marrow adipocytes

Bone marrow adipose tissue (BMAT or MAT) is a distinct type of fat depot, also referred to as "yellow fat". Resembling white adipocytes, BMATs carry a large unilocular lipid vacuole that hosts a distinct type of fatty acids, as compared to WATs. Bone marrow adipocytes develop postnatally, and marrow adiposity is mainly dependent on age, bone area, and gender. Through development, yellow fat replaces hematopoietic red marrow to account for 50-70% of bone marrow volume in adults(118). The functional metabolic resemblance of BMATs to either WATs or BATs has been extensively investigated by different groups and shown to be site-dependent. BMAs can exhibit WATs or BATs-like properties depending on their source such as long bone versus vertebrae (118).

Accumulating evidence has demonstrated a link between marrow adiposity and bone remodeling in both humans and rodents. Studies have demonstrated a negative correlation between BMAT amounts and bone mass in models of aging, calorie restriction, ovariectomy, and glucocorticoid stimulation. It is suggested that BMATs modulate bone remodeling through paracrine actions. In response to stimuli (catecholamines, glucocorticoids, and cytokines), BMAs get heavily involved in bone remodeling. BMAs can secrete leptin and adiponectin enhancing MSCs commitment into the osteoblast lineage. Concurrently, BMAs enhance osteoclastogenesis via RANKL and TNF-α production. Though debatable, the secretion of saturated fatty acids by BMAs can influence osteoblast and osteoclast functions (118). Altogether, BMATs have been shown to be metabolically distinct as compared to other fat depots and closely involved in bone remodeling. Further investigation is needed to characterize the reciprocal regulation of BMAT functions by osteoblasts, osteoclasts, and hematopoietic cells.

1.7.4 Adipocyte differentiation

Adipocytes derive from multipotent mesenchymal stromal cells. The process of adipogenesis is split into two phases: commitment and terminal differentiation. Committed MSCs differentiate into preadipocytes and further into mature adipocytes, suited for lipid transport and synthesis, insulin sensitization, and paracrine signaling. The transcriptional cascade that regulates adipocyte differentiation has been dissected, revealing the transcription factors, cytokines/adipokines, and regulatory pathways in action. We will focus on key transcriptional regulators of adipocyte differentiation, expressed by all types of adipocytes.

The peroxisome proliferator- activated receptor gamma (PPARγ), a member of the nuclear-receptor superfamily, is the master regulator of adipogenesis. PPARγ is so potent that it can induce the adipogenic differentiation of nonadipogenic cells such as fibroblasts and myoblasts (116). The expression of PPARγ is necessary and sufficient by itself for adipocyte differentiation. This key role in adipogenesis is not surprising, as most adipogenic regulatory signaling targets PPARγ expression and activity, directly or through pro-adipogenic factors that function in part, via PPARγ (116). The specific inactivation of *Pparγ* in adipose tissues protects mice against high-fat diet-induced obesity and insulin resistance (119). Moreover, the *in vitro* inactivation of PPARγ blocks adipogenesis and enhances osteoblastogenesis of BMSCs. Multiple studies have linked PPARγ to bone loss in diabetic patients and changes in bone

marrow adiposity and osteoblastogenesis with aging (120). Altogether, PPARγ is a potent regulator of adipocytic differentiation in all fat depots and a key player in the bone-fat switch game during mesenchymal differentiation. CCAAT enhancer-binding proteins (C/EBP) family members including C/EBPα, C/EBPβ, and C/EBPδ are also crucial for adipogenic differentiation. The bZIP factors C/EBPα, C/EBPβ, and C/EBPδ bind to different adipogenic promoters during differentiation. C/EBPβ and C/EBPδ are early inducers of adipocytic terminal differentiation, whose expression is indispensable for the induction of C/EBPα and PPARγ. Interestingly, the induction of C/EBPα is abrogated in the absence of PPARγ, further emphasizing the crucial role of PPARγ during differentiation (121). In addition to PPARγ and C/EBPs, a cascade of the Kruppel-like factors (KLFs), modulates adipogenic differentiation. KLFs play both pro-adipogenic (KLF5,KLF6, and KLF15) and anti-adipogenic(KLF2 and KLF7) functions during adipogenic differentiation. The inhibitory and activating functions of KLFs converge at the regulation of *Pparg2* promoter (121). In addition to classic adipogenic transcription factors and due to their specialized functions, brown adipocytes express a set of transcription factors and regulators, unique to their depot. The list includes thermogenic and mitochondrial genes including UCP-1, PPARγ co-activator-1α (PGC1α), transcriptional cofactor PRD1-BF-1-RIZ1 homologous domain-containing protein-16 (PRDM16), and cell death-inducing DNA fragmentation factor alpha-like effector A (CIDEA) (116).

The commitment of preadipocytes is a prerequisite for adipogenic terminal differentiation. In response to adipogenic stimuli, the expression of metabolic genes and adipokines is activated, shaping the functional phenotype of adipose tissues. The fatty acid-binding protein 4 (FABP4;AP2), glucose transporter 4 (GLUT4;SLC2A4), leptin, and adiponectin are markers of terminally differentiated adipocytes. Notwithstanding the contribution of other adipogenic regulators, it is the proper expression of PPARγ and C/EBPs that ensures sustained gene expression in mature adipocytes. Glucocorticoid stimulation, BMP/TGF-β signalling, cAMP-mediated activation of both protein kinase A (PKA)-dependent and PKA-independent pathways, and the mitogen-activated protein kinase (MAPK) pathway, are main components of the adipogenic program driving the differentiation of both MSCs and preadipocytes (122). In addition to adipogenic regulation, those pathways and others modulate the crosstalk between adipocytes and osteoblasts, by regulating MSCs commitment and differentiation.

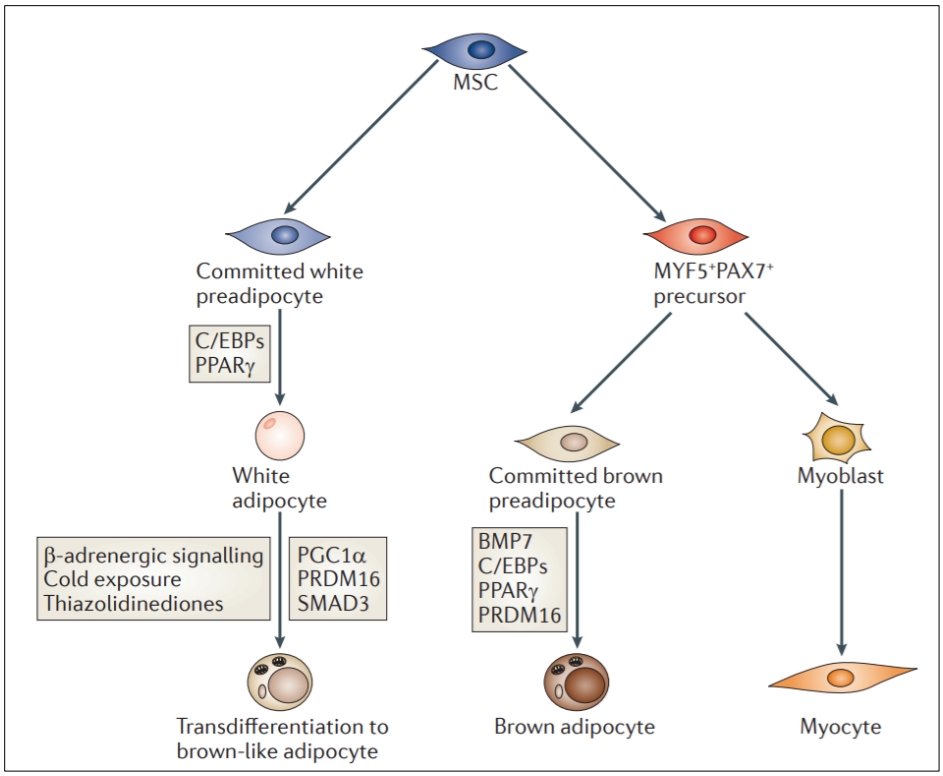

Figure 1. 6 Developmental origins and differentiation of adipocytes

For a long time, it was thought that both white and brown adipocytes are derived from the same precursor cell. However, recent studies have shown that brown adipocytes share a common MYF5 $^{+}$/PAX7 $^{+}$ precursor with muscle cells. The MYF5 $^{+}$/PAX7 $^{+}$ precursors give rise to committed brown preadipocytes that undergo terminal differentiation or myoblasts that differentiate into myocytes. The molecular regulators of brown adipocytes terminal differentiation are the bone morphogenetic protein 7 (BMP7), peroxisome proliferator activated receptor-γ (PPARγ), CCAAT/enhancer-binding proteins (C/EBPs), and the transcriptional co-regulator PR domain-containing 16 (PRDM16). White adipocytes can also be stimulated to display characteristics of brown adipocytes by β-adrenergic signalling, cold exposure and thiazolidinediones, which seem to function through the indicated factors. MSC, mesenchymal stem cell; MYF5, myogenic factor 5; PAX7, paired-box 7; PGC1α, PPARγ co-activator 1α. (Reproduced by permission from Springer Nature: Nature Reviews Molecular Cell Biology, Forming functional fat: a growing understanding of adipocyte differentiation, Cristancho AG. , Lazar MA. 2011).

1.8 The PTH axis and bone anabolism

This section is adapted from our literature review entitled " New PTH Signals Mediating Bone Anabolism" published by Hariri H et al. in 2017 (123).

"Parathyroid hormone (PTH), an 84-amino acid peptide hormone, is an important regulator of calcium homeostasis. The parathyroid gland senses low levels of circulating calcium through the calcium-sensing receptor and in response secretes PTH. The endocrine function of PTH is elicited by its direct effect on bone and kidneys and indirect effect on the gastrointestinal tract. High levels of PTH promotes calcium and phosphorus release by activating osteoclast-mediated resorption of bone. At the level of the kidney, it acts to decrease calcium excretion and phosphorus reabsorption. The indirect effect of PTH is mediated by vitamin D activation, that in turn stimulates the absorption of dietary calcium and phosphorus from the gut (124, 125)."

"The profound effect of PTH on the skeleton shapes bone microarchitecture and modulates its strength. Chronic and excessive infusion of PTH has been associated with bone loss. Primary hyperparathyroidism (PHPT) is one classical example mimicked by continuous PTH administration, associated with osteopenia (126), accelerated bone loss (127), and increased bone turnover. However, intermittent administration of PTH at a low dosage promotes bone formation in a time interval referred to as the anabolic window (128). This osteoanabolic effect is antagonized by the activation of bone resorption afterwards, yet the net effect is enhanced bone formation (129, 130)." While new therapeutics are in the pipeline, at the time of writing this report the intermittent treatment with teriparatide (the N-terminal fragment of PTH (1-34)), abaloparatide (parathyroid hormone-related protein, PTHrP), and romosozumab (humanized monoclonal antibody against sclerostin) are the only U.S. Food and Drug Administration (FDA)-approved osteoanabolic therapies (131).

1.8.1 The PTH-PTH1R-G proteins signaling

"PTH signals in cells by activating the Parathyroid Hormone Receptor 1 (PTH1R), a seven-transmembrane domains G protein-coupled receptor (GPCR) that belongs to the class B secretin-like GPCR family (132). In bone, chondrocytes, osteoblasts, and osteocytes express PTH1R (133). In mice, deletion of *Pth1r* either globally or in the osteoblastic lineage (osteoblasts or osteocytes) impairs proper bone development and the capacity of bone tissue to respond to PTH treatment. Systemic deletion of *Pth1r* results in mild cortical thickening in

specific regions of long bones accompanied by a more profound decrease of trabecular bone development (134). Osteoblast-specific inactivation with the osteocalcin-driven Cre (OC- Cre) yields a similar phenotype (135). A mild osteopenic phenotype has also been reported when *Pth1r* is deleted from osteocytes postnatally using a tamoxifen-inducible Dmp1-CRE driver (136). However, different results were reported when *Pth1r* was constitutively deleted from osteocytes. These animals show an increased trabecular and cortical bone volume at 3 months of age, resulting from a low bone turnover state (137, 138). A significant finding, regardless of the steady-state bone phenotype of mice in which *Pth1r* is ablated in osteocytes, is that the anabolic response to PTH is blunted in those animals (137, 138). These results indicate the importance of the osteocyte cell population for PTH-induced bone gain responses."

" PTH1R is coupled to different G proteins including the Gαs, the Gαq11 and the Gαq12/13 subunits which respectively primarily mediate their intracellular effects through the activation of the adenylate cyclase (ADCY), the phospholipase C (PLC) and the Ras homolog gene family, member A (RHOA) (139, 140). Within this wide range of signaling cascades activated by PTH, it has been demonstrated that its anabolic function is mainly mediated by the activation of the Gαs-dependent accumulation of cyclic AMP (92) and activation of Protein Kinase A (PKA) and not by Gαq-mediated PLC activation. This was initially examined using various amino-terminal fragments of PTH that differentially activate Gαs- or Gαq-mediated signalling (141). PTH(1–34) activates both cAMP production and PLC, while PTH (1–31) only activates cAMP synthesis (142-144). On the other hand, PTH(3–38) only activates the PLC pathway (143, 144). Anabolic effects were measured upon daily injections of PTH(1–34) and PTH(1–31), but not PTH(3–38) (145, 146). These studies established that PTH-stimulated cAMP production is sufficient for mediating the anabolic effect, but activation of the PLC pathway is insufficient. These classical biochemistry studies have now been confirmed using mouse molecular genetics approaches and osteoblast-specific, postnatal inactivation of Gαs (147-149)."

"The important role of the Gαs-dependent pathway in PTH-mediated bone acquisition was confirmed using mice expressing a constitutively active PTH1R (caPTH1R) systemically. These mice show a drastic increase of trabecular bone volume (150), but this abnormal increase of bone volume is completely reversed when Gαs is postnatally deleted from the osteoblasts (149). Interestingly, the same study also showed than even if the intermittent PTH (iPTH)-

mediated increase of bone mass is blunted in mice lacking osteoblast expression of Gαs, PTH is still able to increase osteoblast numbers and bone formation rates (149). This discovery illustrates well the complexity of PTH signaling in bone cells. It also suggests that other pathways are required to work in collaboration with Gαs-dependent signalisation to improve bone mass following PTH stimulation. One possibility would involve the βarrestin 2-dependent pathway, which is a Gαs-independent cascade that has been shown to be involved in iPTH-induced bone formation (151-153)."

" The cAMP second messenger activates the PKA-dependent signaling cascade as well as a PKA-independent pathway that involves the Rap guanine nucleotide exchange factor (GEF) 3 and 4 (also called EPAC). While the physiological importance of the latter remains to be demonstrated in bone, the bone anabolic function of PKA has been confirmed using a transgenic approach (154, 155). Forcing the expression of a constitutively active form of PKA (caPKA) in osteoblasts led to an important increase of the bone volume in long bones (155). This phenotype is associated with an increase of bone turnover and aligns with the phenotype observed in mice expressing caPTH1R specifically in osteocytes (156, 157). Interestingly, the increased bone volume observed when caPKA is expressed in osteoblasts is more dramatic than the increase observed when the transgene is only expressed in osteocytes (154, 155). Here again, this difference suggests that the PKA axis is not the only one required to mediate the anabolic action of PTH on bone."

1.8.2 Signaling pathways of PTH-mediated bone anabolism

" PTH signaling is a common factor mediating the crosstalk amongst osteoblasts, osteocytes, and osteoclasts. At the cellular level, the biological effect of PTH is mediated through signaling cascades and downstream targets controlling proliferation, maturation, and differentiation events. Because of its clinical relevance, extensive work has been performed to uncover the key signaling pathways modulated by PTH."

"Optimal activation of PTH1R by PTH involves its interaction with the LDL receptor related protein 6 (LRP6) (158-161). When *Lrp6* expression is disrupted in mice, the expression of the sclerostin (SCL) gene (*Sost*) and the anabolic action of iPTH are blunted (159). It has been suggested that N-Cadherin regulates the amount of LRP5/LRP6 complex at the plasma membrane (162). This indirectly impacts the abundance of PTH1R/LRP6 complexes by affecting

the LRP6 pool available for an interaction with PTH1R (160). This model is supported by ablation of the *Cdh2* gene (coding for N-Cadherin) in mice which increases membrane PTH1R/LRP6 complexes and promotes *Sost* downregulation and bone formation following iPTH treatment (160, 163). LRP6 availability and activity is mainly regulated via interaction with extracellular ligands and phosphorylation of its intracellular domain (reviewed in (164-166)). However, mechanisms regulating *Lrp6* transcription remain largely unknown. Kulkarni and colleagues (167) reported that *Lrp6* expression can be modulated by PTH, but the exact mechanism still needs to be determined."

"PTH signaling activates the different nodes of the Wingless-related integration site (Wnt) signal transduction network in osteoblastic cells. Wnt signaling plays a significant role in bone metabolism. Once activated, it fates mesenchymal stem cells (MSCs) to osteogenic commitment, regulates pre-osteoblast proliferation, differentiation, and survival, and controls osteoclastic bone resorption by augmenting osteoprotegerin (OPG) production (reviewed in (22)). Wnt proteins bind to a dual-receptor complex of the frizzled (Fzd) receptor and the LRP5 and LRP6 coreceptors, stabilizing its main downstream effector β-catenin and triggering the transcription of Wnt target genes. Recent studies have shown that the anabolic effect of PTH can be altered by the Wnt/LRP6/β-catenin axis. As discussed before, PTH-bound PTH1R engages with LRP6 and activates β-catenin in osteoblasts and osteocytes (161) and this PTH-induced activation is completely abrogated in *Lrp6* deficient mice (159). This interaction appears to be exclusive to LRP6, as the loss of LRP5 does not affect the anabolic actions of intermittent PTH (168). Although PTH activates β-catenin in osteoblasts (160, 169), studies using mice with β-catenin-deficient osteocytes revealed that the anabolic effects of PTH therapy in the trabecular compartment does not require osteocytic β-catenin (170)."

"An established mechanism by which PTH exerts its anabolic effect in bone is through the suppression of the sclerostin (SCL) gene (*SOST)*. SCL is a potent Wnt antagonist, mainly secreted by osteocytes. *SOST* regulation by PTH remains a hot area for investigation by different research groups. Kramer and colleagues (171) reported contradictory evidence from studies in *Sost* transgenic and *Sost*-deficient mice (172, 173), raising questions about whether PTH-induced bone gain requires the downregulation of *Sost* or not. A recent study performed in osteocyte-

specific *Sost* transgenic mice has resolved this discrepancy, presenting evidence that PTH can activate alternative anabolic pathways independently of *Sost* suppression (137)."

1.8.3 Basic domain-leucine zipper transcription factors and PTH signal transduction

"In response to PTH, the basic domain-leucine zipper (bZIP) transcription factor, cAMP response element binding protein (CREB), is phosphorylated (174). It then stimulates the transcription of genes that encode for members of the AP-1 family of bZIP factors, *Fos* and *Jun* (174-176). A recent study has linked the class III HDAC, Sirtuin 1 (SIRT1), to the PTH-mediated regulation of the *Mmp13* promoter. The mechanism involves the direct binding of SIRT1 to cJUN and this interaction at the AP-1 site within the *Mmp13* promoter blocks AP-1 activity and downregulates *Mmp13* (177). Interestingly, the authors further showed that the deacetylation of cJUN by SIRT1 is cAMP dependent (177)."

In the context of PTH anabolism, we have focused on describing the effectors of the anabolic effect of PTH in bone. One emerging pathway involves the transcriptional coregulator NACA (Nascent polypeptide associated complex And Coregulator alpha).

1.9 Coregulatory scaffolding proteins

Coregulatory proteins provide an additional layer of transcriptional control in the nucleus. Studies have described gene-specific regulatory complexes responsible for functional modifications in chromatin accessibility to transactivation modulators and chromatin remodelers (178, 179). One example is the role of SATB2 during osteoblast differentiation. *Satb2* originally identified as the cleft palate gene is a nuclear scaffolding protein implicated in transcriptional regulation. *Satb2-/-* mice exhibit craniofacial defects and impaired osteoblast differentiation. SATB2 interacts with ATF4 and Runx2 to drive the expression of Runx2-target genes and thereby stimulate osteoblast differentiation (180).

1.9.1 NACA: A transcriptional coregulator

One intriguing question in our laboratory focuses on the coregulatory functions of NACA in osteoblasts. Initially, NACA was cloned as the alpha chain of the nascent-polypeptide-associated complex (NAC), responsible for the fidelity of sorting and translocation of polypeptides from the ribosome. NAC is a heterodimeric cytosolic chaperone containing 2 subunits, NACA and β-NAC (BTF3) (181, 182). BTF3 is a general transcription factor that interacts with the basal transcriptional machinery at proximal promoter regions (182-184). Interestingly, a recent study

has shown that NAC (via the N terminus of the βNAC subunit) can block the aggregation of polyglutamine-expanded (polyQ) proteins and amyloid-β 40 (Aβ40) peptides associated with Huntington's disease and age-related protein pathologies (185).

In 1998, Yotov and Moreau et.al amplified NACA from mineralizing osteoblast cells (186), opening the door for the complete characterization of this protein and its function in osteoblast biology. The NACA-BTF3 heterodimerization has been shown to be essential for NAC ribosomal-dependent activities but a role for the uncomplexed NACA subunit remained to be characterized. Past work from our laboratory and others have shown that NACA has a DNA binding domain, a calcium binding EF-hand motif, and a NAC domain essential for DNA binding and nuclear localization (182, 187, 188). Same studies have demonstrated that NACA can potentiate the activity of the chimeric activator GAL4/VP-16 *in vitro*, by acting as a transcriptional coactivator (186). Additionally, lessons acquired from different promoter studies have indicated that although NACA can bind DNA, it cannot initiate transcription on its own (188-190).

To better understand the regulatory functions of NACA, it was crucial to identify transcriptional partners of this protein. Studies have demonstrated that cJUN is a top candidate as NACA is implicated in AP-1 transcriptional regulation of target genes. In one regulatory scheme, NACA interacts with cJUN to stabilize the interaction of cJUN homodimers with chromatin and extends another arm to bridge the interaction between cJUN homodimers and the basal transcription machinery (186). This interaction was shown to enhance AP-1-mediated transcription of the *Osteocalcin* promoter in differentiated osteoblasts, where the DNA-binding activities of NACA are indispensable (189, 191). In addition to cJUN, NACA can potentiate the transcritptional activity of JUND in osteoblasts. A recent study has demonstrated that both NACA and JUND coactivate *Lrp6* gene expression in osteoblasts (192). The significance of this transcriptional regulation lies in the outcome, as this is the first characterization of *Lrp6* gene regulation and its impact on priming PTH subsequent responses in osteoblasts. More examples of NACA-mediated regulation of AP-1 transcription include the transcriptional control of *Col1a1* and *Mmp9* gene promoters during osteoblast differentiation (186, 189-191).

After reviewing the coactivating functions of NACA, we will highlight the other facet of this protein as a transcriptional corepressor. Studies from our laboratory have confirmed the binding of NACA to the *Osteocalcin* and *Myogenin* gene promoters in osteoblasts and myoblasts (193). The differential regulation of both promoters during osteogenesis and myogenesis suggests a

promoter- and cell- specific functions for NACA. The regulatory scheme of those promoters depends on the interaction and recruitment of HDACs by NACA in specific cell lineages. The N-terminal (12-69) fragment of NACA binds the corepressors HDAC1 and HDAC3 and regulates the transcription of the *Osteocalcin* and *Myogenin* promoters in myoblasts and osteoblasts, respectively (193). In this context, the docking functions of NACA ensure the inhibition of *Myogenin* in differentiated osteoblasts and *Osteocalcin* in cells destined to the myogenic lineage (193).

Altogether, our work has revealed a dynamic transcriptional control exerted by NACA during differentiation either by potentiating AP-1 transcription in osteoblasts or by recruiting corepressors to lineage-specific promoters.

1.9.2 NACA: The cytoplasmic-nuclear shuttle

The coregulatory functions of NACA are highly dependent on phosphorylation events carried out by multiple kinases. Post-translational modification by phosphorylation is one of the most important mechanisms regulating protein function, localization, and stability. *In vitro* and *in vivo* studies have characterized different phosphorylation events modulating the subcellular localization and activity of NACA. Those studies have revealed the identity of kinases, phosphatases, and signaling pathways associated with NACA's functions in osteoblast cells. In this section, we will review the work done by our group and others to identify different effectors modulating the activity of NACA.

The ubiquitous kinase glycogen synthase kinase 3beta (GSK3β) phosphorylates NACA on Thr-159 residue of the C-terminal end, thus triggering the degradation of NACA by the 26S proteasome system. The inhibition of the kinase leads to the stabilization and nuclear accumulation of NACA, while mutating the phosphoacceptor sites of GSK3β on NACA enhances its coactivation potency (194). Additionally, NACA is phosphorylated by casein kinase 2 (CK2). The phosphorylation of NACA by CK2 at Ser-25, Thr-27, Ser29 and Ser-34 activates the chromosome region maintenance 1 (CRM1) - mediated nuclear export of the protein. The N-terminus phosphorylated sequence by CK2 is thought to be the signal for NACA's nuclear export (195). Moreover, the cell adhesion to fibronectins stimulates the phosphorylation of NACA by the integrin linked kinase (ILK) on Ser-43, thus inducing the nuclear import of NACA in osteoblasts (196). Similarly, the phosphorylation of NACA by PKA on Ser-99 induces its nuclear translocation in response to PTH signaling in osteoblasts. Phospho-S99-NACA

accumulates in osteoblasts exposed to PTH (1-34) and this accumulation is abrogated by an S99A mutation but further enhanced by a phosphomimetic residue (S99D). The same study has also shown that PTH (1-34) induces the accumulation of NACA at the *Osteocalcin* promoter in osteoblasts (197). Current studies in our laboratory are focused on understanding the physiological relevance of this modification using site-directed mutagenesis of NACA at S99 in knock-in mice models.

As the search for more kinases regulating NACA's shuttling and activity is still going, we have recently investigated the role of phosphatases in this matter. Addison et al. have identified the protein phosphatase 1 catalytic subunit α (PP1A) as a NACA-associated phosphatase. The Ser/Thr PP1A phosphatase dephosphorylates NACA at Thr-89, Ser-151 and Thr-174 in MC3T3-E1 osteoblastic cells. Interestingly, the dephosphorylation of NACA by PP1A enhances its nuclear accumulation and potentiates AP-1 transcriptional activity, osteogenic differentiation, and matrix mineralization *in vitro* (198). Collectively, the reviewed studies show that the NACA cytoplasmic-nuclear shuttle is driven, in part, by reversible phosphorylation, thus regulating its coactivating functions in osteoblast gene transcription.

1.9.3 The physiological relevance of NACA

The physiological relevance of NACA phosphorylation has been demonstrated *in vivo*. The first evidence of this significance is a knock-in mouse model with a non-phosphorylatable serine-to-alanine mutation at position 43 (S43A). NACA S43A mice exhibited reduced mass of immature and woven-type bone with an increase in osteocyte number. The S43A mutation decreased the nuclear translocation of NACA and reduced *Ocn* promoter occupancy and gene transcription (196). This phenotype was strikingly similar to the phenotype of mice that lack the expression of Gαs in early osteoblasts (199). As previously mentioned, Gαs is a proximal downstream effector of PTH signaling and a mediator of its anabolic effect in bone. The notion of a genetic link between Gαs and NACA has been further strengthened by an altered gene dosage in compound heterozygous mouse model ($G\alpha s^{ob+/-}$; $Naca^{+/-}$). Those mice exhibited osteopenia with reduced bone mass, increased number of osteocytes, and enhanced expression of *Sost* (197). The work of Pellicelli et al. has supported the physiological significance of the PTH-Gαs-PKA-NACA pathway in osteoblasts, identifying both *Osteocalcin* and *Lrp6* as downstream targets of this pathway. The same approach using chromatin immunoprecipitation with deep sequencing (ChIP-Seq) against NACA and RNA-Seq gene expression profiling in PTH-treated

osteoblast cells, has identified two novel targets of the PTH-Gαs-PKA-NACA pathway: The Nuclear factor interleukin-3-regulated (*Nfil3*) and the Ubiquitin-specific peptidase 53 (*Usp53*).

1.9.3.1 *Nfil3*

Nfil3 (also known as E4-binding protein 4) is a basic leucine zipper (bZIP) transcription factor (200). E4-binding protein 4 (E4bp4) was initially isolated by screening for its ability to bind the ATF site of the adenovirus E4 promoter and repress its activity (200). Later, Nfil3 protein was isolated from a human T-cell cDNA library where it binds to the CRE/ATF regulatory sequences of the IL3 promoter (201). It was suggested that Nfil3/E4bp4 can act both as a transcriptional activator and a transcriptional repressor in a promoter-specific fashion.

In order to regulate the transcription of target gene promoters, bZIP members form either homodimers or heterodimers that bind specific DNA stretches. The bZIP superfamily of transcription factors include the cAMP response element binding protein (CREB)/activating transcription factor, activator protein 1, CCAAT enhancer binding protein (C/EBP), nuclear factor (erythroid-derived 2), and proline and acidic residue rich (PAR) families (202). As a bZIP member, Nfil3 recognizes a homologous consensus binding sequence to the cAMP-responsive DNA element (CRE), consensus C/EBPβ and PAR binding sites (203). Sharing a common recognition site with NFIL3, CREB, and C/EBPβ suggests a potential interaction among the different bZIP members at the level of regulating the transcription of common gene products.

NFIL3 has been implicated in diverse processes regulating immune cell function (201, 204-206), circadian rhythm oscillations (202, 207), cell survival versus apoptosis (205, 208), and anti-inflammatory responses (202). PTH, PGE2, and cAMP analogs are known to activate *Nfil3* expression (209, 210). Rapid induction of *Nfil3* can also be achieved by the direct binding of the glucocorticoid receptor (GR) to the *Nfil3* gene distal promoter in thymocytes (211).

In the context of bone biology, *Nfil3* is a well described transcriptional repressor responding to PTH treatment in osteoblasts (210, 212). NFIL3 was shown to repress neuronal CREB targets (213), PTH-regulated Cox-2 promoter activity (210), and osteoblast gene transcription (210, 212). A clear characterization of *Nfil3* function and regulation in osteoblasts is still missing.

1.9.3.2 *Usp53*

USP53 belongs to the ubiquitin-specific protease (USP) superfamily of deubiquitinating enzymes (214, 215). The genomic landscape encompasses about 58 different USPs, few of which have a clear assigned function and substrate. Domain structure analysis indicated that most USPs bear a core catalytic domain in addition to N-and C-terminal extensions defining substrate specificity and protein-protein interaction decisions (215, 216). Based on sequence analysis, USP53 along with five other USP members (USP39, USP50, USP52, USP54, and USPL1) are predicted to be inactive (217). The lack of a functional histidine residue in the USP53 catalytic domain renders the protein devoid of catalytic activity and this was further confirmed using *in vitro* ubiquitination assays (217, 218).

USP53 has been associated with human syndromes of pleiotropic effects on different tissues. Initially, a duplicated genomic locus encompassing *MYOZ2*, *FABP2*, and *USP53* accompanied a severe phenotype of Cantu syndrome in a patient with cardiomegaly, hypertrichosis, bone deformities, and severe obesity (219). More recently, *USP53* has been linked to pediatric cholestatic liver disease. The study identified a homozygous truncating mutation in *USP53* in a family diagnosed with liver cholestasis and hearing loss (220). Along the same line, whole exome sequencing in 7 patients from unrelated families has identified 10 biallelic pathogenic variants in *USP53*, all contributing to the defective hepatobiliary condition in those patients (221). The listing of different clinical manifestations converging at *USP53* supports a central function for the gene in regulating developmental processes.

Reviewing public expression datasets shows that *Usp53* is expressed in a wide range of internal, nervous, reproductive, and secretory organs. Two main isoforms of *Usp53* (long isoform; NM_133857.3 and short isoform; AK045953) have been described and the full-length *Usp53* transcript has been shown to be predominant in mouse cochlear extracts (218). This study has linked *Usp53* to progressive hearing loss in *mambo* mice carrying a missense mutation in the *Usp53* catalytic domain. The suggested underlying mechanism involved a disrupted interaction between USP53 and tight junction proteins (218). Except for this study, the contribution of *Usp53* to any developmental pathway has not been addressed.

1.10 Rationale, hypothesis, and objectives

The daily injection of parathyroid hormone (PTH) increases bone mass and protects against osteoporotic fractures, however it has several limitations. The expensive costs and inconvenient route of administration of PTH is burdensome to most patients. Moreover, PTH is not recommended for use in children with metabolic bone diseases such as Osteogenesis Imperfecta. Additionally, a complete picture of PTH mechanism of action is still missing. Therefore, it is important to find alternative therapeutic options, possibly by targeting enzymes in the signaling cascade downstream of PTH, that modulate osteoblastic gene expression, differentiation, and function.

We have shown that PTH induces the phosphorylation of NACA at Ser99 enhancing its nuclear translocation and activation of target genes. We have also demonstrated the physiological significance of the PTH-Gαs-PKA-NACA pathway *in vivo* (197). Our genome-wide approach has identified *Nfil3* and *Usp53* as potential targets mediating the PTH-NACA signaling in osteoblasts. Reviewing the literature, we have noted that the functional characterization of *Nfil3* in osteoblasts is missing and that despite the work done to identify *USP53* variants, the functional and mechanistic characterization underlying *USP53*-related pathologies has not been covered yet. Consequently, we **hypothesized** that *Nfil3* and *Usp53* mediate the PTH-NACA signaling modulating osteoblast biology and PTH anabolism *in vitro* and *in vivo*.

The first objective of this research project is to identify and characterize the mechanism that regulates *Nfil3* transcription and expression in osteoblasts as well as its role in osteoblast and osteocyte differentiation (**Chapter III)**.

USP53 was initially identified as part of a gene duplication associated with Cantu syndrome, a condition of hypertrichosis, cardiomegaly, severe bone deformities, and obesity (219). At the time of starting this research project this was the only published study linked to USP53, with no assigned biological functions in any tissue. The human phenotype associated with USP53 as well as our ChIP-Seq and RNA-Seq findings in PTH- treated osteoblasts have shifted all the efforts to uncover the biological functions of *Usp53 in vitro* (**Chapter IV**) and *in vivo* (**Chapter V**). Consequently, chapter **IV** focuses on the role of *Usp53* in regulating mesenchymal differentiation *in vitro* and chapter **V** offers the full skeletal characterization of *Usp53*-deficient mice and more.

Chapter II: MATERIALS AND METHODS

2.1. Chromatin immunoprecipitation (ChIP), Chip Sequencing (ChIP-Seq), and RNA-Sequencing (RNA-Seq)

Conventional ChIP assay, ChIP-Seq, and RNA-Seq were performed as previously described [24]. For ChIP-PCR, *Nfil3* promoter fragments were amplified using 5'-AAAGGTGCTGGCACCACG -3 ' forward and 5 ' - CAGCTGCTACCCGCTGTC- 3 ' reverse primers. The ChIP-Seq against NACA has identified a peak in Chromosome 3 (3qG1); Chr3: 122,984,707- 122,984,915. For ChIP-PCR, *Usp53* promoter fragment was amplified using 5' - CTGAAACCCACAGAACCCCG -3 ' forward and 5 ' - GGATTTCCACGGCAGACGC - 3 ' reverse primers. Reactions were performed using Power SYBR™ Green master mix following the manufacturer's instructions (ThermoFisher Scientific) and carried out in a QuantStudio 7 Flex Real-Time PCR System (ThermoFisher Scientific).

2.2. RNA Isolation and Quantitative Real-Time PCR

Total RNA was extracted from cells or tissues using TRIzol reagent following the manufacturer's instructions (Invitrogen). Using the high-capacity cDNA reverse transcription kit (Thermo Fisher Scientific), 1-2 µg of RNA were reverse-transcribed into cDNA following the manufacturer's protocol. Gene expression was assessed using the Taqman™ Fast Advanced Master Mix (Thermo Fisher Scientific) and the following TaqMan primers: (Supplementary Table 5.2).

Expression levels of *Usp53* (long and short isoforms) were assessed using the Power SYBR™ Green PCR Master Mix (Thermo Fisher Scientific) and the following isoform-specific oligonucleotide primers: *Usp53* short isoform, forward, 5′-GAAGTGTCCTAGTAACTGTGGCC-3′ , and reverse, 5′-GAATGAAAGCAACTGTGATACCCC-3′; *Usp53* long isoform, forward, 5′-CGACACAGGGATTTGGTTGATG-3′, and reverse, 5′-CAGAGGTGTAGCTCTCATGGG-3′; and *Gapdh*, forward, 5′-CATCACTGCCACCCAGAAGACTG-3′, and reverse, 5′-ATGCCAGTGAGCTTCCCGTTCAG-3′. All reactions were carried out in a 7500 real-time PCR system (Thermo Fisher Scientific).

For bone and fat tissues, samples were collected, flash-frozen in liquid nitrogen and stored at -80°C. For long bones, bone marrow was flushed with PBS prior to freezing. Samples were homogenized in TRIzol using a tissue homogenizer (Polytron) following the manufacturer's instructions (Invitrogen) and then processed for gene expression analysis.

2.3. Plasmids, Antibodies, and Reagents

The wildtype-NACA , NACA-S99D mutant (197), and NACA delta DBD (69-80) mutant (189) expressing vectors were previously described. The affinity-purified chicken anti-NACA (222) and the rabbit polyclonal anti-NACA-phosphoS99 (anti-pS99) (197) antibodies have also been previously reported. PTH(1–34) was purchased from Bachem (Torrance, CA) and N^6-benzoyladenosine cAMP (6Bnz-cAMP; catalog no. B009) was from Biolog (Bremen, Germany). Ascorbic acid, β-glycerophosphate, dexamethasone (Dex), 3-isobutyl-1-methylxanthine (IBMX), insulin, and hexadimethrine bromide were obtained from Sigma-Aldrich. The pLenti-C-Myc-DDK *Usp53* expression vector (MR224743L1) encoding the full-length transcript (NM-133857) was purchased from Origene. Cycloheximide (CHX) was obtained from Sigma-Aldrich. Recombinant human bone morphogenetic protein-2 (BMP-2) was obtained from Life Technologies.

2.4. Cell culture systems

2.4.1 Cell lines

ST2 stromal cells (obtained from Riken Cell bank, Tsukuba, Japan) and MC3T3-E1 (subclone 4) osteoblastic cell line (a gift from Dr. Renny T. Franceschi, University of Michigan, Ann Arbor, MI) were cultured in minimum essential medium alpha (α-MEM, Gibco) supplemented with 10% fetal bovine serum (FBS, Hyclone, Logan, UT), 100 U/ml penicillin, and 100 µg/ml streptomycin at 37°C in a humidified atmosphere with 5% CO2. HEK293T cells (ATCC) were cultured in Dulbecco's modified Eagle's medium (DMEM,Gibco) supplemented with 10% FBS. IDGSW3 cells (EKC001, Kerafast) were expanded in proliferation conditions at 33°C in αMEM with 10% FBS, 100 U/ml penicillin, 100 µg/ml streptomycin, and 50 U/ml IFN-γ on rat tail type 1 collagen-coated plates. For osteocytic cultures, IDG-SW3 cells were plated at 80,000 cells/cm2 in osteogenic medium (37°C with 50 µg/ml ascorbic acid and 4 mM β-glycerophosphate in the absence of IFN-γ) (15).

2.4.2 Primary cells

2.4.2.1. Calvaraie

Primary osteoblasts were isolated from calvariae of 2-d-old mice as described previously (223). Briefly, calvariae were dissected and washed in phosphate-buffered saline (PBS). Calvariae were subjected to two consecutive digestions (15 and 30 min) at 37°C in α-MEM

containing increasing concentrations of collagenase P (Roche) and 0.25% trypsin (Life Technologies). Supernatants of the first two digests were discarded and fresh digestion medium containing collagenase P and 0.25% trypsin was added. Calvariae were then incubated at 37°C for 60 min, with vigorous shaking every 10 min. This step was repeated one more time. After that, cells and bone pieces were spun, resuspended in complete medium (α-MEM supplemented with 10% fetal bovine serum (FBS)), and plated separately. Cells were kept 2 to 4 days before passaging for experiments. Only fraction 4, representing the more mature osteoblast population, was used for *in vitro* experiments in this study. Mouse embryonic fibroblasts were isolated from E13.5 embryos as described previously (224). MEFs were maintained in Dulbecco's Modified Eagle's Medium (DMEM) (Life Technologies) containing 4.5 g/L D-glucose and 10% FBS. Passage 2 MEF cells were used in subsequent experiments.

2.4.2.2. Bone marrow stromal cells (BMSCs)

Murine BMSCs were isolated from 6-8 week old mice as previously described (225). Briefly, tibia and femoral marrow compartments were used to isolate BMSCs. After cutting the epiphysis, the femurs and tibia were flushed with complete media using a 27-gauge needle. The flushed cells were then filtered using a 70-µm filter mesh to get rid of bone chips and cell clumps. Finally, the cells were resuspended in additional complete medium and cultured in DMEM supplemented with 20% FBS, 100 U/ml penicillin, and 100 µg/ml streptomycin sulfate for differentiation experiments. Alternatively, flushed bone marrow suspensions were processed for osteoclast precursors isolation and differentiation.

2.5. Short hairpin RNA (shRNA) Gene Silencing

Vectors expressing the short hairpin RNAs (shRNAs) targeting *Naca* were generated as previously described (192). Vectors expressing shRNAs targeting *Creb1* (shCreb TRC no. 0000096633, and TRC no. 0000301658), *Nfil3* (shNfil3, TRC no. 0000082339 and TRC no. 0000082338), *Usp53* (shUsp53, TRC no. 0000030914; shUsp53.1, TRC no. 0000030918) and the non-targeted control shRNA (shScr; #SHC016) were purchased from Sigma-Aldrich. For stable silencing of *Nfil3*, *Naca, Creb1,* and *Usp53,* lentiviral particles were prepared by transfecting HEK-293T cells with 10 µg of shRNA expressing vector, 7.5 µg psPAX2 (viral packaging vector, a gift from Dr. Didier Trono; Addgene plasmid #12260), and 2.5 µg pMD2.G (viral envelope encoding vector, a gift from Dr. Didier Trono; Addgene plasmid #12259), using

X-treme GENE HP (Roche, through Sigma-Aldrich) according to manufacturer's instructions. Lentivirus-enriched medium was collected at 24h and 48h post transfection, filtered using a 0.45 μm filter (Millipore, Billerica, MA), and supplemented with 8 μg/ml hexadimethrine bromide (Polybrene, Sigma-Aldrich). The lentiviral medium was used to infect IDG-SW3, BMSCs or ST2 or MC3T3-E1 cells for 24 h cells. Infected cells were then cultured in the presence of 2.5 μg/ml (BMSCs, ST2, and IDG-SW3) or 5 μg/ml (MC3T3-E1) of puromycin for selection. Selection was performed for 5 days.

2.6. Western Blotting

Whole cell extracts were prepared from MC3T3-E1, ST2, HEK-293T or MEF cells. Cells were washed twice with ice-cold PBS (1x) and scraped with lysis buffer (300mM NaCl, 50mM HEPES, pH 7.6, 1% Triton X-100, and protease/phosphatase inhibitor cocktail (Cell Signaling)). Cells were then kept on ice for 10 min and briefly sonicated with 1 pulse for 15 sec using an Ultrasonic dismembrator model 500 (Thermo Fisher Scientific, Waltham, MA). Following sonication, cells were spun down at 4°C for 15 min at maximum speed. Supernatant was aliquoted and stored at -80°C. For western blots, equal amounts of cell extracts (10 μg protein) were resuspended in 6X Laemmli buffer. The samples were boiled for 5 min and run on a denaturing SDS-PAGE for 1.5 h then transferred to a PVDF membrane (Amersham, UK). The membrane was blocked for 45 min in 5% non-fat dry milk. After blocking, the membrane was incubated with the primary antibody diluted 1:1000 in 5% non-fat dry milk or bovine serum albumin (BSA), overnight at 4°C. The membrane was later incubated with the secondary antibody conjugated with horseradish-peroxidase, anti-mouse, or anti-rabbit- HRP, diluted 1:20,000. Development was done using the Western Lightening Chemiluminescence Kit (Perkin Elmer, Akron, OH, USA). The protein bands were visualized by autoradiography. The blots were probed with the following antibodies: rabbit anti-USP53 (HPA035844, Prestige antibodies, Sigma-Aldrich), rabbit-anti-TAK1 (#5206, Cell Signaling), rabbit- anti-TAB2 (#3745, Cell Signaling), rabbit-anti-TAB1 (ab76412, abcam), mouse-anti-DYKDDDDK (#8146, Cell Signaling), rabbit- anti-phospho-p38 MAPK (#4511, Cell Signaling), rabbit- anti-p38 MAPK (#8690, Cell Signaling), rabbit-anti-PPARγ (#2443, Cell Signaling), mouse-anti- GAPDH (HRP Conjugate) (#51332, Cell Signaling), mouse anti-αTubulin (catalog no. T6074), Sigma-Aldrich), Rabbit anti-CREB (catalog no. 9197) and rabbit antiE4BP4/NFIL3 (catalog no. 14312) were purchased from Cell Signaling.

2.7. Vector Cloning

The *Nfil3* promoter fragment (-818/+182 bp) and the *Usp53* promoter fragment (-2325/+238bp) were amplified from MC3T3-E1 cell genomic DNA. The fragments were subcloned into the pGL4.10[LUC2] vector (Promega, Madison, WI) using KpnI and NheI restriction sites that were added during the PCR step. All generated vectors were verified by sequencing. Primer sequences and plasmids are available upon request.

2.8. Luciferase Assay

MC3T3-E1 cells were seeded at a density of 20,000 cells/well, 14h prior to transfection. In each well, 300 ng of *Nfil3* or 300 ng of *Usp53* promoter reporter vector and 15 ng of Renilla luciferase internal control vector (pRL-null, Promega) were transfected using the lipofectamine LTX and PLUS Reagent kit following the manufacturer's instructions (Invitrogen). 100 ng of NACA- S99D mutant or NACA delta DBD (69-80) mutant and 50 ng of CREB-expressing vector (MR204788, Origene) or 50 ng of cJUN-expressing vector (35) were co-transfected. Twenty-four (24) h post transfection, the dual-luciferase assay was performed according to the manufacturer's protocol (Promega) and signal was measured using a VICTOR Nivo multimode microplate reader (Perkin Elmer, Waltham, MA). Results were calculated by normalizing Firefly relative light units to Renilla relative light units and are expressed as fold-change over the empty vector. When indicated, cells were treated with 100 nM PTH(1-34) for 24 h before luciferase measurement.

2.9. Differentiation Assays

2.9.1. Osteogenic Differentiation

ST2 cells, BMSCs, calvarial osteoblasts or MC3T3-E1 cells were plated at 50,000 cells/cm^2 for differentiation assays. To induce osteogenic differentiation of ST2 cells, cells were incubated in α-MEM medium at 37°C with the supplementation of 50 µg/ml of ascorbic acid and 100 ng/ml of BMP2 (Gibco). To induce osteogenic differentiation of MC3T3-E1 cells, cells were incubated in α-MEM medium at 37°C with the supplementation of 50 µg/ml of ascorbic acid and 10 mM of β-glycerophosphate.

To induce osteogenic differentiation of calvarial osteoblasts, cells were incubated in complete α-MEM medium with the supplementation of 50 µg/ml of ascorbic acid (Sigma-Aldrich), 10 mM of β-glycerophosphate (Sigma-Aldrich), and 10nM dexamethasone (Sigma-

Aldrich). Medium was changed every 2 days for the duration of the experiment. For MEF cultures, cells were plated at a density of 50,000 cells/cm^2 for osteogenic differentiation. Cells were induced in complete DMEM medium supplemented with 100 µg/ml of ascorbic acid (Sigma-Aldrich), 10 mM of β-glycerophosphate (Sigma-Aldrich), and 20 ng/ml BMP-2 (Life Technologies). Medium was changed every other day for 15 days.

2.9.2. Adipogenic Differentiation

ST2 cells, BMSCs and MEF cells were plated at 50,000 cells/cm^2 for adipogenic differentiation. BMSCs and MEF cells were incubated in DMEM medium and ST2 cells in α-MEM medium at 37°C with 0.5 mM of 3-isobutyl-1-methylxanthine (IBMX, Sigma-Aldrich), 1 µM dexamethasone, 1 µg/ml insulin (Sigma-Aldrich), and 1 µM rosiglitazone (Sigma-Aldrich) for the first day. On day 2, differentiation medium was changed and supplemented with only insulin (1 µg/ml) and rosiglitazone (1 µM). Complete medium (without supplements) was used from day 4 until the end of the differentiation assay. For ST2 cells and BMSCs, medium was changed every other day for 8 days. For MEFs, medium was changed every other day for 15 days.

2.10. Staining

2.10.1. Cell Staining

Alizarin red staining was performed on MC3T3-E1 cells on day 21 of osteogenic differentiation. Briefly, cells were fixed in 70% ethanol for 1 h at -20°C and then incubated with alizarin red solution (40 mM, pH 4.2) (Sigma-Aldrich) for 15 min at RT. Cells were then washed with dH_2O to remove excess stain. Finally, cells were washed with PBS (1x) for 15 min and photographed. Alkaline phosphatase (ALP) staining was performed on ST2 cells on day 6 of osteogenic differentiation. Staining was performed using the TRACP and ALP double-stain kit (TAKARA) following the manufacturer's instructions. Cells were fixed in 10% formalin at RT. Von Kossa staining for mineralized matrix was performed using 5% silver nitrate. Oil red O (Sigma-Aldrich) staining was performed to detect lipid accumulation. Following fixation, cells were rinsed with dH_2O and then 60% isopropanol for 2-5 min. Cells were then incubated with Oil Red O solution for 5 min. Finally, cells were rinsed 3-4 times with dH_2O and photographed.

Mature osteoclasts were stained for tartrate resistant acid phosphatase (TRAP) using the TRACP and ALP double-stain kit (TAKARA) following the manufacturer's instructions.

Number of osteoclast nuclei was counted in 50 random fields for each condition at a 20X magnification.

2.10.2. Picrosirius Red Staining

To visualize the deposited collagen type I matrix, we performed picrosirius red staining on IDG-SW3 cultures. Cells were stained with Sirius Red F3BA (Sigma-Aldrich) and quantified using a microplate reader at 562 nm as previously described (226).

2.10.3. Immunohistochemical Staining of Collagen Type-I

IDG-SW3 cells were plated at a density of 80,000 cells/cm2 , on non-collagen-coated plastic tissue culture plates, in differentiation medium. At each indicated timepoint, cells were washed with PBS twice, fixed with 95% ethanol for 10 min and then washed with PBS three times. Cultures were incubated with blocking solution (2% BSA in PBS) for 1 hour at room temperature and then incubated overnight with polyclonal anti-collagen type I antibody (AB749P, EMD Millipore) (diluted 1:400 in 1% BSA in PBS) at 4°C. Cultures were then washed with PBS three times and incubated for 45 minutes with Alexa Fluor594 conjugated goat anti-rabbit IgG (H+L) (diluted 1:500 in 1% BSA in PBS; Invitrogen). Finally, cells were washed with PBS 5 times and nuclei were stained with ProLong Gold antifade reagent with DAPI (ThermoFisher Scientific). Images were acquired using a Leica DMR fluorescence microscope (Leica Microsystems, Wetzlar, Germany) connected to a digital DP70 camera (Olympus, Center Valley, PA). Image processing included whole image channel filtering to remove noise and whole image adjustment of brightness, contrast, color balance, and sharpening using Adobe Photoshop v.12.1. Photoshop images were then flattened and imported into Adobe Illustrator v.15.1 to build the final montages.

2.11. Electrophoresis Mobility Shift Assay (EMSA)

EMSA assays were performed as described elsewhere (192). HEK-293 cells were transfected with 10 µg of NACA-expressing vector (192). 24hrs following transfection, cells were treated for 1 h with 100 µm 6Bnz-cAMP to induce phosphorylation of NACA at residue Serine 99 and nuclear translocation (192). Oligonucleotide probes spanning the NACA binding site (NACAbds) within the *Usp53* promoter region (5'-ACCCCGGCTCAGATCCCGCG-3′) or the positive control NACAbds from the *Myoglobin* promoter region (5′-AGGGCCAGAGAAAGACA-3′) (188) were synthesized with a GG overhang. The probes were

32P-labeled using [α32P]- dCTP (PerkinElmer, Waltham, MA) and Klenow DNA Polymerase I (New England Biolabs, Ipswich, MA).

2.12. In vivo osteogenesis assay

Murine BMSCs were isolated from 6-wk-old C57BL/6N male mice (obtained from Charles River Canada Laboratories) as described in the above sections. 2 x10^6 shScr or shUsp53-knockdown BMSCs were seeded in Gelfoam absorbable collagen sponges (Pfizer) and implanted subcutaneously on the backs of 6-wk-old athymic nude mice (Crl:NIH-Lystbg Foxn1nu Btkxid; 201; Charles River Laboratories). After 4 weeks, the transplants (n=4 for both shScr and shUsp53) were harvested and further processed for micro-CT and histological analysis. For micro-CT, transplants were fixed in 4% PFA in PBS for 48 h at room temperature and washed with 1x phosphate-buffered saline. Transplants were then scanned with a 6-µm pixel size using a Skyscan 1272 µCT system (Bruker, Belgium). The parameters were 5 µm pixel size, 50 kV, 194 µA, 0.5 mm Al filter, angular rotation step of 0.450, and an exposure time of 500 ms with a total scan duration of 45min. Three-frame averaging was used to improve the signal-to-noise ratio. After scanning, 3-dimensional (3D) microstructural image data were reconstructed using the manufacturer's software (Skyscan NRecon). For histology, transplants were then decalcified in EDTA and embedded in paraffin. Paraffin blocks were sectioned (6-µm) and stained with H&E or incubated with specific primary antibodies against Osterix (1/100; ab22552; Abcam) or Perilipin (1/200; ab3526; Abcam). Prior to immunostaining, sections were pretreated with citrate buffer (pH 6.0) and heated for 10 min at a temperature between 95°C and 100°C for antigen retrieval. Primary antibodies were detected using Alexa Fluor® 594 conjugated goat anti-rabbit IgG (H+L) (1/250; Invitrogen). Nuclei were stained with ProLong® Gold antifade reagent with DAPI (Thermo Fisher Scientific). Images were acquired using a Leica DMR fluorescence microscope (Leica Microsystems, Wetzlar, Germany) connected to a digital DP70 camera (Olympus, Center Valley, PA). Image processing included whole image channel filtering to remove noise and whole image adjustment of brightness, contrast, color balance, and sharpening using Adobe Photoshop v. 12.1. Photoshop images were then flattened and imported into Adobe Illustrator v. 15.1 to build the final montages.

2.13. Animal Experimentation

All animal procedures were reviewed and approved by the McGill Institutional Animal Care and Use Committee and followed the guidelines of the Canadian Council on Animal Care, conforming to the relevant regulatory standards. Mice were kept in an environmentally controlled barrier animal facility with a 12-h light/12-h dark cycle and were fed mouse chow and water *ad libitum*. ES cell blastocyst microinjection was performed at the Montreal Clinical Research Institute (IRCM) transgenic core facility in Montreal.

2.13.1. Mouse and ES cells generation

Embryonic stem cells (ES, JM8A3.N1) harboring a *Usp53* promoter-driven targeting cassette (L1L2-Bact-P) were purchased from the European Mouse Mutant Cell Repository (EUMMCR). Homologous recombination of *Usp53* targeting vector in male ES cells (C57BL/6N mouse cells, P5) produced a conditional 'knockout-first' allele with a neomycin-resistance cassette and a LacZ reporter gene inserted between the third and the fourth *Usp53* exons (*Usp53*$^{tm1a(EUCOMM)HMGU}$, Fig.1A, top).

ES cells containing the recombined allele were injected into C57BL/6N blastocysts and reimplanted in CD1 pseudopregnant females. One chimeric male bearing the recombined allele was mated with C57BL/6N female mice to obtain heterozygotes *Usp53*$^{tm1a(EUCOMM)HMGU}$. These mice were then mated with transgenic mice expressing Cre recombinase ubiquitously under the control of a human cytomegalovirus (*CMV*) promoter. Recombination at *loxP* sites resulted in deletion of both the neomycin-resistance selection cassette and *Usp53* critical region encompassing exons 4,5, and 6, generating a *Usp53* null allele (tm1b) (Fig.1A, bottom). Back crossing to C57BL/6N mice generated heterozygous (HET, tm1b/wt) mice free of recombinase expression. Wildtype (WT, wt/wt) and homozygous (KO, tm1b/tm1b) males and females were obtained by subsequent crossings of heterozygotes. All mice used in this work were maintained on a C57BL/6N genetic background. Colony establishment and maintenance were performed as per EUCOMM guidelines (227) and summarized in Figure 5. Biological replicates *N*= 8-10 mice/group were used for all experiments except for dynamic histomorphometry *N*=5.

2.13.2. Mouse genotyping

Genotyping of animals was performed by PCR using DNA extracted from tail and ear snips. We followed the EUCOMM/KOMP-CSD gel-based genotyping guidelines for primer

design and genotyping strategies, to genotype the 'knockout-first' allele and all other studied alleles. The wildtype, HET, and KO alleles were amplified by a PCR reaction incorporating three primers (a,b, and c, Fig.1B). Amplified fragment length from a WT mouse is 550 bp and 888 bp for HET or KO mice (Fig.1B). Primer sequences will be provided upon request.

2.13.3. Beta-galactosidase activity detection

Embryonic and postnatal samples (embryos, long bones, calvariae, and skin) were dissected and cleaned of soft tissues. For whole mounts, embryos were incubated in 2% PBS-buffered paraformaldehyde fixative solution for 1-3 h at 4°C . Embryos were incubated in 0.1% X-gal buffer for 6 h at 37°C in the dark. Samples were then rinsed in PBS and postfixed in 4% PFA overnight at 4°C. Finally, embryos were briefly cleared in ethanol and imaged. Adult bone samples were fixed in 4% PBS-buffered formaldehyde for 1-2 h at 4°C. Bone samples were preincubated in 30% sucrose solution overnight and snap-frozen by liquid nitrogen and 2-methyl butane (Sigma-Aldrich) in embedding medium (OCT, Thermo Fisher Scientific) in cryomolds. Cryomolds were then sectioned at 5µm-thick cross-sectional sections using a CryoStaR NX70 (Thermo Scientific) and samples were kept at -80°C until further processing.

For β-galactosidase activity, LacZ expression was detected by staining with X-gal (5-bromo-4-chloro-3-indolyl β-D galactopyranoside, Promega). Briefly, frozen sections were washed 3 times in a LacZ wash buffer containing 2mM MgCl2, 0.01% sodium deoxycholate, 0.02% NP-40 in 100mM sodium phosphate buffer at 4°C. Sections were stained overnight at 30°C in a humidified chamber in LacZ staining buffer containing 1 mg/ml X-gal. Sections were then washed, postfixed in 4% formaldehyde, and counterstained with nuclear fast red solution (Sigma-Aldrich). Pictures were taken using a Leica DMR fluorescence microscope (Leica Microsystems, Wetzlar, Germany) connected to a digital DP70 camera (Olympus, Center Valley, PA).

2.13.4. Skeletal tissue preparations

Skeletal tissue preparation of 2-d-old mice was performed as described previously (228). In brief, newborns were collected, skinned, and cleaned of internal organs. Skeletons were then fixed overnight in 95% ethanol at RT. To stain cartilage, skeletons were submerged in a solution of 0.015% alcian blue 8GX dye (Sigma-Aldrich) and then cleared in 95% ethanol for 24 h. Alcian blue stained skeletons were treated with 2% potassium hydroxide to dissolve extra soft

tissues. The mineralized tissues were stained by 0.005% alizarin red S (Sigma-Aldrich) solution for 3-4 h at RT. Finally, stained skeletons were cleared with an equimolar solution of glycerol and 1% potassium hydroxide at RT, until ready for imaging.

2.13.5. Bone histomorphometry

Femurs from 6-week-old female mice were dissected and fixed in 4% PFA for 24 h at 4°C, dehydrated with graded concentrations of ethanol, and either embedded in methyl methacrylate resin or processed for μCT analysis. For dynamic histomorphometry, bone formation rates and other parameters were assessed after calcein double labeling. Calcein (Sigma-Aldrich) was dissolved in calcein buffer (0.15M NaCl and 2% $NaHCO_3$) and injected twice at 0.125 mg/g body weight 7 and 2 days prior to mice sacrifice. Resin-embedded femurs were sectioned at 5 μm-thick cross-sectional sections using a Rotary microtome model RM2255 (Leica Microsystems). All quantifications were acquired with a fluorescent microscope (DMR; Leica) equipped with a QImaging camera. Analysis of the parameters was performed using the BioquantOsteo software (BioQuant, Nashville, TN). For static histomorphometry, μCT was performed using a SkyScan 1272 high-resolution μCT scanner connected to a Hamamatsu 10-megapixel camera. Scan settings are as follows: voxel size 4.5 μm, high resolution, 60 kV, 166 μA, and a 0.25-mm aluminum (AL) filter. Integration time was set at 550 ms, and 3 images were captured every 0.45° through 180° rotation. Reconstruction was performed using SkyScan Recon software and analyzed using SkyScan CT Analysis software. For femoral trabecular parameters, a region of interest (ROI) was defined starting at 0.75 mm proximal to the growth plate of femurs and extending 1.85 mm in the direction of the diaphysis where trabeculae were no longer visible. For femoral cortical parameters, ROI was defined starting at 0.25mm above the third trochanter landmark. A region of 0.5mm in height at midshaft was analyzed.

2.13.6 Blood Biochemistry

Blood from 6-week-old female mice was collected at sacrifice by cardiac puncture. Serum was isolated using a serum separator tube (BD Microtainer tubes; BD, Franklin Lakes, NJ) following the manufacturer's instructions, aliquoted, and stored at −80°C. The C-terminal telopeptide α1 chain of type I collagen (CTX) was detected using the RatLaps enzyme immunoassay (EIA), the N-terminal propeptide of type I procollagen (PINP) was detected using the Rat/Mouse PINP competitive enzyme immunoassay, and mouse tartrate-resistant acid

phosphatase form 5b (TRACP 5b) was detected using an immunofixed enzyme activity assay (Immunodiagnostic Systems, Scottsdale, AZ) following the manufacturer's instructions. For determination of parathyroid hormone (PTH (1-84)) serum levels, MicroVue^{TM} Bone mouse PTH (1-84) kit (Immunotopics, QUIDEL) was used following the manufacturer's instructions. For quantitative measurements of serum calcium and phosphate, detection kits (SCKISUI Diagnostics) were used following the manufacturer's protocol. Absorbances were read using a VICTOR Nivo multimode microplate reader (Perkin Elmer, Waltham, MA).

2.13.7 Mechanical testing

Femoral mid-diaphyseal mechanical properties were measured via three-point bending test. Briefly, femurs from 6-week-old mice were dissected and kept frozen at −20°C in PBS-soaked gauze until testing. Frozen femurs were equilibrated to RT and loaded to failure in a three-point bending assay using an Instron model 5943 single column table frame machine. Samples were positioned anterior surface down and loaded centrally at a cross-head speed of 0.05 mm/s and a support distance of 6 mm. Whole-bone mechanical properties were assessed by the generated force vs. displacement data.

Tibial tissue mechanical properties were analyzed by cyclic micro-indentation using the BioDent 1000™ Reference Point Indentation (RPI) instrument (Active Life Scientific, Inc., Santa Barbara, CA) using BP2 probes. Briefly, tibias of 6-week-old mice were dissected and freshly-analyzed in PBS by micro-indentation. Four sites (1 mm apart) extending all over the flat surface of the tibia were analyzed, using the tibia-fibula junction as a landmark for a start point. As per published protocols (229), twenty indentation cycles were performed at 2 Hz with a maximum force of 2N at each site. Prior to testing, probes were tested on a PMMA (Poly methyl methacrylate) block according to manufacturer’s instructions. Tissue- mechanical properties were assessed by the generated force vs. distance RPI data. Measurements were averaged for each sample and used to calculate the mean for each group.

2.13.8 Marrow fat quantification by osmium staining and CT

Tibias of 8-week-old female mice were stained with osmium tetroxide for marrow fat analysis as previously described (230). Briefly, tibias were dissected and fibulas were removed prior to processing. Intact tibias were fixed in 10% methanol-free formaldehyde solution for 24 h at 4°C (Thermo Scientific), rinsed with water, and processed for decalcification in 14% EDTA,

pH 7.4, for 14 days. Samples were first washed with water and then with Sorensen's phosphate buffer pH (7.2) in 1.5 ml microtubes. All subsequent steps were performed in the fume hood. With extreme caution, 4% osmium tetroxide vials (Electron Microscopy Services, Hatfield, PA) were diluted in Sorensen's buffer to make a 1% staining solution. Tibias were stained in 1% osmium tetroxide solution and incubated for 48 h at RT on a rotating wheel. Stained tibias were then carefully washed, in the same tube, with Sorensen's buffer twice for 3 h and then overnight. Samples were then moved to a clean set of 1.5 ml microtubes containing 1 ml of Sorensen's buffer and stored at 4°C until μCT analysis. At this point, tubes were removed from fume hood for μCT analysis. Osmium tetroxide wastes (tips, tubes, liquids) were deactivated in corn oil (Sigma-Aldrich) and discarded in osmium tetroxide labelled solid and liquid waste containers.

MicroCT. Stained tibias were embedded in 1% agarose and marrow fat content was scanned using a SkyScan 1272 high-resolution μCT scanner. Scan settings are as follows: voxel size 7.9μm, 70 kV, 142 μA, and a 0.5-mm aluminum (AL) filter. Exposure time was set at 1750 ms, and 3 images were captured every 0.4° through 180° rotation. Reconstruction was performed using SkyScan Recon software and analyzed using SkyScan CT Analysis software. Quantification of marrow adipose tissue volume included the ROI starting at tibia/fibula junction to the distal end of the bone.

2.14. Histology

Adipose tissue embedding and processing was performed as described previously (231). Briefly, adipose depots of 6-week-old females were dissected, weighed, and fixed in 10% formalin solution for 72 h at 4°C. Samples were then kept in 70% ethanol for 48 h, subsequently dehydrated in increasing concentrations of ethanol, and processed in paraffin at 60°C. Processed samples were embedded into paraffin blocks and stored at 4°C prior to sectioning. Embedded tissue samples were sectioned at 5 μm-thick cross-sectional sections using a paraffin microtome (Leica 2155 rotary paraffin microtome, Leica microbiosystems, Wetzlar, Germany). Finally, sections were deparaffinized and stained with H&E stain. Pictures were taken using a Leica DMR fluorescence microscope (Leica Microsystems, Wetzlar, Germany) connected to a digital DP70 camera (Olympus, Center Valley, PA).

2.15. Osteoclast cultures and differentiation

Bone marrow stem cells were isolated from long bones (tibia and femur) of 6-8-week-old mice as described in the above sections. For osteoclast primary cultures, bone marrow suspensions were centrifuged at 1000 rpm for 5 min. The resulting cell pellet was resuspended in red blood cell (RBC) lysis buffer (Sigma-Aldrich), incubated for 10 min on ice and washed twice with complete medium by centrifugation at 1,000 rpm for 5 min. Bone marrow cell pellets were resuspended in complete α-MEM medium supplemented with M-CSF (25 ng/ml, R&D system) plated, and incubated overnight. Cell medium was collected, spun, and resuspended in complete medium. Viable osteoclast precursors were counted, plated for differentiation in complete medium supplemented with M-CSF (25 ng/ml) and RANKL (100 ng/ml, R&D system), and incubated at 37°C in a humidified atmosphere with 5% CO2. Culture medium was changed on day 3 and mature osteoclasts were observed by day 5 of differentiation.

2.16. Transwell Cocultures

Transwell chamber culture system (Thermo Scientific) was used to assess the paracrine communication between osteoclast precursors and osteoblast cells. BMSCs of 8-week-old mice were isolated and differentiated into osteoblasts as described in the above sections. First, BMSCs were seeded at confluency in transwell inserts (upper chamber) harboring a 0.4 μm- sized pore polycarbonate membrane and induced in an osteogenic medium for 12 days. At D10 of osteogenic differentiation, osteoclast precursors were isolated from long bones of 8-week-old mice as described in the above sections. The day after, OC precursors were counted and seeded at confluency in 12-well plates (lower chamber). After 24 h of attachment, osteoblast inserts were added to the 12-well plates marking the start of the coculture. The coculture was maintained in α-MEM medium supplemented with 10% FBS and 25 ng/ml M-CSF for 12-15 days or until mature osteoclasts starts to form. Medium was changed carefully every 3 days for the duration of the coculture. For this experiment, RANKL was not added to the medium of any culture.

2.17. Immunoprecipitation and MS

HEK-293T cells were transfected with either Myc-DDK-tagged Usp53 vector (bait) or Flag-GFP (control) using the calcium/phosphate transfection method. After 48h, cells were lysed and homogenized in IP buffer (150 mM NaCl, 50 mM Tris-HCl at pH 7.5, 1% NP-40, and

protease/phosphatase inhibitor cocktail (Cell Signaling). One (1) mg of lysate was then incubated with 30 µl of anti-Flag M2 magnetic beads (Sigma-Aldrich) overnight at 4ºC on a rotating wheel. Immunocomplexes were washed 4 times with IP buffer on a magnetic stand (Ambion), prior to MS processing. For regular IPs performed in HEK-293T or MEF or ST2 cells, immunocomplexes were resuspended in 2X Laemmli buffer, boiled for 5 min and then used for western blotting. Co-Immunoprecipitation (co-IP) assays were performed as previously described (198).

Proteins (bait and control) bound on the beads were reduced with DTT, alkylated with iodoacetic acid, and digested with trypsin. The lyophilized peptides were re-solubilized in 0.1% aqueous formic acid/2% acetonitrile and then loaded onto a Thermo Acclaim Pepmap (Thermo, 75 µm ID X 2 cm with 3 µm C18 beads) precolumn and then onto an Acclaim Pepmap Easyspray (Thermo, 75 µm X 15 cm with 2 µm C18 beads) analytical column separation using a Dionex Ultimate 3000 uHPLC at 220 nl/min with a gradient of 2-35% organic (0.1% formic acid in acetonitrile) over 2 h. Peptides were analyzed using a Thermo Orbitrap Fusion mass spectrometer operating at 120,000 resolution (FWHM in MS1, 15,000 for MS/MS) with HCD sequencing of all peptides with a charge of 2+ or greater. The raw data were converted into *.mgf format (Mascot generic format) and searched using Mascot 2.3 against human sequences (Swissprot). The database search results were then loaded onto Scaffold Q+ Scaffold_4.4.8 (Proteome Sciences) for spectral counting statistical treatment and data visualization. Scaffold (version Scaffold_4.7.5, Proteome Software Inc., Portland, OR) was used to validate MS/MS based peptide and protein identifications. Peptide identifications were accepted if they could be established at greater than 95.0% probability by the Peptide Prophet algorithm (232) with Scaffold delta-mass correction. Protein identifications were accepted if they could be established at greater than 99.9% probability and contained at least 2 identified peptides. Protein probabilities were assigned by the Protein Prophet algorithm (233). Statistical significance was assessed using *t*-test ($P<0.05$). Mass spectroscopy was performed at the Research Institute of the McGill University Health Centre (Proteomics RIMUHC).

2.18. Cell-based assays

Cells were treated with 100 nM PTH(1-34) or vehicle for the indicated time before RNA isolation. For cell-based assays, MEF cultures were differentiated into osteoblasts for 10 days.

Cells were fasted in serum-free media for 16 h and treated with 50 ng/ml of BMP-2 for 45 min prior to protein extraction. To assess changes in PPARγ protein levels, MEF cultures were differentiated into adipocytes for 10 days prior to protein extraction. For ST2 cultures, PPARγ protein stability was assessed by cycloheximide (100 μg/ml) treatment at different timepoints prior to protein extraction.

2.19 Statistical analyses

Data are presented as means ± one standard deviation (SD). Comparisons were made by analysis of variance (ANOVA) with *post hoc* tests (Bonferroni's test), or unpaired *t-tests*. A probability (P) value lower than 0.05 was accepted as significant.

Chapter III: *Nfil3*, a target of the NACA transcriptional coregulator, affects osteoblast and osteocyte gene expression differentially

3.1. *Nfil3* is a target of the PTH-NACA signaling axis in osteoblasts

Previous studies from our laboratory have shown that PTH(1-34) stimulation of osteoblasts induces the phosphorylation of NACA at residue S99, and its subsequent nuclear translocation and binding to the *Bglap2* (197) and *Lrp6* promoters (192). Our goal was to identify additional target promoters downstream of the PTH-activated NACA axis that could be involved in the anabolic effect of iPTH in bone. One study by Ozkurt and Tetradis (210) has previously identified *Nfil3* as a PTH target in osteoblasts. Our results suggest that PTH-activated NACA is implicated in this regulation, as NACA bound to a fragment of the proximal promoter of *Nfil3* (nucleotides -394 to -181 relative to the annotated transcription initiation site) in ChIP-Seq assays of PTH-treated MC3T3-E1 osteoblasts (Fig.3.1 A). To validate the ChIP-Seq results, we performed a conventional ChIP against NACA in MC3T3-E1 cells under the same conditions and amplified the *Nfil3* promoter region corresponding to the ChIP-Seq peak. Using pan-specific anti-NACA antibodies, results show that following PTH(1-34) stimulation for 30 min, NACA was recruited to the *Nfil3* amplified promoter fragment. Results show an enrichment of 5-fold as compared to vehicle treated cells or the ChIP performed with naive IgG (Fig.3.1 B). RNA-Seq data of PTH-treated MC3T3-E1 cells show a 10-fold increase in *Nfil3* transcript levels compared to vehicle-treated cells (Fig.3.1 C). Treatment of primary osteoblast cultures with the hormone induced the expression of *Nfil3* in a similar manner. The expression of *Nfil3* peaked at 2 h of treatment and declined by 4 h (Fig.3.1 D).

These data confirm that *Nfil3* is a PTH(1-34) target in osteoblasts, where NACA can be involved directly or indirectly in the regulation of its expression following PTH treatment.

3.2. Knockdown of NACA and CREB affect the response of *Nfil3* to PTH(1-34) stimulation

Yotov et.al (188) have characterized the DNA binding site of the NACA protein as a loose consensus sequence centered around 5′g/cCAg/cA-3′. *In silico* analysis of the Nfil3 promoter region between nucleotides -818 and +182 using the MatInspector software (234) identified one potential binding site for NACA and two binding sites for the cAMP response element binding protein (CREB) (data not shown). The predicted binding site for NACA (5′-CGGCCAGAGAAGG-3′, between nucleotides -211 and -198) lies within the peak identified by ChIP-Seq analysis (data not shown). The distal potential binding site for CREB lies between

nucleotides -69 and -49 and the proximal one between nucleotides -37 and -21 relative to the annotated transcription initiation site (data not shown).

The ChIP-Seq data indicated the binding of NACA to the *Nfil3* promoter. In order to investigate the role of NACA in *Nfil3* gene regulation, we used a short hairpin RNAs (shRNAs)-mediated knockdown approach to target *Naca* in MC3T3-E1 cells. The knockdown of NACA (using shαNAC.1 or shαNAC.2) was confirmed by immunoblotting compared to MC3T3-E1 cells stably expressing a scrambled shRNA (shScr) (Fig.3.2 A). We checked the effect of NACA knockdown on *Nfil3* mRNA expression levels. The knockdown of NACA did not affect the expression levels of *Nfil3* at the basal levels (Fig.3.2 B, *grey bars*). PTH(1-34) stimulation of shScr-expressing MC3T3-E1 cells increased the expression levels of *Nfil3* by 7-fold. The magnitude of the PTH(1-34) response was significantly reduced in NACA knockdown MC3T3-E1 cells (Fig.3.2 B, *black bars*). The data indicate that NACA has no effect on the basal transcription of *Nfil3*, however it contributes to its PTH-mediated transcriptional induction. We then checked the effect of CREB knockdown on *Nfil3* mRNA expression levels. The knockdown of CREB (using shCREB.1 or shCREB.2) was confirmed by immunoblotting compared to MC3T3-E1 cells stably expressing a scrambled shRNA (shScr) (Fig.3.2 C). Knockdown of CREB reduced the expression levels of *Nfil3* by 70% at the basal levels (Fig.3.2 D, *grey bars*). PTH(1-34) stimulation of shScr-expressing MC3T3- E1 cells increased the expression levels of *Nfil3* by 6-fold. The PTH(1-34) response was completely blunted in CREB knockdown MC3T3-E1 cells (Fig.3.2 D, *black bars*). The data indicate that CREB is essential for the transcription of *Nfil3* at basal levels and following PTH(1-34) induction.

3.3. CREB-mediated transcription from the proximal *Nfil3* promoter requires NACA

We cloned a fragment of the *Nfil3* promoter corresponding to nucleotides -818 to +182 bp (818/+182bp) relative to the annotated transcription start site into a luciferase reporter vector. We assessed the effect of NACA knockdown on the activity of the cloned promoter fragment. The knockdown of NACA using shαNAC.1 or shαNAC.2 shRNAs resulted in >50% reduction in *Nfil3* promoter activity as compared to reporter gene expression of MC3T3-E1 cells transfected with shScr (Fig.3.3A). The PTH(1- 34) stimulation of the promoter activity was completely abolished in NACA-knockdown cells (Fig.3.3 A). These results show that the presence of NACA

is important for *Nfil3* promoter activity. It also indicates that NACA is an important element for the proper induction of *Nfil3* by PTH.

The *in silico* predictions suggest a potential role for CREB along with NACA in the transcriptional regulation of the promoter. This scenario is plausible as previous studies have highlighted the need for a *bona fide* transcription factor partner such as the basic domain-leucine zipper (bZIP) homodimeric AP-1 family member cJUN to regulate transcription in conjunction with NACA, as the coregulator lacks a transcriptional activation domain (190). We did not detect any modulation of the *Nfil3* promoter activity when overexpressing NACA alone or in combination with AP-1 transcription factors such as cJUN, cFOS, JUND, and ATFs (Supplementary Figure.3.1 A,B). Besides, it is well known that PTH1R signaling induces CREB-mediated transcription of target genes in osteoblasts (235, 236). Considering this, we tested first whether CREB knockdown impacts transcription from the cloned promoter fragment. The knockdown of CREB using shCREB.1 or shCREB.2 shRNAs resulted in 50% reduction in *Nfil3* promoter activity as compared to reporter gene expression of MC3T3-E1 cells transfected with shScr (Fig.3.3 B). The PTH(1- 34) stimulation of the promoter activity was dramatically abolished in CREB-knockdown cells (Fig.3.3 B). We next tested whether CREB activates the transcription of the cloned promoter fragment alone or in combination with NACA. The activity of the -818/+182bp promoter fragment was strongly boosted following CREB overexpression in MC3T3-E1 cells (Fig.3.3 C, *grey bars*). This activation was further potentiated with PTH(1-34) treatment for 6h (Fig.3.3 C, *black bars*), suggesting that *Nfil3* is a PTH-CREB regulated target in osteoblasts. The CREB activation of the 818/+182bp promoter fragment was abrogated in NACA-knockdown MC3T3-E1 cells (Fig.3.3 D). Taken together, the results indicate a role for NACA and CREB in the regulation of the *Nfil3* promoter. It also suggests a role for NACA in the CREB-mediated activation of the promoter.

3.4. *Nfil3* knockdown modulates osteoblast and osteocyte gene expression differentially

Previous studies have highlighted the role of *Nfil3* as a transcriptional repressor in different cell lines, including osteoblasts (210, 212). However, little is known about the role of *Nfil3* in osteocytes. To address this question, we first checked the expression levels of *Nfil3* during MC3T3-E1 and IDG-SW3 cells differentiation (Fig.3.4 A). In IDG-SW3 osteocytic cells,

steady state *Nfil3* mRNA levels increased by 4-fold (CT= 27 to 25) after 14 days of differentiation, compared to only 2-fold (CT= 27 to 26) for MC3T3- E1 cells (Fig.3.4 A).

In order to investigate the role of *Nfil3* through differentiation, we then used a pool of shRNAs to target *Nfil3* in MC3T3-E1 and IDG-SW3 cells. We first assessed the efficacy of the knockdown by Western blotting against NFIL3 in both cell lines. Stably-infected cells with shNfil3 exhibited around 50% reduction in NFIL3 protein levels in MC3T3-E1 (Fig.3.4 B) and IDG-SW3 cells (Fig.3.5 A). Stably-infected MC3T3-E1 cells with either shScr or shNfil3 were set to differentiate in osteogenic medium for 21 days. Gene expression analysis confirmed the significant reduction of *Nfil3* mRNA levels (Fig.3.4 C). *Nfil3* knockdown enhanced the expression of early osteoblastic markers such as *Sp7*, *Runx2* and *Col1a1*, in addition to late differentiation markers including *Alpl* and *Bglap2* (Fig.3.4 C). These results support the previously reported role of NFIL3 as an osteoblastic transcriptional repressor (210, 212).

We then stained the cells for calcium deposition by the alizarin red technique to assess whether reducing *Nfil3* expression affected osteoblast mineralization. We did observe a significant increase in calcium deposition in *Nfil3*-knockdown MC3T3-E1 cultures (Fig.3.4 D).

Osteocytic IDG-SW3 cells stably infected with either shScr or shNfil3 were cultured under differentiation conditions (15) for 35 days. Gene expression analysis confirmed the significant reduction of *Nfil3* mRNA levels (Fig.3.5 B). Interestingly, *Nfil3* knockdown in differentiating IDG-SW3 cells reduced the expression of early osteocytic markers such as Dentin matrix protein1 (*Dmp1*), Phosphate regulating endopeptidase homolog X-Linked (*Phex*), and *Alpl* (Fig. 3.5 B). The knockdown of *Nfil3* also decreased the expression levels of mature osteocytic markers such as *Sost* and *Fgf-23* (Fig.3.5 B). In addition, *Nfil3* knockdown reduced the expression of osteoblast-related targets such as *Col1a1* and *Sp7* (Fig.3.5 B) during the 35 days time course of IDG-SW3 cells differentiation. We interpret this data to mean that in osteocytes, NFIL3 does not exhibit the function of a transcriptional repressor.

The decrease in *Col1a1* mRNA expression levels was further validated by Picrosirius red staining, used to visualize collagen fibers. After 14 days of differentiation, *Nfil3* knockdown cells showed decreased collagen staining as compared to control cultures, with a 50% reduction in collagen amounts (Fig.3.6 A). The collagen immunostaining of the same cultures revealed that

while overall type I collagen levels were reduced in *Nfil3* knockdown cultures, collagen secretion was not disturbed through differentiation (Fig.3.6 B).

3.5. FIGURES AND TABLES

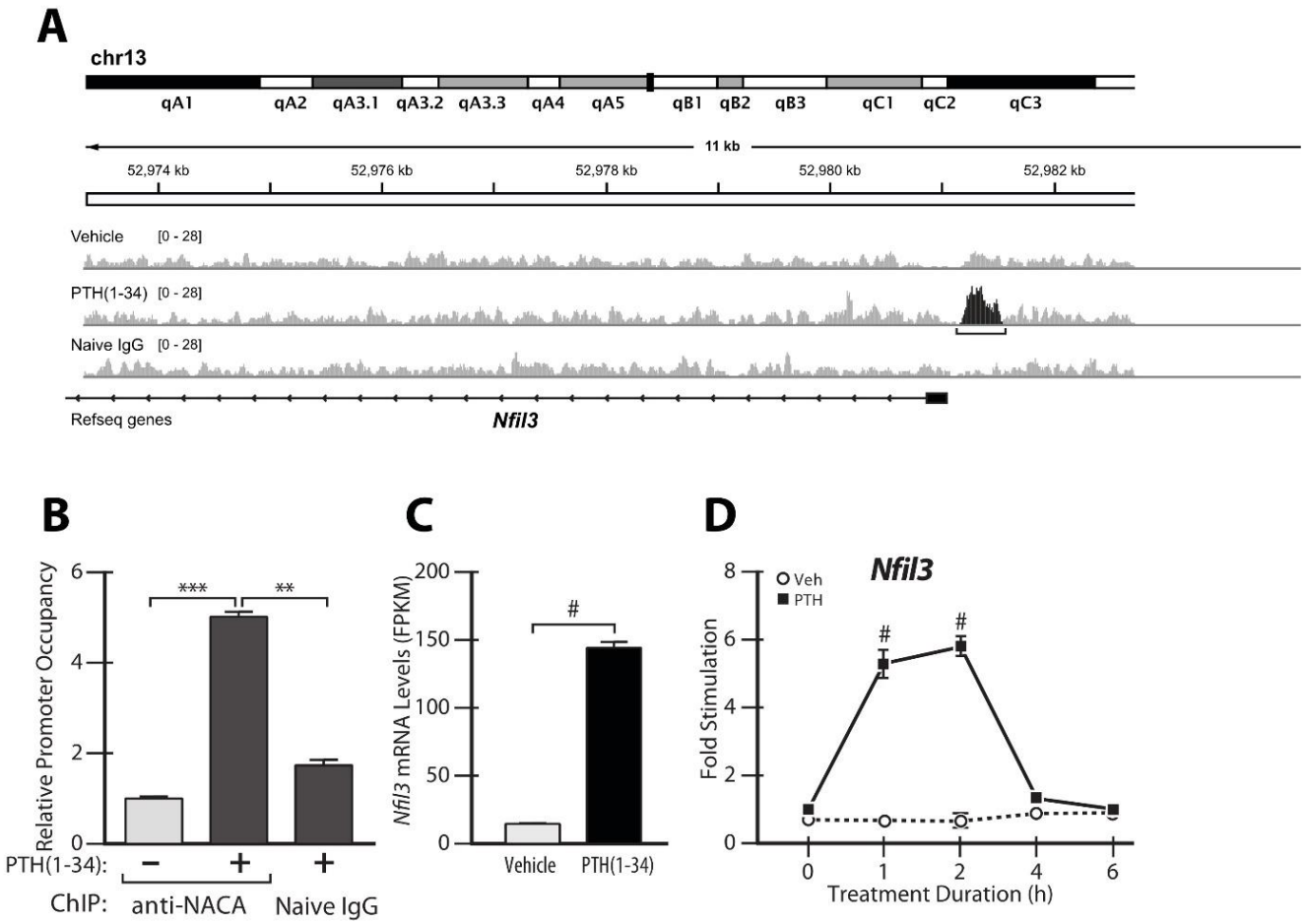

Figure 3.1 ChIP-Seq and RNA-Seq identify Nfil3 as a PTH-NACA regulated target gene in osteoblasts.

A, Representative profile of peaks (bracketed) obtained on the *Nfil3* gene by ChIP-Seq. ChIP-Seq was performed on MC3T3-E1 cells treated with vehicle or 100 nM PTH(1–34) for 30 min using an anti-NACA or naive IgG as negative control. B, NACA binds the proximal *Nfil3* promoter. Quantitative chromatin immunoprecipitation (ChIP) was performed on MC3T3-E1 cells treated with vehicle or 100nM PTH(1-34) for 30 min using anti-NACA-specific antibody or naive IgG as negative control. Input and ChIP products were amplified by SYBR green PCR using specific primers flanking the NACA binding site within the *Nfil3* promoter. Relative promoter occupancy was calculated as enrichment over vehicle treated cells, which was ascribed an arbitrary value of 1. Results are means ± SD of three independent experiments (n=3). C, Expression levels of *Nfil3* determined by RNA-sequencing done on mRNA isolated from MC3T3-E1 cells treated with vehicle or PTH(1-34) for 1 h. Results are presented as fragments per kilobase of exon per million fragments mapped (FPKM). D, Quantitative reverse transcription PCR of *Nfil3* gene expression using mRNA isolated from primary osteoblast cells treated with vehicle or 100 nM PTH(1–34) for the indicated time points. Results are means ± SD of three independent experiments (n=3). **, $P < 0.01$; ***, $P < 0.001$; #, $P < 0.0001$; ANOVA with Bonferroni's post-hoc test for panels B and D; unpaired *t*-test was used for panel C.

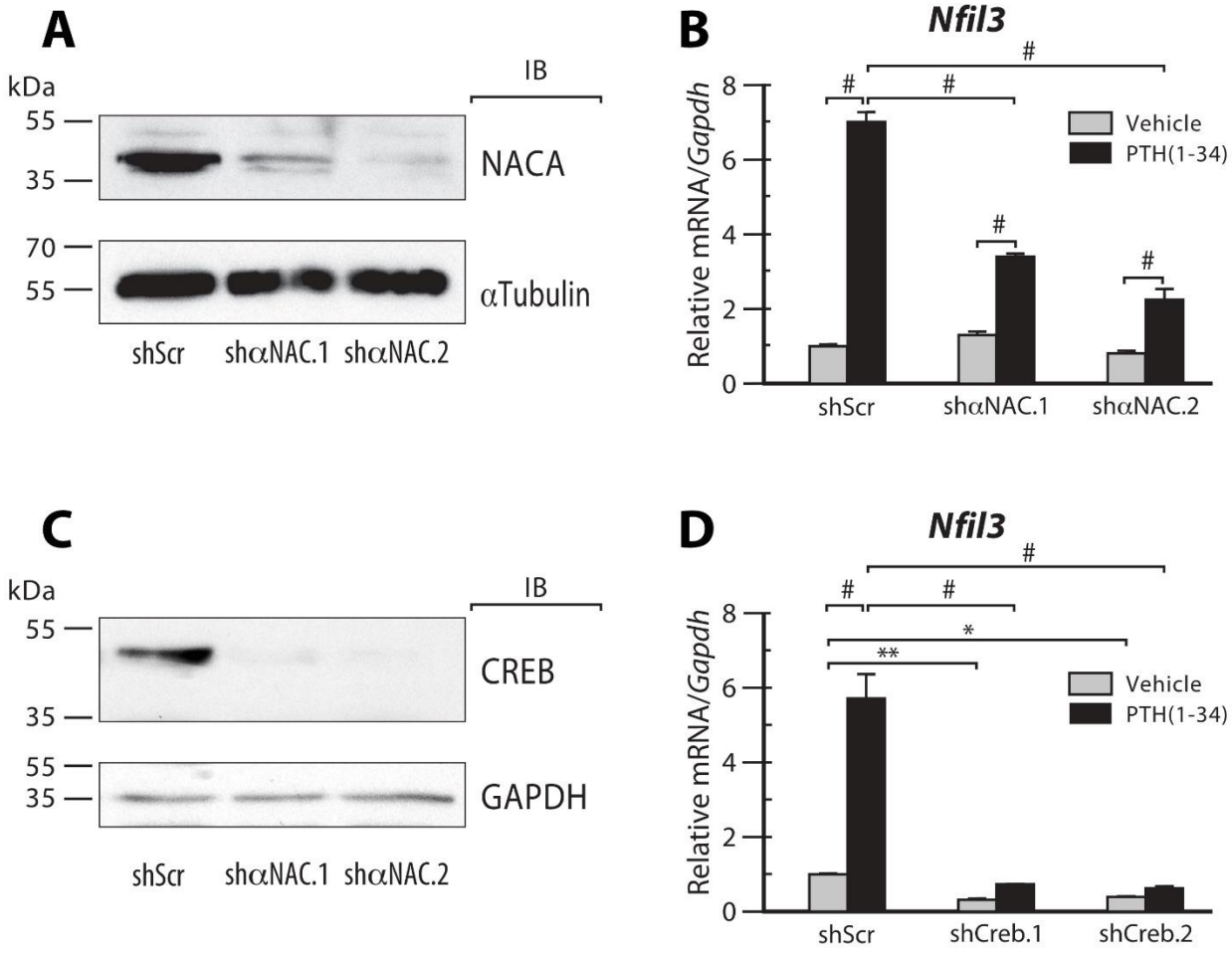
A
kDa
IB
55
35
NACA
70
55
αTubulin
shScr
shαNAC.1
shαNAC.2
B
Nfil3
Relative mRNA/Gapdh
Vehicle
PTH(1-34)
shScr
shαNAC.1
shαNAC.2
C
kDa
IB
55
35
CREB
55
35
GAPDH
shScr
shαNAC.1
shαNAC.2
D
Nfil3
Relative mRNA/Gapdh
Vehicle
PTH(1-34)
shScr
shCreb.1
shCreb.2

Figure 3.2 Knockdown of NACA and CREB reduces the response of *Nfil3* to PTH.

A, C, immunoblot of whole cells extracts from MC3T3-E1 cells stably expressing shRNAs targeting *Naca* (shαNAC.1 and shαNAC.2) or *Creb1* (shCreb.1 and shCreb.2), and non-targeted shRNA (shScr) as control. Membranes were probed with anti-NACA or anti-CREB and anti-αTubulin or anti-GAPDH antibodies as loading controls. B,D, Quantitative reverse transcription PCR of *Nfil3* gene expression using mRNA isolated from the stably transfected cells treated with vehicle or 100 nM PTH(1– 34) for 2 h. Data are expressed relative to levels measured in the shScr expressing cells treated with vehicle and are presented as the means ± SD of three independent experiments (n=3). *, $P < 0.05$; **, $P < 0.01$; ***, $P < 0.001$; #, $P < 0.0001$; ANOVA with Bonferroni's post-hoc test.

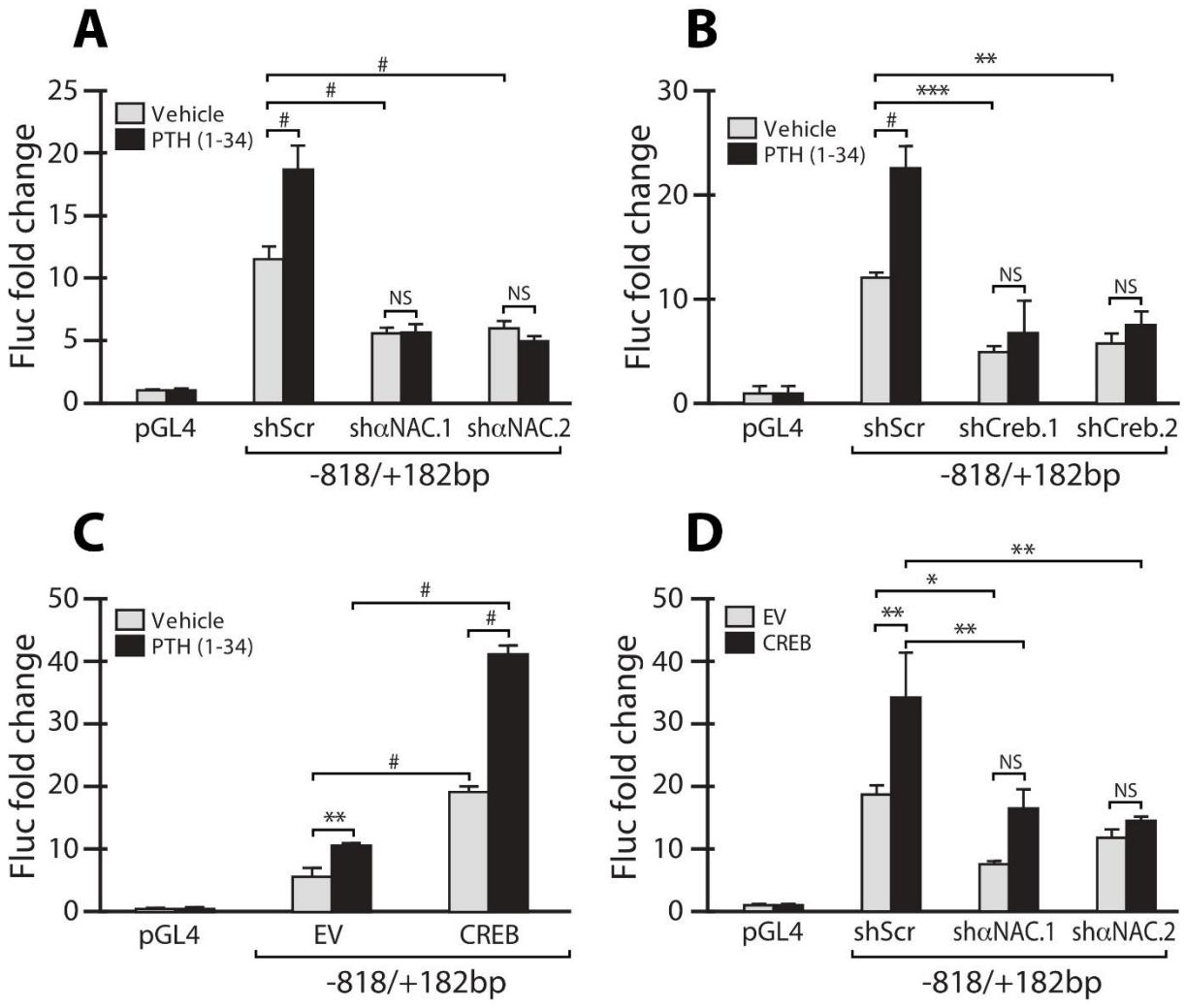
A
Fluc fold change
Vehicle
PTH (1-34)
pGL4
shScr
shαNAC.1
shαNAC.2
-818/+182bp
NS
B
Fluc fold change
Vehicle
PTH (1-34)
pGL4
shScr
shCreb.1
shCreb.2
-818/+182bp
NS
C
Fluc fold change
Vehicle
PTH (1-34)
pGL4
EV
CREB
-818/+182bp
D
Fluc fold change
EV
CREB
pGL4
shScr
shαNAC.1
shαNAC.2
-818/+182bp
NS

Figure 3.3 NACA and CREB regulate the promoter activity of *Nfil3*.

Firefly luciferase (Fluc) reporter assays. A, MC3T3-E1 cells stably expressing shRNAs targeting *Naca* (shαNAC.1 and shαNAC.2) or scrambled shRNA (shScr) as a control were transfected with the *Nfil3* promoter reporter vector (-818/+182bp). Cells were treated with vehicle or 100 nM PTH(1-34) for 6 h before measuring luciferase expression. B, MC3T3-E1 cells stably expressing shRNAs targeting *Creb1* (shCreb.1 and shCreb.2) or scrambled shRNA (shScr) as a control were transfected with the *Nfil3* promoter reporter vector (-818/+182bp). Cells were treated with vehicle or 100 nM PTH (1-34) for 6 h before measuring luciferase expression. C, MC3T3-E1 cells transfected with the -818/+182bp vector alone or together with a CREB expression vector. Cells were treated with vehicle or 100 nM PTH(1-34) for 6 h before measuring luciferase expression. D, MC3T3-E1 cells stably expressing shαNAC.1, shαNAC.2 or the control shScr were transfected with the -818/+182bp vector alone or together with a CREB expression vector. Empty pGL4 vector was used as a negative control. Firefly luciferase counts were normalized to *Renilla* counts. Results are presented as the mean fold induction SD; $n \geq 3$. *, $P < 0.05$; **, $P < 0.01$; ***, $P < 0.001$; #, $P < 0.0001$; NS, not significant; ANOVA with Bonferroni's post-hoc test.

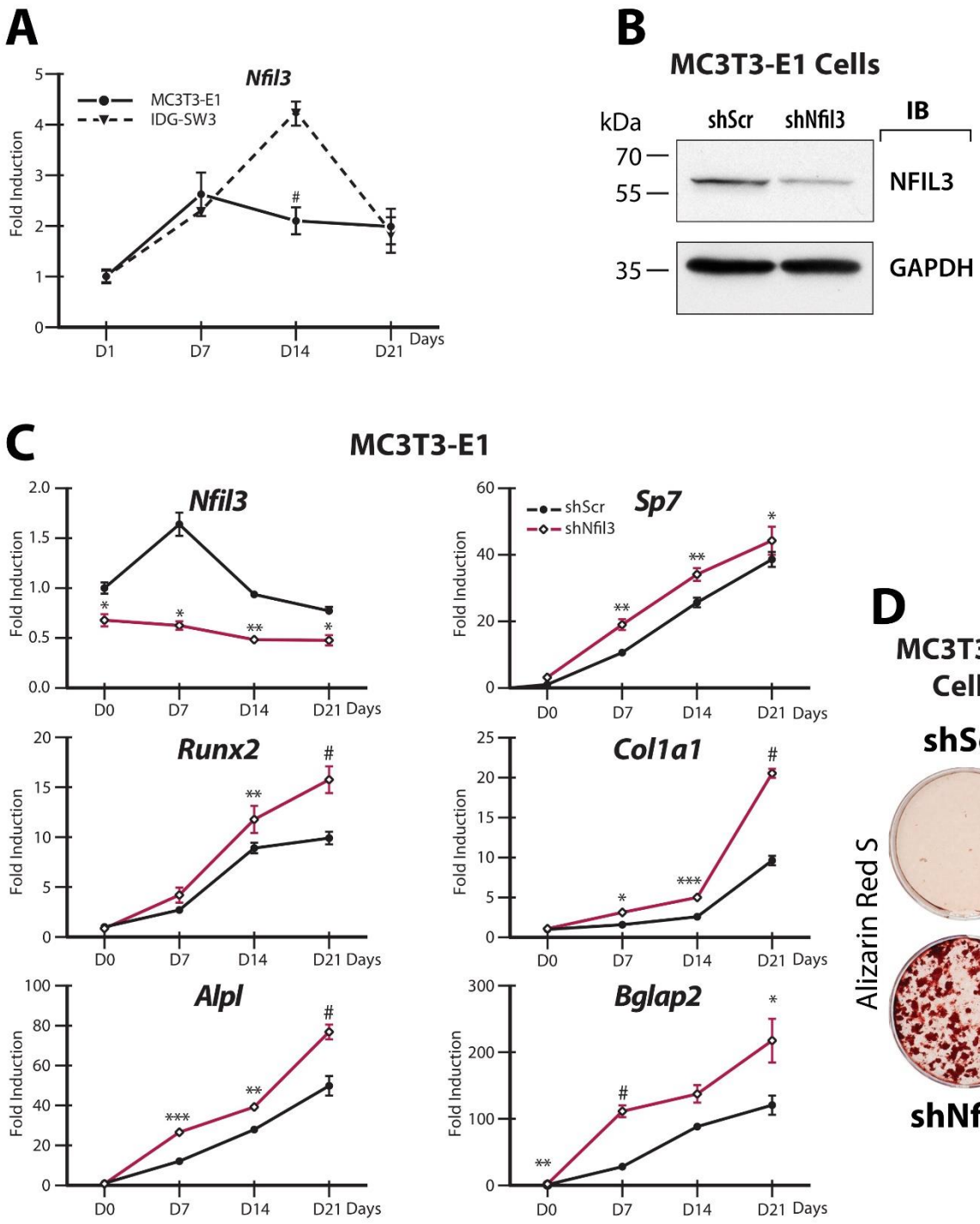
A
Nfil3
MC3T3-E1
IDG-SW3
Fold Induction
Days
D1
D7
D14
D21
B
MC3T3-E1 Cells
kDa
shScr
shNfil3
IB
70
55
NFIL3
35
GAPDH
C
MC3T3-E1
Nfil3
Sp7
shScr
shNfil3
Runx2
Col1a1
Alpl
Bglap2
Fold Induction
D0
D7
D14
D21 Days
D
MC3T3-E1
Cells
shScr
Alizarin Red S
shNfil3

Figure 3.4 Impact of *Nfil3* knockdown in osteoblasts.

A, Expression of *Nfil3* mRNA in IDG-SW3 cells (dotted line) and MC3T3-E1 cells (solid line). Quantitative RT-qPCR using *Nfil3*-specific TaqMan probe, normalized to *Gapdh*, was performed on RNA isolated from cultures differentiated for 21 days in osteogenic medium. B, Western blot analysis of NFIL3 expression. Total protein isolated from MC3T3-E1 cells stably transfected with shScr or shNfil3 at D1, confirming the knockdown of *Nfil3*. GAPDH was used as a loading control. C, Gene expression analysis of osteoblast differentiation markers. Quantitative RT-qPCR using TaqMan probes against osteoblast differentiation markers, normalized to *Gapdh*, was performed on RNA isolated from shScr-stably transfected (black line) or shNfil3-stably transfected (red line) pools of MC3T3-E1 cells differentiated for 21 days in osteogenic medium. ShScr-stably expressing cultures were used as controls to compare expression levels. D, MC3T3-E1 cultures were cultured in differentiation medium for 12 days and stained for calcium deposition by alizarin red S staining.

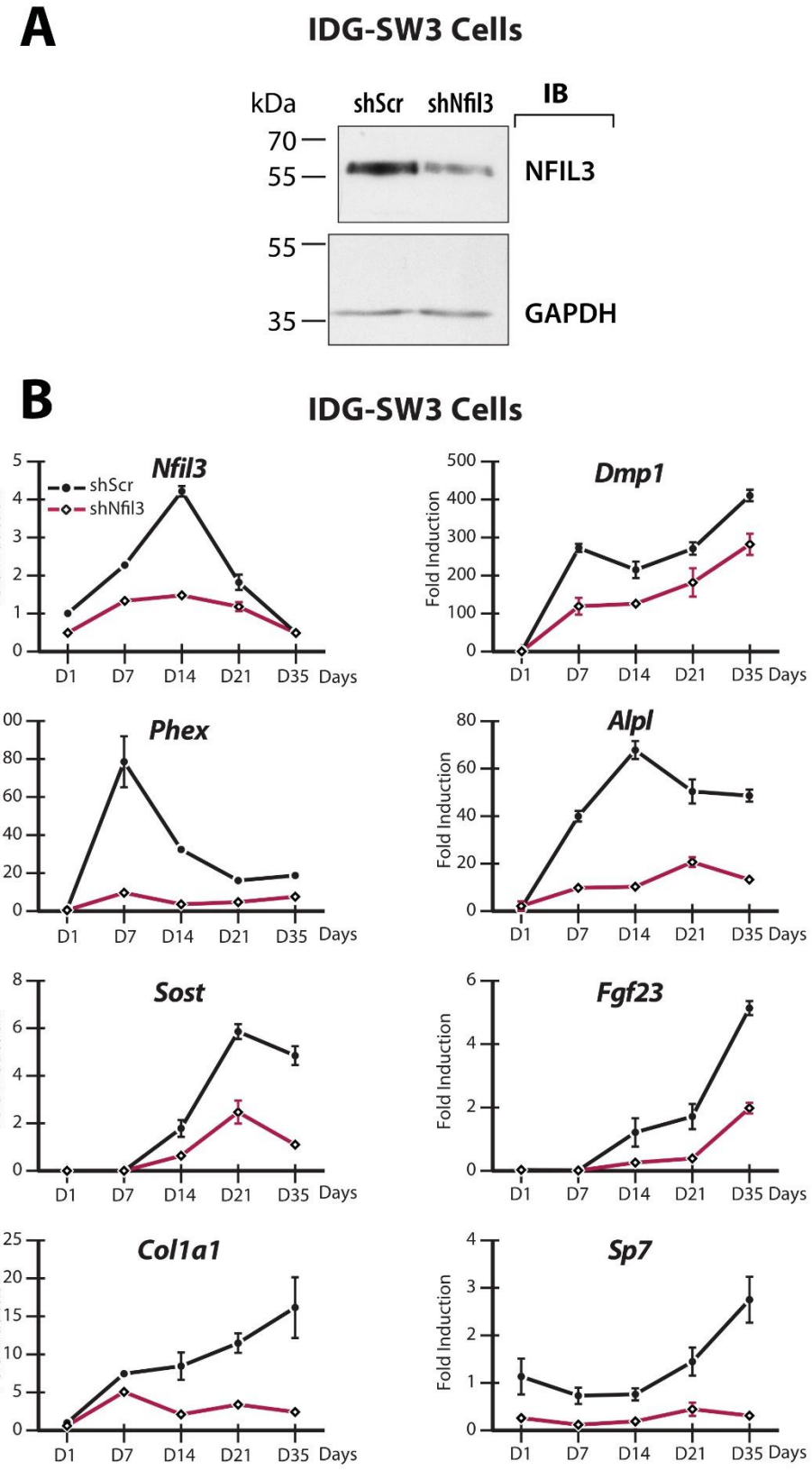
A
IDG-SW3 Cells
kDa
shScr
shNfil3
IB
70
55
NFIL3
55
35
GAPDH
B
IDG-SW3 Cells
Nfil3
shScr
shNfil3
Dmp1
Phex
Alpl
Sost
Fgf23
Col1a1
Sp7
Fold Induction
D1
D7
D14
D21
D35
Days

Figure 3.5 Impact of *Nfil3* knockdown in osteocytes.

A, Western blot analysis of NFIL3 expression. Total protein isolated from IDG-SW3 cultures stably transfected with shScr or shNfil3 at D1, confirming the knockdown of *Nfil3*. GAPDH was used as a loading control. B, Gene expression analysis of osteocyte differentiation markers., was performed on RNA isolated from shScr-stably transfected (black line) or shNfil3-stably transfected (red line) pools of IDG-SW3 cells cultured for 35 days under differentiation conditions. ShScr-stably expressing cultures were used as controls to compare expression levels. Results are means ± SD of three independent experiments (n=3). *, $P < 0.05$; **, $P < 0.01$; ***, $P < 0.001$; #, $P < 0.0001$; ANOVA with Bonferroni's post-hoc test.

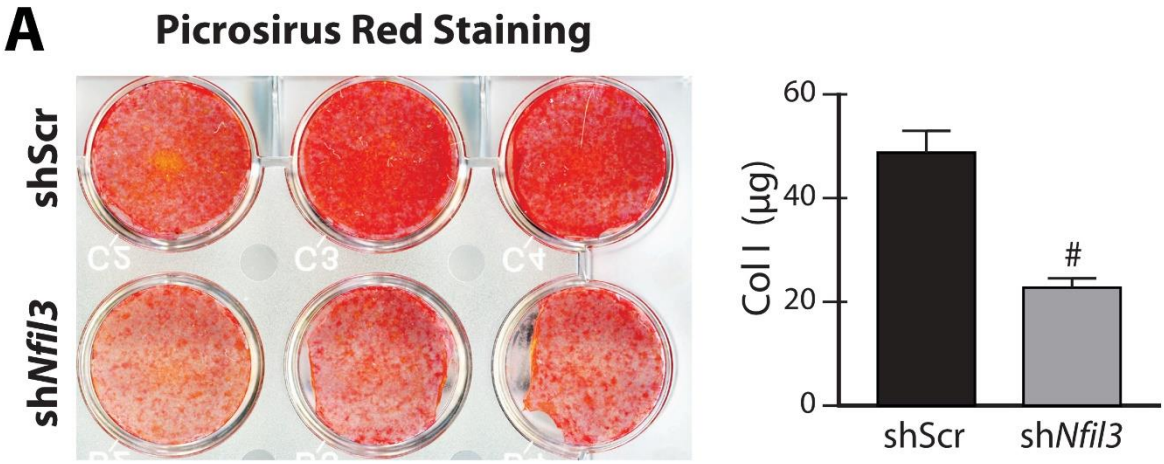
A
Picrosirus Red Staining
shScr
shNfil3
C5
C3
C4
Col I (µg)
60
40
20
0
#
shScr
shNfil3

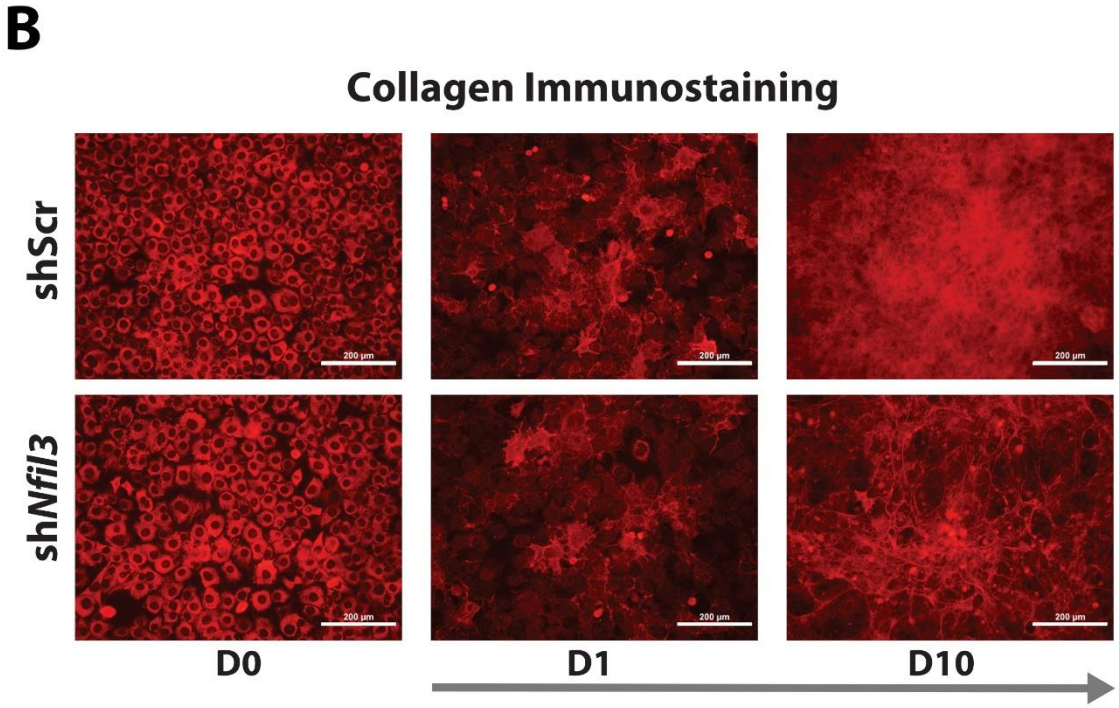
B
Collagen Immunostaining
shScr
shNfil3
200 µm
D0
D1
D10

Figure 3.6 Collagen amounts but not secretion are affected by *Nfil3* silencing.

A, Picrosirius red staining of *Nfil3*-knockdown IDG-SW3 cells and control cells, cultured in differentiation medium for 14 days. Quantification of picrosirius red staining is shown on the right. Data is represented as means ± SD; n=3. #, $P < 0.0001$; unpaired *t*-test. B, Collagen immunostaining of IDG-SW3 cells cultured in differentiation medium. IDG-SW3 cell cultures stably expressing shRNA targeting *Nfil3* or non-targeted shRNA (shScr) were fixed and immunostained with anti-collagen type 1 antibody at indicated timepoints. D, days. Magnification bar, 200 μ.

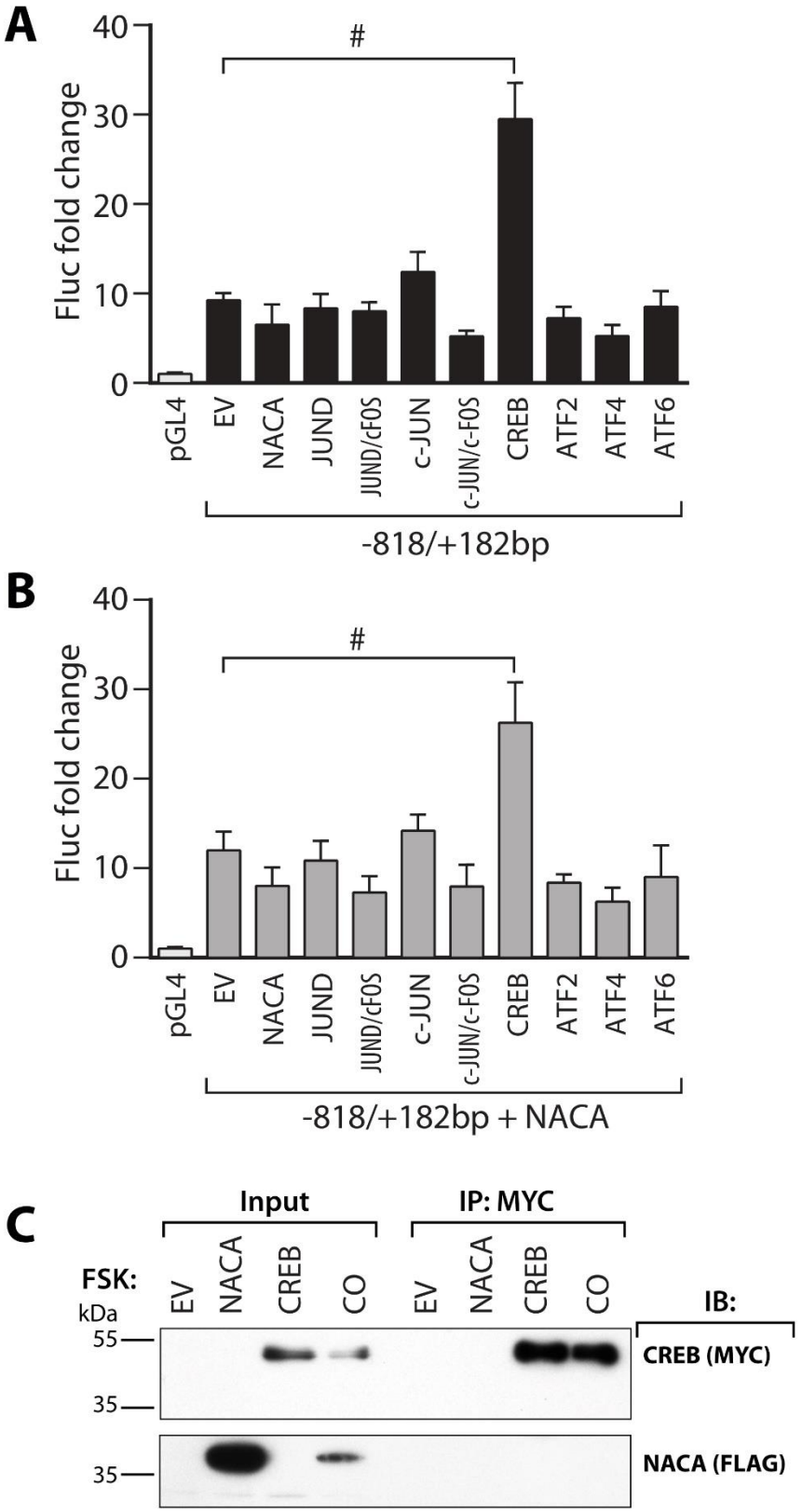
A
Fluc fold change
40
30
20
10
0
#
pGL4
EV
NACA
JUND
JUND/cFOS
c-JUN
c-JUN/c-FOS
CREB
ATF2
ATF4
ATF6
-818/+182bp
B
Fluc fold change
40
30
20
10
0
#
pGL4
EV
NACA
JUND
JUND/cFOS
c-JUN
c-JUN/c-FOS
CREB
ATF2
ATF4
ATF6
-818/+182bp + NACA
C
Input
IP: MYC
FSK:
EV
NACA
CREB
CO
EV
NACA
CREB
CO
IB:
kDa
55
35
CREB (MYC)
35
NACA (FLAG)

Supplementary Figure 3.1 Absence of Nfil3 promoter response to AP-1 or ATF transcription factors.

A, B, Firefly luciferase (Fluc) reporter assay. MC3T3-E1 cells were transfected with the -818/+182bp promoter fragment with expression vectors for NACA, JUND, c-FOS, cJUN, CREB, ATF2, ATF4, andATF6, alone (A) or in combination with NACA (B). EV, empty vector. PGL4 vector was used as a negative control and Firefly luciferase counts were normalized to *Renilla* counts. Results are presented as the mean fold induction SD; n≥3. #, $P < 0.0001$; ANOVA with Bonferroni's post-hoc test. C, Immunoprecipitation assay (IP) to test for physical interaction between CREB and NACA. MC3T3-E1 cells expressing empty vector (EV) or NACA-FLAG and MYC-CREB alone or together (CO) were lysed and immunoprecipitated (IP) with anti-MYC antibody beads and probed for NACA-FLAG. Cultures were treated with 100 nM Forskolin prior to IP.

CONNECTING TEXT BETWEEN CHAPTERS III AND IV

We have discussed the importance of identifying new target promoters downstream of the PTH-NACA pathway in understanding the molecular actions of PTH and uncovering potential therapeutic alternatives (Sections 1.8 and 1.9). In chapter **III**, we have demonstrated the transcriptional regulation and biological role of *Nfil3* in osteoblasts and highlighted its differential role in regulating osteoblast vs osteocyte differentiation *in vitro*. Another target identified by our strategy was *Usp53*. The identification of *Usp53* as a target gene of the PTH-NACA pathway in osteoblasts provided a window to study the gene's function in bone. Besides, the human phenotype (Cantu syndrome) associated with the USP53 duplication study raised an intriguing question about the biological role of this gene in different tissues, especially bone and fat (219). Consequently, we have a unique opportunity to be the first research group to unravel the contribution of *Usp53* to skeletal development.

This led us to the work presented in Chapter IV . The second study focuses on the identification of *Usp53* as a target of the PTH-NACA pathway in PTH- treated MC3T3-E1 cells, using ChIP-Seq and RNA-Seq gene profiling. To study the transcriptional regulation of *Usp53*, *in silico* promoter analysis was performed and binding sequences for NACA and other transcription factors (TFs) were determined. Strategies of transient overexpression and shRNAs-mediated knockdown were used to test the role of candidate transcription factors in this regulation downstream of PTH. The second part of the study describes the function of *Usp53* in regulating mesenchymal differentiation. For this aim, shRNAs-mediated knockdown of *Usp53* was performed in different cell lines (MC3T3-E1, ST2, and BMSCs) and systems (*in vitro and ex vivo*), to assess the impact of *Usp53* deletion on mesenchymal lineage-making decisions.

Chapter IV: Ubiquitin specific protease *Usp53* regulates osteoblast versus adipocyte lineage commitment

4.1. The PTH-NACA pathway regulates *Usp53* in osteoblasts

Our laboratory has characterized the binding of NACA to multiple gene promoters in osteoblasts. In one study, the PTH (1-34) stimulation of osteoblasts induces the phosphorylation of NACA at S99, its subsequent nuclear translocation and binding to the *Bglap2* promoter (197). Another study has highlighted the role of NACA along with JUND in *Lrp6* transcriptional regulation in MC3T3-E1 cells (192). More recently, we have demonstrated the transcriptional regulation of the *Nfil3* promoter by NACA and CREB in MC3T3-E1 cells (chapter 3).

To further our understanding of the significance of the PTH-activated NACA pathway in bone, we performed Chromatin Immunoprecipitation with deep sequencing (ChIp-Seq) in PTH-treated MC3T3-E1 osteoblast-like cells to identify genome-wide DNA- binding sites of NACA. This strategy identified the Ubiquitin-Specific Peptidase 53 (*Usp53*) as a candidate gene target for NACA in osteoblasts (Fig.4.1 A). Binding of NACA to the proximal promoter of *Usp53* was confirmed by ChIP-PCR on MC3T3-E1 cells stimulated with PTH (1-34) or vehicle under the same conditions (Fig.4.1 B). We amplified the *Usp53* promoter region corresponding to the peak identified by ChIP-Seq. Using an anti-pS99-NACA-specific antibody, results show a significant enrichment of the *Usp53* promoter by NACA in vehicle-treated cells as compared to naive IgG. This enrichment was further enhanced by 4-fold following 100 nM PTH (1-34) treatment for 30 min. In parallel, PTH-responsive genes were identified by RNA-Seq gene expression profiling in PTH-treated MC3T3-E1 cells. RNA-Seq performed on MC3T3-E1 cells stimulated for 60 min with 100 nM PTH (1-34), showed a 3-fold increase in *Usp53* transcript levels as compared to vehicle-treated cells (Fig.4.1 C). This increase in *Usp53* transcript levels was further confirmed using quantitative RT-qPCR in primary calvarial osteoblasts treated with vehicle or 100 nM PTH (1-34) at different time points. The expression of *Usp53* increased after 1hr of treatment, peaked at 2h of treatment and then returned to basal levels by 6h (Fig.4.1 D).

The ChIP-Seq data indicated the binding of NACA to the proximal region of *Usp53* promoter. In order to investigate the role of NACA in *Usp53* gene regulation, we used a short hairpin RNAs (shRNAs)-mediated knockdown approach to target *Naca* in MC3T3-E1 cells. We checked the effect of NACA knockdown on *Usp53* mRNA expression levels. The knockdown of NACA did not impact the expression levels of *Usp53* at the basal levels (Fig.4.1 E). PTH(1-34) stimulation of shScr-expressing MC3T3-E1 cells increased the expression levels of *Usp53* by 3-

fold. The PTH(1-34) response was completely blunted in NACA knockdown MC3T3-E1 cells (Fig.4.1 E).

Together, our data show that *Usp53* is a PTH target in osteoblasts, where NACA can be involved directly or indirectly in the regulation of its expression following PTH treatment. The data also indicate that NACA has no effect on the basal transcription of *Usp53*, however it contributes to its PTH-mediated transcriptional induction.

4.2. *Usp53* promoter hosts a functional binding site for NACA

Our data show that NACA has an impact on the transcriptional regulation of *Usp53* following PTH(1-34) stimulation. Yotov et al. have characterized the DNA binding domain of the NACA protein to a loose consensus sequence centered around 5′-g/cCAg/cA-3′ (188). *In silico* analysis of the *Usp53* promoter region between nucleotides -1000 and +94 using MatInspector software (234) identified one potential binding site for NACA and one binding site for the cAMP response element binding protein (CREB) (Fig.4.2 A). The predicted proximal binding site of NACA to the promoter (5′-GGCTCAGATCCCC-3′, between nucleotides -333 and -345) lies within the peak identified by ChIP-Seq analysis (Fig.4.2 A).

In order to further validate the binding of NACA to its potential binding site (bds) within the *Usp53* promoter, we performed an electrophoretic mobility shift assay (EMSA) using probes corresponding to NACAbds. The binding of NACA to the *Myoglobin* promoter was used as a positive control in these experiments (188). The formation of mobility shift complexes (Fig.4.2 B, lanes 2 and 6) confirmed the binding of proteins from nuclear extracts to the probes harbouring NACAbds. We further confirmed the presence of NACA in the shifted DNA-protein complexes. The addition of anti-NACA antibody to the reactions super shifted (SS) the formed complexes (Fig.4.2 B, lanes 4 and 8). This supershift was not observed when adding naïve IgG (Fig.4.2 B, lanes 3 and 7). In order to further validate the fidelity of NACA binding, we mutated its potential binding site within the *Usp53* promoter. The 5′- GGCTCAGATCCCC-3′ NACA binding site was mutated to 5′-GGCTCgGgTCCCC-3’. The formation of a DNA-protein complex was abrogated when incubating NACA protein extracts with mutated NACAbds probes (Fig.4.2 B, lane 10). These experiments confirm the binding of NACA to its cognate site within the *Usp53* proximal promoter.

4.3. NACA is required for the cJUN/CREB- mediated synergistic regulation of the *Usp53* promoter

We cloned a fragment of the *Usp53* promoter corresponding to nucleotides -2325 to +238 bp (-2325/+238bp) relative to the annotated transcription start site into the pGL4.10[LUC2] reporter vector. In order to check the functionality of the NACA binding site, we implemented site-directed mutagenesis and shRNA-mediated knockdown techniques. The 5′-GGCTCAGATCCCC -3′ NACA binding site was mutated to 5′-GGCTCgGgTCCCC-3′ in the context of the -2325/+238bp promoter fragment. The cloned promoter fragment (-2325/+238bp) carrying a wild-type response element for NACA (Wt-NACAbds) showed a 10-fold increase in the transcriptional activity of the luciferase reporter as compared to cells transfected with pGL4 vector (Fig.4.3 A). The *Usp53* promoter activity was reduced by 40% when we transfected the same fragment carrying a mutated sequence of the NACA response element (Mut-NACAbds) (Fig.4.3 A, *black bars*). The mutation abrogated the PTH-induced activation of the cloned *Usp53* fragment, resulting in > 50% reduction in the promoter activity (Fig.4.3 A, *grey bars*). Interestingly, the knockdown of NACA using shαNAC.1 or shαNAC.2 shRNAs resulted in > 80% reduction in *Usp53* promoter activity as compared to reporter gene expression of MC3T3-E1 cells transfected with shScr (Fig.4.3 B, *black bars*). The absence of NACA blunted the induction of the *Usp53* promoter fragment by PTH (Fig.4.3 B, *grey bars*). Taken together, these results show that the presence of NACA and its proper binding to its response element is critical for promoter activity.

A potential binding site for CREB lies between nucleotides -5 and -14 relative to the annotated transcription initiation site, within the *Usp53* proximal promoter (Fig.4.2 A). The *in silico* predictions suggest a potential role for CREB along with NACA in the transcriptional regulation of the promoter. This scenario is not surprising. We have recently shown that both NACA and CREB can regulate the transcription of the *Nfil3* promoter in MC3T3-E1 cells (Hariri et al. 2020. Submitted). Besides, previous studies have highlighted the need for a *bona fide* transcription factor partner such as the basic domain-leucine zipper (bZIP) homodimeric AP-1 family member cJUN to regulate transcription, as NACA lacks a transcriptional activation domain (190, 237). Considering this, we tested whether CREB along with cJUN activate the transcription of the cloned promoter fragment alone or in combination with NACA.

We first assessed the cJUN-CREB activation of the *Usp53* cloned fragment in *Naca*-knockdown cells. The cloned promoter fragment (-2325/+238bp) showed a 10-fold increase in the transcriptional activity of the luciferase reporter as compared to cells transfected with pGL4 vector (Fig.4.3 C, *black bars*). The overexpression of 50ng of cJUN expression vector did not induce a statistically significant increase in the promoter activity. However, the activity of the -2325/+238bp promoter fragment was significantly increased by 4-fold following CREB overexpression in MC3T3-E1 cells transfected with shScr (Fig.4.3 C, *black bars*). The overexpression of both cJUN and CREB expression vectors in the same condition further enhanced the promoter activity by 2- fold, as compared to CREB alone (Fig.4.3 C, *black bars*). This enhanced activity highlighted the combinatorial actions of the cJUN/CREB complex in regulating the *Usp53* promoter activity. Interestingly, this additive activation was completely abolished in MC3T3-E1 cells transfected with NACA shRNAs (Fig.4.3 C, *light and dark grey bars*). It is important to note that the absence of NACA did not affect the promoter activation when either cJUN or CREB were transfected alone (Fig.4.3 C, *light and dark grey bars*).

We then investigated whether the binding of NACA to DNA is needed for the optimal promoter activation carried by cJUN and CREB. To mimic the PTH(1-34) effect on NACA translocation, we overexpressed NACA-S99D mutant; a phosphomimetic form of NACA that shows enhanced nuclear localization (197). As described in figure 4.3 C, similar patterns of promoter activation were seen when overexpressing cJUN and CREB, alone or combined (Fig.4.3 D, *black bars*). The overexpression of NACA-S99D mutant or a NACA mutant lacking its DNA binding domain (delta DBD(69-80)) had no effect on the cJUN or CREB-mediated activation of the promoter fragment (Fig.4.3 D, *light and dark grey bars*). However, overexpressing NACA-S99D along with cJUN and CREB in MC3T3-E1 cells boosted the promoter activity as compared to conditions with cJUN and CREB alone (Fig.4.3 D, *grey bar*). This enhanced activity was not seen when overexpressing the delta DBD (69-80) NACA mutant in the same condition (Fig.4.3 D, *dark grey bar*).

We interpret this data to mean that NACA is important for the combined actions of cJUN and CREB in the regulation of *Usp53* promoter activity.

4.4. *Usp53* affects mesenchymal cell lineage selection and differentiation *in vitro*

Two main isoforms of *Usp53* have previously been described: a full-length isoform comprising 15 coding exons and a short isoform containing exons 1-7 of the Usp53 gene (218). Little is known about the expression of *Usp53* in different lineages. We analyzed the expression of the two isoforms by RT-qPCR in long and flat bones as well as in fat compartments of wild-type mice at 3-weeks of age (Supplementary Figure 4.1). *Usp53* was expressed in calvaria and tibia and in white (gonadal) and brown (interscapular) fat. In all tissues tested, the expression of the long, full-length isoform was predominant.

To examine the putative role of *Usp53* in mesenchymal cell differentiation, we targeted its expression in ST2 stromal cells. Short hairpin RNAs (shRNAs) targeting *Usp53* (shUsp53) or a control scrambled shRNA (shScr) were transfected into ST2 cells and stable pools expressing the distinct shRNAs were established. The stably transfected cells were differentiated in either osteogenic or adipogenic medium for 6 days. The expression levels of *Usp53* showed a significant 50% reduction following knockdown and remained stable through the osteoblast differentiation regimen (Fig.4.4 A). Knockdown of *Usp53* in MC3T3-E1 cells using the shUsp53 vector resulted in significant reduction in USP53 protein levels (Supplementary Figure 4.2 B).

We then monitored the level of transcripts expressed during early- and late-stage osteoblastic differentiation. The knockdown of *Usp53* enhanced the expression of early-stage osteoblast markers, such as *Osterix* (*Sp7*) and *Dlx5* as well as late-stage osteoblast markers such as osteocalcin (*Bglap2*) and alkaline phosphatase (*Alpl*) (Fig.4.4 B). Alkaline phosphatase activity was markedly increased in the absence of *Usp53*, assessed by staining at Day 6 (Fig.4.4 C). These results show that the absence of *Usp53* enhanced osteoblast differentiation. Similar results were obtained upon analysis of MC3T3-E1 osteoblast-like cells. *Usp53*-knockdown MC3T3-E1 cells exhibited a drastic increase in osteocalcin (*Bglap2*) and *Alpl* expression levels throughout differentiation together with increased calcium deposition as assessed by Alizarin Red Staining (Supplementary Figure 4.2). We interpret these results to mean that *Usp53* inhibits osteoblastogenesis of both bipotential stromal cells and committed osteoblasts.

We also cultured the *Usp53* knockdown ST2 cells in adipogenic medium for 6 days. Again, the expression levels of *Usp53* were stable throughout adipocyte differentiation and significant knockdown was measured (Fig.4.4 D). Interestingly, the expression levels of early-

adipogenic activators such as *Fabp4* and *C/ebpα* as well as late adipogenic markers such as *Pparγ* and *C/ebpβ* were reduced (Fig.4.4 E). This translated into decreased lipid accumulation as assessed by Oil Red O Staining at Day 6 (Fig.4.4 F). Thus, the absence of *Usp53* caused a substantial reduction in adipocytic differentiation capacity. Taken together, our data suggest that *Usp53* is a regulator of the lineage-making decisions of mesenchymal cells, altering their differentiation into osteoblasts or adipocytes reciprocally.

4.5. *Usp53* affects mesenchymal cell lineage-making decisions and differentiation *in vivo*

To ensure that the observed effects were not restricted to established cell lines, we performed an *in vivo* differentiation assay with murine bone marrow stromal cells (BMSCs, also known as bone-marrow derived mesenchymal stem cells) (238). BMSCs were isolated from femoral and tibial bone of C57BL/6 wild-type male mice and infected with shUsp53 or the control shScr and their ability to form bone or fat *in vivo* was assessed (Fig.4.5 A).

The expression level of *Usp53* showed a 50% reduction following knockdown in BMSCs (Fig. 4.5 B). Cells were implanted on collagen scaffolds and inserted subcutaneously into female immunocompromised mice (Fig.4.5 A). Four (4) weeks after surgery, the mice (N=4) were sacrificed and the implants were processed for microcomputed tomography (micro-CT) and histological analysis. Initially, sections were stained with H&E, which stains the newly deposited bone matrix. BMSCs expressing shUsp53 showed increased H&E staining (Fig.4.5 C). Bone formation was also assessed by micro-CT. The relative bone volume versus tissue volume (BV/TV) was higher in *Usp53* knockdown implants as compared to control, but the experimental variation prevented to reach statistical significance (Fig.4.5 F). To further confirm the presence of bone cells, we performed immunostaining using an anti-SP7 (Osterix) antibody to identify osteoblasts. *Usp53* knockdown implants showed an increase in Osterix staining as compared to control (Fig.4.5 D). Quantification was performed by counting Osterix-positive cells in different histological sections. *Usp53* knockdown implants showed a significant increase in Osterix-positive cells (Fig.4.5 D, rightmost panel). Adipocytes were detected by immunostaining with an anti-perilipin antibody, which detects surface-associated lipid droplets present in adipocytes. *Usp53* knockdown implants showed reduced perilipin staining as compared to control (Fig.4.5 E), and this decrease was statistically significant (Fig. 4.5 E, rightmost panel). We conclude that

a decrease in *Usp53* expression enhanced osteoblastogenesis and suppressed adipogenesis *in vivo*.

4.6. FIGURES AND TABLES

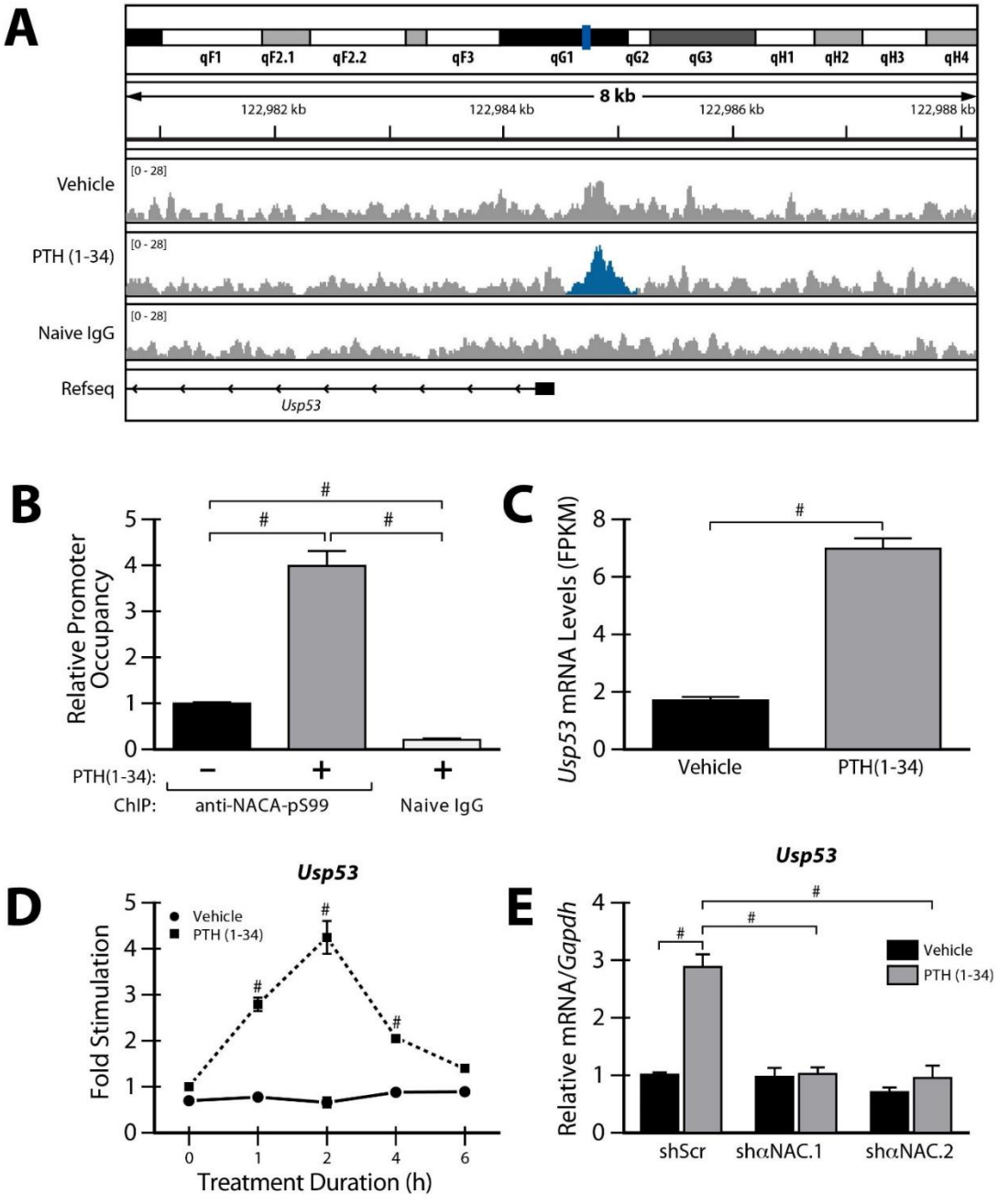

Figure 4.1 ChIP-Seq and RNA-Seq identify *Usp53* as a target of the PTH-NACA axis in osteoblasts.

A, Representative profile of peaks (highlighted in blue) obtained on the *Usp53* gene by ChIP-Seq. ChIP-Seq was performed on MC3T3-E1 cells treated with vehicle or 100 nM PTH(1–34) for 30 min using an anti-NACA-pS99 or naive IgG as negative control. B, NACA binds the proximal *Usp53* promoter. Quantitative chromatin immunoprecipitation (ChIP) was performed on MC3T3-E1 cells treated with vehicle or 100nM PTH(1-34) for 30 min using anti-NACA-pS99- specific antibody or naive IgG as negative control. Input and ChIP products were amplified by SYBR green PCR using specific primers flanking the NACA binding site within the *Usp53* promoter. Relative promoter occupancy was calculated as enrichment over vehicle treated cells, which was ascribed an arbitrary value of 1. Results are means ± SD of three independent experiments (n=3). C, Expression levels of *Usp53* determined by RNA-sequencing done on mRNA isolated from MC3T3-E1 cells treated with vehicle or PTH(1-34) for 1 h. Results are presented as fragments per kilobase of exon per million fragments mapped (FPKM). D, Quantitative reverse transcription PCR of *Usp53* gene expression using mRNA isolated from primary osteoblast cells treated with vehicle or 100 nM PTH(1–34) for the indicated time points. E, Quantitative reverse transcription PCR of *Usp53* gene expression using mRNA isolated from the stably transfected ST2 cells (shScr, shαNAC.1, or shαNAC.2) treated with vehicle or 100 nM PTH(1– 34) for 2 h. Data are expressed relative to levels measured in the shScr expressing cells treated with vehicle. Results are means ± SD of three independent experiments (n=3). $^{\#}$, $P < 0.0001$; ANOVA with Bonferroni's *post-hoc* test for panels B,D, and E; unpaired *t*-test was used for panel C.

A

-406 bp

CGACTCCCTAAGGGGACCGCCGGGGTGCCGACCCAGCAATGGCTGAAACC

NACA

CACAGAACCCCGGCTCAGATCCCCGCGCATCCGCACTCAGGCTGCAAAGC

CGCCAACCAAGGCGGACGACGGCGGGACGCCCGCGTCTGCCGTGGAAATC

CGCCGCAGTCCCCAGCCCACCACGCAGCCGCTCGCCGATCCGCCACGTCC

CGTCTCACAGCCCGCCCCGCGCGCCACCCCCGCGTCGGGGCAGAAGCCCG

AGCCCTGCTCTCGCGGGATCTCGCGCCTCACACAAGCCCTCGGAAAGGGA

GCATCACCCGCGGGAAAGCCGGGAACTCACGTGCGGGGGcGGGGcGGGGc

CREB

GGGGcGaGacGaGGAGGCGGGCCCGGCGCAAGGGGGCGGGGCGTCCTGAC

GCGGGGGAAGGCGGGGTCCAGAGACCTGTTGATCGCAGGTGTCACTGCCC

AGACCGGCCCCTGGGTCTTGGGCGTGCGCGCATGCTCTGCGCGGGTCTGG

+94 bp

B

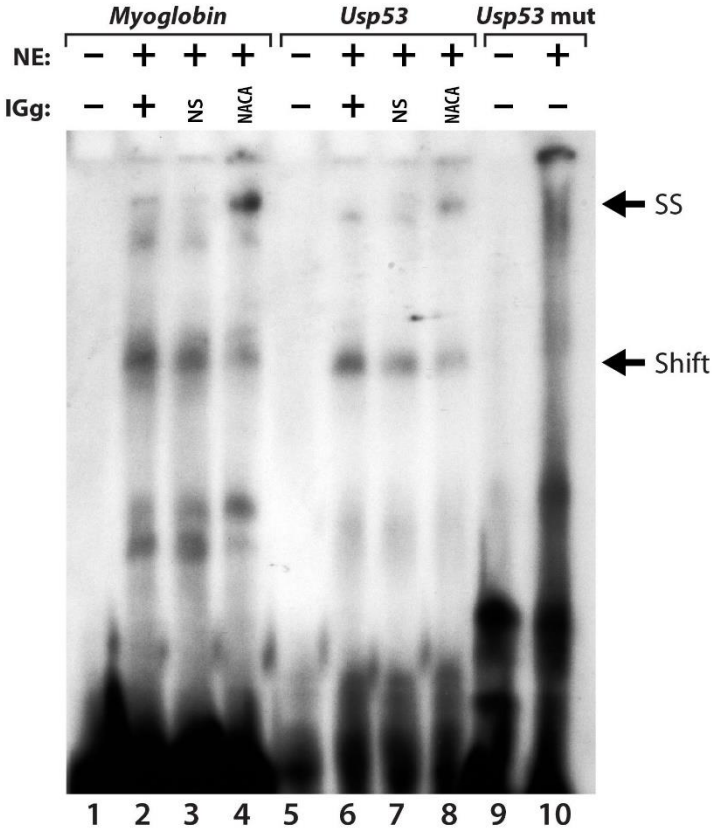

Figure 4.2 The proximal promoter of *Usp53* contains binding sites for NACA and CREB

A, Mouse *Usp53* promoter sequence from nucleotide −406 to nucleotide +94 relative to the transcriptional initiation site (arrow). Nucleotides bracketed and in bold represent the peak identified by ChIP-Seq. Highlighted are putative binding sites for NACA and CREB identified using Mat Inspector (Genomatix software suite). B, Autoradiograph of an electrophoretic mobility shift assay (EMSA) performed using either a probe containing the NACAbds sequence present in the *Myoglobin* (lanes 1 to 4) or the *Usp53* promoter (lanes 5 to 8), or a probe with a mutated NACAbds sequence present in the *Usp53* promoter (*Usp53* mut; lanes 9 and 10). Probes were incubated with nuclear extracts (NE) proteins from HEK293 cells overexpressing NACA and treated with 6Bnz-cAMP or with binding buffer as negative control. Super shift (SS; top arrow) was performed by adding anti-NACA or naive, non-specific (NS) IgG to the binding reactions.

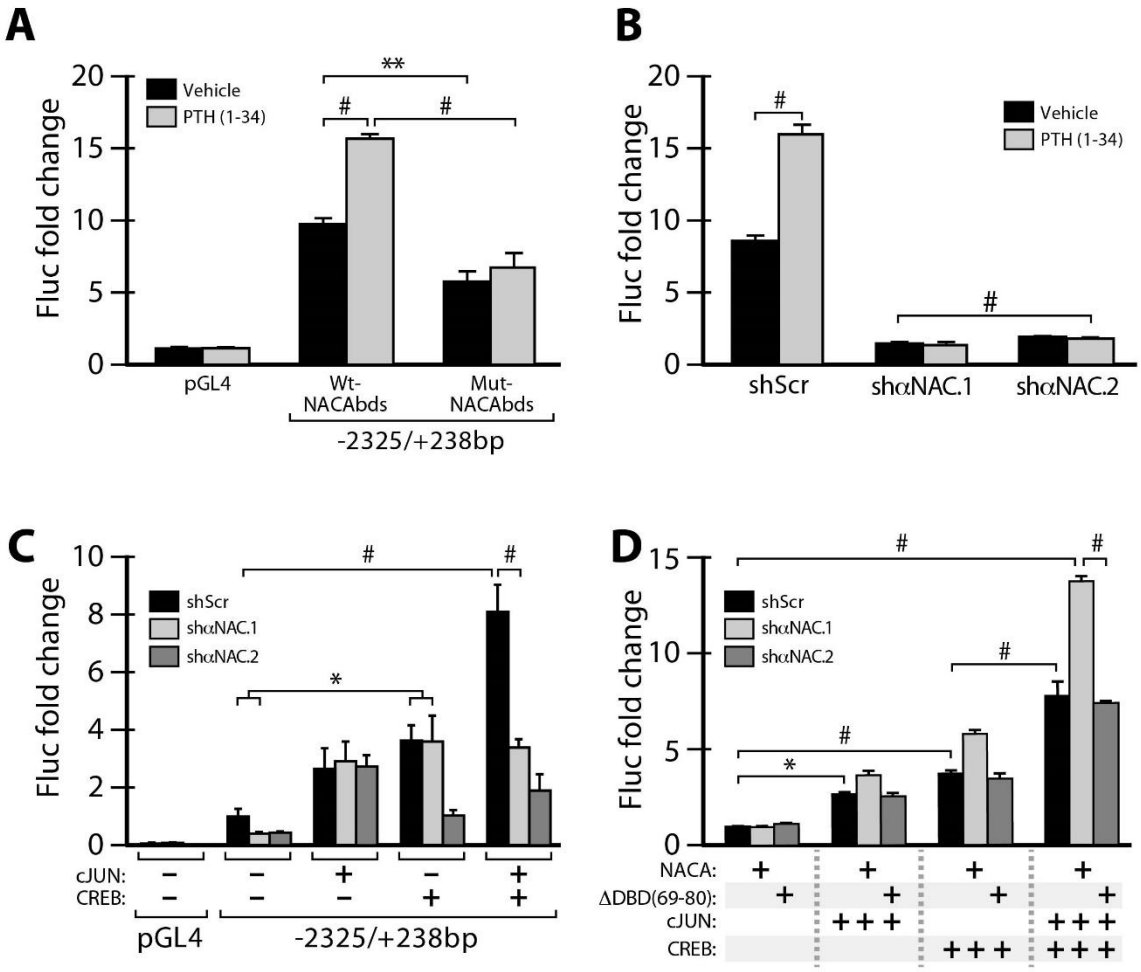
A
Fluc fold change
Vehicle
PTH (1-34)
pGL4
Wt-NACAbds
Mut-NACAbds
-2325/+238bp
B
shScr
shαNAC.1
shαNAC.2
C
cJUN:
CREB:
D
NACA:
ΔDBD(69-80):

Figure 4.3 NACA, cJUN, and CREB are implicated in *Usp53* promoter regulation

A, Firefly luciferase (Fluc) reporter assay was performed using MC3T3-E1 cells overexpressing wildtype or mutated *Usp53*-Luc vector (-2325/+238bp). The mutated region lies in the proximal NACA binding site of the *Usp53*-Luc vector. B and C, Firefly luciferase (Fluc) reporter assay was performed using MC3T3-E1 cells stably expressing shRNAs targeting *Naca* (shαNAC.1 and shαNAC.2) or scrambled shRNA (shScr) as a control by lentiviral infection. When indicated, cells were treated with vehicle or 100 nM PTH (1-34) for 24 h before performing the assay. C, Firefly luciferase (Fluc) reporter assay in MC3T3-E1 cells transfected with *Usp53*-Luc vector (-2325/+238bp) alone or along with cJUN and/or CREB expression vectors. D, Firefly luciferase (Fluc) reporter assay in MC3T3-E1 cells transfected with *Usp53*-Luc vector (-2325/+238bp) alone or along with NACA-S99D or NACA mutant deltaDBD (69-80), cJUN and/or CREB expression vectors. Cells were treated with 100 nM PTH (1-34) for 24 h before performing the assay. Empty pGL4 vector was used as a negative control. Firefly luciferase counts were normalized to Renilla counts. Results are presented as the mean fold induction ± SD. *, P≤0.05; **, P≤0.01; $^{\#}$, P<0.0001; ANOVA with Bonferroni's *post-hoc* test for all panels.

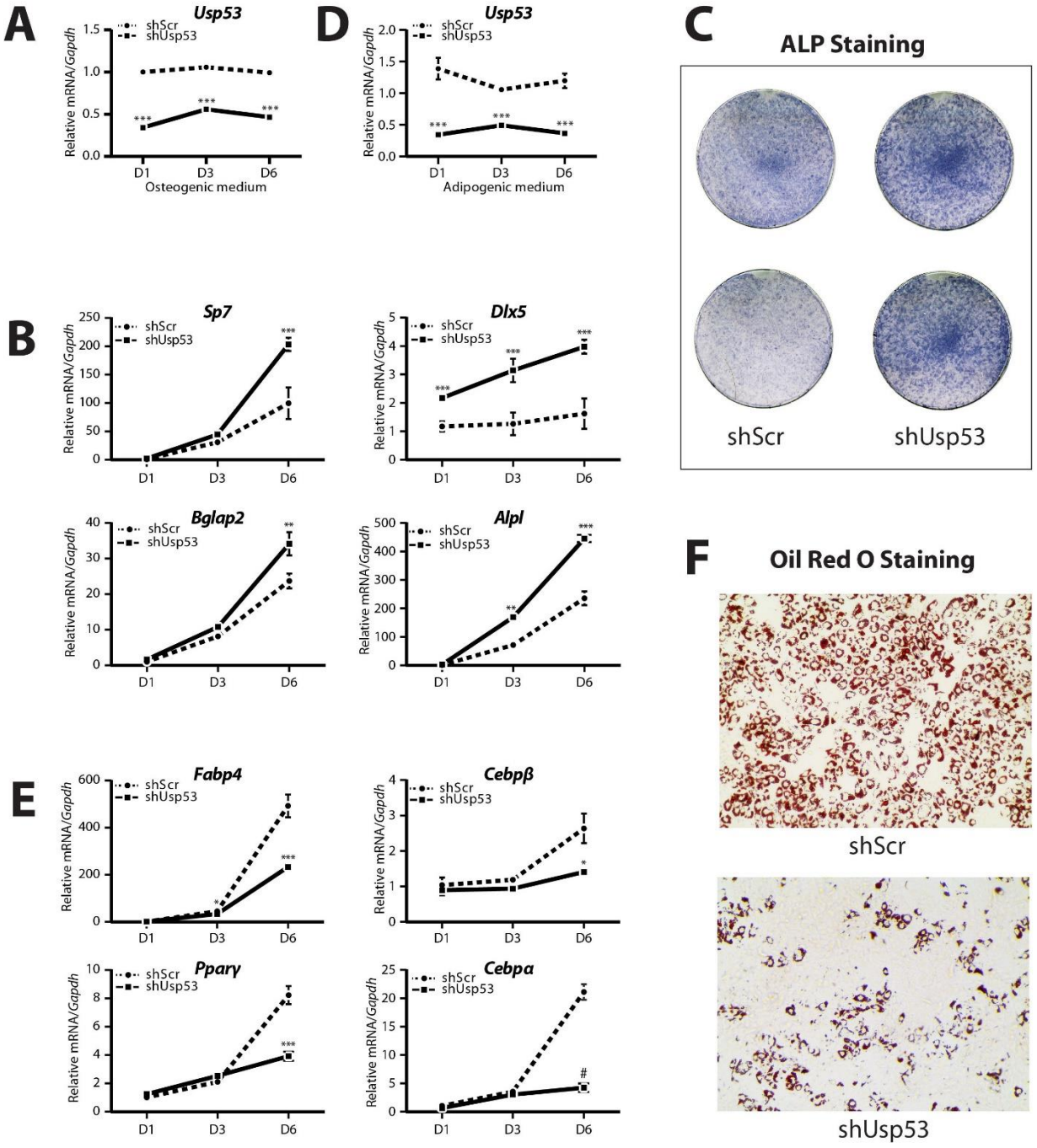
A
Usp53
shScr
shUsp53
Relative mRNA/Gapdh
D1
D3
D6
Osteogenic medium
D
Usp53
Adipogenic medium
C
ALP Staining
shScr
shUsp53
B
Sp7
Dlx5
Bglap2
Alpl
E
Fabp4
Cebpβ
Pparγ
Cebpα
F
Oil Red O Staining
shScr
shUsp53

Figure 4.4 *Usp53* controls osteogenic and adipogenic fate determination in vitro

ST2 cells expressing scrambled shRNAs (shScr) targeting control and shRNAs targeting *Usp53* were grown under osteogenic conditions (A) or adipogenic conditions (D) for 6 days. Gene expression analysis of osteogenic (B) or adipogenic (E) differentiation markers. Quantitative RT-qPCR using TaqMan probes against osteoblast or adipocyte differentiation markers, normalized to *Gapdh*, was performed on RNA isolated from shScr-stably transfected (dashed line) or shUsp53-stably transfected (solid line) pools of ST2 cells grown for 6 days in osteogenic or adipogenic medium. ST2 cultures were examined for ALP staining at day 12 (C) or oil red O at day 6 (F). Magnification bar 200 μ.

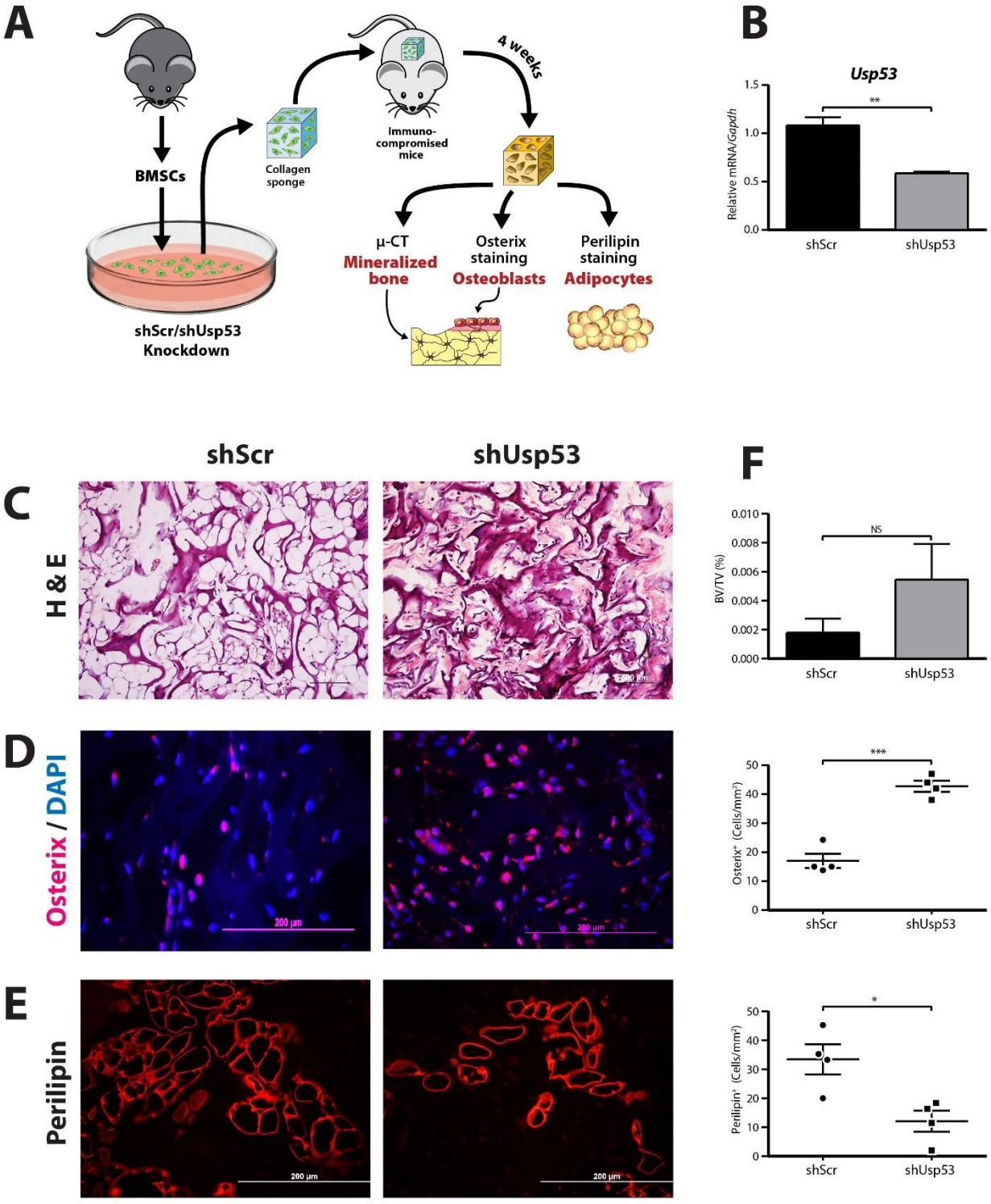
A
BMSCs
Collagen sponge
Immuno-compromised mice
4 weeks
shScr/shUsp53 Knockdown
μ-CT
Mineralized bone
Osterix staining
Osteoblasts
Perilipin staining
Adipocytes
B
Usp53
Relative mRNA/Gapdh
1.5
1.0
0.5
0.0
**
shScr
shUsp53
shScr
shUsp53
C
H & E
D
Osterix / DAPI
E
Perilipin
200 μm
F
BV/TV (%)
0.010
0.008
0.006
0.004
0.002
0.000
NS
Osterix+ (Cells/mm²)
50
40
30
20
10
0
***
Perilipin+ (Cells/mm²)
*

Figure 4.5 *Usp53* knockdown enhances osteoblastogenesis and inhibits adipogenesis in vivo

A, In vivo differentiation assay. A scheme showing the workflow of the *in vivo* osteogenesis assay performed on immunocompromised mice. B, Knockdown of *Usp53* in bone marrow stromal cells (BMSCs). Quantitative RT-qPCR using TaqMan probe against *Usp53*, normalized to *Gapdh*, was performed on RNA isolated from stable BMSCs cultures transfected with shScr or shUsp53. C, H & E staining of murine implants (shScr and shUsp53) after 4-weeks of BMSCs transplantation embedded in collagen sponge. D, Immunostaining of the implants (shScr and shUsp53) showing Osterix staining for osteoblasts (97) and DAPI staining for nuclei (blue). Quantification of Osterix-positive osteoblast cells (rightmost panel). E, Immunostaining of the implants (shScr and shUsp53) showing Perilipin staining for adipocytes (97). Quantification of perilipin-positive adipocytes (rightmost panel). F, Micro-CT analysis of the newly formed bone in the implants. Bone volume/tissue volume (BV/TV). $^{*}p<0.05$, $^{**}p<0.01$, $^{***}p<0.001$, NS; not significant; *t-test* was used in all panels.

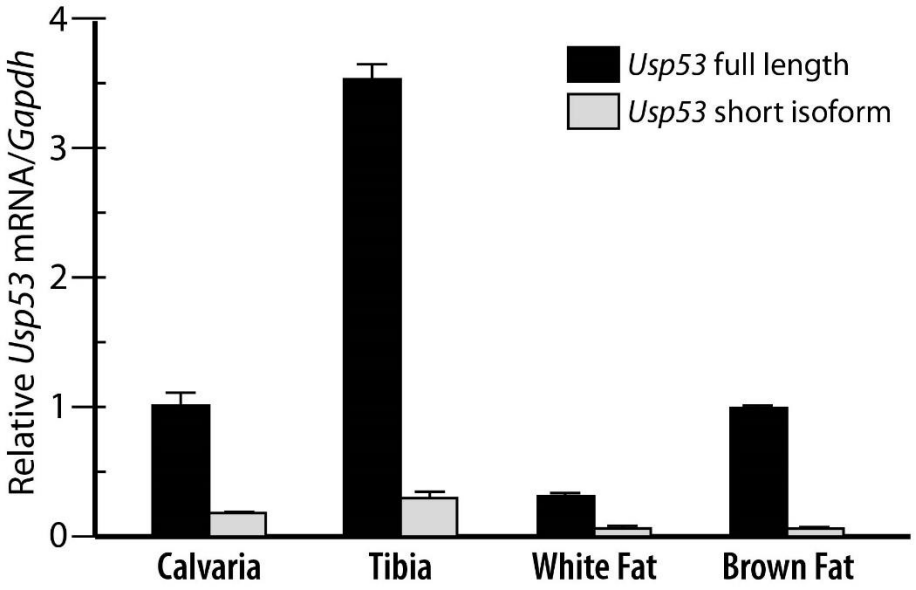
Relative Usp53 mRNA/Gapdh
4
3
2
1
0
Usp53 full length
Usp53 short isoform
Calvaria
Tibia
White Fat
Brown Fat

Supplementary Figure 4.1 *Usp53* long isoform is the predominant in skeletal tissues

Gene expression analysis of *Usp53* expression in different skeletal tissues of wildtype C57BL/6 mice (n=4). Quantitative RT-qPCR using isoform-specific primers against *Usp53*, normalized to *Gapdh*, was performed on RNA isolated from long and flat bones as well as gonadal (white fat) and interscapular (brown fat). Results are presented as means ± SD.

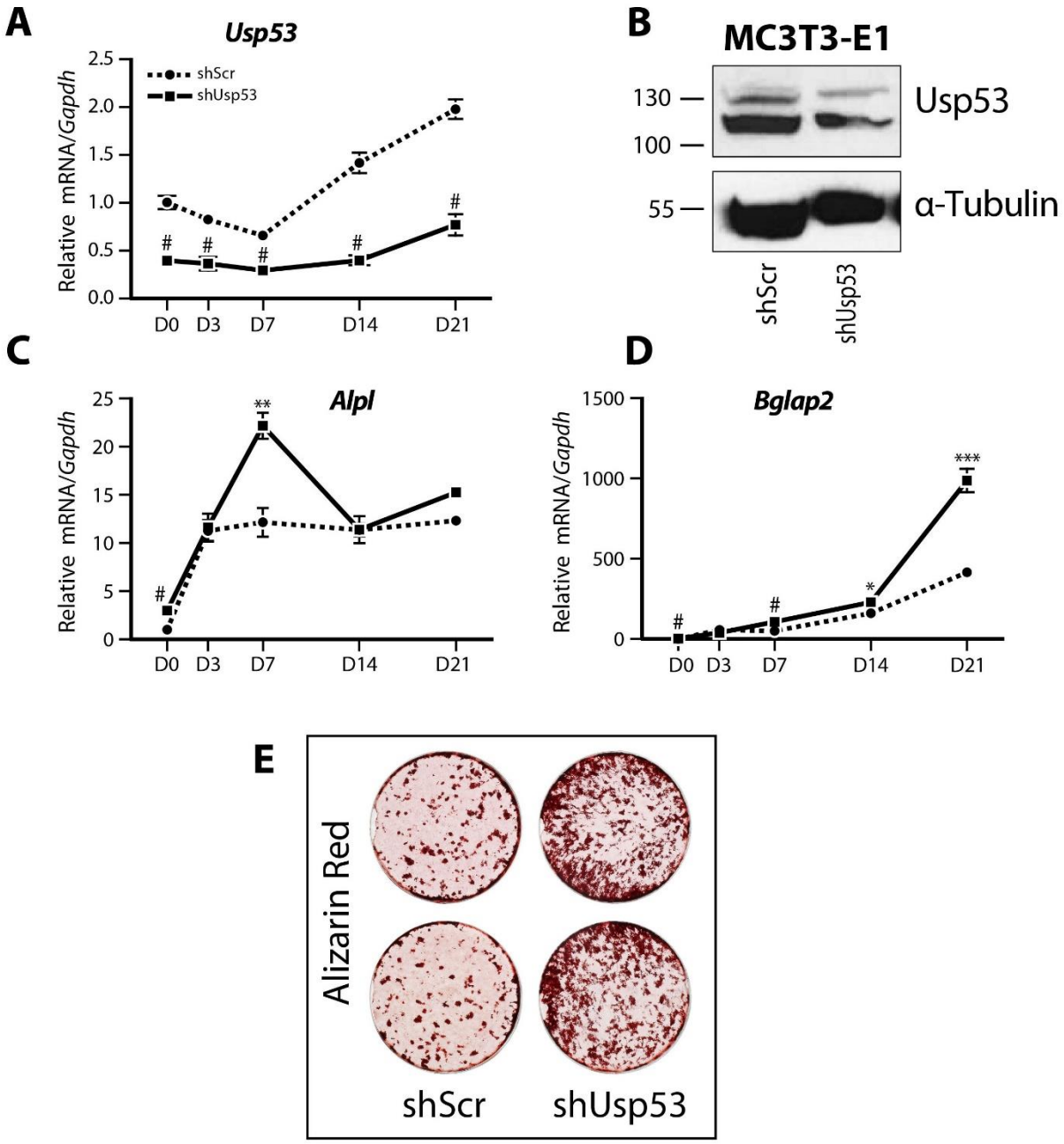
A
Usp53
shScr
shUsp53
Relative mRNA/Gapdh
2.5
2.0
1.5
1.0
0.5
0.0
D0 D3 D7 D14 D21
B
MC3T3-E1
130
100
55
Usp53
α-Tubulin
shScr
shUsp53
C
Alpl
Relative mRNA/Gapdh
25
20
15
10
5
0
D0 D3 D7 D14 D21
D
Bglap2
Relative mRNA/Gapdh
1500
1000
500
0
D0 D3 D7 D14 D21
E
Alizarin Red
shScr
shUsp53

Supplementary Figure 4.2 *Usp53* knockdown enhances the differentiation of committed osteoblasts

A,C, and D Knockdown of *Usp53* in MC3T3-E1 cells and gene expression analysis of osteogenic differentiation markers. Quantitative RT-qPCR using probes against *Usp53*, *Alpl*, and *Bglap2*, normalized to *Gapdh*, was performed on RNA isolated from shScr-stably transfected (dashed line) or shUsp53-stably transfected (solid line) pools of MC3T3-E1 cells differentiated for 21 days in osteogenic medium. B, Western blot analysis of Usp53 expression. Total protein isolated from MC3T3-E1 cells stably transfected with shScr or shUsp53 at D1, confirming the knockdown of *Usp53*. α- tubulin was used as a loading control. E, MC3T3-E1 cultures were examined for calcium deposition using alizarin red staining at D21.

CONNECTING TEXT BETWEEN CHAPTERS IV and V

We have previously reviewed the molecular pathways and regulators mediating PTH signaling in bone. The described molecular cascades regulate osteoblast commitment, differentiation, and function (Sections 1.8 and 1.9). The work presented in chapter IV has identified *Usp53* as a downstream target of the PTH-NACA axis in osteoblasts and unfolded a potential role for *Usp53* in regulating mesenchymal stem cell lineage selection. We have shown that the knockdown of *Usp53* enhances osteoblastogenesis and inhibits adipogenesis *in vitro* in ST2 cells and *ex vivo* in BMSCs. The findings of chapter IV could explain the skeletal phenotype reported in a patient carrying a duplication mutation within *USP53* genomic locus (219). Consequently, we have focused on characterizing the biological function of *Usp53* in vivo.

This led us to the work presented in chapter V. This chapter focuses on the *in vivo* characterization of *Usp53* null mice, generated by global inactivation of the gene using a CMV-*Cre* deleter strain. Chapter V covers the developmental role of *Usp53* in mesenchyme-derived tissues including bone and adipose tissues. We track the expression of *Usp53* by examining X-gal staining of tissues isolated from *Usp53* null-LacZ reporter mice. The impact of *Usp53* ablation on bone and fat development has been assessed by microcomputed tomography (Micro-CT) analyses, mechanical testing, gene expression analyses, dynamic histomorphometry, and histology. Additionally, we assess the contribution of *Usp53* to mesenchymal differentiation using different culture systems of cells isolated from long bones (BMSCs), calvaria, and embryos
(mouse embryonic fibroblasts (MEFs).

Finally, we uncover the molecular mechanisms underlying the observed phenotypes in *Usp53* null mice and mediating the biological function of Usp53. For this aim, we perform mass spectrometry (MS) to identify protein partners of USP53. Meaningful interactions have been further validated and characterized by immunoprecipitation assays and western blotting in primary cells. Changes in major pathways regulating both adipogenic and osteogenic signaling arms have been examined by western blotting in *Usp53*-deficient and wildtype primary cells. The work presented in chapter V is the results section a draft of a manuscript describing the biological role of *Usp53 in vivo* (In preparation).

Chapter V: *Usp53* regulates mesenchymal stem cell differentiation and bone turnover *in vivo*

5.1. Usp53 is expressed during skeletal development

Since we identified *Usp53* as a PTH-responsive gene in osteoblasts (Hariri et al., MCB. Accepted with revisions), we investigated its contribution to skeletal development. To study the function of *Usp53 in vivo* we generated a targeted allele (*Usp53* "knockout-first" tm1a, Fig.5.1 A) of *Usp53* and obtained heterozygous and homozygous null mice with the lacZ tracer allele at the *Usp53* locus by crossing tm1a mice to the CMV-*Cre* deleter strain (Fig.5.1 A). The different genotypes, wildtype (WT, wt/wt), heterozygous (HET, tm1b/wt), and homozygous null (KO, tm1b/tm1b) were examined by PCR assays on DNA isolated from calvarial cultures of mice at P2 (Fig.5.1 B). We report the expression of *Usp53* in different tissues, especially bone and fat. Gene expression analysis of tissues isolated from KO *Usp53* mice and their wildtype littermates has further confirmed the deletion of *Usp53* in the different assayed tissues (Fig.5.1 C).

As expression can dictate function, we tracked the expression of the $Usp53^{lacZ}$ allele *in vivo* and assayed heterozygous mice for β-galactosidase (β-gal) activity. The expression of $Ups53^{lacZ}$ was first assessed during embryonic development at E15.5. The X-gal staining of whole mount embryos (E15.5) showed a strong blue staining of $Usp53^{lacz/+}$ embryos as compared to wildtype littermates (Fig.5.1 D, *right*). Prominent staining was detected in different skeletal tissues including the skull, mandibles, maxilla, spine, and ribs. To be noted is the strong staining also detected in the skin of $Usp53^{lacz/+}$ embryos (Fig.5.1 D, *right*, and Supplementary Fig. 5.1 A). Examination of long bones at higher magnification showed an intense staining in newly formed long bones of the forelimbs and hindlimbs (Fig.5.1 D, *right*). The staining was noted in the developing diaphysis and intensified at the ends of the long bones in the cartilaginous growth plates (Fig.5.1 D, *right*). We then investigated the expression of *Usp53* during postnatal development at P0 and P21 (Fig.5.2 A-D). For this aim, we examined the β-gal staining of neonatal bones to identify the cell types expressing *Usp53*. X-gal staining was detected in osteoblast cells of the periosteal and spongy bone portions of calvarial sections of $Usp53^{lacz/+}$mice at P0 (Fig.5.2 A). This expression was not restricted to this developmental stage as different portions of long bones showed similar staining at P21. Positive staining of clusters of chondrocytes was detected throughout the growth plate of long bones, where intense X-gal staining distinguished the hypertrophic zone of $Usp53^{lacz/+}$ mice at P21 (Fig.5.2 B). Moreover, populations of osteoblast and osteocyte cells showed strong X-gal staining in the diaphysis of

long bones of *Usp53*$^{lacz/+}$ mice (Fig.5.2 C). Likewise, the metaphysis of long bones showed intense X-gal staining of different cell populations embedded in the trabecular region including osteoblasts and osteoclasts (Fig.5.2 D). Wildtype littermates did not show any detectable X-gal staining in any of those sites through different developmental stages (Fig.5.2 A-D). The lack of staining in wildtype littermates confirmed that the detected X-gal staining in *Usp53*$^{lacz/+}$ mice is the result of the targeted transgene expression and not the result of endogenous β-gal expression.

These data show that *Usp53* is expressed in the skeleton during embryonic and postnatal development. The expression pattern of *Usp53* suggests an important function for this gene in regulating the development of bone, and possibly other tissues derived from embryonic mesenchyme.

5.2. Germline inactivation of *Usp53* results in developmental bone defects and low bone mass

To understand the role of *Usp53* through bone development, we characterized the skeletal phenotype of *Usp53* null mice. All genotypes appeared grossly normal during embryonic development and at later stages of gestation. Though viable, the examination of *Usp53* null neonates revealed some skeletal defects at P2. *Usp53* null neonates had small body sizes distinguished by short limbs (Fig.5.3 A, panel a), asymmetrical distribution of ossification centers along the sternum (Fig.5.3 A, panel b), and a decrease in mineralized matrices of the sternum and vertebrae as compared to wildtypes (Fig.5.3 A, panels b, c). This decrease in body size and weight was more pronounced, and statistically significant, at 6-weeks of age (Fig.5.3 B). *Usp53* null mice were hypocalcemic (Supplementary Fig.5.1 B) and normophosphatemic (Supplementary Fig.5.1 C), with moderately elevated circulating levels of PTH (1-84) that were not statistically significant (Supplementary Fig.5.1 D). Static histomorphometry of distal femurs obtained by MicroCT (μCT) showed a marked decrease in both trabecular and cortical bone compartments of *Usp53* null mice (Fig.5.3 C). The loss of *Usp53* caused a significant decrease in bone volume accompanied by diminished trabecular and cortical thickness (Fig.5.3 D, E, *upper panels*). Other trabecular parameters of the appendicular skeleton including trabecular number and connectivity density as well as cortical parameters including cortical bone area and the mean polar moment of inertia were also affected in a similar manner (Fig.5.3 D, E, *lower panels*). Moreover, the analysis of *Usp53* heterozygous mice at 6-weeks of age showed a decrease in

trabecular bone parameters (Supplementary Fig.5.1 E). However, no changes were detected in cortical indices in those mice as compared to wildtypes (Supplementary Fig.5.1 F).

We performed dynamic histomorphometry to obtain measures of bone formation and resorption. The data did not reveal any differences in bone formation parameters (Fig.5.4 A-F), most importantly mineralized surface per bone surface (Fig.5.4 A), mineral apposition rate (Fig.5.4 B), and bone formation rate (Fig.5.4 C). These data suggested that decreased bone formation did not contribute to the low bone mass detected in *Usp53* null mice. Alternatively, it could result from increased bone resorption and turnover. Serum analysis showed an increase in the bone formation marker Procollagen type I propeptides (PINP) (Fig.5.5 A) and the bone resorption marker C-terminal telopeptide of type I collagen (CTX-1) (Fig.5.5 B) in *Usp53* null mice as compared to wildtypes. Besides, serum levels of the Tartrate-resistant acid phosphatase 5b (TRAcP5b), an osteoclast-specific bone resorption marker, were also elevated in *Usp53* null mice (Fig.5.5 C). These results indicate that the decrease in bone mass is attributable to increased bone resorption, as the increase in serum Tracp5b levels reflects elevated osteoclast numbers. Results of RT-qPCR analysis of tibial bone RNA indicated an increase in osteoclast-related markers further supporting the hypothesis of enhanced bone resorption. *Usp53*-deficient bones exhibited increased levels of cathepsin K (*Ctsk*) and tartrate-resistant acid phosphatase type 5 (*Acp5*), with no significant alterations in expression levels of osteoblast- and osteocyte-related genes, except for *Runx2* (Fig.5.5 D and Supplementary Fig.5.1 G). Importantly, the expression of *Rankl*; an osteoblast-secreted cytokine and a master regulator of osteoclastogenesis, was upregulated in *Usp53*-deficient bones with no significant changes in *Opg* expression levels (Fig.5.5 D). This caused a marked increase in the *Rankl*/*Opg* ratio (Fig.5.5 D).

Collectively, these data identify *Usp53* as a novel regulator of skeletal growth and bone mass. The global inactivation of *Usp53* leads to low bone mass achieved by increased bone turnover rate. The functional consequences of this inactivation resulted in a significant increase in markers of osteoclast number and activity rendering osteoblast-specific markers unchanged. These data support the model that increased bone resorption underlies the low bone phenotype observed in *Usp53*-deficient mice. Results presented in subsequent sections of this study address whether the role of *Usp53* involves a cell autonomous effect on osteoclast number and activity or an indirect osteoblast-assisted regulation of osteoclast function through paracrine signaling.

5.3. Effects of *Usp53* inactivation on bone strength and microarchitecture

The μCT analysis of *Usp53*-deficient femurs indicated a decrease in diaphyseal (cortical) parameters, which may affect mechanical bone properties (Fig.5.3 E). To investigate whether the low bone mass reported in *Usp53* null mice is associated with high risk of fracture, we assessed the biomechanical and structural properties of *Usp53*-deficient bones (Fig.5.6 A-H). We first assessed whole-bone mechanical properties of femurs at mid-diaphysis by three-point bending (3-pt-bending) technique. The analysis of *Usp53*-deficient femurs at 6-weeks of age showed a marked decrease in biomechanical parameters including stiffness, ultimate load, work-to-yield, and work-to-fracture (Fig.5.6 A-D). The interrelated decrease in these parameters reflects an overall decline in whole bone's strength of *Usp53* null mice. Also, the decrease in the work needed to fracture the bone was associated with a decrease in post-yield displacement (Supplementary Fig.S5.1 H). The reduction in both parameters converges to reflect compromised toughness and ductility of *Usp53*-deficient bones.

We also assessed changes in bone microarchitecture of tibias using the reference point indentation (RPI) technique. The micro-indentation of freshly-harvested tibias at 6-weeks of age indicated an increase in RPI variables including indentation distance increase (IDI, Fig.5.6 E), total indentation distance (TID, Fig.5.6 F), and first cycle indentation distance ($ID1^{st}$, Fig.5.6 G) of *Usp53*-deficient bones. This was accompanied with a decrease in the mean unloading slope (US, Fig.5.6 H). These data obtained from different indentation sites along the tibial cortical surface suggest that the material properties of *Usp53*-deficient bones are poor and its microarchitecture is less sophisticated as compared to wildtype bones.

Taken together, these data show that the loss of *Usp53* decreases the biomechanical and structural quality of bone, probably making it more prone to fracture. Comparing both data sets, a correlation shows up associating the decrease in biomechanical strength given by 3-pt-bending with poor bone quality at the tissue level revealed by RPI in *Usp53* null mice.

5.4. Variable impacts of *Usp53* inactivation on adipose tissue development

Bone and adipose tissues are derived from a common multipotent mesenchymal progenitor. To investigate whether *Usp53* inactivation affects adipose tissue development, we examined the changes in three peripheral adipose depots: gonadal white adipose tissues (gWAT), inguinal white adipose tissues (iWAT), and interscapular brown adipose tissues (iBAT). At 6-

weeks of age, we found that iWAT depots were significantly bigger, with no significant change in gWAT or iBAT depot masses of *Usp53* null mice (Fig.5.7 A). It is yet to be determined whether the change in iWAT depot mass is due to changes in adipocyte number and/or diameter. Interestingly, the examination of histological sections of gWAT (Fig.5.7 B, *left panel*) and iWAT (Fig.5.7 B, *right panel*) depots showed an increase in fat 'beiging'. This increase in fat beiging was associated with a prominent increase in uncoupling protein 1 (*Ucp1*) expression levels in both gWAT (Fig.5.7 C) and iWAT (Fig.5.7 D) depots of *Usp53* null mice. Moreover, gene expression analysis of gWAT (Fig.5.7 C) and iBAT (Fig.5.7 E) depots did not show any changes in mRNA levels of classical gene markers of adipogenesis. However, the analysis of iWAT depots showed an increase in expression levels of early-adipogenic activators such as fatty acid binding protein 4 (*Fabp4)* and CCAAT/enhancer binding protein α (*C/ebpα*) as well as the late adipogenic marker CCAAT/enhancer binding protein β (*C/ebpβ*) (Fig.5.7 D).

These data show that *Usp53* is involved in adipose tissue development. The global inactivation of *Usp53* had no impact on brown fat adipogenesis and variable effects on gWAT and iWAT differentiation programs. The increased beiging of iWAT depots along with the striking beiging of gWAT suggest alterations in the metabolic program of *Usp53* null mice, achieved by a *Ucp1*-dependent mechanism. It remains to be determined whether *Usp53* has a cell autonomous effect on adipogenic differentiation of early progenitors or alters systemic signalling to regulate adipose tissue development and function.

5.5. *Usp53* inactivation increases marrow adipogenesis

Bone marrow adipose tissue (BMAT) is a distinct adipose depot of unique origins. Changes in marrow adiposity have been associated with alterations in bone mass in both human and mice. To assess the impact of *Usp53* deletion on marrow adipogenesis, we have quantified and characterized the BMAT populations residing in the long bones of *Usp53* null mice. Using osmium tetroxide (OsO_4) μCT analyses we visualized and quantified the volume of marrow adipocytes occupying the region extending from tibia/fibula junction to distal end of intact tibias of 8-week old mice. *Usp53*-deficient tibias exhibited more adipocytes in the distal end as compared to controls (Fig.5.8 A) and μCT quantification further validated the significant increase in BMAT in tibias of *Usp53* null mice, as compared to WT and heterozygous (HET) mice (Fig.5.8 B). To further examine the BMAT cell populations occupying the bone marrow

cavity, we performed gene expression analyses of total bone marrow (BM) extracts. The analyses indicated a significant increase in adipocyte transcription factors including *Pparg* and differentiation adipocytic markers including *Fabp4* and adiponectin (*AdipoQ*) (Fig.5.8 C). Importantly, the analysis of whole bone marrow indicated an increase in *Rankl* expression in *Usp53* null mice as compared to wildtypes (Fig.5.8 D).

Combined, these data show that *Usp53* depletion enhances bone marrow adipogenesis and further supports a role for *Usp53* in adipocyte differentiation. The enhanced expression of *Rankl* detected in whole bone marrow contributes to the systemic pool of RANKL in *Usp53* null mice. It suggests that increased marrow adipogenesis and *Rankl* expression are associated with the low bone mass phenotype in *Usp53*-deficient mice.

5.6. *Usp53* inactivation regulates cell fate determination of mesenchymal progenitors

Bone-forming osteoblasts, adipocytes and chondrocytes arise from a common mesenchymal precursor. The bone and adipose tissue alterations detected in *Usp53* null mice suggest a central function for *Usp53* in regulating cell lineage differentiation. To functionally assess the role of *Usp53* at the cellular level, we examined the multipotent differentiation potentials of primary bone marrow-derived stem cells (BMSCs). Under osteogenic conditions, *in vitro* cultures of *Usp53*-deficient BMSCs showed no change in the expression of early osteoblastic markers including *Sp7*, *Runx2*, *Col1a1*, and *Alpl* (Fig.5.9 A, Osteo). However, we detected a significant decrease in osteocalcin (*Bglap2*) expression levels of *Usp53*-deficient cultures (Fig.5.9 A, Osteo). This decrease in *Bglap2* expression was accompanied by reduced mineralization capacity of *Usp53*-deficient cultures when assayed for mineral deposition by Von Kossa staining (Fig.5.9 B, *top*). Interestingly, these cultures exhibited elevated expression of *Rankl* that led to an increase in *Rankl* to *Opg* ratio (Fig.5.9 A, Osteo). The effect of *Usp53* ablation was also assessed in primary calvarial cultures. *Usp53*-deficient calvarial cultures exhibited decreased expression levels of both early and late osteoblastic markers including *Sp7*, *Runx2*, *Col1a1*, *Alpl,* and *Bglap2* along with reduced matrix mineralization (Supplementary Fig.5.2 A).

The adipogenic stimulation of *Usp53*-deficient BMSC cultures failed to induce adipocytic differentiation markers including *Pparg*, *Fabp4*, and *AdipoQ* (Fig.5.9 A, Adipo) and this was further demonstrated by a drastic reduction in the formation of oil red O-positive

adipocytes (Fig.5.9 B, *bottom*). Moreover, we employed mouse embryonic fibroblasts (MEFs) as another source for stem cell populations, to assess the impact of *Usp53* depletion on mesodermal cell differentiation. The analyses of *Usp53*-deficient MEF cultures induced by osteogenic or adipogenic cocktails led to a similar gene expression pattern in both lineages, as compared to BMSC cultures (Supplementary Fig.5.2 B). However, we detected an upregulation of *Sp7* and *Alpl* expression levels (Supplementary Fig.5.2 B, Osteo) and a downregulation in *Cebpα/β* expression levels (Supplementary Fig.5.2 B, Adipo) in *Usp53*-deficient MEF cultures, changes that were not observed in the BMSC culture system. We attribute this difference in gene regulation to the differences in the gene expression profile and origin of the two stem cell populations, as one is acquired embryonically and the other postnatally.

Taken together, these data suggest that *Usp53* acts as a modulator of the cell fate program. The ablation of *Usp53* restrains the commitment of stem cells toward the adipocyte lineage. Also, terminal osteoblastic differentiation and mineralization are compromised in the absence of *Usp53*. Our data does not allow to rule out a differential role for *Usp53* in committed osteoblasts (calvarial cultures) versus early stem cell progenitors. Importantly, the pronounced increase in *Rankl/Opg* ratio in knockouts suggest a role for *Usp53* in regulating osteoclast differentiation.

5.7. Increased osteoclastogenesis leads to low bone mass in *Usp53* null mice

Bone-resorbing osteoclasts and bone-forming osteoblasts are coupled by paracrine signaling. Our data suggest a non cell-autonomous effect for *Usp53* on osteoclast formation and differentiation, rather than aberrant osteogenesis leading to the observed low bone mass. We first tested the possibility of a direct effect for *Usp53* ablation on osteoclast differentiation. To do this, we induced bone marrow (BM) precursors to undergo osteoclastogenesis *in vitro* using a cocktail of RANKL and M-CSF. Gene expression analyses of differentiated osteoclast cultures showed no change in all osteoclast gene markers including the receptor for RANK-ligand (*Rank*), nuclear factor of activated T-lymphocytes (*Nfatc1*), *Ctsk*, and *Acp5* (Fig.5.9 C). The same cultures did not show any difference between the two genotypes, when assayed for TRAP staining (Fig.5.9 D). We next tested the possibility of an indirect effect for *Usp53* ablation on osteoclast differentiation, involving osteoblast cells. To test this possibility, we induced the differentiation of BM precursors in a transwell coculture system. BM precursors and osteoblast

cells were cultured in separate compartments separated by a permeable membrane allowing for the exchange of secreted proteins and ligands (Fig.5.10 A). The experimental setup allowed the examination of different combinations of BM precursors and osteoblast cells from both genotypes (Fig.5.10 B). Surprisingly, no change was detected in the gene expression of osteoclast differentiation markers for any condition (Fig.5.10 C). The same cultures were examined for TRAP staining. Wildtype and KO osteoclast precursors co-cultured with WT-osteoblasts showed similar TRAP staining patterns of osteoclasts with different nuclei number (Fig.5.10 D, panel 1 and 3 and Fig.5.10 E). We observed an increase in TRAP-stained osteoclasts with more than 5 nuclei when WT and KO osteoclast precursors were cultured with KO osteoblasts (Fig.5.10 D, panels 2 and 4 and Fig.5.10 E*).* Interestingly, KO osteoclast precursors with KO osteoblasts cocultures showed increased number and surface area occupied by huge osteoclasts with more than 5 nuclei, as compared to all other cultures (Fig.5.10 D, E).

These data support increased osteoclastogenesis as one reason leading to low bone mass in *Usp53*-deficient mice. The coculture observations show that the inactivation of *Usp53* enhances osteoclastogenesis through osteoblasts, probably due to increased RANKL production. It also suggests a direct impact on osteoclast formation and maturation and raise a question about the role of *Usp53* in regulating osteoblast-osteoclast coupling mechanisms.

5.8. USP53 interacts with the TAK1-TAB complex

Little is known about the mechanism of action of USP53, which is enzymatically inactive (217, 218). This suggests an alternative function that most likely involves protein-protein interactions. One study has reported that USP53 interacts with ZO-1/TJP1 and ZO-2/TJP2 tight junction scaffolding proteins in polarized epithelial cells of the ear in mice (218). In order to identify additional proteins interacting with USP53 that could explain its effect on mesenchymal cell lineage-making decisions and differentiation, we used Mass Spectrometry (MS). Flag epitope-tagged USP53 was overexpressed in HEK-293T cells and immunoprecipitated with anti-Flag beads to pull down interacting complexes. Flag-GFP was used as control.

MS identified 45 proteins which were exclusively bound by Flag-USP53, 11 proteins bound by Flag-GFP, and 119 proteins that immunoprecipitated with both (Fig.5.11 A). We analyzed the list of proteins uniquely interacting with USP53 to identify meaningful interactions that can explain its role in mesenchymal cell differentiation. Frequent background contaminants

were eliminated by comparison to the contaminant repository for affinity purification (CRAPome: http://www.crapome.org) (239), bringing down the total to 33 unique interactants. The MS data validated the previously reported interaction of USP53 with the ZO-2/TJP2 protein and revealed several hits for deubiquitinases such as: USP15, USP9X, and OTUD4 (Supplementary Table 5.1). Interestingly, the proteomics analysis uncovered an interaction with the transforming growth factor β (TGFβ)-activated kinase 1-TAB complex, a multicomponent complex regulated by BMP/TGFβ signaling (240-242). The list of proteins uniquely interacting with USP53 included TAK1 (also known as MAP3K7) and its binding proteins TAB1 and TAB2 (Fig.5.11 B).

We validated the interaction of USP53 with the TAK1/TAB1/TAB2 complex through co-immunoprecipitation. Flag-USP53 was immunoprecipitated from overexpressing HEK-293T cells, and complexes were eluted and analyzed by western blotting. Epitope-tagged USP53 interacted with endogenous TAK1, TAB1, and TAB2 (Fig.5.11 C). This data suggested that USP53 may have a role in TAK1/TAB1/TAB2 complex formation and downstream signaling.

5.9. *Usp53* depletion disrupts TAK1-TAB complex formation and alters downstream signaling

The previously unrecognized interaction of USP53 with the TAK1/TAB1/TAB2 complex may help elucidate the mechanism by which *Usp53* modulates mesenchymal cell differentiation and bone mass. Previous studies have shown that the assembly of TAK1 with its binding proteins TAB1 and TAB2 is essential for the autophosphorylation-induced activation of TAK1 (241, 243). We tested whether the ablation of *Usp53* could affect the assembly of the complex and/or its activity. Endogenous TAK1 was immunoprecipitated from MEF cultures of wildtype and KO mice. Immunoblotting against endogenous TAB2 proteins revealed a marked decrease in the amounts of protein interacting with TAK1 in the KO cultures (Fig.5.11 D, *top and middle*). However, we could not document the interaction between TAK1 and TAB1 in MEF cultures (Fig.5.11 D, *bottom*) and we owe this to the limited options of commercially available antibodies against TAB1. This result was also validated in ST2 cells stably infected with shUsp53 or the shScr control where a decrease in TAK1-bound TAB2 and TAB1 proteins were observed in the absence of Usp53 (Supplementary Fig.5.3 A).

It is well established that BMPs and TGFβ signal through the TAK1/TAB1/TAB2 complex (240-242). We set out to determine whether BMP signaling was altered by decreased TAK1/TAB1/TAB2 complex formation secondary to *Usp53* depletion. We assessed the activation of the canonical and noncanonical BMP signaling targets Smad 1/5/8, JNK, and p38. We did not detect any significant changes in the phosphorylation of Smad1/5/8 or JNK1/2 with or without activation in MEF cultures of both genotypes (data not shown). However, decreased p38 phosphorylation was detected in KO MEF cultures treated with BMP-2 for 30 min (Fig.5.11 E). Reduced mRNA expression of adipogenic markers was detected in *Usp53*-deficient cultures (Fig.5.9 A). We examined if *Usp53* ablation could also affect their protein stability. Assaying MEFs cultured in adipogenic medium by immunoblotting indicated a decrease in PPARγ protein levels in KO cultures (Fig.5.11 F). This result was also validated in ST2 cells. We inhibited protein synthesis in ST2 cells stably expressing shUsp53 or the shScr control using cycloheximide (CHX) and chased PPARγ protein levels at intervals. Immunoblotting (Supplementary Fig.5.3 B) and quantification of the signal (Supplementary Fig.5.3 C) showed that the PPARγ protein was less stable in *Usp53* knockdown cells as compared to control.

Collectively, we propose a model by which USP53 interacts with the TAK1/TAB1/TAB2 complex regulating the differentiation of adipocytes, osteoblasts, and osteoclasts. The ablation of *Usp53* destabilizes the complex blocking p38 phosphorylation and *Pparg* transcription, thus restraining adipocyte differentiation. The destabilization of the complex can regulate osteoblasts and increase RANKL production by an as yet unknown mechanism. Subsequently, the increase in RANKL production can activate osteoclastogenesis leading to low bone mass in *Usp53* null mice. The regulation of the TAK1/TAB1/TAB2 complex activity by RANK/RANKL signaling is well established (244). It is yet to be revealed whether the pathways regulating osteoclast maturation and activity are also affected by this scenario in *Usp53*-null mice (Fig.5.12).

Breeding scheme

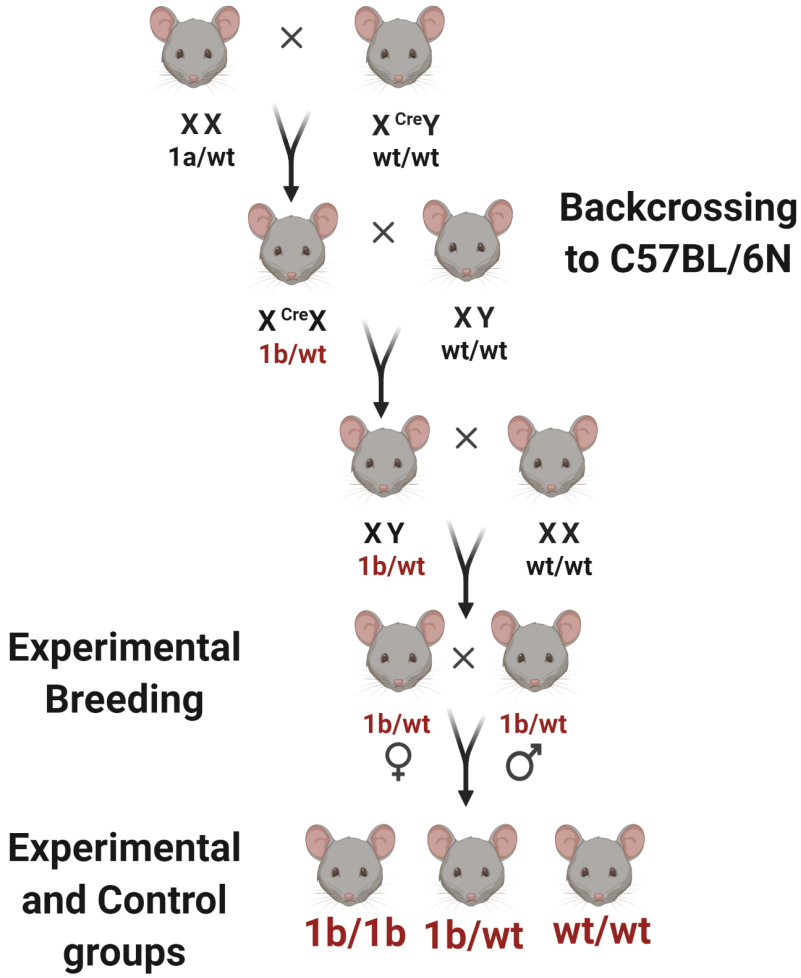

Figure 5.0 *Usp53* knockout colony establishment and maintenance

Schematic showing the breeding scheme and strategy to generate *Usp53* knockout mice. Male *CMV*-Cre mice were crossed with female tm1a heterozygotes and all female offspring genotyped for conversion to tm1b. The Cre recombinase was then removed by crossing tm1b heterozygotes to C57BL/6N males. Recombinase negative males were then used in further breedings to establish heterozygous x heterozygous breeding pairs. Experimental breedings of heterozygotes (1b/wt) gave rise to homozygous knockout (1b/1b) and wildtype (wt/wt) mice.

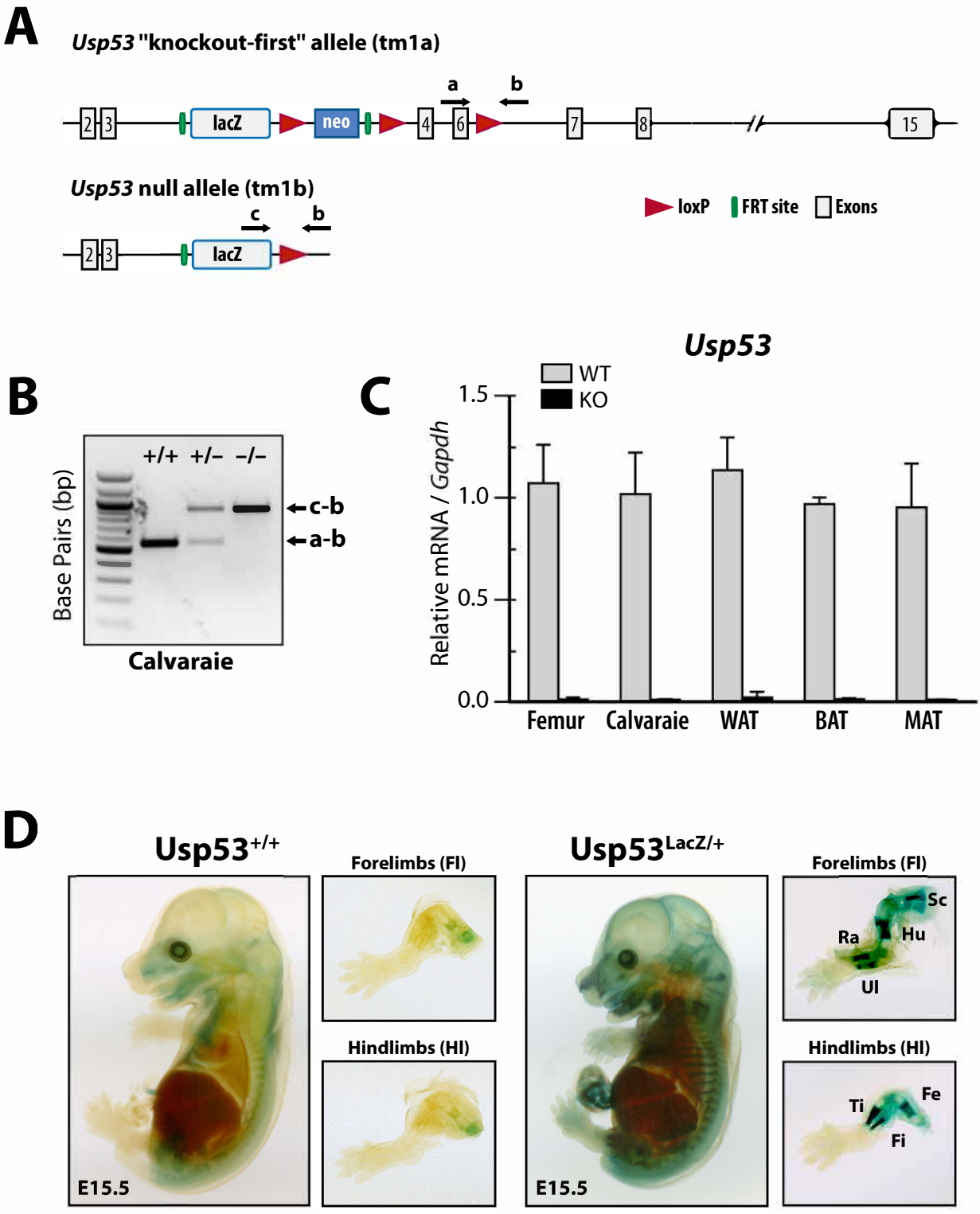
A
Usp53 "knockout-first" allele (tm1a)
a
b
2
3
lacZ
neo
4
6
7
8
15
Usp53 null allele (tm1b)
c
b
2
3
lacZ
loxP
FRT site
Exons
B
+/+
+/–
–/–
Base Pairs (bp)
c-b
a-b
Calvaraie
C
Usp53
WT
KO
Relative mRNA / Gapdh
1.5
1.0
0.5
0.0
Femur
Calvaraie
WAT
BAT
MAT
D
Usp53+/+
Forelimbs (Fl)
Hindlimbs (Hl)
E15.5
Usp53LacZ/+
Forelimbs (Fl)
Sc
Ra
Hu
Ul
Hindlimbs (Hl)
Ti
Fe
Fi
E15.5

Figure 5.1 Generation of *Usp53* knockout mice

A, Schematic showing the targeting strategy to generate the *Usp53* null allele. *Usp53* knockout-first allele (EUCOMM targeting allele tm1a, top) consists of 15 coding exons (white boxes). *Usp53* null allele was generated by crosses of *Usp53* knockout-first allele to *Cmv-Cre* strain that cuts and recombines *LoxP* sites (red arrows), thus removing the neomycin-resistance cassette (neo) and exons 4,5, and 6, generating *Usp53* null allele (tm1b) The image also depicts the primers used to detect the *Usp53* null allele ("a", "b", "c"; black arrows) and *Frt* sites (green bars). B, Agarose gel of PCR products generated using primers "a", "b", and "c" to detect the different genotypes. Genomic DNA isolated from calvarial cell cultures was used as a starting material for PCR reactions. C, Gene expression analysis of the deletion efficiency of *Usp53* allele in different tissues from knockout (KO, n=10) compared to wildtype (WT, n=8) mice. Results are normalized to *Gapdh* expression and are given as means ± SD. D, Whole-mount X-gal staining of embryos with the indicated genotypes at E15.5. X-gal staining of forelimbs (Fl) and hindlimbs (Hl) with the indicated genotypes at E15.5. Sc, scapula; Hu, humerus; Ra, radius; Ul, ulna; Ti, tibia; Fe, femur; Fi, fibula.

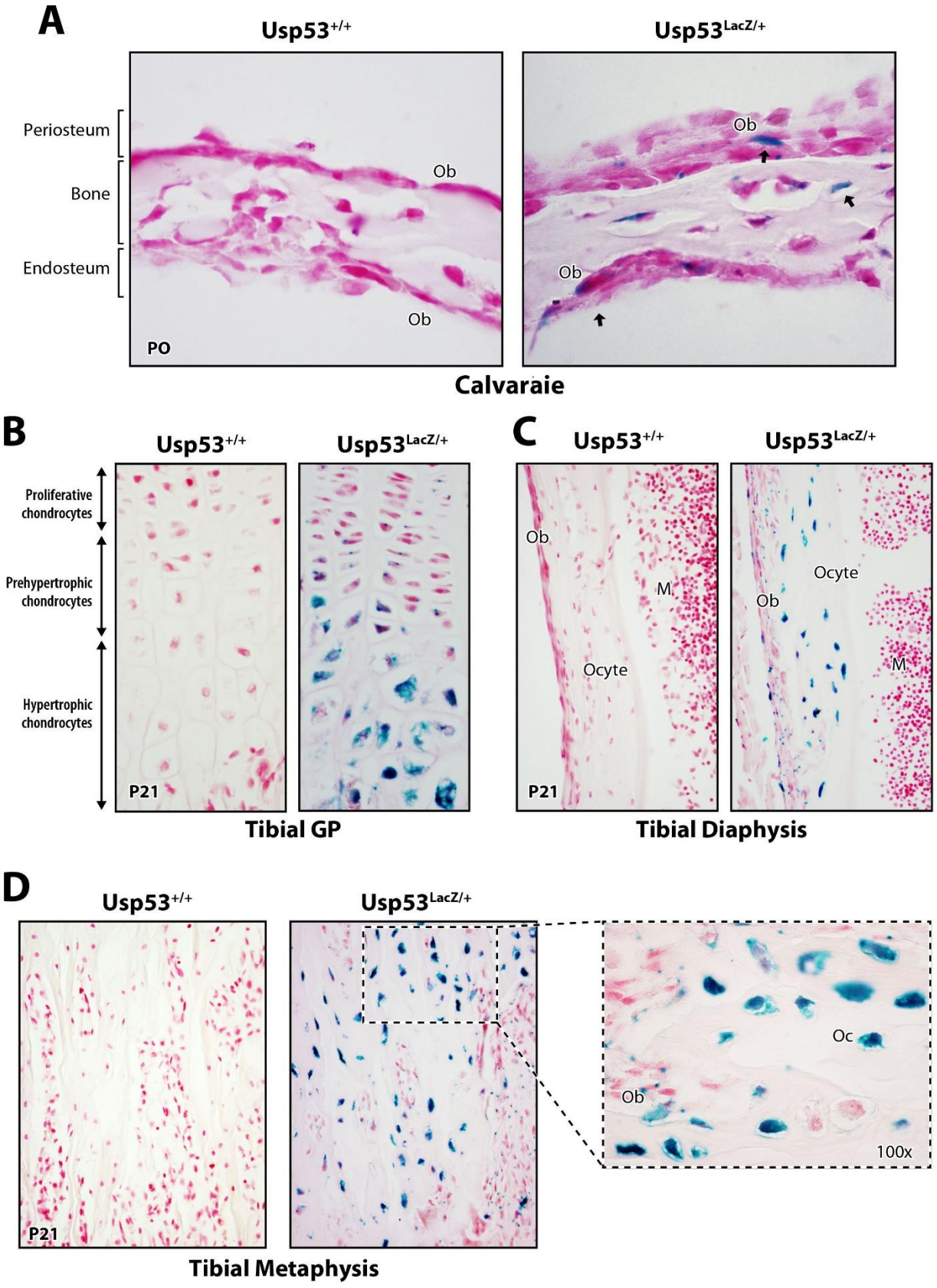
A
Usp53+/+
Usp53LacZ/+
Periosteum
Bone
Endosteum
Ob
Ob
Ob
Ob
PO
Calvaraie
B
Usp53+/+
Usp53LacZ/+
Proliferative chondrocytes
Prehypertrophic chondrocytes
Hypertrophic chondrocytes
P21
Tibial GP
C
Usp53+/+
Usp53LacZ/+
Ob
M
Ocyte
P21
Ocyte
Ob
M
Tibial Diaphysis
D
Usp53+/+
Usp53LacZ/+
P21
Oc
Ob
100x
Tibial Metaphysis

Figure 5.2 Extensive distribution of *Usp53* in bone tissues

A, Histological sections of X-gal-stained calvarial tissues with the indicated genotypes at P0. Blue staining of osteoblasts (Ob, arrows) at periosteal, endosteal surfaces and inside bone (right panel). B,C,D, X-gal staining of long bones at P21. B, Histological sections of X-gal-stained tibial growth plate with the indicated genotypes at P21. Blue staining of proliferative and prehypertrophic chondrocytes was weak compared to intense staining of hypertrophic chondrocytes (right panel). C, Histological sections of X-gal-stained tibial diaphysis with the indicated genotypes at P21. Intense blue staining of osteocytes (Ocyte) in diaphyseal cortical bone and osteoblasts (Ob) lining the diaphyseal periosteal surface. No staining was detected in the marrow (M). D, Histological sections of X-gal-stained tibial metaphysis with the indicated genotypes at P21. Intense staining was detected in different cell types (right panel) including osteoblasts (Ob) and osteoclasts (Oc) in the trabecular zone of the metaphysis (magnified dashed box, 100x).

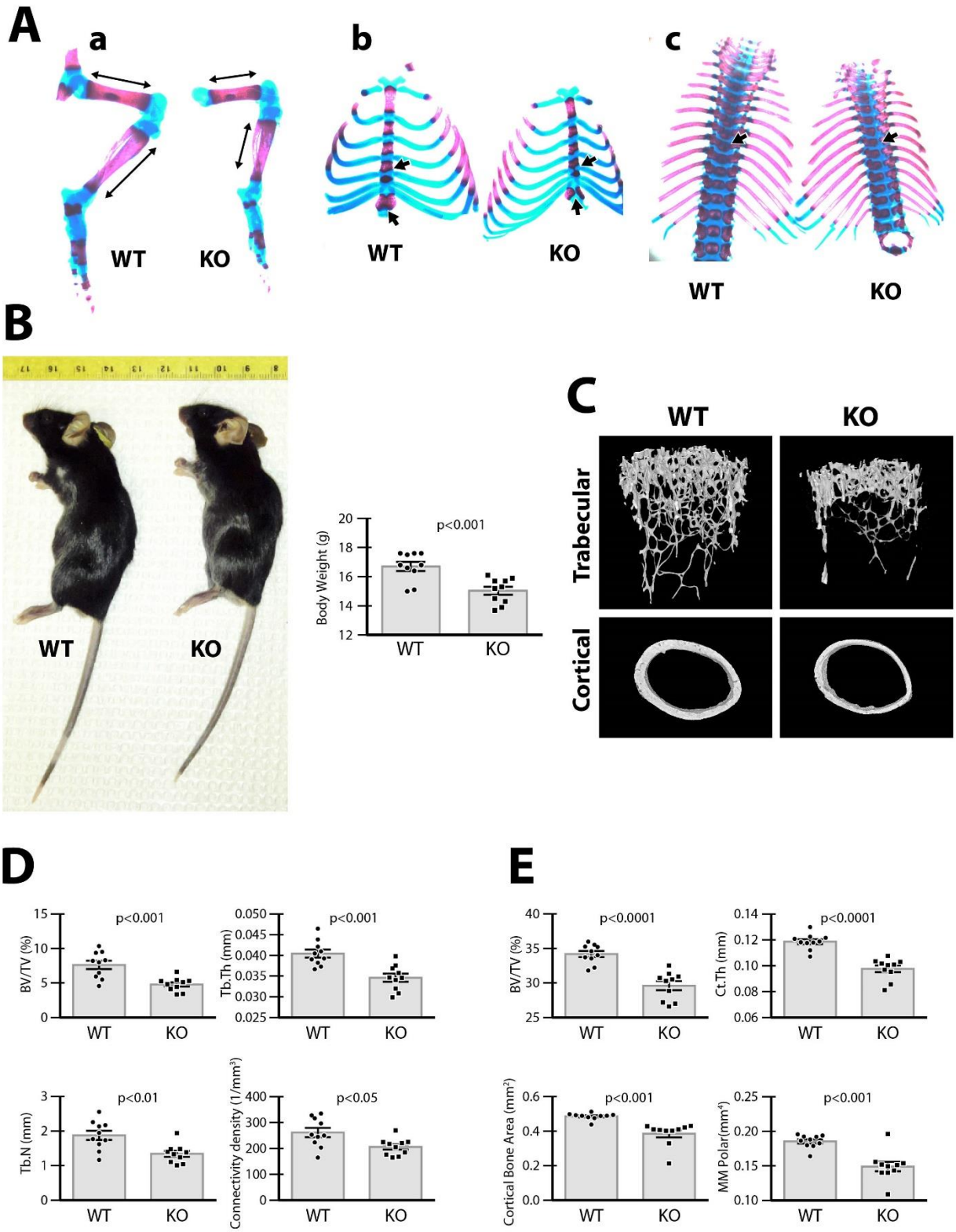
A
a
WT
KO
b
WT
KO
c
WT
KO
B
WT
KO
Body Weight (g)
p<0.001
WT
KO
C
WT
KO
Trabecular
Cortical
D
BV/TV (%)
p<0.001
Tb.Th (mm)
p<0.001
Tb.N (mm)
p<0.01
Connectivity density (1/mm³)
p<0.05
E
BV/TV (%)
p<0.0001
Ct.Th (mm)
p<0.0001
Cortical Bone Area (mm²)
p<0.001
MM Polar(mm⁴)
p<0.001

Figure 5.3 Germline Inactivation of *Usp53* leads to defects in bone development

A, Alizarin red and Alcian blue-stained skeletal preparations of wildtype (WT) and *Usp53* null (KO) neonates. *Usp53* null neonates show: (a) short tibias and femurs (arrows), (b) mineralization and cartilaginous sternal defects (arrowheads), (c) mineralization defects of vertebrae (arrowheads). Bone is stained in red and cartilage in blue. B, Gross images of 6-week-old WT and KO mice (left panel) and their body weights (right panel). Significant changes in body weight among the two genotypes ($P < 0.001$); unpaired *t*-test. C, Micro-CT (μCT) images of trabecular bone of the femoral metaphyseal region (top) and cortical bone of diaphysis (bottom). D and E, Histograms representing trabecular (D) and cortical (E) structural parameters of WT and KO mice (n=10) obtained by μCT analyses. KO mice show a significant decrease in all trabecular (D) and cortical (E) indices. Trabecular parameters are trabecular bone volume/tissue volume (BV/TV), trabecular thickness (Tb.Th), trabecular number (Tb.N), and connectivity density. Cortical parameters are cortical bone volume/tissue volume (BV/TV), cortical thickness (Ct.Th), cortical bone area, and mean polar moment of inertia (MMI polar). Results are given as means ± SD. $P < 0.05$ was considered significant; unpaired *t*-test.

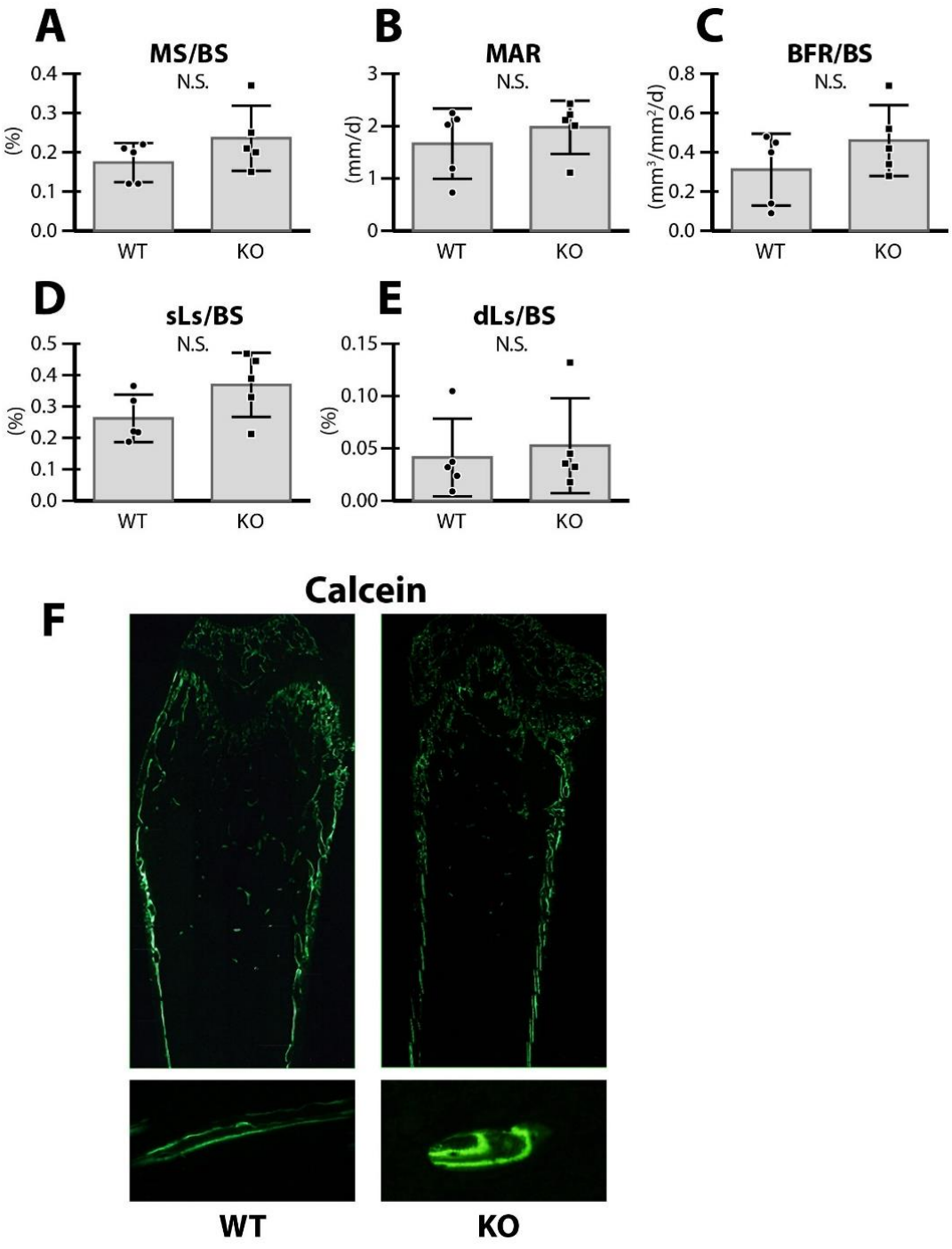
A
MS/BS
N.S.
(%)
0.4
0.3
0.2
0.1
0.0
WT
KO
B
MAR
N.S.
(mm/d)
3
2
1
0
WT
KO
C
BFR/BS
N.S.
(mm³/mm²/d)
0.8
0.6
0.4
0.2
0.0
WT
KO
D
sLs/BS
N.S.
(%)
0.5
0.4
0.3
0.2
0.1
0.0
WT
KO
E
dLs/BS
N.S.
(%)
0.15
0.10
0.05
0.00
WT
KO
F
Calcein
WT
KO

Figure 5.4 Osteoblast-related dynamic histomorphometry parameters are not affected by *Usp53* inactivation

A to E, Dynamic histomorphometry of femurs from 6-week-old mice (n=5). No significant changes were detected for osteoblast-related dynamic parameters including mineralized surface per bone surface (MS/BS), mineral apposition rate (MAR), bone formation rate per bone surface (BFR/BS), single labeled surfaces per bone surface (sLs/BS), and double labeled surfaces per bone surface (dLs/BS) (unpaired *t*-test. N.S., not significant). F, Calcein-stained images of femurs from 6-week-old mice (top) and individual trabeculae (bottom) showing no significant difference in interlabeled distances between WT and KO.

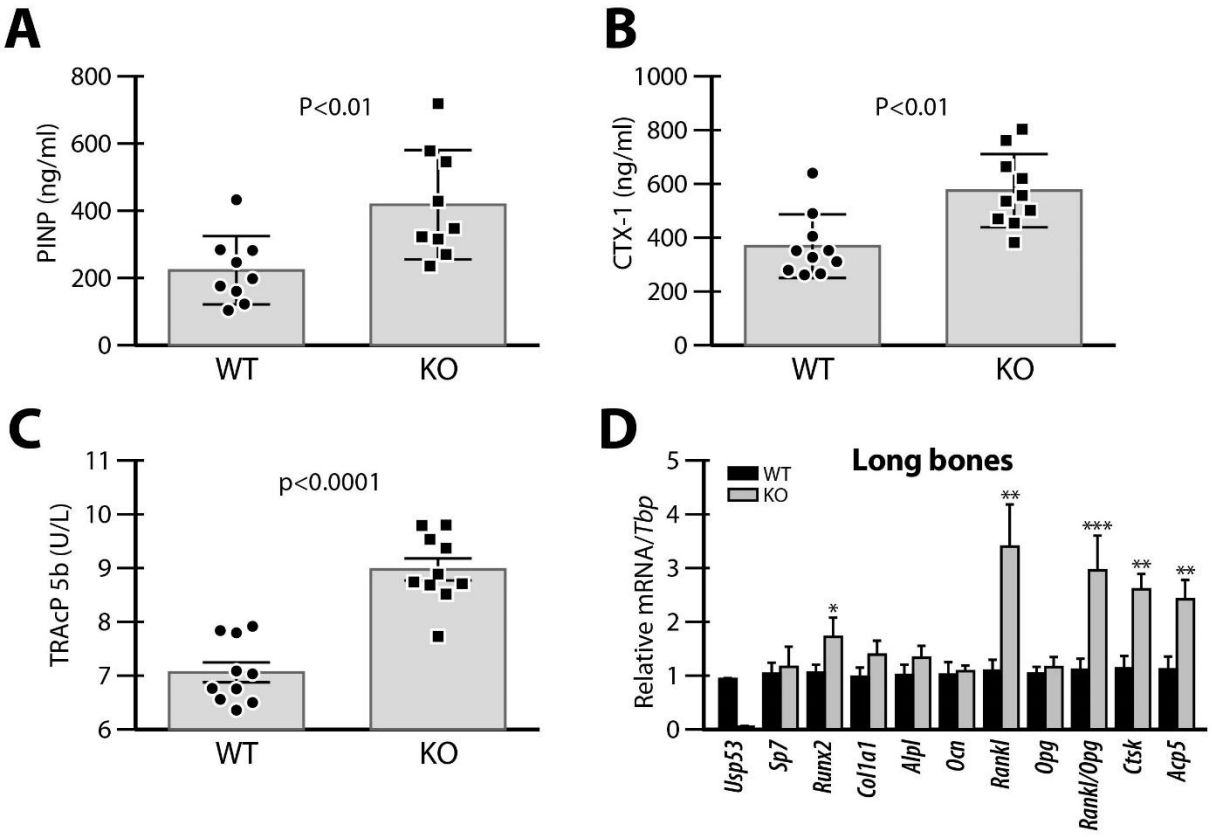
A
PINP (ng/ml)
800
600
400
200
0
P<0.01
WT
KO
B
CTX-1 (ng/ml)
1000
800
600
400
200
0
P<0.01
WT
KO
C
TRAcP 5b (U/L)
11
10
9
8
7
6
p<0.0001
WT
KO
D
Long bones
WT
KO
Relative mRNA/Tbp
5
4
3
2
1
0
**
*
**
***
**
**
Usp53
Sp7
Runx2
Col1a1
Alpl
Oc
Rankl
Opg
Rankl/Opg
Ctsk
Acp5

Figure 5.5 *Usp53* null mice exhibit increased bone turnover rate

A,B,C, Blood biochemistry analysis of 6-week-old mice (n=10). KO mice show: increased levels of the N-terminal propeptide of type I procollagen (PINP) (A), C-terminal telopeptide α1 chain of type I collagen (CTX-1) (B), and tartrate-resistant acid phosphatase form 5b (TRAcP 5b) (C). $P < 0.05$ was considered significant; unpaired *t*-test. D, Gene expression analysis of osteoblast and osteoclast-selective genes in long bones of WT and KO mice at 6-weeks of age (n=10). Results are normalized to *Tbp* expression and are given as means ± SD. *, $P < 0.05$; **, $P < 0.01$; ***, $P < 0.001$; unpaired *t*-test.

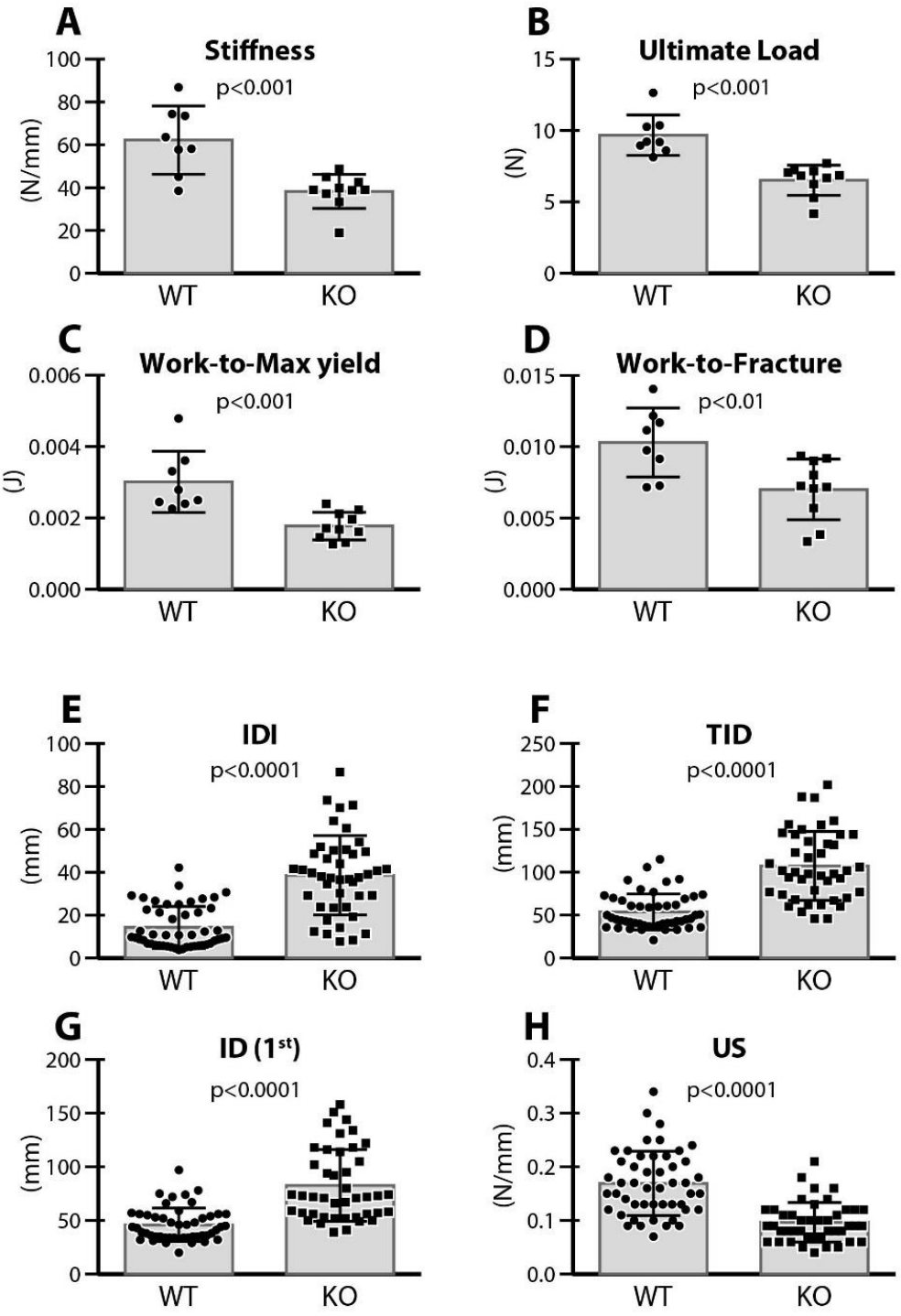
A
Stiffness
p<0.001
(N/mm)
100
80
60
40
20
0
WT
KO
B
Ultimate Load
p<0.001
(N)
15
10
5
0
WT
KO
C
Work-to-Max yield
p<0.001
(J)
0.006
0.004
0.002
0.000
WT
KO
D
Work-to-Fracture
p<0.01
(J)
0.015
0.010
0.005
0.000
WT
KO
E
IDI
p<0.0001
(mm)
100
80
60
40
20
0
WT
KO
F
TID
p<0.0001
(mm)
250
200
150
100
50
0
WT
KO
G
ID (1st)
p<0.0001
(mm)
200
150
100
50
0
WT
KO
H
US
p<0.0001
(N/mm)
0.4
0.3
0.2
0.1
0.0
WT
KO

Figure 5.6 *Usp53* inactivation compromises bone mechanical strength and properties

A-D, Three-point bending testing. Femurs of KO mice show a significant decrease in all biomechanical parameters including stiffness (A), ultimate load (B), work-to-maximum yield (C), and work-to-fracture (D). Results are given as means ± SD. E-H, Reference point indentation testing. Tibias of KO mice show a significant increase in the following parameters: indentation distance increase (IDI) (E), total indentation distance (TID) (F), and indentation distance of first cycle (ID 1^{st}) (G), except for the unloading slope (US) (H). Results are given as means of all measurements along the tibia ± SD. $P < 0.05$ was considered significant; unpaired *t*-test.

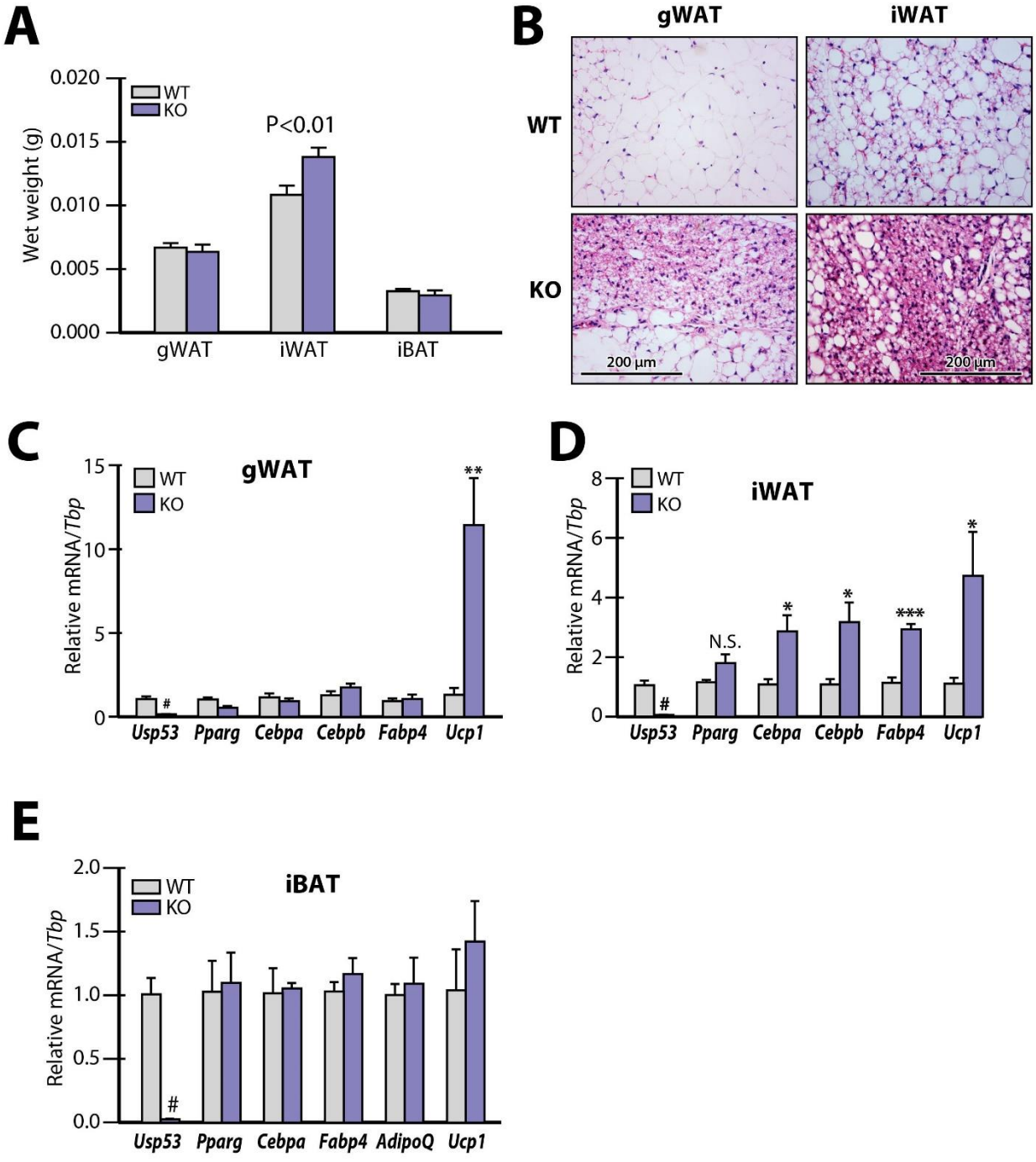
A
Wet weight (g)
0.020
0.015
0.010
0.005
0.000
WT
KO
P<0.01
gWAT
iWAT
iBAT
B
gWAT
iWAT
WT
KO
200 μm
200 μm
C
gWAT
Relative mRNA/Tbp
15
10
5
0
WT
KO
**
#
Usp53
Pparg
Cebpa
Cebpb
Fabp4
Ucp1
D
iWAT
Relative mRNA/Tbp
8
6
4
2
0
WT
KO
N.S.
*
*
***
*
#
Usp53
Pparg
Cebpa
Cebpb
Fabp4
Ucp1
E
iBAT
Relative mRNA/Tbp
2.0
1.5
1.0
0.5
0.0
WT
KO
#
Usp53
Pparg
Cebpa
Fabp4
AdipoQ
Ucp1

Figure 5.7 Impact of Usp53 ablation on adipose tissue development

A, Weights of freshly-harvested adipose depots normalized to total body weights of 6-week-old mice (n=10). Weights of Inguinal white adipose tissues (iWAT) show a significant increase between the two genotypes ($P<0.01$). B, Histological sections of white adipose tissue depots stained with H&E. Gonadal white adipose tissues (gWAT, left panel) and inguinal white adipose tissues (iWAT, right panel) of KO (bottom) mice show increased beiging compared to WT (top). C,D,E, Gene expression analysis of adipogenic-selective genes in adipose tissue depots. KO mice show: no significant differences in adipogenic markers of gWAT (C) and iBAT (E), significant increase in adipogenic markers of iWAT (D), and significant increase in *Ucp1* expression levels of gWAT and iWAT (C and D). Results are normalized to *Tbp* expression and are given as means ± SD. *, $P < 0.05$; **, $P < 0.01$; ***, $P < 0.001$; #, $P<0.0001$; N.S., not significant; unpaired *t*-test.

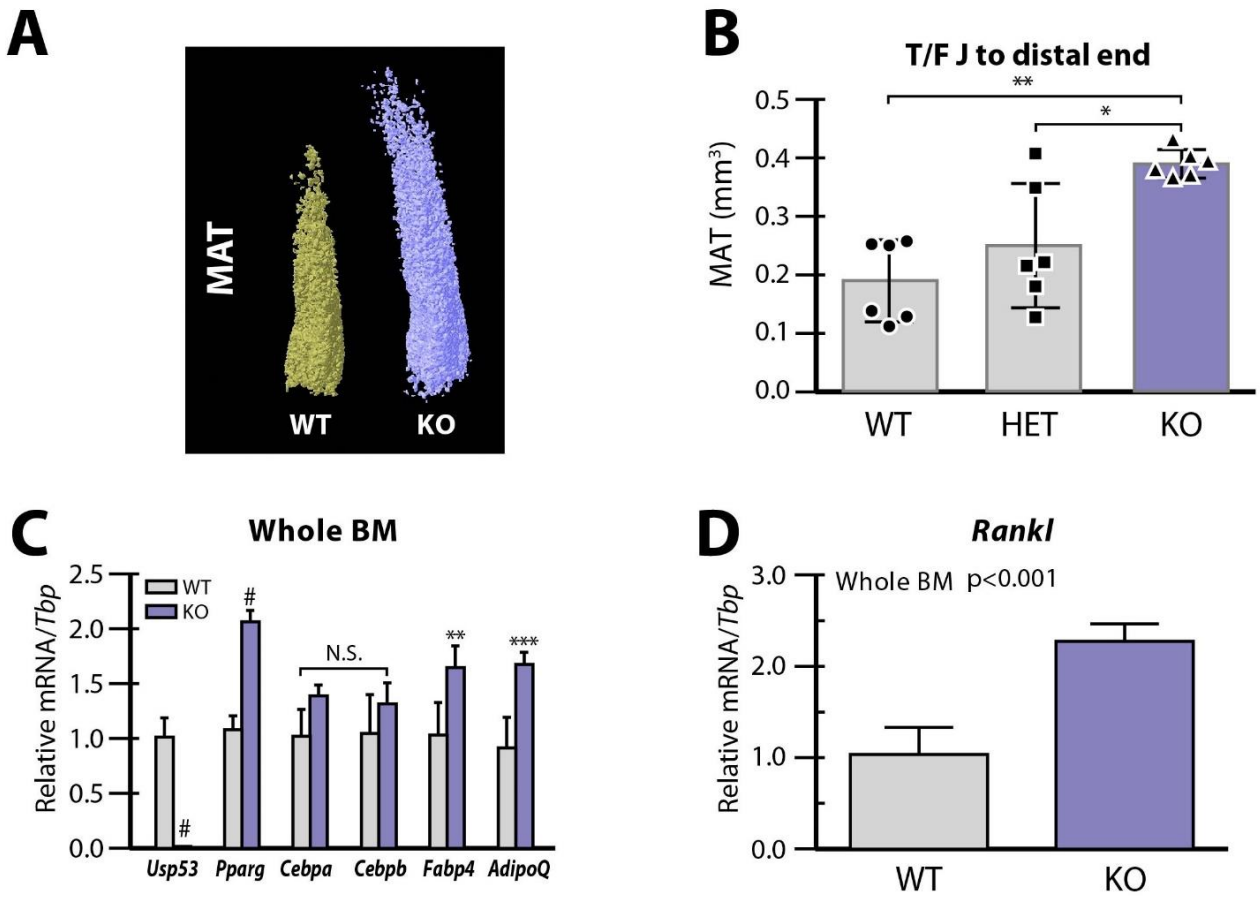
A
MAT
WT
KO
B
T/F J to distal end
**
*
MAT (mm³)
0.5
0.4
0.3
0.2
0.1
0.0
WT
HET
KO
C
Whole BM
Relative mRNA/Tbp
2.5
2.0
1.5
1.0
0.5
0.0
WT
KO
#
#
N.S.
**
***
Usp53
Pparg
Cebpa
Cebpb
Fabp4
AdipoQ
D
Rankl
Whole BM p<0.001
Relative mRNA/Tbp
3.0
2.0
1.0
0.0
WT
KO

Figure 5.8 Increased marrow adipogenesis due to *Usp53* inactivation

A, μCT images of marrow adipose tissues (MAT) starting at tibia/fibula junction (T/F J) and extending to distal end of tibias from 8-week-old mice. μCT images show increased marrow adipogenesis in KO (right, light violet) mice compared to WT (left, yellow). B, Quantification of marrow adipocytes by μCT analyses of the region starting at tibia/fibula junction and extending to distal end of tibias, showing a significant increase in KO mice, as compared to WT and heterozygous (HET) mice (n=6). Results are given as means ± SD. *, $P < 0.05$; **, $P < 0.01$; ANOVA with Bonferroni's *post-hoc* test. C, Gene expression analysis of adipogenic markers of whole bone marrow showing increased expression in KO mice, as compared to WT. D, Gene expression analysis showing significant increase in *Rankl* expression levels in KO mice as compared to WT ($P<0.01$). Results are normalized to *Tbp* expression and are given as means ± SD. **, $P < 0.01$; ***, $P < 0.001$; #, $P<0.0001$; N.S., not significant; unpaired *t*-test.

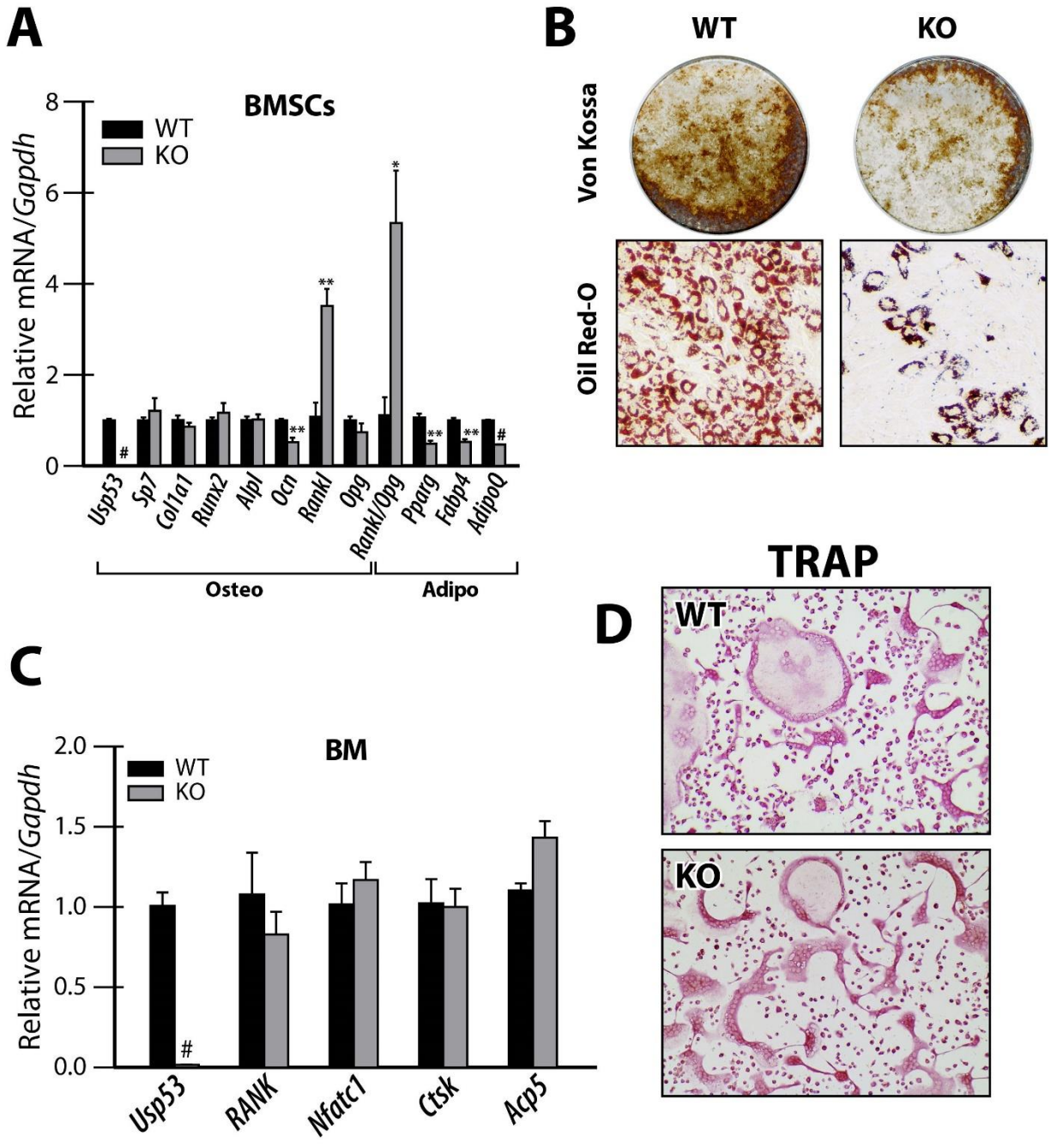
A
BMSCs
WT
KO
Relative mRNA/Gapdh
8
6
4
2
0
Usp53
Sp7
Col1a1
Runx2
Alpl
Ocn
Rankl
Opg
Rankl/Opg
Pparg
Fabp4
AdipoQ
Osteo
Adipo
B
WT
KO
Von Kossa
Oil Red-O
C
BM
WT
KO
Relative mRNA/Gapdh
2.0
1.5
1.0
0.5
0.0
Usp53
RANK
Nfatc1
Ctsk
Acp5
D
TRAP
WT
KO

Figure 5.9 *Usp53* inactivation inhibits osteogenic and adipogenic differentiation of mesenchymal stem cells

A, WT and KO BMSCs were cultured in inducing osteogenic (Osteo) conditions for 10 days or adipogenic (Adipo) for 8 days and analyzed by RT-qPCR analysis for expression of osteoblast-selective genes and adipocyte-selective genes, Von Kossa staining for mineral deposition (B, top), and oil red O staining for lipid production (B, bottom). C, Bone marrow (BM) osteoclast precursors were cultured in inducing osteoclastogenic conditions for 5 days and analyzed by RT-qPCR analysis for expression of osteoclast-selective genes and TRAP staining (D). Results are normalized to *Gapdh* expression and are given as means ± SD. *, $P < 0.05$; **, $P < 0.01$; #, $P<0.0001$; unpaired *t*-test.

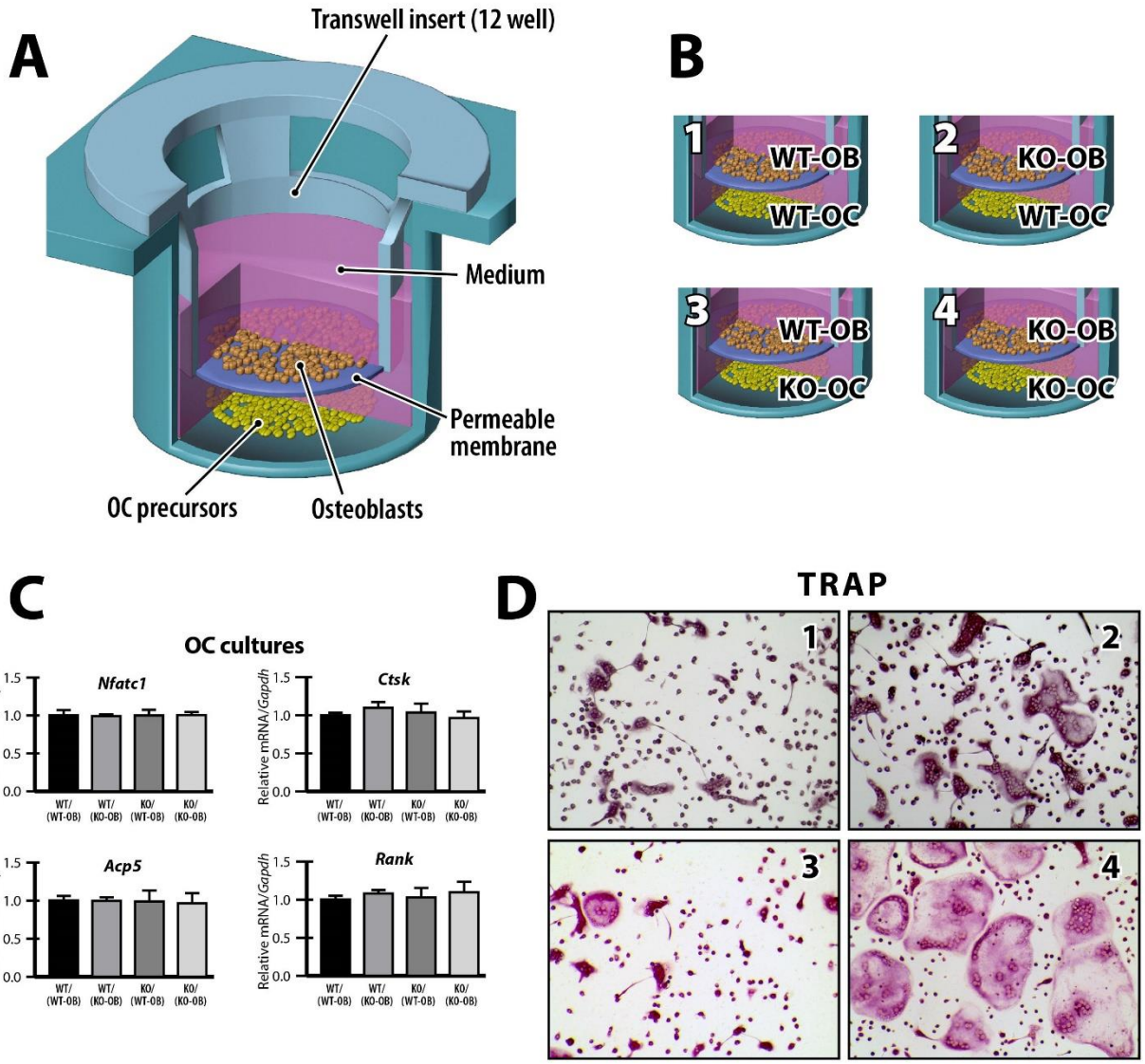
A
Transwell insert (12 well)
Medium
Permeable membrane
OC precursors
Osteoblasts
B
1
WT-OB
WT-OC
2
KO-OB
WT-OC
3
WT-OB
KO-OC
4
KO-OB
KO-OC
C
OC cultures
Nfatc1
Ctsk
Acp5
Rank
Relative mRNA/Gapdh
WT/ (WT-0B)
WT/ (KO-0B)
KO/ (WT-0B)
KO/ (KO-0B)
D
TRAP
1
2
3
4
E
1 nuclei
2 nuclei
3-5 nuclei
>5 nuclei
TRAP(+) / field

Figure 5.10 *Usp53* inactivation enhances osteoclastogenesis

A, Schematic showing the transwell coculture system used to coculture osteoclast (OC) precursors and osteoblasts. B, Schematic showing the four different assayed combinations of WT/KO osteoclasts and osteoblasts, labeled 1 to 4. C, Gene expression analysis for expression of osteoclast-selective genes for the assayed combinations. D, TRAP staining of cultures of the assayed combinations labeled 1 to 4 to match the conditions shown in panel B. E, Quantification of osteoclast nuclei number for each assayed combination. 50 random fields were examined for each combination and number of nuclei was counted. Results are given as means ± SD. *, $P < 0.05$; ***, $P < 0.001$; #, $P<0.0001$; ANOVA with Bonferroni's *post-hoc* test.

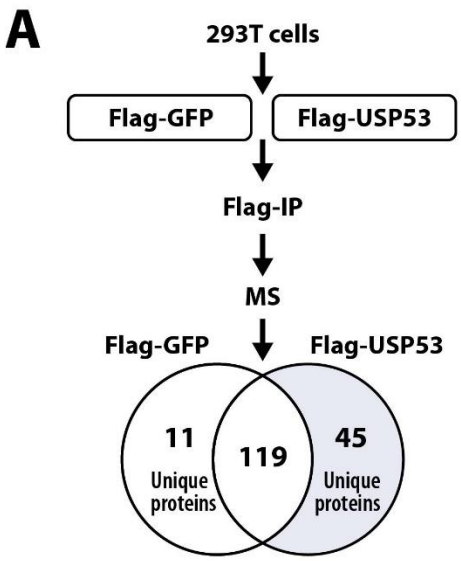

B

	Proteins[1]	Peptides[2]
Bait	**USP53**	28
Hit	TAB1	7
Hit	TAB2	6
Hit	MAP3K7 (TAK1)	4

[1] Identified proteins;
P> 99.9% with at least 2 identified peptides

[2] Identified peptides; Peptide threshold > 95%

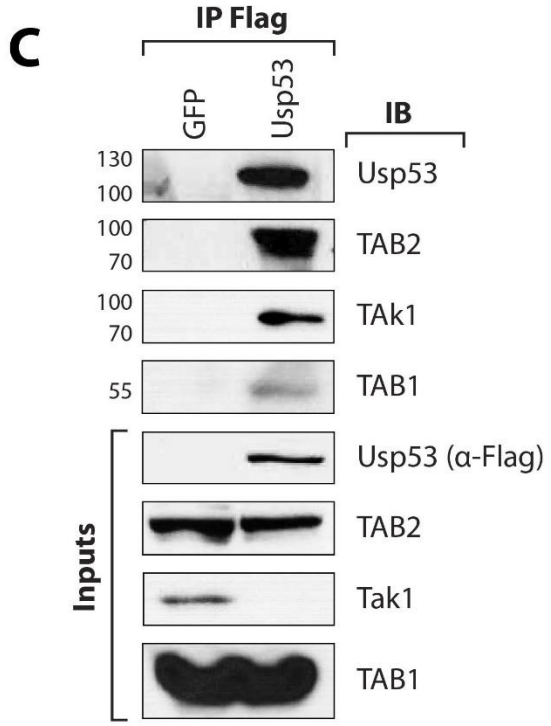

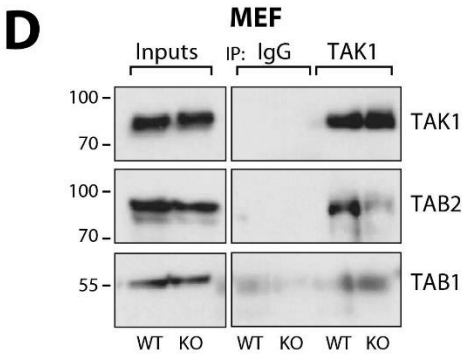

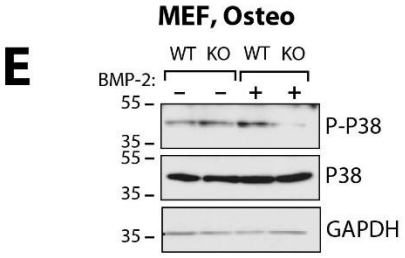

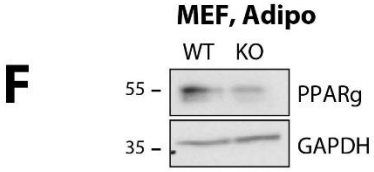

Figure 5.11 USP53 interacts with the TAK1/TAB1/TAB2 complex and regulates P38 phosphorylation and PPARγ stability

A, Schematic showing the workflow of Mass Spectrometry (MS) in HEK-293T cells detailing the implemented strategy and outcomes. B, Table summarizing the main proteins identified as interactants of USP53 and their corresponding numbers of peptides, identified by MS. C, Validation of the interaction of Usp53 with the TAK1/TAB1/TAB2 complex proteins in HEK-293T cells. Immunoprecipitation (IP) of flag-tagged Usp53 and immunoblotting (IB) against endogenous TAK1,TAB1,and TAB2 interacting proteins. D, Assessing the assembly of the TAK1/TAB1/TAB2 complex in WT and KO mouse embryonic fibroblast (MEFs) cells. Endogenous TAK1 proteins were immunoprecipitated in WT and KO MEF cells and interacting endogenous partners were immunoblotted using specific antibodies. IgGs were used as controls for IPs. E, Examining changes in P38 phosphorylation in WT and KO MEF cells cultured in osteogenic medium for 12 days and treated with BMP-2 (50ng/ml) for 45 min prior to protein extraction. Whole-cell lysates were analyzed by western blotting to detect P-P38, and P38 proteins using specific antibodies. F, Examining changes in PPARγ protein levels in WT and KO MEF cells cultured in adipogenic medium for 12 days. Whole-cell lysates were analyzed by western blotting to detect PPARγ proteins using specific antibodies. GAPDH was used as a loading control.

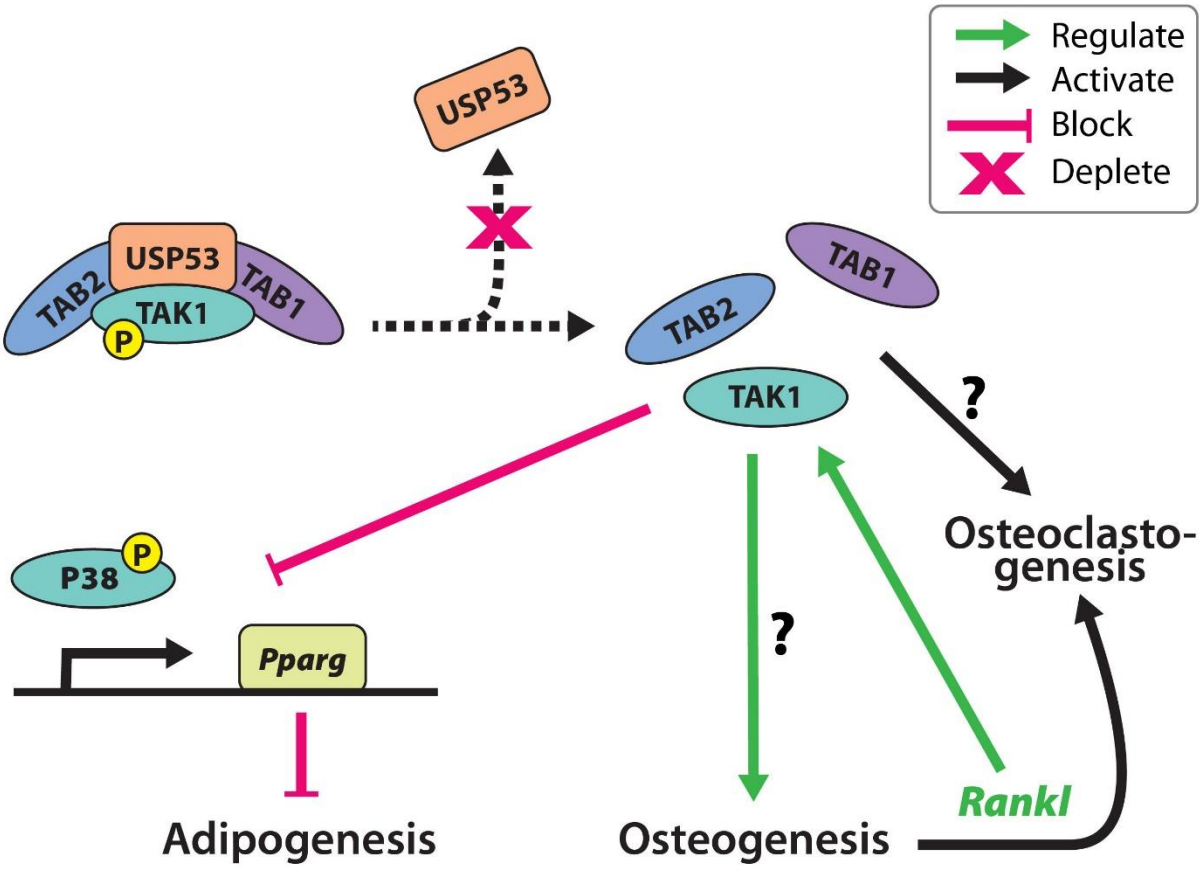
Regulate
Activate
Block
Deplete
USP53
TAB2
USP53
TAB1
TAK1
P
TAB2
TAB1
TAK1
?
Osteoclasto-
genesis
P38
P
Pparg
?
Rankl
Adipogenesis
Osteogenesis

Figure 5.12 Mechanistic model of Usp53 function

In bone marrow stem cells, the absence of USP53 disrupts the TAK1/TAB1/TAB2 complex formation. The disruption of complex assembly inhibits the phosphorylation of P38 and decreases the stability of PPARγ protein, thus impairing adipogenesis. Also, the disruption of complex formation regulates unknown pathways impacting osteoblast terminal differentiation and increasing *Rankl* production. Increased production of *Rankl* by osteoblasts enhances osteoclastogenesis. The Rank/Rankl signaling regulates the TAK1/TAB1/TAB2 complex regulating the formation and maturation of osteoclasts. It is yet to be determined whether USP53 has a direct effect on osteoclast maturation and activity signaling pathways.

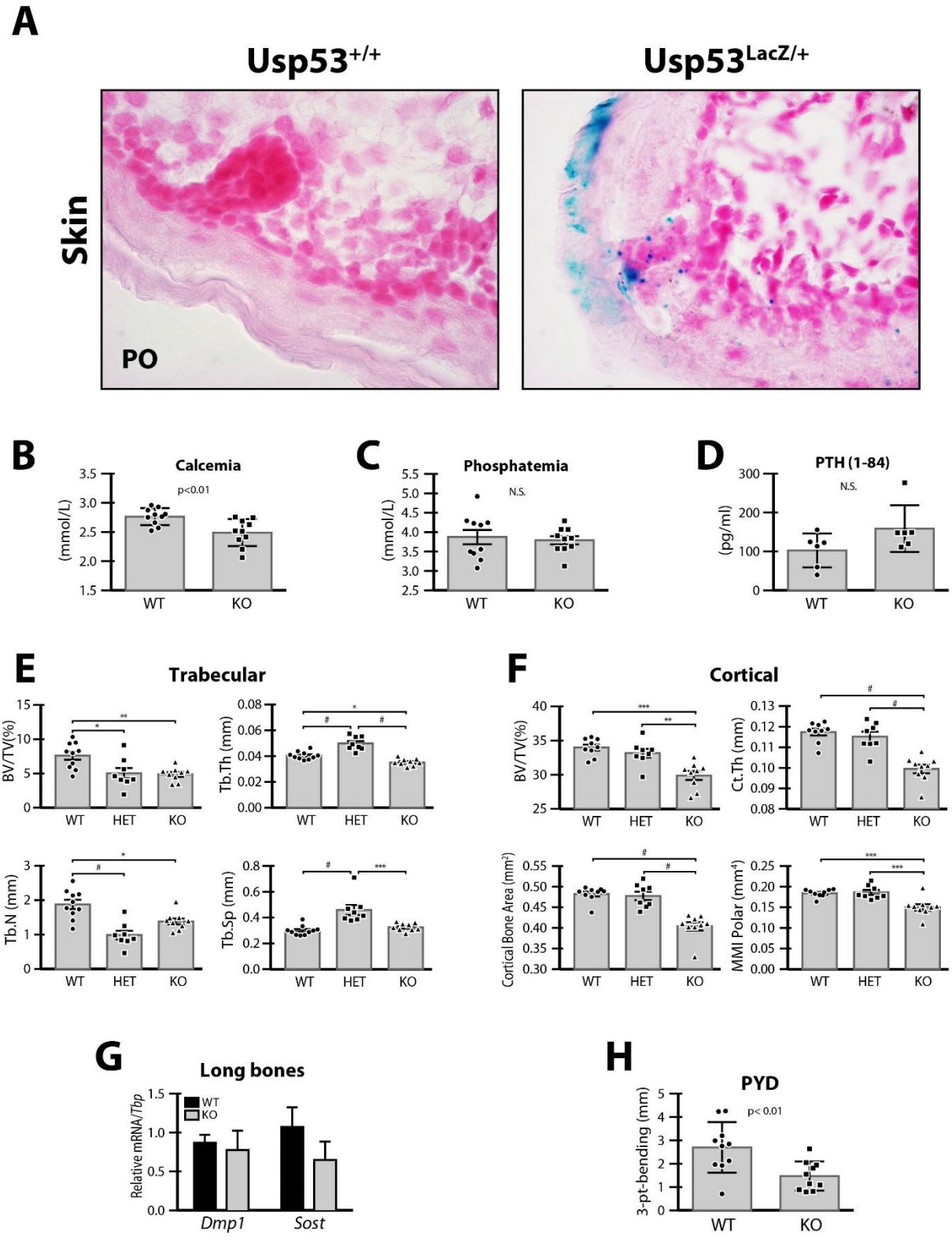
A
Usp53+/+
Usp53LacZ/+
Skin
PO
B
Calcemia
p<0.01
(mmol/L)
WT
KO
C
Phosphatemia
N.S.
(mmol/L)
WT
KO
D
PTH (1-84)
N.S.
(pg/ml)
WT
KO
E
Trabecular
BV/TV(%)
Tb.Th (mm)
Tb.N (mm)
Tb.Sp (mm)
WT
HET
KO
F
Cortical
BV/TV(%)
Ct.Th (mm)
Cortical Bone Area (mm²)
MMI Polar (mm⁴)
WT
HET
KO
G
Long bones
Relative mRNA/Tbp
WT
KO
Dmp1
Sost
H
PYD
p< 0.01
3-pt-bending (mm)
WT
KO

Supplementary Figure 5.1 Additional characterization of the phenotype of Usp53-deficient mice

A, Histological sections of X-gal-stained skin tissues with the indicated genotypes at P0. Blue staining in the epidermis of the skin (right panel).

B,C,D, Blood biochemistry analysis of calcium (B), phosphate (C), and PTH(1-84) (D) levels of the indicated genotypes at 6-weeks of age. KO mice show a significant decrease in calcium levels ($P<0.01$).

E,F, Histograms representing trabecular (E) and cortical (F) structural parameters of WT, HET, and KO mice (n=8-9) obtained by μCT analyses. Trabecular parameters are trabecular bone volume/tissue volume (BV/TV), trabecular thickness (Tb.Th), trabecular number (Tb.N), and trabecular separation (Tb.Sp). Cortical parameters are cortical bone volume/tissue volume (BV/TV), cortical thickness (Ct.Th), cortical bone area, and mean polar moment of inertia (MMI polar). Results are given as means ± SD. *, $P < 0.05$; **, $P < 0.01$; ***, $P < 0.001$; #, $P<0.0001$; N.S., not significant; ANOVA with Bonferroni's *post-hoc* test.

G, Gene expression analysis of osteocyte-selective genes in long bones of WT and KO mice at 6-weeks of age (n=10). Results are normalized to *Tbp* expression and are given as means ± SD; unpaired *t*-test.

H, Three-point bending testing. Femurs of KO mice show a significant decrease in the biomechanical parameter post yield displacement (PYD) ($P<0.01$); unpaired *t*-test.

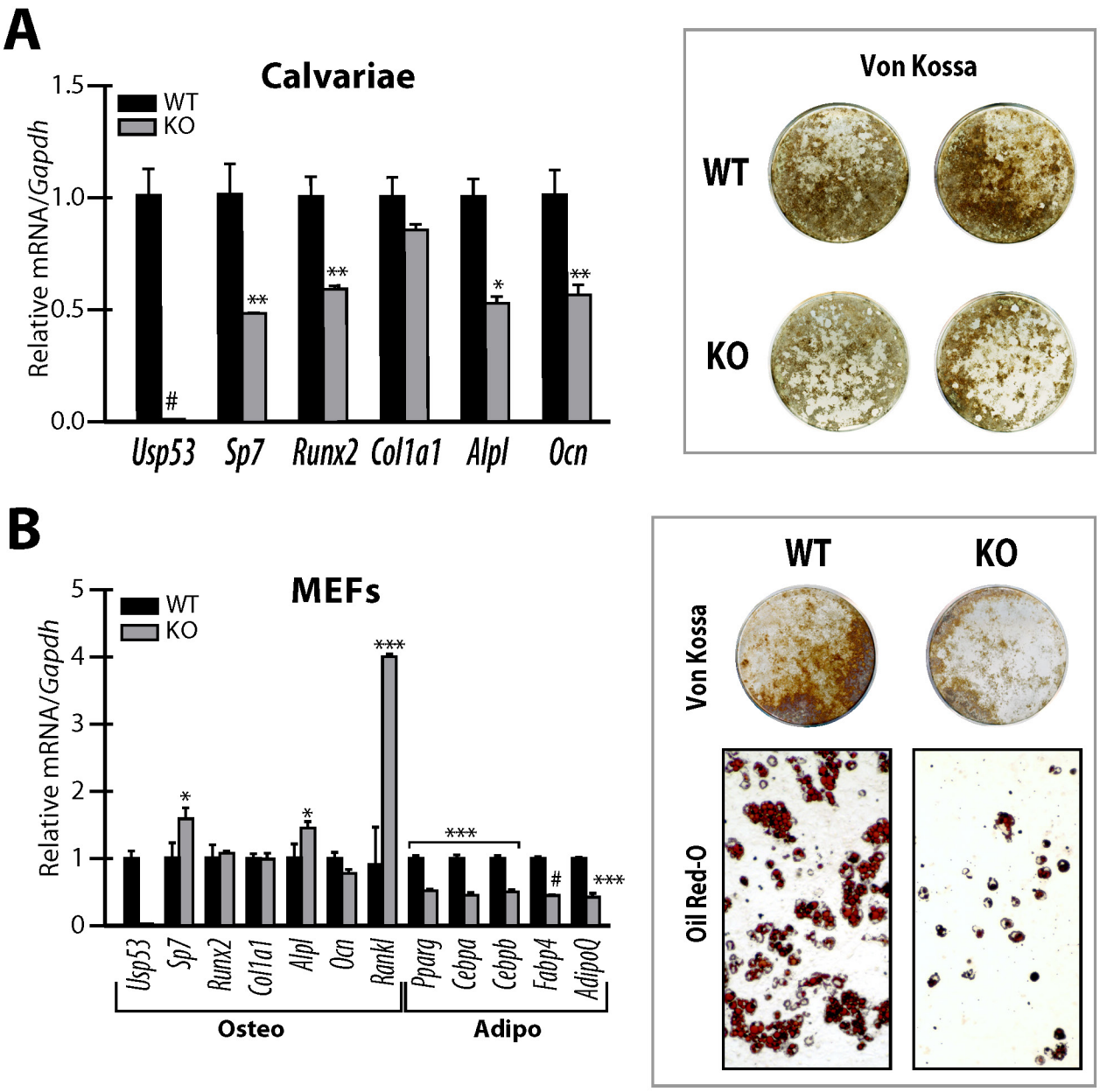
A
Calvariae
WT
KO
Relative mRNA/Gapdh
1.5
1.0
0.5
0.0
#
**
**
*
**
Usp53
Sp7
Runx2
Col1a1
Alpl
Ocn
Von Kossa
WT
KO
B
MEFs
WT
KO
Relative mRNA/Gapdh
5
4
3
2
1
0
*
*
***
***
#
***
Usp53
Sp7
Runx2
Col1a1
Alpl
Ocn
Rankl
Pparg
Cebpa
Cebpb
Fabp4
AdipoQ
Osteo
Adipo
WT
KO
Von Kossa
Oil Red-O

Supplementary Figure 5.2 *Usp53* inactivation inhibits osteogenic and adipogenic differentiation of primary osteoblasts and embryonic fibroblasts

A, WT and KO calvarial cells were cultured in inducing osteogenic (Osteo) conditions for 10 days and analyzed by RT-qPCR analysis for expression of osteoblast-selective genes and Von Kossa staining for mineral deposition (right, top). B, WT and KO MEFs were cultured in inducing osteogenic (Osteo) conditions or adipogenic (Adipo) for 12 days and analyzed by RT-qPCR analysis for expression of osteoblast-selective genes and adipocyte-selective genes, Von Kossa staining for mineral deposition (B, right top), and oil red O staining for lipid production (B, right bottom). Results are normalized to *Gapdh* expression and are given as means ± SD. *, $P < 0.05$; **, $P < 0.01$; ***, $P < 0.001$; #, $P<0.0001$; unpaired *t*-test.

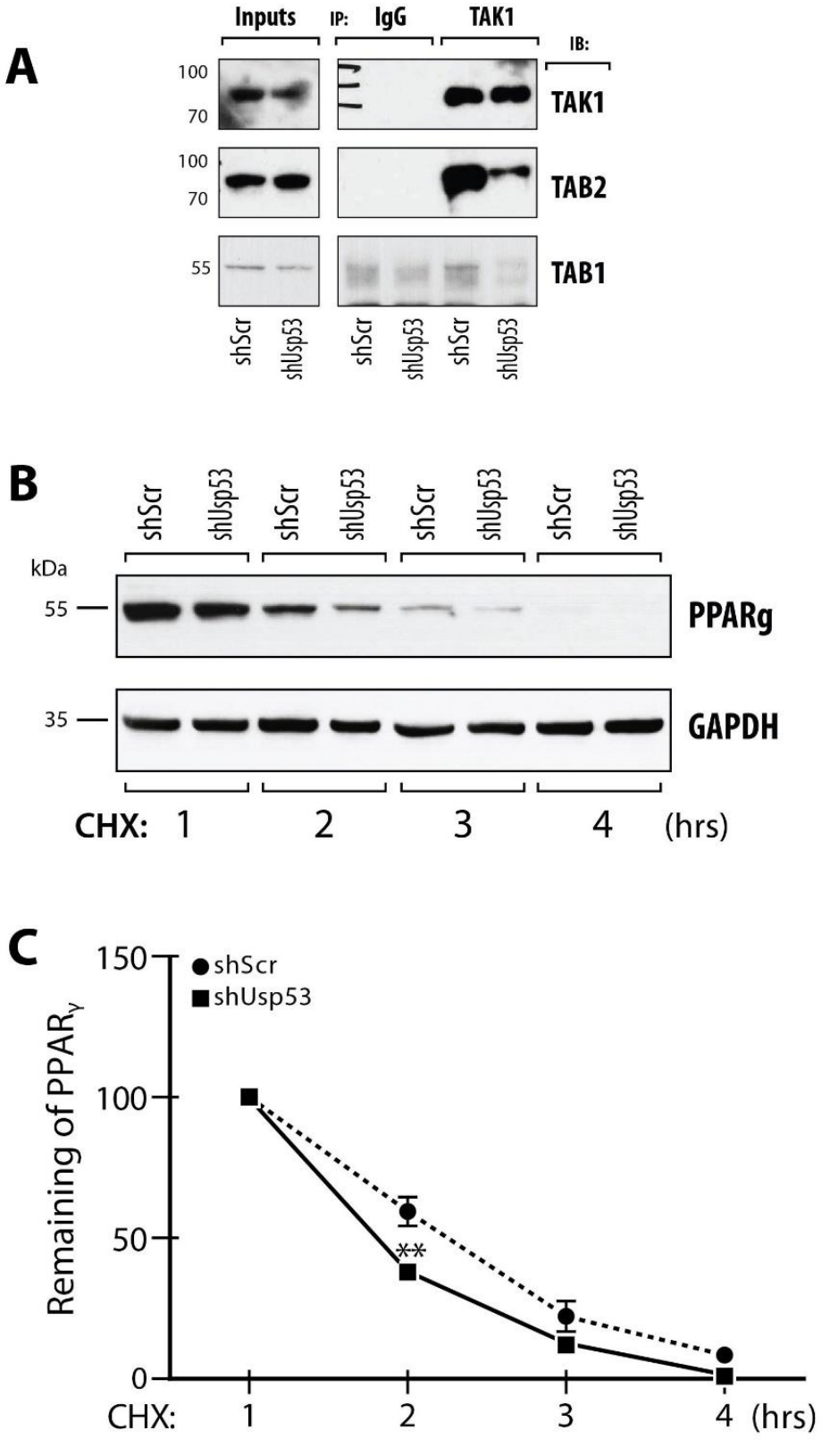
A
Inputs
IP:
IgG
TAK1
IB:
100
70
TAK1
100
70
TAB2
55
TAB1
shScr
shUsp53
shScr
shUsp53
shScr
shUsp53
B
shScr
shUsp53
shScr
shUsp53
shScr
shUsp53
shScr
shUsp53
kDa
55
PPARg
35
GAPDH
CHX: 1 2 3 4 (hrs)
C
150
100
50
0
shScr
shUsp53
Remaining of PPARγ
**
CHX: 1 2 3 4 (hrs)

Supplementary Figure 5.3 USP53 interacts with the TAK1/TAB1/TAB2 complex in bipotential ST2 cells and impacts PPARγ stability

A, Assessing the assembly of the TAK1/TAB1/TAB2 complex in ST2 cells. ST2 cells were stably-infected with shScr and shUsp53 lentiviral vectors. Endogenous TAK1 proteins were immunoprecipitated in shScr and shUsp53-infected ST2 cells and interacting endogenous partners were immunoblotted using specific antibodies. IgGs were used as controls for IPs. B, Cycloheximide (CHX) chase assay to assess PPARγ protein stability in shScr and shUsp53-infected ST2 cells. GAPDH was used as a loading control. C, Quantification of the remaining PPARγ protein amounts (%) through CHX chase assay in ST2 cells. **, $P < 0.01$; unpaired *t*-test.

Number	Identified proteins	Accession Number	Molecular Weight	T-Test (p-value)	Flag-USP53 (R1)	Flag-USP53 (R2)	Flag-GFP (R1)	Flag-GFP (R2)	Quantitative Profile
1	Eukaryotic translation initiation factor 4B OS=Homo sapiens GN=EIF4B PE=1 SV=2	IF4B_HUMAN	69 kDa	< 0.00010	109	99	0	0	GFP low, USP53 high
2	RNA-binding protein 10 OS=Homo sapiens GN=RBM10 PE=1 SV=3	RBM10_HUMAN	104 kDa	0.00086	50	43	0	0	GFP low, USP53 high
3	Tight junction protein ZO-2 OS=Homo sapiens GN=TJP2 PE=1 SV=2	ZO2_HUMAN	134 kDa	0.0012	47	40	0	0	GFP low, USP53 high
4	Crk-like protein OS=Homo sapiens GN=CRKL PE=1 SV=1	CRKL_HUMAN	34 kDa	0.0037	31	25	0	0	GFP low, USP53 high
5	Protein arginine N-methyltransferase 5 OS=Homo sapiens GN=PRMT5 PE=1 SV=4	ANM5_HUMAN	73 kDa	< 0.00010	24	22	0	0	GFP low, USP53 high
6	Cluster of Protein phosphatase 1B OS=Homo sapiens GN=PPM1B PE=1 SV=1 (PPM1B_HUMAN)	PPM1B_HUMAN [2]	53 kDa	0.00011	29	27	0	0	GFP low, USP53 high
7	Bcl-2-associated transcription factor 1 OS=Homo sapiens GN=BCLAF1 PE=1 SV=2	BCLF1_HUMAN	106 kDa	< 0.00010	14	13	0	0	GFP low, USP53 high
8	Methylosome protein 50 OS=Homo sapiens GN=WDR77 PE=1 SV=1	MEP50_HUMAN	37 kDa	0.0021	20	20	0	0	GFP low, USP53 high
9	Serine/threonine-protein kinase 38 OS=Homo sapiens GN=STK38 PE=1 SV=1	STK38_HUMAN	54 kDa	0.0007	26	25	0	0	GFP low, USP53 high
10	Uncharacterized protein C11orf84 OS=Homo sapiens GN=C11orf84 PE=1 SV=3	CK084_HUMAN	41 kDa	< 0.00010	12	11	0	0	GFP low, USP53 high
11	Thyroid hormone receptor-associated protein 3 OS=Homo sapiens GN=THRAP3 PE=1 SV=2	TR150_HUMAN	109 kDa	0.0042	15	12	0	0	GFP low, USP53 high
12	Methylosome subunit pICln OS=Homo sapiens GN=CLNS1A PE=1 SV=1	ICLN_HUMAN	26 kDa	0.0021	13	13	0	0	GFP low, USP53 high
13	Spindlin-1 OS=Homo sapiens GN=SPIN1 PE=1 SV=3	SPIN1_HUMAN	30 kDa	< 0.00010	11	10	0	0	GFP low, USP53 high
14	Serine/threonine-protein phosphatase 2A 65 kDa regulatory subunit A alpha isoform OS=Homo sapiens GN=PPP2R1A PE=1 SV=4	2AAA_HUMAN	65 kDa	0.036	13	8	0	0	GFP low, USP53 high
15	Growth factor receptor-bound protein 2 OS=Homo sapiens GN=GRB2 PE=1 SV=1	GRB2_HUMAN	25 kDa	0.0021	5	5	0	0	GFP low, USP53 high
16	6-phosphofructo-2-kinase/fructose-2,6-bisphosphatase 3 OS=Homo sapiens GN=PFKFB3 PE=1 SV=1	F263_HUMAN	60 kDa	0.0021	7	7	0	0	GFP low, USP53 high
17	OTU domain-containing protein 4 OS=Homo sapiens GN=OTUD4 PE=1 SV=4	OTUD4_HUMAN	124 kDa	0.0094	8	6	0	0	GFP low, USP53 high
18	TGF-beta-activated kinase 1 and MAP3K7-binding protein 1 OS=Homo sapiens GN=TAB1 PE=1 SV=1	TAB1_HUMAN	55 kDa	0.0021	7	7	0	0	GFP low, USP53 high
19	Cluster of Probable ubiquitin carboxyl-terminal hydrolase FAF-X OS=Homo sapiens GN=USP9X PE=1 SV=3 (USP9X_HUMAN)	USP9X_HUMAN [2]	292 kDa	0.002	6	5	0	0	GFP low, USP53 high
20	Calmodulin-regulated spectrin-associated protein 3 OS=Homo sapiens GN=CAMSAP3 PE=1 SV=2	CAMP3_HUMAN	135 kDa	0.033	8	5	0	0	GFP low, USP53 high
21	Tyrosine-protein kinase JAK1 OS=Homo sapiens GN=JAK1 PE=1 SV=2	JAK1_HUMAN	133 kDa	0.0021	9	9	0	0	GFP low, USP53 high
22	NK-tumor recognition protein OS=Homo sapiens GN=NKTR PE=1 SV=2	NKTR_HUMAN	166 kDa	0.014	7	5	0	0	GFP low, USP53 high
23	Influenza virus NS1A-binding protein OS=Homo sapiens GN=IVNS1ABP PE=1 SV=3	NS1BP_HUMAN	72 kDa	0.0021	4	4	0	0	GFP low, USP53 high
24	Serine/threonine-protein kinase 38-like OS=Homo sapiens GN=STK38L PE=1 SV=3	ST38L_HUMAN	54 kDa	< 0.00010	13	12	0	0	GFP low, USP53 high
25	TGF-beta-activated kinase 1 and MAP3K7-binding protein 2 OS=Homo sapiens GN=TAB2 PE=1 SV=1	TAB2_HUMAN	76 kDa	0.0021	6	6	0	0	GFP low, USP53 high
26	Trinucleotide repeat-containing gene 6B protein OS=Homo sapiens GN=TNRC6B PE=1 SV=4	TNR6B_HUMAN	194 kDa	0.0021	3	3	0	0	GFP low, USP53 high
27	U4/U6 small nuclear ribonucleoprotein Prp31 OS=Homo sapiens GN=PRPF31 PE=1 SV=2	PRP31_HUMAN	55 kDa	0.0021	5	5	0	0	GFP low, USP53 high
28	Fragile X mental retardation syndrome-related protein 1 OS=Homo sapiens GN=FXR1 PE=1 SV=3	FXR1_HUMAN	70 kDa	0.0021	6	6	0	0	GFP low, USP53 high
29	Rabankyrin-5 OS=Homo sapiens GN=ANKFY1 PE=1 SV=2	ANFY1_HUMAN	128 kDa	0.04	5	3	0	0	GFP low, USP53 high
30	Myotubularin-related protein 14 OS=Homo sapiens GN=MTMR14 PE=1 SV=2	MTMRE_HUMAN	72 kDa	0.0021	5	5	0	0	GFP low, USP53 high
31	Mitogen-activated protein kinase kinase kinase 7 OS=Homo sapiens GN=MAP3K7 PE=1 SV=1	M3K7_HUMAN	67 kDa	0.0021	4	4	0	0	GFP low, USP53 high
32	Serine/arginine repetitive matrix protein 2 OS=Homo sapiens GN=SRRM2 PE=1 SV=2	SRRM2_HUMAN	300 kDa	0.0021	3	3	0	0	GFP low, USP53 high
33	Serine/threonine-protein phosphatase 2A catalytic subunit alpha isoform OS=Homo sapiens GN=PPP2CA PE=1 SV=1	PP2AA_HUMAN	36 kDa	0.076	2	1	0	0	[]
34	Insulin-degrading enzyme OS=Homo sapiens GN=IDE PE=1 SV=4	IDE_HUMAN	118 kDa	0.0021	3	3	0	0	GFP low, USP53 high
35	SLAIN motif-containing protein 2 OS=Homo sapiens GN=SLAIN2 PE=1 SV=2	SLAI2_HUMAN	63 kDa	0.076	2	1	0	0	[]
36	Ubiquitin carboxyl-terminal hydrolase 15 OS=Homo sapiens GN=USP15 PE=1 SV=3	UBP15_HUMAN	112 kDa	0.0021	2	2	0	0	GFP low, USP53 high
37	Fragile X mental retardation protein 1 OS=Homo sapiens GN=FMR1 PE=1 SV=1	FMR1_HUMAN	71 kDa	0.0021	3	3	0	0	GFP low, USP53 high
38	Serine/threonine-protein phosphatase PGAM5, mitochondrial OS=Homo sapiens GN=PGAM5 PE=1 SV=2	PGAM5_HUMAN	32 kDa	0.076	2	1	0	0	[]
39	DNA damage-binding protein 1 OS=Homo sapiens GN=DDB1 PE=1 SV=1	DDB1_HUMAN	127 kDa	0.0021	2	2	0	0	GFP low, USP53 high
40	F-box only protein 3 OS=Homo sapiens GN=FBXO3 PE=1 SV=3	FBX3_HUMAN	55 kDa	0.0021	2	2	0	0	GFP low, USP53 high
41	Protein LSM14 homolog A OS=Homo sapiens GN=LSM14A PE=1 SV=3	LS14A_HUMAN	51 kDa	0.0021	2	2	0	0	GFP low, USP53 high
42	Serine/threonine-protein kinase RIO1 OS=Homo sapiens GN=RIOK1 PE=1 SV=2	RIOK1_HUMAN	66 kDa	0.0021	2	2	0	0	GFP low, USP53 high
43	Low molecular weight phosphotyrosine protein phosphatase OS=Homo sapiens GN=ACP1 PE=1 SV=3	PPAC_HUMAN	18 kDa	0.0021	2	2	0	0	GFP low, USP53 high
44	Cleavage and polyadenylation specificity factor subunit 5 OS=Homo sapiens GN=NUDT21 PE=1 SV=1	CPSF5_HUMAN	26 kDa	0.0021	2	2	0	0	GFP low, USP53 high
45	40S ribosomal protein S28 OS=Homo sapiens GN=RPS28 PE=1 SV=1	RS28_HUMAN	8 kDa	0.0021	2	2	0	0	GFP low, USP53 high
46	Mitochondrial import inner membrane translocase subunit TIM50 OS=Homo sapiens GN=TIMM50 PE=1 SV=2	TIM50_HUMAN	40 kDa	0.42	2	0	0	0	[]

Supplementary Table 5. 1 Mass Spectroscopy data showing USP53 interactants in HEK-293T cells.

Gene	Taqman
Nfil3	Mm00600292_s1
Creb1	Mm00501607
Dlx5	Mm00438430
Usp53	Mm00476778-m1
Sp7	Mm00504574-m1
Runx2	Mm00501578
Col1α1	Mm00801666_g1
Alpl	Mm00475834-m1
Bglap2	AIWR1XJ
Tnfsf11	Mm00441906_m1
Tnfrsf11b	Mm00435454_m1
Tnfrsf11a	Mm00437132_m1
Nfatc1	Mm01265944_m1
Ctsk	Mm00484039_m1
Acp5	Mm00475698_m1
Pparg2	Mm00440940-m1
Cebpα	Mm00514283-s1
Cebpβ	Mm00843434-s1
Fabp4	Mm00445878-m1
AdipoQ	Mm00456425_m1
Ucp1	Mm01244861_m1
Gapdh	Mm99999915-g1
Tbp	Mm01277042_m1
Dmp1	Mm01208363_m1
Sost	Mm00470479_m1
Phex	Mm00448119_m1
Fgf23	Mm00445621_m1

Supplementary Table 5. 2 Taqman probes used in this study.

Chapter VI : DISCUSSION

The data presented in the previous chapters are an outcome of hypotheses and research strategies implemented to identify and characterize novel targets of PTH signaling in osteoblast cells. Genome-wide investigation using ChIP-Seq against NACA and RNA-Seq in PTH(1-34)-treated osteoblasts paved the way for further characterization of the PTH-NACA pathway and its physiological significance. The PTH-signaling umbrella shelters the two identified target genes *Nfil3* and *Usp53*, through the regulation of NACA in osteoblasts.

6.1. *Nfil3*: a Déjà-vu PTH target with distinct function

We have previously shown that the PTH-Gαs-PKA-NACA signaling axis is physiologically relevant, as its impairment reduces bone mass and increases osteocyte number in mice (197). So far, we have fully characterized two transcriptional targets of NACA in osteoblasts, *Bglap2* (189) and *Lrp6* (192). Our recent work on *Lrp6* regulation suggested a feed-forward mechanism that increases the expression of the LRP6 co-receptor, thus amplifying PTH responses in osteoblasts (192). The same unbiased strategy has identified *Nfil3* as a target of NACA following its activation by PTH in osteoblasts. Here, we show that at least in part, *Nfil3* transcription is regulated by CREB and requires the presence of NACA. We also show that *Nfil3* impacts osteoblast and osteocyte gene expression in a distinct manner during differentiation.

Nfil3, also known as E4BP4, is a basic leucine zipper transcription factor, initially identified through its ability to bind and repress viral promoter sequences (200, 203). It has been implicated in diverse processes regulating immune cell function (201, 204-206, 245), circadian rhythm oscillations (202, 207), cell survival versus apoptosis (205, 208), and anti-inflammatory responses (202). PTH, PGE2, and forskolin are known to activate *Nfil3* expression (209, 210). Rapid induction of *Nfil3* can also be achieved by the direct binding of the glucocorticoid receptor (GR) to the *Nfil3* gene distal promoter in thymocytes (211). Our RNA-Seq data in MC3T3-E1 cells and gene expression monitoring of PTH-treated primary osteoblasts confirm the rapid induction of *Nfil3* following PTH treatment, as was reported previously (209, 210). This induction by PTH was shown to require the activation of PKA in osteoblasts (209). However, a complete mechanism of *Nfil3* transcriptional regulation is still missing.

We have previously shown that PTH stimulates the PKA-dependent phosphorylation of NACA on residue Serine 99 to provoke its import into the nucleus (197). The ChIP-Seq data reported herein show that NACA binds to the *Nfil3* gene proximal promoter following PTH

treatment. Our results support a model in which regulation of *Nfil3* expression by PTH requires phosphorylation of NACA which accumulates at the promoter after receiving the stimulus, a mechanism analogous to what we reported for *Bglap2* and *Lrp6* promoter activity (192, 197).

In the nucleus of osteoblast cells, NACA interacts with bZIP family transcription factors and potentiates their activity. NACA enhances AP-1 transcriptional activity by binding to cJUN homodimers and stabilizing their interaction with chromatin (189, 190, 237). It can also potentiate the activity of JUND on the *Lrp6* promoter (192). We did not observe any stimulation of *Nfil3* transcription by cJUN or JUND, alone or in combination with NACA (Supplementary Figure 3.1). A previous study has shown that Nfil3 gene expression is regulated by the cAMP-PKA-CREB pathway in primary adult dorsal root ganglion neurons and that CREB binds the promoter after a sciatic nerve crush (213). Genome-wide promoter binding studies did not identify *Nfil3* as a CREB regulated target in PC12, HEK293, or IDG-SW3 cells (246-248). However, our data show that CREB stimulates *Nfil3* transcription and that this activation requires NACA. Despite extensive efforts using several methods, we were not able to detect any physical interaction between CREB and NACA in HEK293 or MC3T3-E1 cells, at steady state or in Forskolin-treated cultures (e.g. Supplementary Figure 3.1 C), even when Jun family members were co-expressed (data not shown). We cannot exclude that the failure was technical. Alternatively, it is possible that CREB heterodimerizes with an as yet unidentified bZIP transcription factor to bridge its interaction with NACA and maintain the stability of the transcriptional regulatory complex to the *Nfil3* promoter.

Our study focused on characterizing the transcriptional regulation of the proximal promoter region (<1Kb) of *Nfil3*. NACA and CREB bind to proximal binding hotspots (ones close to the nearest transcription start site (TSS)) of the *Nfil3* promoter. Proximal binding of transcription factors is conserved and shared across different tissues (207). Consequently, it is likely that NACA and CREB regulate the proximal promoter region of *Nfil3* in a similar manner in osteocytes.

NFIL3 acts as transcriptional regulator that recognizes and binds to the E4BP4 response element (EBPRE): 5'-[GA]TTA[CT]GTAA[CT]3'. The EBPRE consensus sequence resembles the cAMP response element (CRE; 5'-TGACGTCA-3') bound by CREB. NFIL3 was characterized as a master transcriptional repressor, shown to repress neuronal CREB targets

(213), PTH-regulated Cox-2 promoter activity (210), and osteoblast gene transcription (210, 212). Our knockdown data in MC3T3-E1 cells is consistent with previously published data highlighting the repressive role of *Nfil3* in osteoblasts.

It appeared counter-intuitive that the induction of the expression of an osteoblastic transcriptional repressor could contribute to the mechanisms propagating the anabolic effect of PTH. However, the knockdown of *Nfil3* in IDG-SW3 osteocytic cells inhibited the expression of early and late osteocyte markers, suggesting that in osteocytes, NFIL3 acts as a positive regulator of gene expression. This suggests that the PTH-induced, NACA/CREB-dependent induction of *Nfil3* expression in osteocytes could be involved in the iPTH anabolic effect. How does NFIL3 convert from a repressor to an activator of gene transcription in closely related cell types? Even though both osteoblasts and osteocytes originate from the same precursor, the gene expression profiles of the two cell populations are distinct. St. John et al. (249) have reported substantial differences in the epigenetic profile of osteoblasts and osteocytes. *Sp7* and *Pth1r* are two examples of highly distinct epigenetic loci in the two cell populations (249). It can be postulated that differential epigenetic histone marks modulate the accessibility of NFIL3 to target promoters or enhancers in osteoblasts vs. osteocytes, thus providing an explanation for the distinct role of the transcription factor in the two cell populations. Alternatively, post-translational modification of the protein could impact function, either directly or through interaction with partner molecules. It has been reported that phosphorylation of NFIL3, or the loss of site-specific SUMOylation, increase its transcriptional activity and cause NFIL3 to exhibit either more repressive or more stimulating activity depending on the target promoter. One example is the upregulation of *Notch1* by NFIL3 SUMOylation- or phosphorylation mutants in natural killer cells (250).

Our study describes a mechanism for *Nfil3* transcriptional regulation downstream of the PTH-NACA signaling pathway. It also highlights a distinct role for *Nfil3* in the control of osteoblast vs. osteocyte gene expression.

6.2. *Usp53*: *In vitro* characterization

In addition to *Lrp6* (192) and *Nfil3*, we have added *Usp53* to the list of target genes regulated by the PTH-NACA pathway in osteoblasts. This finding was significant as the literature lacks any characterization of *Usp53* regulation or function in any tissue. Moreover, the most frequent genetic changes associated with Cantu syndrome, i.e. activating mutations of components of KATP channels (251, 252), do not readily explain the bone abnormalities associated with the most severe manifestations of the condition. We reviewed other reported mutations in patients with severe phenotypes and were intrigued by a patient who had more than 3 copies of *USP53* genomic DNA in her genome and suffered, in addition to hypertrichosis and cardiomegaly, from several bone abnormalities and severe obesity (BMI>40) (219). The phenotypic manifestation of this genomic aberration as well as the identification of *Usp53* as a target of the PTH-NACA pathway led us to investigate the transcriptional regulation of *Usp53* and assess whether *Usp53* may have a function in mesenchymal cell lineage specification.

Little is known about the upstream signaling regulating *Usp53* expression. One study has reported the induction of *USP53* in human bone marrow MSCs when treated with BMP-2 and Wnt3a together (253). This is the first report demonstrating the regulation of *Usp53* by PTH signaling. The ChIP-Seq data reported herein show that PTH-activated NACA was recruited to the proximal promoter region of *Usp53*. The same regulatory model has been previously reported for *Bglap2*, *Lrp6*, and *Nfil3* promoters in osteoblasts highlighting their functions in fine-tuning PTH signaling (in the case of *Lrp6*) or modulating osteoblast and osteocyte differentiation and function (for *Bglap2* and *Nfil3*) (197, 254) (chapter **III**). It is yet to be determined whether the PTH-induction of *Usp53* in osteoblasts dictates an osteoanabolic or osteocatabolic effect on bone.

Lessons learnt from different promoters regulated by the PTH-NACA pathway helped uncover the missing pieces in the *Usp53* regulatory scheme. We have previously shown that NACA engages with bZIP family transcription factors and potentiates their activity. cJUN and JUND are two partners of NACA regulating the expression of the *Bglap2* and *Lrp6* promoters, respectively. In addition, we have recently characterized the transcriptional regulation of the *Nfil3* promoter by both NACA and CREB in osteoblasts (chapter 3). Our data herein suggest that NACA is indispensable for *Usp53* promoter activity, its response to PTH, and its full activation

by the cJUN-CREB complex. In this respect, it is plausible to hypothesize that cJUN and CREB heterodimerize (255) and interact with NACA to achieve the optimal potentiation of the *Usp53* promoter. The cJUN partner of the heterodimer would mediate the interaction of the dimer with NACA, considering that we could not detect any physical contacts between NACA and CREB.

USP53 has been reported to be expressed in skeletal muscle, hair follicles, and cardiac muscle (219). We have further detected its expression in bone tissue (calvaria and tibia) and adipose tissue (white fat and brown fat). The prevalence of the full-length isoform is most likely related to its function in those tissues.

We provide evidence that USP53 is involved in mesenchymal cell lineage-making decisions. We show that the knockdown of *Usp53* in ST2 stromal cells and BMSCs enhances osteogenesis and inhibits adipogenesis, both *in vitro* and *in vivo*. Osteoblasts and adipocytes originate from a common mesenchymal precursor whose fate is regulated by critical signaling pathways and key transcription factors (256). Commitment to a lineage appears to be mutually exclusive, and a number of studies have shown that pathways that induce adipogenesis inhibit osteogenesis, and vice-versa.

Since increased copy number (and presumably increased expression) was reported in the patient with multiple bone abnormalities, we first attempted overexpression strategies by transient transfection or infection with constitutive or inducible *Usp53* expression vectors. In all cases, mesenchymal cells did not survive the addition of extraneous *Usp53* coding sequence (data not shown). When *Usp53* expression was decreased using shRNA-mediated knockdown, we measured a marked upregulation of early- and late-stage osteoblast differentiation markers and a concomitant inhibition of the expression of early and late adipogenic markers. The increase in osteogenic marker expression was accompanied by enhanced ability to secrete and mineralize the extracellular matrix. Similar results were obtained by knocking down *Usp53* in committed MC3T3-E1 osteoblastic cells. Thus, the reduction of *Usp53* expression affects differentiation and mineralization in bipotential mesenchymal cells as well as after mesenchymal progenitors have committed to the osteoblast fate.

This is the first report characterizing the regulation and function of *Usp53 in vitro*. In summary, we show that *Usp53* expression is induced by the PTH-activated NACA axis in osteoblasts. We also offer a mechanism involving the NACA-cJUN-CREB trio regulating *Usp53* transcription. Our data strongly indicates that *Usp53* regulates the lineage fate of mesenchymal cells by enhancing osteoblastogenesis and inhibiting adipogenesis. At the pathological level, increased marrow fat content is observed in bone loss conditions such as age-related osteoporosis (257-259). It will prove interesting to inactivate *Usp53* in mesenchymal precursors *in vivo* and uncover the molecular mechanism by which USP53 alters mesenchymal differentiation.

6.3. *Usp53*: a master developmental regulator

The broad spectrum of developmental defects observed in multiple patients carrying *USP53* variants is fascinating. Our previous work focusing on PTH signaling identified *Usp53* as a responsive gene potentially involved in the anabolic effect of PTH in osteoblasts. Also, manipulating *Usp53* dosage in bipotential mesenchymal precursors, by knockdown strategies, favored osteogenesis over adipogenesis (chapter V). The link between *USP53*-associated pathologies in skeletal tissues and our findings provided a window to investigate the developmental function of *Usp53* in mice. We here show that the global inactivation of *Usp53* causes significant abnormalities in bone and adipose tissues. The constellation of skeletal defects in *Usp53* null mice are due to a direct role for USP53 in commitment and lineage differentiation of mesenchymal progenitors. Our data also indicates an indirect effect for *Usp53* ablation on osteoclastogenesis and more broadly on the differentiation of other tissues of mesenchymal origin.

The resultant skeletal alterations due to *Usp53* ablation harmonize with those associated with the duplication of *USP53* genomic locus in the human Cantu syndrome study (219) and can be linked to the role of USP53 in regulating mesenchymal lineage selection. The bone abnormalities reported in the Cantu syndrome patient include rib synostosis and scoliosis (219), mimicking the ones reported in our study and supporting a role for *Usp53* in inhibiting osteoblast terminal differentiation and matrix mineralization. Though it would appear counter-intuitive that carrying 3 genomic DNA copies of *USP53* in humans and depleting *Usp53* in mice will lead to the same phenotypic outcome. This can be explained by the differences between the human

(Q70EK8) and the mouse (P15975) protein sequence (72%), that may lead to different protein interactions and function in each specie. Besides, it is unknown whether this patient suffered other unreported defects in bone development that parallel the low bone mass phenotype caused by increased osteoclastogenesis in *Usp53* null mice. Moreover, the low bone mass accompanied with increased marrow adiposity in *Usp53* null mice recapitulated the phenotype observed in osteoporotic patients (257-259). It is highly likely that increased RANKL production by marrow adipocytes contributes to the low bone mass phenotype in *Usp53* null mice. However, the molecular cues mediating the increase in marrow adiposity are unknown.

The severe obesity (BMI>40) reported in the Cantu patient appear to be linked to *USP53* duplication (219), as the inactivation of *Usp53* in mice blocks adipocyte lineage commitment and differentiation. This does not exclude the possibility that the severe obesity can be also related to the duplication of *FABP2* within the same locus (219).The distinct impact of *Usp53* inactivation on WAT versus BAT development can be linked to the different developmental origins of the two depots (116, 260, 261) and potentially due to depot-specific functions of *Usp53*. To be noted, the adipogenic induction of MEF and BMSC cultures by hormonal cocktails *in vitro* is a representation of white adipogenesis *in vivo*, not brown adipogenesis. Investigating depot-specific effects of *Usp53* depletion will require adipogenic induction of white and brown adipose cell precursors isolated from distinct adipose depots. In addition, the increased beiging of iWAT depots as well as the striking beiging of gWAT that has not been reported before, suggest a role for *Usp53* in mediating *Ucp1*-dependent beiging mechanisms. Alternatively, it can be a result of systemic regulation of adipose tissues and energy metabolism by other endocrine organs (96, 117). The contribution of *Usp53* to energy metabolism regulation will be addressed in future work.

Investigating non-skeletal alterations -the phenotypes not studied in detail- in *Usp53* null mice led to meaningful observations. The expression of *Usp53* was not restricted to skeletal tissues, as we have detected strong X-gal staining in the epidermis of the skin. Congenital hypertrichosis is a signature of Cantu syndrome and has been linked to *USP53* duplication (219). Kurban et al. have validated the expression of *USP53* in hair follicles and immunolocalized USP53 to the outer root sheath of the hair follicle in the skin (219). Hair follicle stem cells (HFSCs) are of mesenchymal origins and give rise to mesenchymal compartments of the hair follicle including the dermal sheath and dermal papilla (262, 263). Consequently, it is plausible

to hypothesize that *Usp53* ablation affects the mesenchymal stem cell niche of hair follicles, leading to arrested hair follicle cycling and potentially alopecia.

Another observation is the hypocalcemic phenotype of *Usp53* female null mice. One would anticipate that increased bone resorption will liberate more calcium into the circulation, but this was not the case. Interestingly, *USP53* has been identified as a causative gene of normal or low serum gamma-glutamyltransferase (GGT) cholestatic liver disease (220, 221); a condition by which the bile flow from the liver is reduced or blocked. In one family carrying a *USP53* homozygous truncating mutation, patients were diagnosed with cholestatic liver disease, unexplained hypocalcemia, and hearing loss (220). More recently, 10 pathogenic *USP53* variants have been reported in 7 patients with low GTT intrahepatic cholestasis (221). In the context of cholestasis, calcium signaling regulates bile flow from hepatocytes into cholangiocytes in the bile duct and calcium dysregulation is the main feature of the disease (264, 265). It is yet to be determined, whether the observed hypocalcemia is a secondary phenotype caused by liver cholestasis in *Usp53* null mice.

The proteomics data revealed a novel interaction of USP53 with the TAK1/TAB1/TAB2 complex. The lack of USP53 proteolysis activity suggests that its role may be mediated through protein-protein interactions. This is supported by the reported interaction of USP53 with ZO-1/TJP1 and ZO-2/TJP2 tight junction scaffolding proteins in polarized epithelial cells of the ear in mice (218). The interaction of USP53 with ZO-2/TJP2 protein has been further validated in our MS data. Since it is an inactive ubiquitin specific protease (218), USP53 could mediate TAK1/TAB1/TAB2 complex formation simply as a protein scaffold. However, USP18 has been shown to modulate TAK1-dependent signaling in a protease-independent manner by masking ubiquitination sites from further modification (266). This mechanism can be envisaged for USP53. Alternatively, USP53 may act as a decoy, protecting the TAK1/TAB1/TAB2 complex from other deubiquitinases. However, the possibility that USP53 has retained some catalytic activity as a deubiquitinase has recently been considered as one study showed that USP53 deubiquitinates FKBP1 in lung adenocarcinoma cell lines (267). To be noted that, while the MS data that we generated revealed interaction of USP53 with other deubiquitinases such as USP15, USP9X, and OTUD4, it did not show any interaction with ubiquitin E3 ligases (Supplementary Table 1). To further assess any involvement of USP53 in deubiquitination pathways, it would be

interesting to perform MS after enriching for ubiquitin moieties, either by overexpressing ubiquitin-expression vectors or by blocking the proteasomal degradation machinery.

Mutations in TAK1 has been associated with frontometaphyseal dysplasia (FMD) in humans (268). Moreover, mice with conditional deletion of TAK1 in cartilage exhibit severe chondrodysplasia, due to impaired BMP signaling (240, 242). As a component of several multi-protein complexes, TAK1 acts as an integrator of multiple stimuli, with outcomes depending on cell type and upstream signal (269). It has been shown to be an important regulator of TGFβ and BMP signaling, affecting both canonical Smad-dependent signaling (Smad1/5/8 and Smad 2/3) and non-canonical Smad-independent signaling (JNK/p38 mitogen-activated protein kinase (MAPK)) (240, 242). Osteoblastogenesis and adipogenesis are impacted through each signaling arm.

Our data shows that reduced expression of USP53 disrupted TAK1/TAB1/TAB2 complex formation. Consequently, we expected changes at the level of the responsiveness of downstream signaling including Smad or MAPK pathways. The phosphorylation of P38 and PPARγ stability are substantially reduced in the absence of *Usp53*, justifying disrupted adipogenic mesenchymal commitment and differentiation in different culture systems. This result is in line with studies showing that TAK1 and TAB1 play a critical role in BMP-mediated differentiation of mesenchymal cells (270). Besides, activation of p38, one of the downstream TAK1 signals, has been shown to be required for maintaining PPARγ protein stability (271). We also assessed changes in the phosphorylation of other signaling effectors including: Smad1/5/8, Smad2/3, JNK1/2, and ERK1/2 and all remained unaffected by the absence of *Usp53* (data not shown). Moreover, our data indicates that increased RANKL production by osteoblasts enhances osteoclastogenesis in *Usp53* null mice. Assessing the impact of *Usp53* ablation on pathways regulating *Rankl* transcription (272) in osteoblasts is crucial and may define a function for USP53 in *Rankl* regulation. Until this date, we have explored changes in phosphorylation of positive (gp130 cytokines) and negative (Wnts) regulators of *Rankl* expression and found no significant changes in the absence of *Usp53*. Currently, other pathways regulating *Rankl* expression are being investigated (90).

We have previously characterized the impact of *Usp53* knockdown on mesenchymal stem cell differentiation. *Usp53*-knockdown impaired adipogenic differentiation of ST2 cells and

BMSCs and enhanced osteogenic differentiation of ST2 and MC3T3-E1 cells (chapter 4). The adipogenic signaling arm was impaired *in vitro* and *in vivo* (data presented in chapters **IV** and **V**), regardless of the culture system used. However, the discrepancy between the *in vitro* and *in vivo* results regarding the regulation of osteoblast differentiation in the absence of *Usp53* is obvious. We assign this contradiction to multiple factors. One element is the difference in the timeline of depleting *Usp53*, as the *CMV-Cre* promoter is expressed during early embryogenesis, most likely before implantation. However, our *in vitro* characterization targeted *Usp53* in well-established mesenchymal cell lines or committed osteoblasts. Another factor is the *in vivo* system referred to in this comparison. A global deletion of *Usp53* may or may not dictate an osteoblast-specific effect for *Usp53* ablation, especially that *Usp53* is expressed in multiple tissues. Establishing an osteoblast-specific (*Ocn-Cre*) or mesenchyme-specific (*Prx1-Cre*) deletion of *Usp53* will offer a better model to define the function of *Usp53* during osteoblast differentiation *in vivo*.

In summary, this is the first report to characterize the expression and function of *Usp53* in mice. We have identified *Usp53* as a novel regulator of skeletal development and pointed to critical developmental functions in multiple organs. The global inactivation of *Usp53* in mice leads to low bone mass due to increased osteoclastogenesis and impaired adipogenesis. We show that *Usp53* regulates adipogenic commitment and differentiation of mesenchymal stem cells, osteoblast terminal differentiation, and *Rankl* expression. The underlying mechanism defining USP53 functions, at least in mesenchymal cells, involves the interaction with TAK1/TAB1/TAB2 complex affecting its assembly and signaling. These findings point to a complex network of pathways controlled by USP53, whose dysregulation contributes to human developmental diseases and abnormalities such as Cantu syndrome, cholestatic liver disease, and hearing loss.

6.4. *Nfil3* and *Usp53*: A masterpiece with broad Implications

The identification of *Nfil3* and *Usp53* as novel targets of the PTH-NACA axis in osteoblasts supports the physiological significance of the pathway in the skeleton. Initially, our laboratory has identified *Bglap2* and *Lrp6* as targets of the PTH-NACA pathway and this work adds *Nfil3* and *Usp53* as key players in the PTH signaling game. Our work can open the door for pharmacological intervention and help develop anabolic treatments for metabolic bone diseases, which may help increase bone mass and protect against bone fractures.

Besides, the functional characterization of *Usp53* broadens our basic understanding of bone and fat biology. Uncovering the biological multi-functions of *Usp53* during development is a scientific achievement. The phenotypic characterization of *Usp53* null mice uncovered different developmental aberrations in skeletal and non-skeletal tissues. The identified murine aberrations recapitulate the multiple abnormalities reported in patients carrying *USP53* variants. We believe that the remaining work to finalize chapter V is essential to put all the pieces of the puzzle together, as our data strongly suggest a role for *Usp53* in hearing and metabolic disorders, in addition to the studied skeletal defects. Study limitations and future goals will be discussed in the next chapter.

Chapter VII: CONCLUSIONS AND FUTURE DIRECTIONS

7.1 *Nfil3*: What is missing and what is next

7.1.1 Expanding the promoter study

Our work (**chapter III**) has demonstrated findings addressing specific questions about *Nfil3* transcriptional regulation and function in osteoblasts. The analysis of the *Nfil3* proximal promoter identified binding sites for NACA and CREB. Following PTH stimulation, we have validated the binding of NACA to the promoter by ChIP-PCR.

We are currently confirming the binding of CREB to the promoter, along with NACA, using ChIP-reChIP PCR assays.

Our study has focused on proximal promoter regions and ignored distal (>1kb upstream from the promoter) promoter binding of transcription factors. The binding of transcription factors to gene distal regions including enhancers is cell-type specific (207) and critical for gene expression regulation during differentiation. Consequently, examining distal regions of *Nfil3* promoter can expand our knowledge of the transcriptional regulation of the gene in osteoblasts vs. osteocytes. It can also uncover major differences in *Nfil3* regulation that can explain its distinct function in the two cell populations.

We can examine the DNA methylation profile of *Nfil3* in both cell populations using ChIP-Seq against active and repressive histone markers. Also, we can investigate the DNA methylation profile of major differentiation markers in both cell populations including *Pth1r* and *Sp7*; examples of highly distinct epigenetic loci in the two cell populations (206).

7.1.2 Exploring the functions of *Nfil3 in vivo*

Reviewing the literature, we could not find any study addressing the function of *Nfil3* during bone development *in vivo*. Future studies in our laboratory will focus on the generation and characterization of bone-specific knockout mouse models for *Nfil3*.

We will cross *Nfil3*-floxed mice to *Col1a1-Cre* or *Ocn-Cre* deleter strains to deplete *Nfil3* in osteoblasts and to *Dmp-1-Cre* deleter strain to delete the gene in osteocytes. The generation of these strains will serve two main objectives : 1. define the function of *Nfil3* in osteoblasts vs osteocytes during bone development and 2. investigate the impact of *Nfil3* ablation on iPTH anabolic responses in mice.

7.2 *Usp53*: A developmental regulator with yet more functions to be unraveled

7.2.1 *Usp53* and PTH anabolism

The second part of our study (**chapters IV and V**) highlighted the biological functions of *Usp53 in vitro* and *in vivo*. The phenotypic characterization of *Usp53* null mice has answered multiple questions focusing on *Usp53* contribution to skeletal development. We have previously indicated that *Usp53* expression is induced following PTH (1-34) treatment. However, it is unknown whether *Usp53* mediates the anabolic effect of PTH on bone *in vivo*.

For this aim, we will check the integrity of PTH responses in *Usp53* null mice by injecting PTH (1-34) intermittently. We anticipate that the anabolic effect of PTH on bone mass will be compromised in *Usp53* null mice as compared to wildtypes.

7.2.2 Mesenchyme-specific ablation of *Usp53*

We have shown that *Usp53* is a regulator of mesenchymal differentiation and highlighted the discrepancy between the *in vitro* and *in vivo* data discussed in chapters 4 and 5. To define the role of *Usp53* in regulating mesenchymal stem cell differentiation, we have generated *Usp53*-floxed mice and crossed it to the *Paired related homeobox 1-Cre (Prx1-Cre)* strain, which is active in the mesenchymal progenitors of the long bones. This work was done in parallel with the work done to generate and characterize *Usp53* null mice. Unfortunately, most of the mice (>50%) with the deletion (Cre-positive) died between embryonic and early postnatal developmental stages. We also faced some difficulties breeding those mice and further expanding the colony.

We have recently obtained a new mice line of the *Prx1-Cre* strain (B6N.Cg-Tg(Prrx1-cre)1Cjt/ErenJ) which will be crossed to *Usp53*-floxed mice and subsequently analyzed for bone and adipose tissue defects.

7.2.3 *Usp53*: The " Off- the record " phenotypes

The phenotypic characterization of *Usp53* null mice has fulfilled the main objectives of the study focusing on the contribution of *Usp53* to skeletal development. At the same time, it raised a couple of intriguing questions about its contribution to systemic regulation and developmental events of non-skeletal tissues.

7.2.3.1 *Usp53* null mice and hearing loss

Multiple studies have reported hearing loss in patients carrying *USP53* pathogenic mutations (220, 221). One study has characterized progressive hearing loss in mice carrying a missense mutation in the catalytic site of Usp53. The same study has suggested a mechanism of protein-protein interaction involving USP53 and tight junction proteins TJP1 and TJP2, underlying the hearing loss phenotype (218). Besides, our MS data have further confirmed the physical interaction between USP53 and TJP2.

We have assessed the hearing capabilities of *Usp53* null mice. We are currently analyzing the results of the auditory brain response (ABR) test of *Usp53* null mice at 6 and 8-weeks of age. We anticipate that knockout mice will exhibit severe hearing impairments, if not deafness, as compared to wildtype littermates. Hearing loss has been assessed at the McGill Auditory Sciences platform at the MUHC.

7.2.3.2 *Usp53* ablation and metabolic activity

The browning of white adipose tissues is one of the most intriguing phenotypic manifestations detected in *Usp53* null mice. This observation opens the door widely for a metabolic investigation assessing metabolic changes in *Usp53* null mice and the impact of *Usp53* inactivation on the systemic regulation of adipogenesis.

This will require extensive work assessing changes in glucose tolerance, insulin sensitivity, and circulating levels of osteocalcin hormone. Potentially, those results will either go into our main manuscript (**chapter V**) or in a separate study characterizing the contribution of *Usp53* to metabolic functions in mice.

7.2.3.3 *Usp53* and liver function

Multiple studies have reported liver cholestasis and hepatobiliary defects in patients carrying *USP53* pathogenic mutations (220, 221). To be noted that TJP2 pathogenic mutations are the main causative mutations of cholestatic liver disease in human and USP53 mutations generated a phenocopy of TJP2-associated liver defects (220, 221).

Assessing the impact of *Usp53* inactivation on liver function is important to interpret the hypocalcemic phenotype of *Usp53* null mice. This will also uncover the contribution of *Usp53* to

the developmental events of the liver and further explain the redundant effects of USP53 and TJP2 mutations on liver function.

Chapter VIII: REFERENCES

1. Robey PG, Boskey AL. The composition of bone. Primer on the metabolic bone diseases and disorders of mineral metabolism. 2009;7:32-8.
2. Feng X, McDonald JM. Disorders of Bone Remodeling. Annual Review of Pathology: Mechanisms of Disease. 2011;6(1):121-45.
3. Teti A. Bone Development: Overview of Bone Cells and Signaling. Current Osteoporosis Reports. 2011;9(4):264.
4. Pourquié O. Vertebrate Segmentation: From Cyclic Gene Networks to Scoliosis. Cell. 2011;145(5):650-63.
5. Almalki SG, Agrawal DK. Key transcription factors in the differentiation of mesenchymal stem cells. Differentiation; research in biological diversity. 2016;92(1-2):41-51.
6. Yang X, Matsuda K, Bialek P, Jacquot S, Masuoka HC, Schinke T, et al. ATF4 is a substrate of RSK2 and an essential regulator of osteoblast biology; implication for Coffin-Lowry Syndrome. Cell. 2004;117(3):387-98.
7. Dansranjavin T, Krehl S, Mueller T, Mueller LP, Schmoll HJ, Dammann RH. The role of promoter CpG methylation in the epigenetic control of stem cell related genes during differentiation. Cell cycle (Georgetown, Tex). 2009;8(6):916-24.
8. Meyer MB, Benkusky NA, Sen B, Rubin J, Pike JW. Epigenetic Plasticity Drives Adipogenic and Osteogenic Differentiation of Marrow-derived Mesenchymal Stem Cells. The Journal of biological chemistry. 2016;291(34):17829-47.
9. Ren J, Huang D, Li R, Wang W, Zhou C. Control of mesenchymal stem cell biology by histone modifications. Cell & bioscience. 2020;10:11.
10. Robling AG, Turner CH. Mechanical signaling for bone modeling and remodeling. Critical reviews in eukaryotic gene expression. 2009;19(4):319-38.
11. Klein-Nulend J, van Oers RF, Bakker AD, Bacabac RG. Bone cell mechanosensitivity, estrogen deficiency, and osteoporosis. Journal of biomechanics. 2015;48(5):855-65.
12. Bonewald LF. The amazing osteocyte. Journal of bone and mineral research : the official journal of the American Society for Bone and Mineral Research. 2011;26(2):229-38.
13. Dallas SL, Prideaux M, Bonewald LF. The osteocyte: an endocrine cell ... and more. Endocr Rev. 2013;34(5):658-90.

14. Paic F, Igwe JC, Nori R, Kronenberg MS, Franceschetti T, Harrington P, et al. Identification of differentially expressed genes between osteoblasts and osteocytes. Bone. 2009;45(4):682-92.
15. Woo SM, Rosser J, Dusevich V, Kalajzic I, Bonewald LF. Cell line IDG-SW3 replicates osteoblast-to-late-osteocyte differentiation in vitro and accelerates bone formation in vivo. Journal of bone and mineral research : the official journal of the American Society for Bone and Mineral Research. 2011;26(11):2634-46.
16. Barragan-Adjemian C, Nicolella D, Dusevich V, Dallas MR, Eick JD, Bonewald LF. Mechanism by which MLO-A5 late osteoblasts/early osteocytes mineralize in culture: similarities with mineralization of lamellar bone. Calcified tissue international. 2006;79(5):340-53.
17. Faul C, Amaral AP, Oskouei B, Hu MC, Sloan A, Isakova T, et al. FGF23 induces left ventricular hypertrophy. The Journal of clinical investigation. 2011;121(11):4393-408.
18. Feng JQ, Ward LM, Liu S, Lu Y, Xie Y, Yuan B, et al. Loss of DMP1 causes rickets and osteomalacia and identifies a role for osteocytes in mineral metabolism. Nature genetics. 2006;38(11):1310-5.
19. Quarles LD. Role of FGF23 in vitamin D and phosphate metabolism: implications in chronic kidney disease. Experimental cell research. 2012;318(9):1040-8.
20. Kamel MA, Picconi JL, Lara-Castillo N, Johnson ML. Activation of beta-catenin signaling in MLO-Y4 osteocytic cells versus 2T3 osteoblastic cells by fluid flow shear stress and PGE2: Implications for the study of mechanosensation in bone. Bone. 2010;47(5):872-81.
21. Kitase Y, Barragan L, Qing H, Kondoh S, Jiang JX, Johnson ML, et al. Mechanical induction of PGE2 in osteocytes blocks glucocorticoid-induced apoptosis through both the beta-catenin and PKA pathways. Journal of bone and mineral research : the official journal of the American Society for Bone and Mineral Research. 2010;25(12):2657-68.
22. Baron R, Kneissel M. WNT signaling in bone homeostasis and disease: from human mutations to treatments. Nature medicine. 2013;19(2):179-92.
23. Poole KE, van Bezooijen RL, Loveridge N, Hamersma H, Papapoulos SE, Lowik CW, et al. Sclerostin is a delayed secreted product of osteocytes that inhibits bone formation. FASEB journal : official publication of the Federation of American Societies for Experimental Biology. 2005;19(13):1842-4.

24. Robling AG, Bellido T, Turner CH. Mechanical stimulation in vivo reduces osteocyte expression of sclerostin. Journal of musculoskeletal & neuronal interactions. 2006;6(4):354.
25. Jahn K, Kelkar S, Zhao H, Xie Y, Tiede-Lewis LM, Dusevich V, et al. Osteocytes Acidify Their Microenvironment in Response to PTHrP In Vitro and in Lactating Mice In Vivo. Journal of bone and mineral research : the official journal of the American Society for Bone and Mineral Research. 2017;32(8):1761-72.
26. Qing H, Divieti Pajevic P, Barry K, Dusevich V, Wysolmerski J, Bonewald L. PTHR1 in osteocytes plays a major role in perilacunar remodeling through the activation of" osteoclastic" genes in osteocytes. Journal of bone and mineral research : the official journal of the American Society for Bone and Mineral Research. 2010;25(Suppl 1):S25.
27. Suda T, Takahashi N, Udagawa N, Jimi E, Gillespie MT, Martin TJ. Modulation of osteoclast differentiation and function by the new members of the tumor necrosis factor receptor and ligand families. Endocr Rev. 1999;20(3):345-57.
28. Ross FP, Teitelbaum SL. alphavbeta3 and macrophage colony-stimulating factor: partners in osteoclast biology. Immunological reviews. 2005;208:88-105.
29. Nakashima T, Hayashi M, Takayanagi H. New insights into osteoclastogenic signaling mechanisms. Trends in endocrinology and metabolism: TEM. 2012;23(11):582-90.
30. Theill LE, Boyle WJ, Penninger JM. RANK-L and RANK: T cells, bone loss, and mammalian evolution. Annual review of immunology. 2002;20:795-823.
31. Tsukasaki M, Hamada K, Okamoto K, Nagashima K, Terashima A, Komatsu N, et al. LOX Fails to Substitute for RANKL in Osteoclastogenesis. Journal of bone and mineral research : the official journal of the American Society for Bone and Mineral Research. 2017;32(3):434-9.
32. Takayanagi H, Kim S, Koga T, Nishina H, Isshiki M, Yoshida H, et al. Induction and activation of the transcription factor NFATc1 (NFAT2) integrate RANKL signaling in terminal differentiation of osteoclasts. Developmental cell. 2002;3(6):889-901.
33. Aliprantis AO, Ueki Y, Sulyanto R, Park A, Sigrist KS, Sharma SM, et al. NFATc1 in mice represses osteoprotegerin during osteoclastogenesis and dissociates systemic osteopenia from inflammation in cherubism. The Journal of clinical investigation. 2008;118(11):3775-89.
34. Asagiri M, Sato K, Usami T, Ochi S, Nishina H, Yoshida H, et al. Autoamplification of NFATc1 expression determines its essential role in bone homeostasis. The Journal of experimental medicine. 2005;202(9):1261-9.

35. Boyle WJ, Simonet WS, Lacey DL. Osteoclast differentiation and activation. Nature. 2003;423(6937):337-42.
36. Teitelbaum SL, Abu-Amer Y, Ross FP. Molecular mechanisms of bone resorption. Journal of cellular biochemistry. 1995;59(1):1-10.
37. Nakashima T, Hayashi M, Fukunaga T, Kurata K, Oh-Hora M, Feng JQ, et al. Evidence for osteocyte regulation of bone homeostasis through RANKL expression. Nature medicine. 2011;17(10):1231-4.
38. Xiong J, Onal M, Jilka RL, Weinstein RS, Manolagas SC, O'Brien CA. Matrix-embedded cells control osteoclast formation. Nature medicine. 2011;17(10):1235-41.
39. Fan Y, Hanai JI, Le PT, Bi R, Maridas D, DeMambro V, et al. Parathyroid Hormone Directs Bone Marrow Mesenchymal Cell Fate. Cell metabolism. 2017;25(3):661-72.
40. Takayanagi H. Osteoimmunology: shared mechanisms and crosstalk between the immune and bone systems. Nature reviews Immunology. 2007;7(4):292-304.
41. Takayanagi H. Osteoimmunology and the effects of the immune system on bone. Nature reviews Rheumatology. 2009;5(12):667-76.
42. Koga T, Inui M, Inoue K, Kim S, Suematsu A, Kobayashi E, et al. Costimulatory signals mediated by the ITAM motif cooperate with RANKL for bone homeostasis. Nature. 2004;428(6984):758-63.
43. Mocsai A, Humphrey MB, Van Ziffle JA, Hu Y, Burghardt A, Spusta SC, et al. The immunomodulatory adapter proteins DAP12 and Fc receptor gamma-chain (FcRgamma) regulate development of functional osteoclasts through the Syk tyrosine kinase. Proceedings of the National Academy of Sciences of the United States of America. 2004;101(16):6158-63.
44. Shinohara M, Koga T, Okamoto K, Sakaguchi S, Arai K, Yasuda H, et al. Tyrosine kinases Btk and Tec regulate osteoclast differentiation by linking RANK and ITAM signals. Cell. 2008;132(5):794-806.
45. Parfitt AM. Targeted and nontargeted bone remodeling: relationship to basic multicellular unit origination and progression. Bone. 2002;30(1):5-7.
46. Bonewald LF. The Role of the Osteocyte in Bone and Nonbone Disease. Endocrinology and metabolism clinics of North America. 2017;46(1):1-18.
47. Sims NA, Martin TJ. Osteoclasts Provide Coupling Signals to Osteoblast Lineage Cells Through Multiple Mechanisms. Annual Review of Physiology. 2020;82(1):507-29.

48. Langdahl B, Ferrari S, Dempster DW. Bone modeling and remodeling: potential as therapeutic targets for the treatment of osteoporosis. Therapeutic advances in musculoskeletal disease. 2016;8(6):225-35.
49. Kronenberg HM. Developmental regulation of the growth plate. Nature. 2003;423(6937):332-6.
50. Lefebvre V, Bhattaram P. Vertebrate skeletogenesis. Current topics in developmental biology. 2010;90:291-317.
51. Long F, Ornitz DM. Development of the endochondral skeleton. Cold Spring Harbor perspectives in biology. 2013;5(1):a008334.
52. Mackie EJ, Ahmed YA, Tatarczuch L, Chen KS, Mirams M. Endochondral ossification: how cartilage is converted into bone in the developing skeleton. The international journal of biochemistry & cell biology. 2008;40(1):46-62.
53. Mackie EJ, Tatarczuch L, Mirams M. The skeleton: a multi-functional complex organ: the growth plate chondrocyte and endochondral ossification. The Journal of endocrinology. 2011;211(2):109-21.
54. Karsenty G, Kronenberg HM, Settembre C. Genetic control of bone formation. Annual review of cell and developmental biology. 2009;25:629-48.
55. Aghajanian P, Mohan S. The art of building bone: emerging role of chondrocyte-to-osteoblast transdifferentiation in endochondral ossification. Bone research. 2018;6:19.
56. Iwata T, Chen L, Li C, Ovchinnikov DA, Behringer RR, Francomano CA, et al. A neonatal lethal mutation in FGFR3 uncouples proliferation and differentiation of growth plate chondrocytes in embryos. Human molecular genetics. 2000;9(11):1603-13.
57. Barna M, Niswander L. Visualization of cartilage formation: insight into cellular properties of skeletal progenitors and chondrodysplasia syndromes. Developmental cell. 2007;12(6):931-41.
58. Smits P, Li P, Mandel J, Zhang Z, Deng JM, Behringer RR, et al. The transcription factors L-Sox5 and Sox6 are essential for cartilage formation. Developmental cell. 2001;1(2):277-90.
59. Bi W, Deng JM, Zhang Z, Behringer RR, de Crombrugghe B. Sox9 is required for cartilage formation. Nature genetics. 1999;22(1):85-9.

60. Nakashima K, Zhou X, Kunkel G, Zhang Z, Deng JM, Behringer RR, et al. The novel zinc finger-containing transcription factor osterix is required for osteoblast differentiation and bone formation. Cell. 2002;108(1):17-29.
61. Arnold MA, Kim Y, Czubryt MP, Phan D, McAnally J, Qi X, et al. MEF2C transcription factor controls chondrocyte hypertrophy and bone development. Developmental cell. 2007;12(3):377-89.
62. Dy P, Wang W, Bhattaram P, Wang Q, Wang L, Ballock RT, et al. Sox9 directs hypertrophic maturation and blocks osteoblast differentiation of growth plate chondrocytes. Developmental cell. 2012;22(3):597-609.
63. Baffi MO, Slattery E, Sohn P, Moses HL, Chytil A, Serra R. Conditional deletion of the TGF-beta type II receptor in Col2a expressing cells results in defects in the axial skeleton without alterations in chondrocyte differentiation or embryonic development of long bones. Developmental biology. 2004;276(1):124-42.
64. Nomura M, Li E. Smad2 role in mesoderm formation, left-right patterning and craniofacial development. Nature. 1998;393(6687):786-90.
65. Spagnoli A, O'Rear L, Chandler RL, Granero-Molto F, Mortlock DP, Gorska AE, et al. TGF-beta signaling is essential for joint morphogenesis. The Journal of cell biology. 2007;177(6):1105-17.
66. Day TF, Guo X, Garrett-Beal L, Yang Y. Wnt/beta-catenin signaling in mesenchymal progenitors controls osteoblast and chondrocyte differentiation during vertebrate skeletogenesis. Developmental cell. 2005;8(5):739-50.
67. Dong Y, Jesse AM, Kohn A, Gunnell LM, Honjo T, Zuscik MJ, et al. RBPjkappa-dependent Notch signaling regulates mesenchymal progenitor cell proliferation and differentiation during skeletal development. Development (Cambridge, England). 2010;137(9):1461-71.
68. Hill TP, Spater D, Taketo MM, Birchmeier W, Hartmann C. Canonical Wnt/beta-catenin signaling prevents osteoblasts from differentiating into chondrocytes. Developmental cell. 2005;8(5):727-38.
69. James AW, Peault B. Perivascular Mesenchymal Progenitors for Bone Regeneration. Journal of orthopaedic research : official publication of the Orthopaedic Research Society. 2019;37(6):1221-8.

70. Yang L, Tsang KY, Tang HC, Chan D, Cheah KS. Hypertrophic chondrocytes can become osteoblasts and osteocytes in endochondral bone formation. Proceedings of the National Academy of Sciences of the United States of America. 2014;111(33):12097-102.
71. Zhou X, von der Mark K, Henry S, Norton W, Adams H, de Crombrugghe B. Chondrocytes transdifferentiate into osteoblasts in endochondral bone during development, postnatal growth and fracture healing in mice. PLoS genetics. 2014;10(12):e1004820.
72. Komori T. Roles of Runx2 in Skeletal Development. Advances in experimental medicine and biology. 2017;962:83-93.
73. Enomoto H, Enomoto-Iwamoto M, Iwamoto M, Nomura S, Himeno M, Kitamura Y, et al. Cbfa1 is a positive regulatory factor in chondrocyte maturation. The Journal of biological chemistry. 2000;275(12):8695-702.
74. Inada M, Yasui T, Nomura S, Miyake S, Deguchi K, Himeno M, et al. Maturational disturbance of chondrocytes in Cbfa1-deficient mice. Developmental dynamics : an official publication of the American Association of Anatomists. 1999;214(4):279-90.
75. Kim IS, Otto F, Zabel B, Mundlos S. Regulation of chondrocyte differentiation by Cbfa1. Mechanisms of development. 1999;80(2):159-70.
76. Komori T, Yagi H, Nomura S, Yamaguchi A, Sasaki K, Deguchi K, et al. Targeted disruption of Cbfa1 results in a complete lack of bone formation owing to maturational arrest of osteoblasts. Cell. 1997;89(5):755-64.
77. Otto F, Thornell AP, Crompton T, Denzel A, Gilmour KC, Rosewell IR, et al. Cbfa1, a candidate gene for cleidocranial dysplasia syndrome, is essential for osteoblast differentiation and bone development. Cell. 1997;89(5):765-71.
78. Maeno T, Moriishi T, Yoshida CA, Komori H, Kanatani N, Izumi S, et al. Early onset of Runx2 expression caused craniosynostosis, ectopic bone formation, and limb defects. Bone. 2011;49(4):673-82.
79. Schroeder TM, Jensen ED, Westendorf JJ. Runx2: a master organizer of gene transcription in developing and maturing osteoblasts. Birth defects research Part C, Embryo today : reviews. 2005;75(3):213-25.
80. Zhang C. Transcriptional regulation of bone formation by the osteoblast-specific transcription factor Osx. Journal of orthopaedic surgery and research. 2010;5:37.

81. Kawane T, Komori H, Liu W, Moriishi T, Miyazaki T, Mori M, et al. Dlx5 and mef2 regulate a novel runx2 enhancer for osteoblast-specific expression. Journal of bone and mineral research : the official journal of the American Society for Bone and Mineral Research. 2014;29(9):1960-9.
82. Kawane T, Qin X, Jiang Q, Miyazaki T, Komori H, Yoshida CA, et al. Runx2 is required for the proliferation of osteoblast progenitors and induces proliferation by regulating Fgfr2 and Fgfr3. Scientific reports. 2018;8(1):13551.
83. Zhou X, Zhang Z, Feng JQ, Dusevich VM, Sinha K, Zhang H, et al. Multiple functions of Osterix are required for bone growth and homeostasis in postnatal mice. Proceedings of the National Academy of Sciences of the United States of America. 2010;107(29):12919-24.
84. Nishimura R, Wakabayashi M, Hata K, Matsubara T, Honma S, Wakisaka S, et al. Osterix regulates calcification and degradation of chondrogenic matrices through matrix metalloproteinase 13 (MMP13) expression in association with transcription factor Runx2 during endochondral ossification. The Journal of biological chemistry. 2012;287(40):33179-90.
85. Baek WY, Lee MA, Jung JW, Kim SY, Akiyama H, de Crombrugghe B, et al. Positive regulation of adult bone formation by osteoblast-specific transcription factor osterix. Journal of bone and mineral research : the official journal of the American Society for Bone and Mineral Research. 2009;24(6):1055-65.
86. Yoshida CA, Komori H, Maruyama Z, Miyazaki T, Kawasaki K, Furuichi T, et al. SP7 inhibits osteoblast differentiation at a late stage in mice. PloS one. 2012;7(3):e32364.
87. Xiao G, Jiang D, Ge C, Zhao Z, Lai Y, Boules H, et al. Cooperative interactions between activating transcription factor 4 and Runx2/Cbfa1 stimulate osteoblast-specific osteocalcin gene expression. The Journal of biological chemistry. 2005;280(35):30689-96.
88. Karsenty G. Transcriptional control of skeletogenesis. Annual review of genomics and human genetics. 2008;9:183-96.
89. Cao H, Yu S, Yao Z, Galson DL, Jiang Y, Zhang X, et al. Activating transcription factor 4 regulates osteoclast differentiation in mice. The Journal of clinical investigation. 2010;120(8):2755-66.
90. Obri A, Makinistoglu MP, Zhang H, Karsenty G. HDAC4 integrates PTH and sympathetic signaling in osteoblasts. The Journal of cell biology. 2014;205(6):771-80.

91. Elefteriou F, Benson MD, Sowa H, Starbuck M, Liu X, Ron D, et al. ATF4 mediation of NF1 functions in osteoblast reveals a nutritional basis for congenital skeletal dysplasiae. Cell metabolism. 2006;4(6):441-51.
92. Xiong J, Piemontese M, Onal M, Campbell J, Goellner JJ, Dusevich V, et al. Osteocytes, not Osteoblasts or Lining Cells, are the Main Source of the RANKL Required for Osteoclast Formation in Remodeling Bone. PloS one. 2015;10(9):e0138189.
93. Bellido T. Osteocyte-Driven Bone Remodeling. Calcified tissue international. 2014;94(1):25-34.
94. Cardoso L, Herman BC, Verborgt O, Laudier D, Majeska RJ, Schaffler MB. Osteocyte apoptosis controls activation of intracortical resorption in response to bone fatigue. Journal of bone and mineral research : the official journal of the American Society for Bone and Mineral Research. 2009;24(4):597-605.
95. Heino TJ, Kurata K, Higaki H, Väänänen HK. Evidence for the role of osteocytes in the initiation of targeted remodeling. Technology and Health Care. 2009;17:49-56.
96. Han Y, You X, Xing W, Zhang Z, Zou W. Paracrine and endocrine actions of bone-the functions of secretory proteins from osteoblasts, osteocytes, and osteoclasts. Bone research. 2018;6:16.
97. Theoleyre S, Wittrant Y, Tat SK, Fortun Y, Redini F, Heymann D. The molecular triad OPG/RANK/RANKL: involvement in the orchestration of pathophysiological bone remodeling. Cytokine & growth factor reviews. 2004;15(6):457-75.
98. Boyce BF, Xing L. Functions of RANKL/RANK/OPG in bone modeling and remodeling. Archives of biochemistry and biophysics. 2008;473(2):139-46.
99. Henriksen K, Andreassen KV, Thudium CS, Gudmann KNS, Moscatelli I, Crüger-Hansen CE, et al. A specific subtype of osteoclasts secretes factors inducing nodule formation by osteoblasts. Bone. 2012;51(3):353-61.
100. Kim B-J, Lee Y-S, Lee S-Y, Park S-Y, Dieplinger H, Ryu SH, et al. Afamin secreted from nonresorbing osteoclasts acts as a chemokine for preosteoblasts via the Akt-signaling pathway. Bone. 2012;51(3):431-40.
101. Boyce BF, Rosenberg E, de Papp AE, Duong LT. The osteoclast, bone remodelling and treatment of metabolic bone disease. European journal of clinical investigation. 2012;42(12):1332-41.

102. Beamer B, Hettrich C, Lane J. Vascular endothelial growth factor: an essential component of angiogenesis and fracture healing. HSS journal : the musculoskeletal journal of Hospital for Special Surgery. 2010;6(1):85-94.
103. Sivaraj KK, Adams RH. Blood vessel formation and function in bone. Development (Cambridge, England). 2016;143(15):2706-15.
104. Xie H, Cui Z, Wang L, Xia Z, Hu Y, Xian L, et al. PDGF-BB secreted by preosteoclasts induces angiogenesis during coupling with osteogenesis. Nature medicine. 2014;20(11):1270-8.
105. Salha S, Gehmert S, Brébant V, Anker A, Loibl M, Prantl L, et al. PDGF regulated migration of mesenchymal stem cells towards malignancy acts via the PI3K signaling pathway. Clinical Hemorheology and Microcirculation. 2018;70:543-51.
106. Bergwitz C, Juppner H. Regulation of phosphate homeostasis by PTH, vitamin D, and FGF23. Annual review of medicine. 2010;61:91-104.
107. Al Rifai O, Chow J, Lacombe J, Julien C, Faubert D, Susan-Resiga D, et al. Proprotein convertase furin regulates osteocalcin and bone endocrine function. The Journal of clinical investigation. 2017;127(11):4104-17.
108. Ferron M, Wei J, Yoshizawa T, Del Fattore A, DePinho RA, Teti A, et al. Insulin signaling in osteoblasts integrates bone remodeling and energy metabolism. Cell. 2010;142(2):296-308.
109. Lacombe J, Karsenty G, Ferron M. In vivo analysis of the contribution of bone resorption to the control of glucose metabolism in mice. Molecular metabolism. 2013;2(4):498-504.
110. Bonneau J, Ferland G, Karelis AD, Doucet E, Faraj M, Rabasa-Lhoret R, et al. Association between osteocalcin gamma-carboxylation and insulin resistance in overweight and obese postmenopausal women. Journal of diabetes and its complications. 2017;31(6):1027-34.
111. Pi M, Wu Y, Quarles LD. GPRC6A mediates responses to osteocalcin in beta-cells in vitro and pancreas in vivo. Journal of bone and mineral research : the official journal of the American Society for Bone and Mineral Research. 2011;26(7):1680-3.
112. Ferron M, Lacombe J, Germain A, Oury F, Karsenty G. GGCX and VKORC1 inhibit osteocalcin endocrine functions. The Journal of cell biology. 2015;208(6):761-76.
113. Lee NK, Sowa H, Hinoi E, Ferron M, Ahn JD, Confavreux C, et al. Endocrine regulation of energy metabolism by the skeleton. Cell. 2007;130(3):456-69.

114. Bianco P, Robey PG. Skeletal stem cells. Development (Cambridge, England). 2015;142(6):1023-7.
115. Grayson WL, Bunnell BA, Martin E, Frazier T, Hung BP, Gimble JM. Stromal cells and stem cells in clinical bone regeneration. Nature reviews Endocrinology. 2015;11(3):140-50.
116. Rosen ED, Spiegelman BM. What we talk about when we talk about fat. Cell. 2014;156(1-2):20-44.
117. DiGirolamo DJ, Clemens TL, Kousteni S. The skeleton as an endocrine organ. Nature Reviews Rheumatology. 2012;8(11):674-83.
118. Hardouin P, Rharass T, Lucas S. Bone Marrow Adipose Tissue: To Be or Not To Be a Typical Adipose Tissue? Frontiers in endocrinology. 2016;7:85.
119. Jones JR, Barrick C, Kim KA, Lindner J, Blondeau B, Fujimoto Y, et al. Deletion of PPARgamma in adipose tissues of mice protects against high fat diet-induced obesity and insulin resistance. Proceedings of the National Academy of Sciences of the United States of America. 2005;102(17):6207-12.
120. Tencerova M, Kassem M. The Bone Marrow-Derived Stromal Cells: Commitment and Regulation of Adipogenesis. Frontiers in endocrinology. 2016;7:127.
121. Rosen ED, MacDougald OA. Adipocyte differentiation from the inside out. Nature Reviews Molecular Cell Biology. 2006;7(12):885-96.
122. Cristancho AG, Lazar MA. Forming functional fat: a growing understanding of adipocyte differentiation. Nature reviews Molecular cell biology. 2011;12(11):722-34.
123. Hariri H, Pellicelli M, St-Arnaud R. New PTH Signals Mediating Bone Anabolism. Current Molecular Biology Reports. 2017;3(2):133-41.
124. Hanley DA, Watson PH, Hodsman AB, Dempster DW. Pharmacological mechanisms of therapeutics: Parathyroid Hormone. In: Bilezikian JP, Raisz LG, Martin TJ, editors. Principles of bone biology. 2. 3rd ed. San Diego: Elsevier; 2008. p. 1661-95.
125. Levine MA. Normal mineral homeostasis. Interplay of parathyroid hormone and vitamin D. Endocr Dev. 2003;6:14-33.
126. Silverberg SJ, Shane E, de la Cruz L, Dempster DW, Feldman F, Seldin D, et al. Skeletal disease in primary hyperparathyroidism. Journal of bone and mineral research : the official journal of the American Society for Bone and Mineral Research. 1989;4(3):283-91.

127. Grey AB, Stapleton JP, Evans MC, Reid IR. Accelerated bone loss in post-menopausal women with mild primary hyperparathyroidism. Clin Endocrinol (Oxf). 1996;44(6):697-702.
128. Pleiner-Duxneuner J, Zwettler E, Paschalis E, Roschger P, Nell-Duxneuner V, Klaushofer K. Treatment of osteoporosis with parathyroid hormone and teriparatide. Calcified tissue international. 2009;84(3):159-70.
129. Dobnig H, Turner RT. The effects of programmed administration of human parathyroid hormone fragment (1-34) on bone histomorphometry and serum chemistry in rats. Endocrinology. 1997;138(11):4607-12.
130. Qin L, Raggatt LJ, Partridge NC. Parathyroid hormone: a double-edged sword for bone metabolism. Trends in endocrinology and metabolism: TEM. 2004;15(2):60-5.
131. Neer RM, Arnaud CD, Zanchetta JR, Prince R, Gaich GA, Reginster JY, et al. Effect of parathyroid hormone (1-34) on fractures and bone mineral density in postmenopausal women with osteoporosis. New England Journal of Medicine. 2001;344(19):1434-41.
132. Cheloha RW, Gellman SH, Vilardaga JP, Gardella TJ. PTH receptor-1 signalling-mechanistic insights and therapeutic prospects. Nature reviews Endocrinology. 2015;11(12):712-24.
133. Santa Maria C, Cheng Z, Li A, Wang J, Shoback D, Tu CL, et al. Interplay between CaSR and PTH1R signaling in skeletal development and osteoanabolism. Semin Cell Dev Biol. 2016;49:11-23.
134. Lanske B, Amling M, Neff L, Guiducci J, Baron R, Kronenberg HM. Ablation of the PTHrP gene or the PTH/PTHrP receptor gene leads to distinct abnormalities in bone development. Journal of Clinical Investigation. 1999;104(4):399-407.
135. Qiu T, Xian L, Crane J, Wen C, Hilton M, Lu W, et al. PTH receptor signaling in osteoblasts regulates endochondral vascularization in maintenance of postnatal growth plate. Journal of bone and mineral research : the official journal of the American Society for Bone and Mineral Research. 2015;30(2):309-17.
136. Powell WF, Jr., Barry KJ, Tulum I, Kobayashi T, Harris SE, Bringhurst FR, et al. Targeted ablation of the PTH/PTHrP receptor in osteocytes impairs bone structure and homeostatic calcemic responses. The Journal of endocrinology. 2011;209(1):21-32.
137. Delgado-Calle J, Tu X, Pacheco-Costa R, McAndrews K, Edwards R, Pellegrini GG, et al. Control of Bone Anabolism in Response to Mechanical Loading and PTH by Distinct

Mechanisms Downstream of the PTH Receptor. Journal of bone and mineral research : the official journal of the American Society for Bone and Mineral Research. 2016.
138. Saini V, Marengi DA, Barry KJ, Fulzele KS, Heiden E, Liu X, et al. Parathyroid Hormone (PTH)/PTH-related Peptide Type 1 Receptor (PPR) Signaling in Osteocytes Regulates Anabolic and Catabolic Skeletal Responses to PTH. The Journal of biological chemistry. 2013;288(28):20122-34.
139. Abou-Samra AB, Juppner H, Force T, Freeman MW, Kong XF, Schipani E, et al. Expression cloning of a common receptor for parathyroid hormone and parathyroid hormone-related peptide from rat osteoblast-like cells: a single receptor stimulates intracellular accumulation of both cAMP and inositol trisphosphates and increases intracellular free calcium. Proceedings of the National Academy of Sciences of the United States of America. 1992;89(7):2732-6.
140. Singh AT, Gilchrist A, Voyno-Yasenetskaya T, Radeff-Huang JM, Stern PH. G alpha12/G alpha13 subunits of heterotrimeric G proteins mediate parathyroid hormone activation of phospholipase D in UMR-106 osteoblastic cells. Endocrinology. 2005;146(5):2171-5.
141. Iida-Klein A, Guo J, Drake MT, Kronenberg HM, Abou-Samra AB, Bringhurst FR, et al. Structural requirements of parathyroid hormone/parathyroid hormone-related peptide receptors for phospholipase C activation and regulation of phosphate uptake. Mineral and Electrolyte Metabolism. 1995;21(1-3):177-9.
142. Takasu H, Gardella TJ, Luck MD, Potts JT, Jr., Bringhurst FR. Amino-terminal modifications of human parathyroid hormone (PTH) selectively alter phospholipase C signaling via the type 1 PTH receptor: implications for design of signal-specific PTH ligands. Biochemistry. 1999;38(41):13453-60.
143. Jouishomme H, Whitfield JF, Chakravarthy B, Durkin JP, Gagnon L, Isaacs RJ, et al. The protein kinase-C activation domain of the parathyroid hormone. Endocrinology. 1992;130(1):53-60.
144. Jouishomme H, Whitfield JF, Gagnon L, Maclean S, Isaacs R, Chakravarthy B, et al. Further definition of the protein kinase C activation domain of the parathyroid hormone. Journal of Bone and Mineral Research. 1994;9(6):943-9.

145. Whitfield JF, Morley P, Willick GE, Ross V, Barbier JR, Isaacs RJ, et al. Stimulation of the growth of femoral trabecular bone in ovariectomized rats by the novel parathyroid hormone fragment, hPTH-(1-31)NH2 (Ostabolin). Calcified tissue international. 1996;58(2):81-7.
146. Armamento-Villareal R, Ziambaras K, Abbasi-Jarhomi SH, Dimarogonas A, Halstead L, Fausto A, et al. An intact N terminus is required for the anabolic action of parathyroid hormone on adult female rats. Journal of Bone and Mineral Research. 1997;12(3):384-92.
147. Ogata N, Shinoda Y, Wettschureck N, Offermanns S, Takeda S, Nakamura K, et al. G alpha(q) signal in osteoblasts is inhibitory to the osteoanabolic action of parathyroid hormone. The Journal of biological chemistry. 2011;286(15):13733-40.
148. Yang D, Singh R, Divieti P, Guo J, Bouxsein ML, Bringhurst FR. Contributions of parathyroid hormone (PTH)/PTH-related peptide receptor signaling pathways to the anabolic effect of PTH on bone. Bone. 2007;40(6):1453-61.
149. Sinha P, Aarnisalo P, Chubb R, Poulton IJ, Guo J, Nachtrab G, et al. Loss of Gsalpha in the Postnatal Skeleton Leads to Low Bone Mass and a Blunted Response to Anabolic Parathyroid Hormone Therapy. The Journal of biological chemistry. 2016;291(4):1631-42.
150. Calvi LM, Sims NA, Hunzelman JL, Knight MC, Giovannetti A, Saxton JM, et al. Activated parathyroid hormone/parathyroid hormone-related protein receptor in osteoblastic cells differentially affects cortical and trabecular bone. Journal of Clinical Investigation. 2001;107(3):277-86.
151. Bohinc BN, Gesty-Palmer D. Arrestins in bone. Prog Mol Biol Transl Sci. 2013;118:335-58.
152. Ferrari SL, Pierroz DD, Glatt V, Goddard DS, Bianchi EN, Lin FT, et al. Bone response to intermittent parathyroid hormone is altered in mice null for {beta}-Arrestin2. Endocrinology. 2005;146(4):1854-62.
153. Gesty-Palmer D, Flannery P, Yuan L, Corsino L, Spurney R, Lefkowitz RJ, et al. A beta-arrestin-biased agonist of the parathyroid hormone receptor (PTH1R) promotes bone formation independent of G protein activation. Sci Transl Med. 2009;1(1):1ra.
154. Kao RS, Abbott MJ, Louie A, O'Carroll D, Lu W, Nissenson R. Constitutive protein kinase A activity in osteocytes and late osteoblasts produces an anabolic effect on bone. Bone. 2013;55(2):277-87.

155. Tascau L, Gardner T, Anan H, Yongpravat C, Cardozo CP, Bauman WA, et al. Activation of Protein Kinase A in Mature Osteoblasts Promotes a Major Bone Anabolic Response. Endocrinology. 2016;157(1):112-26.
156. O'Brien CA, Plotkin LI, Galli C, Goellner JJ, Gortazar AR, Allen MR, et al. Control of bone mass and remodeling by PTH receptor signaling in osteocytes. PloS one. 2008;3(8):e2942.
157. Rhee Y, Allen MR, Condon K, Lezcano V, Ronda AC, Galli C, et al. PTH receptor signaling in osteocytes governs periosteal bone formation and intracortical remodeling. Journal of bone and mineral research : the official journal of the American Society for Bone and Mineral Research. 2011;26(5):1035-46.
158. Li C, Wang W, Xie L, Luo X, Cao X, Wan M. Lipoprotein receptor-related protein 6 is required for parathyroid hormone-induced Sost suppression. Annals of the New York Academy of Sciences. 2016;1364:62-73.
159. Li C, Xing Q, Yu B, Xie H, Wang W, Shi C, et al. Disruption of LRP6 in osteoblasts blunts the bone anabolic activity of PTH. Journal of bone and mineral research : the official journal of the American Society for Bone and Mineral Research. 2013;28(10):2094-108.
160. Revollo L, Kading J, Jeong SY, Li J, Salazar V, Mbalaviele G, et al. N-cadherin restrains PTH activation of Lrp6/beta-catenin signaling and osteoanabolic action. Journal of bone and mineral research : the official journal of the American Society for Bone and Mineral Research. 2015;30(2):274-85.
161. Wan M, Yang C, Li J, Wu X, Yuan H, Ma H, et al. Parathyroid hormone signaling through low-density lipoprotein-related protein 6. Genes & development. 2008;22(21):2968-79.
162. Vinyoles M, Del Valle-Perez B, Curto J, Vinas-Castells R, Alba-Castellon L, Garcia de Herreros A, et al. Multivesicular GSK3 sequestration upon Wnt signaling is controlled by p120-catenin/cadherin interaction with LRP5/6. Molecular cell. 2014;53(3):444-57.
163. Yang H, Dong J, Xiong W, Fang Z, Guan H, Li F. N-cadherin restrains PTH repressive effects on sclerostin/SOST by regulating LRP6-PTH1R interaction. Annals of the New York Academy of Sciences. 2016;1385(1):41-52.
164. Acebron SP, Niehrs C. beta-Catenin-Independent Roles of Wnt/LRP6 Signaling. Trends Cell Biol. 2016;26(12):956-67.
165. Malinauskas T, Jones EY. Extracellular modulators of Wnt signalling. Curr Opin Struct Biol. 2014;29:77-84.

166. Niehrs C, Shen J. Regulation of Lrp6 phosphorylation. Cell Mol Life Sci. 2010;67(15):2551-62.
167. Kulkarni NH, Halladay DL, Miles RR, Gilbert LM, Frolik CA, Galvin RJ, et al. Effects of parathyroid hormone on Wnt signaling pathway in bone. Journal of cellular biochemistry. 2005;95(6):1178-90.
168. Iwaniec UT, Wronski TJ, Liu J, Rivera MF, Arzaga RR, Hansen G, et al. PTH stimulates bone formation in mice deficient in Lrp5. Journal of bone and mineral research : the official journal of the American Society for Bone and Mineral Research. 2007;22(3):394-402.
169. Tian Y, Xu Y, Fu Q, He M. Parathyroid hormone regulates osteoblast differentiation in a Wnt/beta-catenin-dependent manner. Mol Cell Biochem. 2011;355(1-2):211-6.
170. Kedlaya R, Kang KS, Hong JM, Bettagere V, Lim KE, Horan D, et al. Adult-Onset Deletion of beta-Catenin in (10kb)Dmp1-Expressing Cells Prevents Intermittent PTH-Induced Bone Gain. Endocrinology. 2016;157(8):3047-57.
171. Kramer I, Keller H, Leupin O, Kneissel M. Does osteocytic SOST suppression mediate PTH bone anabolism? Trends in endocrinology and metabolism: TEM. 2010;21(4):237-44.
172. Kramer I, Loots GG, Studer A, Keller H, Kneissel M. Parathyroid hormone (PTH)-induced bone gain is blunted in SOST overexpressing and deficient mice. Journal of bone and mineral research : the official journal of the American Society for Bone and Mineral Research. 2010;25(2):178-89.
173. Robling AG, Kedlaya R, Ellis SN, Childress PJ, Bidwell JP, Bellido T, et al. Anabolic and catabolic regimens of human parathyroid hormone 1-34 elicit bone- and envelope-specific attenuation of skeletal effects in Sost-deficient mice. Endocrinology. 2011;152(8):2963-75.
174. Pearman AT, Chou WY, Bergman KD, Pulumati MR, Partridge NC. Parathyroid hormone induces c-fos promoter activity in osteoblastic cells through phosphorylated cAMP response element (CRE)-binding protein binding to the major CRE. The Journal of biological chemistry. 1996;271(41):25715-21.
175. Clohisy JC, Scott DK, Brakenhoff KD, Quinn CO, Partridge NC. Parathyroid hormone induces c-fos and c-jun messenger RNA in rat osteoblastic cells. Mol Endocrinol. 1992;6(11):1834-42.

176. McCauley LK, Koh AJ, Beecher CA, Rosol TJ. Proto-oncogene c-fos is transcriptionally regulated by parathyroid hormone (PTH) and PTH-related protein in a cyclic adenosine monophosphate-dependent manner in osteoblastic cells. Endocrinology. 1997;138(12):5427-33.
177. Fei Y, Shimizu E, McBurney MW, Partridge NC. Sirtuin 1 is a negative regulator of parathyroid hormone stimulation of matrix metalloproteinase 13 expression in osteoblastic cells: role of sirtuin 1 in the action of PTH on osteoblasts. The Journal of biological chemistry. 2015;290(13):8373-82.
178. Lian JB, Stein JL, Stein GS, van Wijnen AJ, Montecino M, Javed A, et al. Runx2/Cbfa1 functions: diverse regulation of gene transcription by chromatin remodeling and co-regulatory protein interactions. Connective tissue research. 2003;44 Suppl 1:141-8.
179. Sepulveda H, Villagra A, Montecino M. Tet-Mediated DNA Demethylation Is Required for SWI/SNF-Dependent Chromatin Remodeling and Histone-Modifying Activities That Trigger Expression of the Sp7 Osteoblast Master Gene during Mesenchymal Lineage Commitment. Molecular and cellular biology. 2017;37(20).
180. Dobreva G, Chahrour M, Dautzenberg M, Chirivella L, Kanzler B, Fariñas I, et al. SATB2 Is a Multifunctional Determinant of Craniofacial Patterning and Osteoblast Differentiation. Cell. 2006;125(5):971-86.
181. Wiedmann B, Sakai H, Davis TA, Wiedmann M. A protein complex required for signal-sequence-specific sorting and translocation. Nature. 1994;370(6489):434-40.
182. Liu Y, Hu Y, Li X, Niu L, Teng M. The Crystal Structure of the Human Nascent Polypeptide-Associated Complex Domain Reveals a Nucleic Acid-Binding Region on the NACA Subunit. Biochemistry. 2010;49(13):2890-6.
183. Parthun MR, Mangus DA, Jaehning JA. The EGD1 product, a yeast homolog of human BTF3, may be involved in GAL4 DNA binding. Molecular and cellular biology. 1992;12(12):5683-9.
184. Zheng XM, Black D, Chambon P, Egly JM. Sequencing and expression of complementary DNA for the general transcription factor BTF3. Nature. 1990;344(6266):556-9.
185. Shen K, Gamerdinger M, Chan R, Gense K, Martin EM, Sachs N, et al. Dual Role of Ribosome-Binding Domain of NAC as a Potent Suppressor of Protein Aggregation and Aging-Related Proteinopathies. Molecular cell. 2019;74(4):729-41.e7.

186. Yotov WV, Moreau A, St-Arnaud R. The alpha chain of the nascent polypeptide-associated complex functions as a transcriptional coactivator. Molecular and cellular biology. 1998;18(3):1303-11.
187. Wang L, Zhang W, Wang L, Zhang XC, Li X, Rao Z. Crystal structures of NAC domains of human nascent polypeptide-associated complex (NAC) and its alphaNAC subunit. Protein & cell. 2010;1(4):406-16.
188. Yotov WV, St-Arnaud R. Differential splicing-in of a proline-rich exon converts alphaNAC into a muscle-specific transcription factor. Genes & development. 1996;10(14):1763-72.
189. Akhouayri O, Quelo I, St-Arnaud R. Sequence-specific DNA binding by the alphaNAC coactivator is required for potentiation of c-Jun-dependent transcription of the osteocalcin gene. Molecular and cellular biology. 2005;25(9):3452-60.
190. Moreau A, Yotov WV, Glorieux FH, St-Arnaud R. Bone-specific expression of the alpha chain of the nascent polypeptide-associated complex, a coactivator potentiating c-Jun-mediated transcription. Molecular and cellular biology. 1998;18(3):1312-21.
191. Akhouayri O, St-Arnaud R. Differential mechanisms of transcriptional regulation of the mouse osteocalcin gene by Jun family members. Calcified tissue international. 2007;80(2):123-31.
192. Pellicelli M, Hariri H, Miller JA, St-Arnaud R. Lrp6 is a target of the PTH-activated alphaNAC transcriptional coregulator. Biochimica et biophysica acta Gene regulatory mechanisms. 2018;1861(2):61-71.
193. Jafarov T, Alexander JW, St-Arnaud R. alphaNAC interacts with histone deacetylase corepressors to control Myogenin and Osteocalcin gene expression. Biochimica et biophysica acta. 2012;1819(11-12):1208-16.
194. Quelo I, Akhouayri O, Prud'homme J, St-Arnaud R. GSK3 beta-dependent phosphorylation of the alpha NAC coactivator regulates its nuclear translocation and proteasome-mediated degradation. Biochemistry. 2004;43(10):2906-14.
195. Quelo I, Gauthier C, St-Arnaud R. Casein kinase II phosphorylation regulates alphaNAC subcellular localization and transcriptional coactivating activity. Gene expression. 2005;12(3):151-63.

196. Quelo I, Gauthier C, Hannigan GE, Dedhar S, St-Arnaud R. Integrin-linked kinase regulates the nuclear entry of the c-Jun coactivator alpha-NAC and its coactivation potency. The Journal of biological chemistry. 2004;279(42):43893-9.
197. Pellicelli M, Miller JA, Arabian A, Gauthier C, Akhouayri O, Wu JY, et al. The PTH-Galphas-protein kinase A cascade controls alphaNAC localization to regulate bone mass. Molecular and cellular biology. 2014;34(9):1622-33.
198. Addison WN, Pellicelli M, St-Arnaud R. Dephosphorylation of the transcriptional cofactor NACA by the PP1A phosphatase enhances cJUN transcriptional activity and osteoblast differentiation. The Journal of biological chemistry. 2019;294(20):8184-96.
199. Wu JY, Aarnisalo P, Bastepe M, Sinha P, Fulzele K, Selig MK, et al. Gsalpha enhances commitment of mesenchymal progenitors to the osteoblast lineage but restrains osteoblast differentiation in mice. The Journal of clinical investigation. 2011;121(9):3492-504.
200. Cowell IG, Skinner A, Hurst HC. Transcriptional repression by a novel member of the bZIP family of transcription factors. Molecular and cellular biology. 1992;12(7):3070-7.
201. Kamizono S, Duncan GS, Seidel MG, Morimoto A, Hamada K, Grosveld G, et al. Nfil3/E4bp4 is required for the development and maturation of NK cells in vivo. The Journal of experimental medicine. 2009;206(13):2977.
202. Cowell IG. E4BP4/NFIL3, a PAR-related bZIP factor with many roles. BioEssays : news and reviews in molecular, cellular and developmental biology. 2002;24(11):1023-9.
203. Cowell IG, Hurst HC. Transcriptional repression by the human bZIP factor E4BP4: definition of a minimal repression domain. Nucleic acids research. 1994;22(1):59-65.
204. Gascoyne DM, Long E, Veiga-Fernandes H, de Boer J, Williams O, Seddon B, et al. The basic leucine zipper transcription factor E4BP4 is essential for natural killer cell development. Nature Immunology. 2009;10:1118.
205. Ikushima S, Inukai T, Inaba T, Nimer SD, Cleveland JL, Look AT. Pivotal role for the NFIL3/E4BP4 transcription factor in interleukin 3-mediated survival of pro-B lymphocytes. Proceedings of the National Academy of Sciences of the United States of America. 1997;94(6):2609-14.
206. Kashiwada M, Levy DM, McKeag L, Murray K, Schröder AJ, Canfield SM, et al. IL-4-induced transcription factor NFIL3/E4BP4 controls IgE class switching. Proceedings of the National Academy of Sciences. 2010;107(2):821-6.

207. Akashi M, Ichise T, Mamine T, Takumi T. Molecular mechanism of cell-autonomous circadian gene expression of Period2, a crucial regulator of the mammalian circadian clock. Molecular biology of the cell. 2006;17(2):555-65.
208. Lin KH, Kuo CH, Kuo WW, Ho TJ, Pai P, Chen WK, et al. NFIL3 suppresses hypoxia-induced apoptotic cell death by targeting the insulin-like growth factor 2 receptor. Journal of cellular biochemistry. 2015;116(6):1113-20.
209. Ozkurt IC, Pirih FQ, Tetradis S. Parathyroid hormone induces E4bp4 messenger ribonucleic acid expression primarily through cyclic adenosine 3',5'-monophosphate signaling in osteoblasts. Endocrinology. 2004;145(8):3696-703.
210. Ozkurt IC, Tetradis S. Parathyroid hormone-induced E4BP4/NFIL3 down-regulates transcription in osteoblasts. The Journal of biological chemistry. 2003;278(29):26803-9.
211. Carey KT, Tan KH, Ng J, Liddicoat DR, Godfrey DI, Cole TJ. Nfil3 Is a Glucocorticoid-Regulated Gene Required for Glucocorticoid-Induced Apoptosis in Male Murine T Cells. Endocrinology. 2013;154(4):1540-52.
212. Pellicelli M, Taheri M, St-Louis M, Beriault V, Desgroseillers L, Boileau G, et al. PTHrP(1-34)-mediated repression of the PHEX gene in osteoblastic cells involves the transcriptional repressor E4BP4. Journal of cellular physiology. 2012;227(6):2378-87.
213. MacGillavry HD, Stam FJ, Sassen MM, Kegel L, Hendriks WTJ, Verhaagen J, et al. NFIL3 and cAMP Response Element-Binding Protein Form a Transcriptional Feedforward Loop that Controls Neuronal Regeneration-Associated Gene Expression. The Journal of Neuroscience. 2009;29(49):15542.
214. Nijman SM, Luna-Vargas MP, Velds A, Brummelkamp TR, Dirac AM, Sixma TK, et al. A genomic and functional inventory of deubiquitinating enzymes. Cell. 2005;123(5):773-86.
215. Reyes-Turcu FE, Ventii KH, Wilkinson KD. Regulation and cellular roles of ubiquitin-specific deubiquitinating enzymes. Annu Rev Biochem. 2009;78:363-97.
216. Hu M, Li P, Li M, Li W, Yao T, Wu JW, et al. Crystal structure of a UBP-family deubiquitinating enzyme in isolation and in complex with ubiquitin aldehyde. Cell. 2002;111(7):1041-54.
217. Quesada V, Diaz-Perales A, Gutierrez-Fernandez A, Garabaya C, Cal S, Lopez-Otin C. Cloning and enzymatic analysis of 22 novel human ubiquitin-specific proteases. Biochem Biophys Res Commun. 2004;314(1):54-62.

218. Kazmierczak M, Harris SL, Kazmierczak P, Shah P, Starovoytov V, Ohlemiller KK, et al. Progressive Hearing Loss in Mice Carrying a Mutation in Usp53. J Neurosci. 2015;35(47):15582-98.
219. Kurban M, Kim CA, Kiuru M, Fantauzzo K, Cabral R, Abbas O, et al. Copy number variations on chromosome 4q26-27 are associated with Cantu syndrome. Dermatology. 2011;223(4):316-20.
220. Maddirevula S, Alhebbi H, Alqahtani A, Algoufi T, Alsaif HS, Ibrahim N, et al. Identification of novel loci for pediatric cholestatic liver disease defined by KIF12, PPM1F, USP53, LSR, and WDR83OS pathogenic variants. Genetics in medicine : official journal of the American College of Medical Genetics. 2019;21(5):1164-72.
221. Zhang J, Yang Y, Gong JY, Li LT, Li JQ, Zhang MH, et al. Low-GGT intrahepatic cholestasis associated with biallelic USP53 variants: Clinical, histological and ultrastructural characterization. Liver international : official journal of the International Association for the Study of the Liver. 2020;40(5):1142-50.
222. Meury T, Akhouayri O, Jafarov T, Mandic V, St-Arnaud R. Nuclear alpha NAC influences bone matrix mineralization and osteoblast maturation in vivo. Molecular and cellular biology. 2010;30(1):43-53.
223. Bakker AD, Klein-Nulend J. Osteoblast isolation from murine calvaria and long bones. Methods in molecular biology (Clifton, NJ). 2012;816:19-29.
224. Durkin ME, Qian X, Popescu NC, Lowy DR. Isolation of Mouse Embryo Fibroblasts. Bio-protocol. 2013;3(18).
225. Soleimani M, Nadri S. A protocol for isolation and culture of mesenchymal stem cells from mouse bone marrow. Nat Protoc. 2009;4(1):102-6.
226. Tullberg-Reinert H, Jundt G. In situ measurement of collagen synthesis by human bone cells with a sirius red-based colorimetric microassay: effects of transforming growth factor beta2 and ascorbic acid 2-phosphate. Histochemistry and cell biology. 1999;112(4):271-6.
227. Coleman JL, Brennan K, Ngo T, Balaji P, Graham RM, Smith NJ. Rapid Knockout and Reporter Mouse Line Generation and Breeding Colony Establishment Using EUCOMM Conditional-Ready Embryonic Stem Cells: A Case Study. Frontiers in endocrinology. 2015;6:105.

228. Rigueur D, Lyons KM. Whole-mount skeletal staining. Methods in molecular biology (Clifton, NJ). 2014;1130:113-21.
229. Diez-Perez A, Güerri R, Nogues X, Cáceres E, Peña MJ, Mellibovsky L, et al. Microindentation for in vivo measurement of bone tissue mechanical properties in humans. Journal of bone and mineral research : the official journal of the American Society for Bone and Mineral Research. 2010;25(8):1877-85.
230. Scheller EL, Troiano N, Vanhoutan JN, Bouxsein MA, Fretz JA, Xi Y, et al. Use of osmium tetroxide staining with microcomputerized tomography to visualize and quantify bone marrow adipose tissue in vivo. Methods in enzymology. 2014;537:123-39.
231. Parlee SD, Lentz SI, Mori H, MacDougald OA. Quantifying size and number of adipocytes in adipose tissue. Methods in enzymology. 2014;537:93-122.
232. Keller A, Nesvizhskii AI, Kolker E, Aebersold R. Empirical statistical model to estimate the accuracy of peptide identifications made by MS/MS and database search. Anal Chem. 2002;74(20):5383-92.
233. Nesvizhskii AI, Keller A, Kolker E, Aebersold R. A statistical model for identifying proteins by tandem mass spectrometry. Anal Chem. 2003;75(17):4646-58.
234. Cartharius K, Frech K, Grote K, Klocke B, Haltmeier M, Klingenhoff A, et al. MatInspector and beyond: promoter analysis based on transcription factor binding sites. Bioinformatics. 2005;21(13):2933-42.
235. Swarthout JT, D'Alonzo RC, Selvamurugan N, Partridge NC. Parathyroid hormone-dependent signaling pathways regulating genes in bone cells. Gene. 2002;282(1):1-17.
236. Zhang R, Edwards JR, Ko S-Y, Dong S, Liu H, Oyajobi BO, et al. Transcriptional regulation of BMP2 expression by the PTH-CREB signaling pathway in osteoblasts. PloS one. 2011;6(6):e20780-e.
237. Quèlo I, Hurtubise M, St-Arnaud R. alphaNAC requires an interaction with c-Jun to exert its transcriptional coactivation. Gene expression. 2002;10(5-6):255-62.
238. Robey PG, Kuznetsov SA, Riminucci M, Bianco P. Bone marrow stromal cell assays: in vitro and in vivo. Methods Mol Biol. 2014;1130:279-93.
239. Mellacheruvu D, Wright Z, Couzens AL, Lambert JP, St-Denis NA, Li T, et al. The CRAPome: a contaminant repository for affinity purification-mass spectrometry data. Nature methods. 2013;10(8):730-6.

240. Gunnell LM, Jonason JH, Loiselle AE, Kohn A, Schwarz EM, Hilton MJ, et al. TAK1 regulates cartilage and joint development via the MAPK and BMP signaling pathways. Journal of bone and mineral research : the official journal of the American Society for Bone and Mineral Research. 2010;25(8):1784-97.
241. Shibuya H, Yamaguchi K, Shirakabe K, Tonegawa A, Gotoh Y, Ueno N, et al. TAB1: an activator of the TAK1 MAPKKK in TGF-beta signal transduction. Science. 1996;272(5265):1179-82.
242. Shim JH, Greenblatt MB, Xie M, Schneider MD, Zou W, Zhai B, et al. TAK1 is an essential regulator of BMP signalling in cartilage. EMBO J. 2009;28(14):2028-41.
243. Takaesu G, Kishida S, Hiyama A, Yamaguchi K, Shibuya H, Irie K, et al. TAB2, a novel adaptor protein, mediates activation of TAK1 MAPKKK by linking TAK1 to TRAF6 in the IL-1 signal transduction pathway. Molecular cell. 2000;5(4):649-58.
244. Feng X, Teitelbaum SL. Osteoclasts: New Insights. Bone research. 2013;1(1):11-26.
245. Xu W, Domingues Rita G, Fonseca-Pereira D, Ferreira M, Ribeiro H, Lopez-Lastra S, et al. NFIL3 Orchestrates the Emergence of Common Helper Innate Lymphoid Cell Precursors. Cell Reports. 2015;10(12):2043-54.
246. Impey S, McCorkle SR, Cha-Molstad H, Dwyer JM, Yochum GS, Boss JM, et al. Defining the CREB regulon: a genome-wide analysis of transcription factor regulatory regions. Cell. 2004;119(7):1041-54.
247. St John HC, Meyer MB, Benkusky NA, Carlson AH, Prideaux M, Bonewald LF, et al. The parathyroid hormone-regulated transcriptome in osteocytes: parallel actions with 1,25-dihydroxyvitamin D3 to oppose gene expression changes during differentiation and to promote mature cell function. Bone. 2015;72:81-91.
248. Zhang X, Odom DT, Koo S-H, Conkright MD, Canettieri G, Best J, et al. Genome-wide analysis of cAMP-response element binding protein occupancy, phosphorylation, and target gene activation in human tissues. Proceedings of the National Academy of Sciences. 2005;102(12):4459-64.
249. St John HC, Bishop KA, Meyer MB, Benkusky NA, Leng N, Kendziorski C, et al. The osteoblast to osteocyte transition: epigenetic changes and response to the vitamin D3 hormone. Mol Endocrinol. 2014;28(7):1150-65.

250. Kostrzewski T, Borg AJ, Meng Y, Filipovic I, Male V, Wack A, et al. Multiple Levels of Control Determine How E4bp4/Nfil3 Regulates NK Cell Development. Journal of immunology (Baltimore, Md : 1950). 2018;200(4):1370-81.
251. Brownstein CA, Towne MC, Luquette LJ, Harris DJ, Marinakis NS, Meinecke P, et al. Mutation of KCNJ8 in a patient with Cantu syndrome with unique vascular abnormalities - support for the role of K(ATP) channels in this condition. Eur J Med Genet. 2013;56(12):678-82.
252. Harakalova M, van Harssel JJ, Terhal PA, van Lieshout S, Duran K, Renkens I, et al. Dominant missense mutations in ABCC9 cause Cantu syndrome. Nature genetics. 2012;44(7):793-6.
253. Guo Y-C, Wang M-Y, Zhang S-W, Wu Y-S, Zhou C-C, Zheng R-X, et al. Ubiquitin-specific protease USP34 controls osteogenic differentiation and bone formation by regulating BMP2 signaling. EMBO J. 2018;37(20):e99398.
254. Pellicelli M, Hariri H, Miller JA, St-Arnaud R. Lrp6 is a target of the PTH-activated alphaNAC transcriptional coregulator. Biochimica et biophysica acta. 2018;1861(2):61-71.
255. Benbrook DM, Jones NC. Heterodimer formation between CREB and JUN proteins. Oncogene. 1990;5(3):295-302.
256. Chen Q, Shou P, Zheng C, Jiang M, Cao G, Yang Q, et al. Fate decision of mesenchymal stem cells: adipocytes or osteoblasts? Cell Death Differ. 2016;23(7):1128-39.
257. Cohen A, Dempster DW, Stein EM, Nickolas TL, Zhou H, McMahon DJ, et al. Increased marrow adiposity in premenopausal women with idiopathic osteoporosis. J Clin Endocrinol Metab. 2012;97(8):2782-91.
258. Justesen J, Stenderup K, Ebbesen EN, Mosekilde L, Steiniche T, Kassem M. Adipocyte tissue volume in bone marrow is increased with aging and in patients with osteoporosis. Biogerontology. 2001;2(3):165-71.
259. Verma S, Rajaratnam JH, Denton J, Hoyland JA, Byers RJ. Adipocytic proportion of bone marrow is inversely related to bone formation in osteoporosis. J Clin Pathol. 2002;55(9):693-8.
260. Sanchez-Gurmaches J, Guertin DA. Adipocytes arise from multiple lineages that are heterogeneously and dynamically distributed. Nature Communications. 2014;5(1):4099.
261. Sanchez-Gurmaches J, Hsiao W-Y, Guertin DA. Highly selective in vivo labeling of subcutaneous white adipocyte precursors with Prx1-Cre. Stem Cell Reports. 2015;4(4):541-50.

262. Rahmani W, Abbasi S, Hagner A, Raharjo E, Kumar R, Hotta A, et al. Hair follicle dermal stem cells regenerate the dermal sheath, repopulate the dermal papilla, and modulate hair type. Developmental cell. 2014;31(5):543-58.
263. Biernaskie J, Paris M, Morozova O, Fagan BM, Marra M, Pevny L, et al. SKPs derive from hair follicle precursors and exhibit properties of adult dermal stem cells. Cell stem cell. 2009;5(6):610-23.
264. Amaya MJ, Nathanson MH. Calcium signaling and the secretory activity of bile duct epithelia. Cell calcium. 2014;55(6):317-24.
265. Oliva-Vilarnau N, Hankeova S, Vorrink SU, Mkrtchian S, Andersson ER, Lauschke VM. Calcium Signaling in Liver Injury and Regeneration. Front Med (Lausanne). 2018;5:192-.
266. Yang Z, Xian H, Hu J, Tian S, Qin Y, Wang RF, et al. USP18 negatively regulates NF-kappaB signaling by targeting TAK1 and NEMO for deubiquitination through distinct mechanisms. Scientific reports. 2015;5:12738.
267. Zhao X, Wu X, Wang H, Yu H, Wang J. USP53 promotes apoptosis and inhibits glycolysis in lung adenocarcinoma through FKBP51-AKT1 signaling. Molecular carcinogenesis. 2020.
268. Wade EM, Daniel PB, Jenkins ZA, McInerney-Leo A, Leo P, Morgan T, et al. Mutations in MAP3K7 that Alter the Activity of the TAK1 Signaling Complex Cause Frontometaphyseal Dysplasia. Am J Hum Genet. 2016;99(2):392-406.
269. Dai L, Aye Thu C, Liu XY, Xi J, Cheung PC. TAK1, more than just innate immunity. IUBMB Life. 2012;64(10):825-34.
270. Zhang Y, O'Keefe RJ, Jonason JH. BMP-TAK1 (MAP3K7) Induces Adipocyte Differentiation Through PPARgamma Signaling. J Cell Biochem. 2017;118(1):204-10.
271. Schild RL, Sonnenberg-Hirche CM, Schaiff WT, Bildirici I, Nelson DM, Sadovsky Y. The kinase p38 regulates peroxisome proliferator activated receptor-gamma in human trophoblasts. Placenta. 2006;27(2-3):191-9.
272. O'Brien CA. Control of RANKL gene expression. Bone. 2010;46(4):911-9.

APPENDIX

COPYRIGHTS AND PERMISSIONS

Figure 1.1

Figure 1.2

Figure 1.3

Figure 1.4 and Figure 1.5

Figure 1.6

REB APPROVAL FOR MICE STUDIES

Special Requests

All | Action Required (1) | Please type to search by Request ID | Search | Clear

1 - 1 of 1 Requests

10 Requests/page

Request Date	Request ID	Publication	Title	Type of Use	Status
09 May 2020	600013196	Annual review of pathology		Republish in a thesis/dissertation	Accepted

1 - 1 of 1 Requests

10 Requests/page

SPRINGER NATURE LICENSE
TERMS AND CONDITIONS

Jul 04, 2020

This Agreement between Shriners Hospital for Children, Canada-Montreal, Department of Human Genetics, McGill University, Montreal,Quebec,Canada -- hadla Hariri ("You") and Springer Nature ("Springer Nature") consists of your license details and the terms and conditions provided by Springer Nature and Copyright Clearance Center.

License Number	4824611407267
License date	May 09, 2020
Licensed Content Publisher	Springer Nature
Licensed Content Publication	Nature Reviews Endocrinology
Licensed Content Title	BMP signalling in skeletal development, disease and repair
Licensed Content Author	Valerie S. Salazar et al
Licensed Content Date	Feb 19, 2016
Type of Use	Thesis/Dissertation
Requestor type	academic/university or research institute
Format	electronic
Portion	figures/tables/illustrations
Number of figures/tables/illustrations	1
High-res required	no

Will you be translating?	no
Circulation/distribution	1 - 29
Author of this Springer Nature content	no
Title	Identification of novel target genes of the PTH-activated NACA transcriptional coregulator in bone
Institution name	McGill University
Expected presentation date	Sep 2020
Portions	Figure 3 entitled: Developmental skeletogenesis
Requestor Location	Shriners Hospital for Children, Canada-Montreal, Department of Human Genetics, McGill University, Montreal,Quebec,Canada 3475 Saint Urbain APT 701 Montreal, QC H2X 2N4 Canada Attn: Shriners Hospital for Children, Canada-Montreal, Department of Human Genetics, McGill University, Montreal,Quebec,Canada
Total	0.00 CAD
Terms and Conditions	

Springer Nature Customer Service Centre GmbH
Terms and Conditions

This agreement sets out the terms and conditions of the licence (the **Licence**) between you and **Springer Nature Customer Service Centre GmbH** (the **Licensor**). By clicking 'accept' and completing the transaction for the material (**Licensed Material**), you also confirm your acceptance of these terms and conditions.

1. Grant of License

1. 1. The Licensor grants you a personal, non-exclusive, non-transferable, world-wide licence to reproduce the Licensed Material for the purpose specified in your order only. Licences are granted for the specific use requested in the order and for no other use, subject to the conditions below.

1. 2. The Licensor warrants that it has, to the best of its knowledge, the rights to license reuse of the Licensed Material. However, you should ensure that the material

you are requesting is original to the Licensor and does not carry the copyright of another entity (as credited in the published version).

1. 3. If the credit line on any part of the material you have requested indicates that it was reprinted or adapted with permission from another source, then you should also seek permission from that source to reuse the material.

2. Scope of Licence

2. 1. You may only use the Licensed Content in the manner and to the extent permitted by these Ts&Cs and any applicable laws.

2. 2. A separate licence may be required for any additional use of the Licensed Material, e.g. where a licence has been purchased for print only use, separate permission must be obtained for electronic re-use. Similarly, a licence is only valid in the language selected and does not apply for editions in other languages unless additional translation rights have been granted separately in the licence. Any content owned by third parties are expressly excluded from the licence.

2. 3. Similarly, rights for additional components such as custom editions and derivatives require additional permission and may be subject to an additional fee. Please apply to Journalpermissions@springernature.com/bookpermissions@springernature.com for these rights.

2. 4. Where permission has been granted **free of charge** for material in print, permission may also be granted for any electronic version of that work, provided that the material is incidental to your work as a whole and that the electronic version is essentially equivalent to, or substitutes for, the print version.

2. 5. An alternative scope of licence may apply to signatories of the STM Permissions Guidelines, as amended from time to time.

3. Duration of Licence

3. 1. A licence for is valid from the date of purchase ('Licence Date') at the end of the relevant period in the below table:

Scope of Licence	Duration of Licence
Post on a website	12 months
Presentations	12 months
Books and journals	Lifetime of the edition in the language purchased

4. Acknowledgement

4. 1. The Licensor's permission must be acknowledged next to the Licenced Material in print. In electronic form, this acknowledgement must be visible at the same time as the figures/tables/illustrations or abstract, and must be hyperlinked to the journal/book's homepage. Our required acknowledgement format is in the Appendix below.

5. Restrictions on use

5. 1. Use of the Licensed Material may be permitted for incidental promotional use and minor editing privileges e.g. minor adaptations of single figures, changes of format, colour and/or style where the adaptation is credited as set out in Appendix 1 below. Any other changes including but not limited to, cropping, adapting, omitting material that affect the meaning, intention or moral rights of the author are strictly prohibited.

5. 2. You must not use any Licensed Material as part of any design or trademark.

5. 3. Licensed Material may be used in Open Access Publications (OAP) before publication by Springer Nature, but any Licensed Material must be removed from OAP sites prior to final publication.

6. Ownership of Rights

6. 1. Licensed Material remains the property of either Licensor or the relevant third party and any rights not explicitly granted herein are expressly reserved.

7. Warranty

IN NO EVENT SHALL LICENSOR BE LIABLE TO YOU OR ANY OTHER PARTY OR ANY OTHER PERSON OR FOR ANY SPECIAL, CONSEQUENTIAL, INCIDENTAL OR INDIRECT DAMAGES, HOWEVER CAUSED, ARISING OUT OF OR IN CONNECTION WITH THE DOWNLOADING, VIEWING OR USE OF THE MATERIALS REGARDLESS OF THE FORM OF ACTION, WHETHER FOR BREACH OF CONTRACT, BREACH OF WARRANTY, TORT, NEGLIGENCE, INFRINGEMENT OR OTHERWISE (INCLUDING, WITHOUT LIMITATION, DAMAGES BASED ON LOSS OF PROFITS, DATA, FILES, USE, BUSINESS OPPORTUNITY OR CLAIMS OF THIRD PARTIES), AND
WHETHER OR NOT THE PARTY HAS BEEN ADVISED OF THE POSSIBILITY OF SUCH DAMAGES. THIS LIMITATION SHALL APPLY NOTWITHSTANDING ANY FAILURE OF ESSENTIAL PURPOSE OF ANY LIMITED REMEDY PROVIDED HEREIN.

8. Limitations

8. 1. ***BOOKS ONLY:***Where **'reuse in a dissertation/thesis'** has been selected the following terms apply: Print rights of the final author's accepted manuscript (for clarity, NOT the published version) for up to 100 copies, electronic rights for use only on a personal website or institutional repository as defined by the Sherpa guideline (www.sherpa.ac.uk/romeo/).

9. Termination and Cancellation

9. 1. Licences will expire after the period shown in Clause 3 (above).

9. 2. Licensee reserves the right to terminate the Licence in the event that payment is not received in full or if there has been a breach of this agreement by you.

Appendix 1 — Acknowledgements:

For Journal Content:
Reprinted by permission from [**the Licensor**]: [**Journal Publisher** (e.g. Nature/Springer/Palgrave)] [**JOURNAL NAME**] [**REFERENCE CITATION** (Article name, Author(s) Name), [**COPYRIGHT**] (year of publication)

For **Advance Online Publication papers:**
Reprinted by permission from [**the Licensor**]: [**Journal Publisher** (e.g. Nature/Springer/Palgrave)] [**JOURNAL NAME**] [**REFERENCE CITATION** (Article name, Author(s) Name), [**COPYRIGHT**] (year of publication), advance online publication, day month year (doi: 10.1038/sj.[JOURNAL ACRONYM].)

For Adaptations/Translations:
Adapted/Translated by permission from [**the Licensor**]: [**Journal Publisher** (e.g. Nature/Springer/Palgrave)] [**JOURNAL NAME**] [**REFERENCE CITATION** (Article name, Author(s) Name), [**COPYRIGHT**] (year of publication)

Note: For any republication from the British Journal of Cancer, the following credit line style applies:

Reprinted/adapted/translated by permission from [**the Licensor**]: on behalf of Cancer Research UK: : [**Journal Publisher** (e.g. Nature/Springer/Palgrave)] [**JOURNAL NAME**] [**REFERENCE CITATION** (Article name, Author(s) Name), [**COPYRIGHT]** (year of publication)

For **Advance Online Publication** papers:
Reprinted by permission from The [**the Licensor**]: on behalf of Cancer Research UK: [**Journal Publisher** (e.g. Nature/Springer/Palgrave)] [**JOURNAL NAME**] [**REFERENCE CITATION** (Article name, Author(s) Name), [**COPYRIGHT**] (year of publication), advance online publication, day month year (doi: 10.1038/sj.[JOURNAL ACRONYM])

For Book content:
Reprinted/adapted by permission from [**the Licensor**]: [**Book Publisher** (e.g. Palgrave Macmillan, Springer etc) [**Book Title**] by [**Book author**(s)] [**COPYRIGHT**] (year of publication)

Other Conditions:

Version 1.2

JOHN WILEY AND SONS LICENSE
TERMS AND CONDITIONS

Jul 04, 2020

This Agreement between Shriners Hospital for Children, Canada-Montreal, Department of Human Genetics, McGill University, Montreal,Quebec,Canada -- hadla Hariri ("You") and John Wiley and Sons ("John Wiley and Sons") consists of your license details and the terms and conditions provided by John Wiley and Sons and Copyright Clearance Center.

License Number	4824670012745
License date	May 09, 2020
Licensed Content Publisher	John Wiley and Sons
Licensed Content Publication	Wiley Books
Licensed Content Title	Endochondral Ossification
Licensed Content Author	Courtney M. Karner, Matthew J. Hilton
Licensed Content Date	Sep 28, 2018
Licensed Content Pages	8
Type of use	Dissertation/Thesis
Requestor type	University/Academic
Format	Electronic

Portion	Figure/table
Number of figures/tables	1
Will you be translating?	No
Title	Identification of novel target genes of the PTH-activated NACA transcriptional coregulator in bone
Institution name	McGill University
Expected presentation date	Sep 2020
Portions	Figure 2.2 on page 3
Requestor Location	Shriners Hospital for Children, Canada-Montreal, Department of Human Genetics, McGill University, Montreal,Quebec,Canada 3475 Saint Urbain APT 701 Montreal, QC H2X 2N4 Canada Attn: Shriners Hospital for Children, Canada-Montreal, Department of Human Genetics, McGill University, Montreal,Quebec,Canada
Publisher Tax ID	EU826007151
Total	0.00 CAD

Terms and Conditions

TERMS AND CONDITIONS

Terms and Conditions

- The materials you have requested permission to reproduce or reuse (the "Wiley Materials") are protected by copyright.

- You are hereby granted a personal, non-exclusive, non-sub licensable (on a stand-alone basis), non-transferable, worldwide, limited license to reproduce the Wiley Materials for the purpose specified in the licensing process. This license, **and any CONTENT (PDF or image file) purchased as part of your order,** is for a one-time use only and limited to any maximum distribution number specified in the license. The first instance of republication or reuse granted by this license must be completed within two years of the date of the grant of this license (although copies prepared before the end date may be distributed thereafter). The Wiley Materials shall not be used in any other manner or for any other purpose, beyond what is granted in the license. Permission is granted subject to an appropriate acknowledgement given to the author, title of the material/book/journal and the publisher. You shall also duplicate the copyright notice that appears in the Wiley publication in your use of the Wiley Material. Permission is also granted on the understanding that nowhere in the text is a previously published source acknowledged for all or part of this Wiley Material. Any third party content is expressly excluded from this permission.

- With respect to the Wiley Materials, all rights are reserved. Except as expressly granted by the terms of the license, no part of the Wiley Materials may be copied, modified, adapted (except for minor reformatting required by the new Publication), translated, reproduced, transferred or distributed, in any form or by any means, and no derivative works may be made based on the Wiley Materials without the prior permission of the respective copyright owner.**For STM Signatory Publishers clearing permission under the terms of the STM Permissions Guidelines only, the terms of the license are extended to include subsequent editions and for editions in other languages, provided such editions are for the work as a whole in situ and does not involve the separate exploitation of the permitted figures or extracts,** You may not alter, remove or suppress in any manner any copyright, trademark or other notices displayed by the Wiley Materials. You may not license, rent, sell, loan, lease, pledge, offer as security, transfer or assign the Wiley Materials on a stand-alone basis, or any of the rights granted to you hereunder to any other person.

- The Wiley Materials and all of the intellectual property rights therein shall at all times remain the exclusive property of John Wiley & Sons Inc, the Wiley Companies, or their respective licensors, and your interest therein is only that of having possession of and the right to reproduce the Wiley Materials pursuant to Section 2 herein during the continuance of this Agreement. You agree that you own no right, title or interest in or to the Wiley Materials or any of the intellectual property rights therein. You shall have no rights hereunder other than the license as provided for above in Section 2. No right, license or interest to any trademark, trade name, service mark or other branding ("Marks") of WILEY or its licensors is granted hereunder, and you agree that you shall not assert any such right, license or interest with respect thereto

- NEITHER WILEY NOR ITS LICENSORS MAKES ANY WARRANTY OR REPRESENTATION OF ANY KIND TO YOU OR ANY THIRD PARTY, EXPRESS, IMPLIED OR STATUTORY, WITH RESPECT TO THE MATERIALS OR THE ACCURACY OF ANY INFORMATION CONTAINED IN THE MATERIALS, INCLUDING, WITHOUT LIMITATION, ANY IMPLIED WARRANTY OF MERCHANTABILITY, ACCURACY, SATISFACTORY QUALITY, FITNESS FOR A PARTICULAR PURPOSE, USABILITY, INTEGRATION OR NON-INFRINGEMENT AND ALL SUCH WARRANTIES ARE HEREBY EXCLUDED BY WILEY AND ITS LICENSORS AND WAIVED BY YOU.

- WILEY shall have the right to terminate this Agreement immediately upon breach of this Agreement by you.

- You shall indemnify, defend and hold harmless WILEY, its Licensors and their respective directors, officers, agents and employees, from and against any actual or threatened claims, demands, causes of action or proceedings arising from any breach of this Agreement by you.

- IN NO EVENT SHALL WILEY OR ITS LICENSORS BE LIABLE TO YOU OR ANY OTHER PARTY OR ANY OTHER PERSON OR ENTITY FOR ANY SPECIAL, CONSEQUENTIAL, INCIDENTAL, INDIRECT, EXEMPLARY OR PUNITIVE DAMAGES, HOWEVER CAUSED, ARISING OUT OF OR IN CONNECTION WITH THE DOWNLOADING, PROVISIONING, VIEWING OR USE OF THE MATERIALS REGARDLESS OF THE FORM OF ACTION, WHETHER FOR BREACH OF CONTRACT, BREACH OF WARRANTY, TORT, NEGLIGENCE, INFRINGEMENT OR OTHERWISE (INCLUDING, WITHOUT LIMITATION, DAMAGES BASED ON LOSS OF PROFITS, DATA, FILES, USE, BUSINESS OPPORTUNITY OR CLAIMS OF THIRD PARTIES), AND WHETHER OR NOT THE PARTY HAS BEEN ADVISED OF THE POSSIBILITY OF SUCH DAMAGES. THIS LIMITATION SHALL APPLY NOTWITHSTANDING ANY FAILURE OF ESSENTIAL PURPOSE OF ANY LIMITED REMEDY PROVIDED HEREIN.

- Should any provision of this Agreement be held by a court of competent jurisdiction to be illegal, invalid, or unenforceable, that provision shall be deemed amended to achieve as nearly as possible the same economic effect as the original provision, and the legality, validity and enforceability of the remaining provisions of this Agreement shall not be affected or impaired thereby.

- The failure of either party to enforce any term or condition of this Agreement shall not constitute a waiver of either party's right to enforce each and every term and condition of this Agreement. No breach under this agreement shall be deemed waived or excused by either party unless such waiver or consent is in writing signed by the party granting such waiver or consent. The waiver by or consent of a party to a breach of any provision of this Agreement shall not operate or be construed as a waiver of or consent to any other or subsequent breach by such other party.

- This Agreement may not be assigned (including by operation of law or otherwise) by you without WILEY's prior written consent.

- Any fee required for this permission shall be non-refundable after thirty (30) days from receipt by the CCC.

- These terms and conditions together with CCC's Billing and Payment terms and conditions (which are incorporated herein) form the entire agreement between you and WILEY concerning this licensing transaction and (in the absence of fraud) supersedes all prior agreements and representations of the parties, oral or written. This Agreement may not be amended except in writing signed by both parties. This Agreement shall be binding upon and inure to the benefit of the parties' successors, legal representatives, and authorized assigns.

- In the event of any conflict between your obligations established by these terms and conditions and those established by CCC's Billing and Payment terms and conditions, these terms and conditions shall prevail.

- WILEY expressly reserves all rights not specifically granted in the combination of (i) the license details provided by you and accepted in the course of this licensing transaction, (ii) these terms and conditions and (iii) CCC's Billing and Payment terms

and conditions.

- This Agreement will be void if the Type of Use, Format, Circulation, or Requestor Type was misrepresented during the licensing process.

- This Agreement shall be governed by and construed in accordance with the laws of the State of New York, USA, without regards to such state's conflict of law rules. Any legal action, suit or proceeding arising out of or relating to these Terms and Conditions or the breach thereof shall be instituted in a court of competent jurisdiction in New York County in the State of New York in the United States of America and each party hereby consents and submits to the personal jurisdiction of such court, waives any objection to venue in such court and consents to service of process by registered or certified mail, return receipt requested, at the last known address of such party.

WILEY OPEN ACCESS TERMS AND CONDITIONS

Wiley Publishes Open Access Articles in fully Open Access Journals and in Subscription journals offering Online Open. Although most of the fully Open Access journals publish open access articles under the terms of the Creative Commons Attribution (CC BY) License only, the subscription journals and a few of the Open Access Journals offer a choice of Creative Commons Licenses. The license type is clearly identified on the article.

The Creative Commons Attribution License

The Creative Commons Attribution License (CC-BY) allows users to copy, distribute and transmit an article, adapt the article and make commercial use of the article. The CC-BY license permits commercial and non-

Creative Commons Attribution Non-Commercial License

The Creative Commons Attribution Non-Commercial (CC-BY-NC)License permits use, distribution and reproduction in any medium, provided the original work is properly cited and is not used for commercial purposes.(see below)

Creative Commons Attribution-Non-Commercial-NoDerivs License

The Creative Commons Attribution Non-Commercial-NoDerivs License (CC-BY-NC-ND) permits use, distribution and reproduction in any medium, provided the original work is properly cited, is not used for commercial purposes and no modifications or adaptations are made. (see below)

Use by commercial "for-profit" organizations

Use of Wiley Open Access articles for commercial, promotional, or marketing purposes requires further explicit permission from Wiley and will be subject to a fee.

Further details can be found on Wiley Online Library
http://olabout.wiley.com/WileyCDA/Section/id-410895.html

Other Terms and Conditions:

v1.10 Last updated September 2015

Paracrine and endocrine actions of bone—the functions of secretory proteins from osteoblasts, osteocytes, and osteoclasts

Author: Yujiao Han et al

Publication: Bone Research

Publisher: Springer Nature

Date: May 24, 2018

SPRINGER NATURE LICENSE
TERMS AND CONDITIONS

Jul 03, 2020

This Agreement between Shriners Hospital for Children, Canada-Montreal, Department of Human Genetics, McGill University, Montreal,Quebec,Canada -- hadla Hariri ("You") and Springer Nature ("Springer Nature") consists of your license details and the terms and conditions provided by Springer Nature and Copyright Clearance Center.

License Number	4825161028155
License date	May 10, 2020
Licensed Content Publisher	Springer Nature
Licensed Content Publication	Nature Reviews Molecular Cell Biology
Licensed Content Title	Forming functional fat: a growing understanding of adipocyte differentiation
Licensed Content Author	Ana G. Cristancho et al
Licensed Content Date	Sep 28, 2011
Type of Use	Thesis/Dissertation
Requestor type	academic/university or research institute
Format	electronic
Portion	figures/tables/illustrations
Number of figures/tables/illustrations	1
High-res required	no

Will you be translating?	no
Circulation/distribution	1 - 29
Author of this Springer Nature content	no
Title	Identification of novel target genes of the PTH-activated NACA transcriptional coregulator in bone
Institution name	McGill University
Expected presentation date	Sep 2020
Portions	Figure 2
Requestor Location	Shriners Hospital for Children, Canada-Montreal, Department of Human Genetics, McGill University, Montreal,Quebec,Canada 3475 Saint Urbain APT 701 Montreal, QC H2X 2N4 Canada Attn: Shriners Hospital for Children, Canada-Montreal, Department of Human Genetics, McGill University, Montreal,Quebec,Canada
Total	0.00 CAD
Terms and Conditions	

Springer Nature Customer Service Centre GmbH
Terms and Conditions

This agreement sets out the terms and conditions of the licence (the **Licence**) between you and **Springer Nature Customer Service Centre GmbH** (the **Licensor**). By clicking 'accept' and completing the transaction for the material (**Licensed Material**), you also confirm your acceptance of these terms and conditions.

1. Grant of License

1. 1. The Licensor grants you a personal, non-exclusive, non-transferable, world-wide licence to reproduce the Licensed Material for the purpose specified in your order only. Licences are granted for the specific use requested in the order and for no other use, subject to the conditions below.

1. 2. The Licensor warrants that it has, to the best of its knowledge, the rights to license reuse of the Licensed Material. However, you should ensure that the material

you are requesting is original to the Licensor and does not carry the copyright of another entity (as credited in the published version).

1. 3. If the credit line on any part of the material you have requested indicates that it was reprinted or adapted with permission from another source, then you should also seek permission from that source to reuse the material.

2. Scope of Licence

2. 1. You may only use the Licensed Content in the manner and to the extent permitted by these Ts&Cs and any applicable laws.

2. 2. A separate licence may be required for any additional use of the Licensed Material, e.g. where a licence has been purchased for print only use, separate permission must be obtained for electronic re-use. Similarly, a licence is only valid in the language selected and does not apply for editions in other languages unless additional translation rights have been granted separately in the licence. Any content owned by third parties are expressly excluded from the licence.

2. 3. Similarly, rights for additional components such as custom editions and derivatives require additional permission and may be subject to an additional fee. Please apply to Journalpermissions@springernature.com/bookpermissions@springernature.com for these rights.

2. 4. Where permission has been granted **free of charge** for material in print, permission may also be granted for any electronic version of that work, provided that the material is incidental to your work as a whole and that the electronic version is essentially equivalent to, or substitutes for, the print version.

2. 5. An alternative scope of licence may apply to signatories of the STM Permissions Guidelines, as amended from time to time.

3. Duration of Licence

3. 1. A licence for is valid from the date of purchase ('Licence Date') at the end of the relevant period in the below table:

Scope of Licence	Duration of Licence
Post on a website	12 months
Presentations	12 months
Books and journals	Lifetime of the edition in the language purchased

4. Acknowledgement

4. 1. The Licensor's permission must be acknowledged next to the Licenced Material in print. In electronic form, this acknowledgement must be visible at the same time as the figures/tables/illustrations or abstract, and must be hyperlinked to the journal/book's homepage. Our required acknowledgement format is in the Appendix below.

5. Restrictions on use

5. 1. Use of the Licensed Material may be permitted for incidental promotional use and minor editing privileges e.g. minor adaptations of single figures, changes of format, colour and/or style where the adaptation is credited as set out in Appendix 1 below. Any other changes including but not limited to, cropping, adapting, omitting material that affect the meaning, intention or moral rights of the author are strictly prohibited.

5. 2. You must not use any Licensed Material as part of any design or trademark.

5. 3. Licensed Material may be used in Open Access Publications (OAP) before publication by Springer Nature, but any Licensed Material must be removed from OAP sites prior to final publication.

6. Ownership of Rights

6. 1. Licensed Material remains the property of either Licensor or the relevant third party and any rights not explicitly granted herein are expressly reserved.

7. Warranty

IN NO EVENT SHALL LICENSOR BE LIABLE TO YOU OR ANY OTHER PARTY OR ANY OTHER PERSON OR FOR ANY SPECIAL, CONSEQUENTIAL, INCIDENTAL OR INDIRECT DAMAGES, HOWEVER CAUSED, ARISING OUT OF OR IN CONNECTION WITH THE DOWNLOADING, VIEWING OR USE OF THE MATERIALS REGARDLESS OF THE FORM OF ACTION, WHETHER FOR BREACH OF CONTRACT, BREACH OF WARRANTY, TORT, NEGLIGENCE, INFRINGEMENT OR OTHERWISE (INCLUDING, WITHOUT LIMITATION, DAMAGES BASED ON LOSS OF PROFITS, DATA, FILES, USE, BUSINESS OPPORTUNITY OR CLAIMS OF THIRD PARTIES), AND
WHETHER OR NOT THE PARTY HAS BEEN ADVISED OF THE POSSIBILITY OF SUCH DAMAGES. THIS LIMITATION SHALL APPLY NOTWITHSTANDING ANY FAILURE OF ESSENTIAL PURPOSE OF ANY LIMITED REMEDY PROVIDED HEREIN.

8. Limitations

8. 1. ***BOOKS ONLY:***Where **'reuse in a dissertation/thesis'** has been selected the following terms apply: Print rights of the final author's accepted manuscript (for clarity, NOT the published version) for up to 100 copies, electronic rights for use only on a personal website or institutional repository as defined by the Sherpa guideline (www.sherpa.ac.uk/romeo/).

9. Termination and Cancellation

9. 1. Licences will expire after the period shown in Clause 3 (above).

9. 2. Licensee reserves the right to terminate the Licence in the event that payment is not received in full or if there has been a breach of this agreement by you.

Appendix 1 — Acknowledgements:

For Journal Content:
Reprinted by permission from [**the Licensor**]: [**Journal Publisher** (e.g. Nature/Springer/Palgrave)] [**JOURNAL NAME**] [**REFERENCE CITATION** (Article name, Author(s) Name), [**COPYRIGHT**] (year of publication)

For **Advance Online Publication papers:**
Reprinted by permission from [**the Licensor**]: [**Journal Publisher** (e.g. Nature/Springer/Palgrave)] [**JOURNAL NAME**] [**REFERENCE CITATION** (Article name, Author(s) Name), [**COPYRIGHT**] (year of publication), advance online publication, day month year (doi: 10.1038/sj.[JOURNAL ACRONYM].)

For Adaptations/Translations:
Adapted/Translated by permission from [**the Licensor**]: [**Journal Publisher** (e.g. Nature/Springer/Palgrave)] [**JOURNAL NAME**] [**REFERENCE CITATION** (Article name, Author(s) Name), [**COPYRIGHT**] (year of publication)

Note: For any republication from the British Journal of Cancer, the following credit line style applies:

Reprinted/adapted/translated by permission from [**the Licensor**]: on behalf of Cancer Research UK: : [**Journal Publisher** (e.g. Nature/Springer/Palgrave)] [**JOURNAL NAME**] [**REFERENCE CITATION** (Article name, Author(s) Name), [**COPYRIGHT]** (year of publication)

For **Advance Online Publication** papers:
Reprinted by permission from The [**the Licensor**]: on behalf of Cancer Research UK: [**Journal Publisher** (e.g. Nature/Springer/Palgrave)] [**JOURNAL NAME**] [**REFERENCE CITATION** (Article name, Author(s) Name), [**COPYRIGHT**] (year of publication), advance online publication, day month year (doi: 10.1038/sj.[JOURNAL ACRONYM])

For Book content:
Reprinted/adapted by permission from [**the Licensor**]: [**Book Publisher** (e.g. Palgrave Macmillan, Springer etc) [**Book Title**] by [**Book author**(s)] [**COPYRIGHT**] (year of publication)

Other Conditions:

Version 1.2

McGill

December 13, 2019

Animal Certificate

This is to certify that **Dr. Rene St-Arnaud, Department of Medicine, Shriners Hospital,** currently holds an approved Animal Use Protocol **# 2001-4491** with McGill University and its Affiliated Hospitals' Research Institutes for the following project:

Animal Use Protocol Title: Gene expression in bone cells: the alphaNAC transcriptional coregulator as a downstream effector of PTH action in bone / The FIAT transcriptional repressor as a drug target for bone regeneration

Start date: December 1, 2019

Expiration date: December 1, 2020

McGill University and Affiliated Hospitals Research Institutes recognize the importance of animal research in our efforts to further our knowledge of natural processes, diseases and conservation. Research, educational and testing projects are conducted with full commitment to the wellbeing of the animal subjects. In order to limit animal use to meritorious research or educational projects, the institution relies on stringent peer review processes, along with assessment of ethical issues by the Animal Care Committee. McGill University recognizes that the use of animals in research, teaching and testing carries significant responsibilities. The institution will continue to develop and maintain guidelines and regulations, following the high standards established by the Canadian Council on Animal Care. It is committed to conducting the highest-quality research and to providing animals with the best care.

Melanie Tremblay, Ph.D
Animal Ethics and Compliance Admin | Animal Compliance Office
Office of Vice-Principal (Research and Innovation)
Suite 325, James Administration Building, McGill University
845 Sherbrooke Street West, Montreal, Quebec, Canada H3A 0G4
animal.approvals@mcgill.ca